Dissertation
submitted to the
Combined Faculty of Mathematics, Engineering and Natural Sciences
of Heidelberg University, Germany
for the degree of
Doctor of Natural Sciences

Put forward by

Philipp Eitner

born in Ludwigshafen (Germany)

Oral examination: 20.10.2025

3D Radiation-Hydrodynamics Stellar Atmospheres and Non-LTE Spectrum Synthesis for Chemical Abundance Measurements of Galactic Stars

Referees:

Dr. Maria Bergemann

Prof. Dr. Norbert Christlieb

Examination Committee:

Prof. Dr. Hans-Walter Rix

Priv.-Doz. Dr. Andreas Bauswein

Zusammenfassung

Präzise Messungen stellarer Elementhäufigkeiten sind ein fundamentales Werkzeug der galaktischen Archäologie und entscheidend für das Verständnis der Geschichte der Milchstraße. Traditionelle Modellierungstechniken basieren auf eindimensionalen (1D), hydrostatischen Sternatmosphären und lokalen thermodynamischen Gleichgewicht (LTE) bei der Spektralsynthese, was sich zunehmend als unzureichend erwiesen hat. In dieser Dissertation untersuche ich, wie sich der Verzicht auf 3D Strahlungshydrodynamik (RHD) und non-LTE (NLTE) Strahlungstransfer auf unser Verständnis der galaktischen Entwicklung auswirkt. Anhand von NLTE-Häufigkeiten von Ni und Fe stelle ich fest, dass LTE-Trends fälschlicherweise auf eine Dominanz klassischer Typ-Ia-Supernovae (SNe Ia) hindeuten, während in NLTE die Entwicklung von [Ni/Fe] am besten durch $\sim 80\,\%$ sub-Chandrasekhar SNe Ia beschrieben wird. Um diese Modellierungseinschränkungen zu überwinden, stelle ich ich `M3DIS` vor – einen neuen, hoch effizienten und flexiblen Code zur Berechnung 3D-RHD-basierter Sternatmosphärenmodelle. `M3DIS` kann Atmosphären vom FGK-Typ in weniger als 5 000 CPU-h relaxieren, was auf mittelgroßen Computerclustern innerhalb von 24 h realisierbar ist. Mit diesen neu entwickelten Werkzeugen richte ich den Fokus auf die metallärmsten Sterne der Galaxie, die häufig eine deutliche Kohlenstoffanreicherung aufweisen (CEMP Sterne), und finde starke 3D-Effekte (bis zu -0.7 dex) auf die Kohlenstoffhäufigkeiten. Je nach Metallizität reduziert dies den Anteil an CEMP-Sternen um bis zu $\sim 30\,\%$, was auf einen um 20 % geringeren Beitrag schwacher Supernovae in der frühen Galaxie hinweist. Diese Dissertation unterstreicht die Notwendigkeit von 3D NLTE in der galaktischen Archäologie und liefert die Werkzeuge, um diese zum neuen Standard der Astronomie zu machen.

Abstract

Precise measurements of stellar chemical abundances are the fundamental tool in Galactic Archaeology, and key to unraveling the formation and evolutionary history of the Milky Way Galaxy. Traditional modeling techniques assume 1D hydrostatic stellar atmospheres and local thermodynamic equilibrium (LTE) in the spectrum synthesis, which is increasingly shown to be inadequate. In this thesis, I investigate how the neglect of 3D radiation hydrodynamics (RHD) and non-LTE (NLTE) radiative transfer influences our understanding of Galactic evolution. By deriving NLTE abundances of Ni and Fe for a large stellar sample, I find that LTE trends wrongfully suggest the dominance of classical type Ia supernovae (SNe Ia), while in NLTE, the [Ni/Fe] evolution is best reproduced by $\sim 80\,\%$ sub-Chandrasekhar-mass SNe Ia. To overcome these limitations of the current modeling, I present `M3DIS`, a new, highly efficient, and flexible code for constructing 3D RHD models of stellar atmospheres. `M3DIS` can relax FGK-type atmospheres in under 5 000 CPU-h, achievable within 24 h on intermediate-size clusters. Using these newly developed tools, I shift the focus towards the most metal-poor stars, which are found to be carbon-enhanced (CEMP stars) in large quantities, and find large 3D effects (up to -0.7 dex) on C abundances. Depending on the metallicity, this reduces the overall CEMP fraction by up to $\sim 30\,\%$, which suggest a 20 % lower contribution from faint supernovae in the early Galaxy. This thesis underlines the need for 3D NLTE modeling in Galactic Archaeology, and provides the tools to make them the new standard in astronomy.

Acknowledgements

This project came to life with the help, encouragement, and support from many, to whom I owe my sincerest gratitude.

My deepest thanks go to my supervisor, Maria Bergemann, for her incredible support and guidance. When I stumbled into your office almost a decade ago, I never could have imagined what an amazing journey lies ahead of me. I am incredibly grateful for everything you have done, your scientific guidance, all the work you put in, and the time you always took to help. You showed me the world of science in a way that I could never have imagined. You made it possible for me to meet so many interesting people and visit places I never thought I would see. I am deeply grateful for your support, patience, and belief in me. Thank you for everything, Maria, I will never forget that.

I also want to thank Norbert Christlieb for agreeing to be the second referee of this thesis. I know your schedule is very full, so again thank you so much for taking the time for me regardless. In addition, I would like to thank Hans-Walter Rix and Andreas Bauswein for taking the time to be part of my examination committee. It is truly an honor, thank you very much.

During my nearly 10 years at MPIA, I met countless amazing people who hold a special place in my heart, which makes it impossible to name them all here. Thank you, Richard, for all the extensive coding sessions in Copenhagen, the museum visits in Chicago, the spiritual temple exploration in Kyoto, and so much more! Thank you Nick for the exciting trip we had to Australia, thank you Ashley, Ivo, Evans, and Amanda for your great hospitality. I also thank Åke and Andrius for their immense help with handling `DISPATCH` and Jonas for his guidance since he joined our group.

The last few years have been difficult, but they would have been impossible without my friends and family. Thank you, Steven, Anna, Mama, and Papa, for always supporting me and always seeing the light at the end of the tunnel. And I especially thank you, Jenny, for always being there for me when I am impossible to be around, cheering me up when I am impossible to cheer up, and believing in me when I myself cannot. Danke für alles, ich liebe dich.

Contents

List of Abbreviations

1D one-dimensional

3D three-dimensional

LTE local thermodynamic equilibrium

NLTE non-LTE

CLV center-to-limb variation

EW equivalent width

CoG curve-of-growth

MLT mixing-length theory

HE hydrostatic equilibrium

HD hydrodynamics

RHD radiation-hydrodynamics

RT radiative transfer

CC core-collapse

SN supernova

SNe supernovae

SN Ia type-Ia supernova

DTD delay-time distribution

M_{Ch} Chandrasekhar mass

SFR star formation rate

IMF initial mass function

BBN Big Bang nucleosynthesis

NSE nuclear statistical equilibrium

CMB cosmic microwave background

WD white dwarf

NS neutron star

BH black hole

AGB asymptotic giant branch

MS main sequence

GCE Galactic chemical evolution

dSph dwarf spheroidal galaxy

UFD ultra-faint dwarf galaxy,

Pop III Population III

CEMP carbon-enhanced metal-poor

4MOST 4-metre multi-Object Spectroscopic Telescope survey

PLATO Planetary Transits and Oscillations of stars

Personal Motivation

It has always fascinated me that the tiny points of light scattered across the night sky are, in truth, enormous balls of gas, unimaginably large, massive, and hot, held together by gravity and situated at distances that stretch the limits of human understanding. Yet, despite all that, they are not beyond our reach. Each photon they send is essentially like a page out of their diary – containing information about themselves, the life of their ancestors, the environment they reside in, and how they will eventually perish – written in a language that we do not understand. It is through the tools of astrophysics – and in particular, through methods of spectroscopy and a deeper physical understanding about the interior of stars – that we are able to translate their message step-by-step.

In recent years, large-scale spectroscopic surveys such as APOGEE, GALAH, LAMOST, and Gaia-ESO have significantly increased the availability of high-resolution spectroscopic data. These efforts have produced vast data sets, containing millions of stellar spectra across various stellar types and Galactic environments, rich with physical and chemical data that await interpretation. Despite significant advancements in stellar atmosphere models and spectral analysis – evolving from basic one-dimensional (1D) hydrostatic models in local thermodynamic equilibrium (LTE) to comprehensive three-dimensional (3D) simulations of sub-surface convection and the photosphere – they still fall short due to numerical complexity and cannot yet process the vast influx of spectral data. Therefore, only simplified models are applied to interpret the spectra from these millions of stars, which may in the end result in misconceptions about the environment they reside in and what their progenitors are.

In this thesis, I show that the use of classical models leads to a distorted understanding of how most white dwarfs exploded in the history of the galaxy and how the first stars ended their lives. I furthermore aim to bridge the gap between models and observations by developing a new 3D radiation-hydrodynamics code that will make on-the-fly 3D non-LTE spectra fitting possible for the upcoming PLATO and 4MOST surveys and will finally allow us to understand better what stars were telling us all along.

“Our telescopes may probe farther and farther into the depths of space; but (...) what appliance can pierce through the outer layers of a star and test the conditions within? (...) We learn what we do learn by awaiting and interpreting the messages dispatched to us by the objects of nature.” – Sir Arthur S. Eddington (1926)

1 Introduction

The starlight that reaches us contains vast information about cosmic history, star formation, and galaxy evolution. The dispersion of this light into spectra reveals the physical state, effective temperature, surface gravity, and chemical composition of these stars. The chemical composition in particular serves as a record of the stellar history, shedding light on their origins and evolution. Accurately measuring these elemental abundances in different stars – with vastly different masses, lifetimes, and ages – across the entire Galaxy allows for the reconstruction of the history of the Milky Way and is thus of major interest across astronomy.

1.1 Stellar Spectroscopy

The quantitative study of stellar spectra began with the discovery of dark lines in the solar spectrum by Joseph von Fraunhofer in 1814. However, the significance of these findings became evident only 45 years later when Gustav Kirchhoff and Robert Bunsen identified that these dark lines matched the emission lines observed in their newly developed "flame spectroscopy" in specific elements. This discovery led them to deduce the presence of these elements in the outer layers of the Sun, since they absorb light at these specific wavelengths (Kirchhoff 1860). Subsequent analyses of stellar spectra resulted in the development of the O, B, A, F, G, K, M classification system, still used today, and led to the conclusion that stars are essentially hot planets containing the same metals as found on Earth.

In 1925, Cecilia Payne-Gaposchkin was the first to apply the newly developed Saha equation, which connects element ionization stages to surrounding temperatures, demonstrating that the spectral class sequence can be explained by varying ionization equilibria in stars of different temperatures, not diverse chemical compositions (Payne-Gaposchkin 1925). She discovered that stars possess metal abundances similar to Earth, but contain far more hydrogen and helium. Her work revealed that hydrogen and helium are the primary elements in stars and the universe, establishing the foundations for stellar physics and chemical evolution.

To determine information about stars from observations of their spectra, models of the outer stellar layers are crucial, as these regions have low enough densities to allow radiation to

escape. These *model atmospheres*, which describe the physical conditions in these layers, are essential to predict the spectral line shapes for specific stellar parameters and abundances, allowing for a comparison with observations (Gray 1992). Historically, quantitative stellar spectroscopy relied on one-dimensional (1D) models in hydrostatic equilibrium (HE), assuming local thermodynamic equilibrium (LTE) with the radiation field. The first grids of these models computed by Gustafsson et al. (1975) and Kurucz (1979) enabled the efficient modeling of spectral features and derivatives of them are still the base-line for stellar diagnostics today when analyzing spectra from millions of stars in large spectroscopic surveys (e.g. Gilmore et al. 2012; Jönsson et al. 2020; Xiang et al. 2019; Buder et al. 2024).

However, as observational techniques and computational resources improve, the limitations of 1D HE models become more and more apparent. It is not at least direct observations of the Sun which reveal that the solar surface is covered with a complex, time-dependent granular pattern, a complicated velocity field which cannot be described by a 1D gas at rest. Parameterizations such as the *Mixing-Length Theory* (MLT, Prandtl 1925; Henyey et al. 1965) were adopted to – at least approximately – account for the influence of convective motions on the atmospheric structure (Gustafsson et al. 2008), while additional ad hoc broadening parameters such as micro- and macro-turbulence were introduced to match observed spectral line shapes (e.g. Struve & Elvey 1934; Gray 1973). These parameters are not emerging self-consistently from models and hence need additional calibration (e.g. Barklem et al. 2002). Besides these inconsistencies, it is furthermore found that observed spectral lines show asymmetries and convective shifts (e.g. Dravins et al. 1981; Balthasar 1984; Allende Prieto et al. 2002; Löhner-Böttcher et al. 2019), which are not reproduced in the 1D HE framework (Asplund et al. 2000) and hence motivate the development of physically more realistic models of stellar atmospheres.

Given that stellar convective motions are intrinsically three-dimensional and time-dependent, the logical progression is transitioning from 1D HE to time-dependent, three-dimensional radiation-hydrodynamics (3D RHD) simulations. These simulations aim to accurately model the turbulent structure and convective velocity fields in stellar atmospheres, including the photosphere crucial for spectral line formation. The first 3D stellar atmosphere models were developed by Nordlund (1982), successfully simulating solar granulation. Advances in computing infrastructure and numerical methods have since enabled the development of improved 3D RHD models with higher spatial resolution and more precise radiation handling (Ludwig et al. 1990) that span extended stellar periods. Notable examples here are the `STAGGER` (e.g. Nordlund & Galsgaard 1995; Collet et al. 2007; Magic et al. 2013a; Collet et al. 2011), `CO5BOLD` (e.g. Freytag et al. 1996; Freytag & Höfner 2008; Ludwig et al. 2009a; Freytag et al. 2012; Ludwig & Steffen 2016), and `MURaM` (e.g. Vögler et al. 2004, 2005; Rempel 2014) codes. In the past, these codes have been successfully applied to simulations of red giant (e.g. Wedemeyer et al. 2017; Klevas et al. 2017) and red supergiant stars

(Chiavassa et al. 2009), small-scale dynamo magnetic fields (e.g. Rempel 2014; Witzke et al. 2023; Riva et al. 2024), coronae (e.g. Rempel 2017), and complex chromosphere radiative transfer (Gudiksen et al. 2011; Przybylski et al. 2022).

Despite significant improvements in 3D models over time, it is mainly computational complexity that prevents them from replacing classical 1D HE models for large-scale applications and limits their applicability to the detailed analysis of individual stars or small stellar samples. Although major achievements in this context were accomplished by Ludwig et al. (2009a) and Magic et al. (2013a); Rodríguez Díaz et al. (2024), who developed the first grids of 3D atmospheres, CIFIST and the STAGGER grid, respectively, the existing grids of model atmospheres are either not publicly available and/or rather sparsely sampling the stellar parameter space (see Sec. 2.1.7). Because the creation of a single model atmosphere with the codes in use today may require weeks of computation time (C. Lagae, priv. conv.) – and the codes furthermore are not public – 3D RHD models at the moment are not capable of replacing 1D HE models for large-scale applications.

The computation of 3D spectra in the post-processing is furthermore computationally demanding. To complicate things further, there have been a number of studies who find a significant influence of non-local thermodynamic equilibrium (non-LTE, NLTE) effects on abundances derived using 1D and also 3D stellar atmospheres of late-type stars.

A frequent issue identified in multiple studies is that abundances derived from lines with different lower energy level excitation potentials – or different ions of the same species – are inconsistent, which has been attributed to ignoring NLTE effects (e.g. Athay & Lites 1972; Ruland et al. 1980; Feltzing & Gustafsson 1998; Bergemann & Gehren 2008; Bergemann 2011; Bergemann et al. 2012a; Sneden et al. 2016; Bergemann et al. 2019). Furthermore, abundances determined under the LTE approximation can differ significantly from those derived with NLTE methods, which has been extensively analyzed for various different species such as, e.g. H (Mashonkina et al. 2008), Li (Asplund et al. 1999; Lind et al. 2009, 2013), and O (Bergemann et al. 2021), Fe-peak elements (Scott et al. 2015) such as Mn (Bergemann & Gehren 2008; Bergemann et al. 2019), Fe (Thévenin & Idiart 1999; Bergemann et al. 2012a; Lind et al. 2012), Ni (Bergemann et al. 2021), and Cr (Bergemann & Cescutti 2010), but also heavier elements (Mashonkina & Gehren 2000; Mashonkina et al. 2008; Gallagher et al. 2020; Mashonkina & Romanovskaya 2022; Storm & Bergemann 2023).

It has also been shown in studies of individual stars, such as selected late-type stars, metal-poor stars, or the Sun (e.g. Asplund et al. 1999, 2009; Ludwig et al. 2009b; Ludwig & Steffen 2016; Bergemann et al. 2019, 2021; Lagae et al. 2023; Lind & Amarsi 2024) that the dynamic velocity fields in combination with temperature and density variations in 3D RHD model atmospheres directly influence the shape of spectral lines and thus stellar parameters and abundances derived from observations. They additionally have been shown to influence

the statistical equilibrium of different species and therefore may impact the departures from LTE differently than observed in 1D studies, which means that the effects of 3D and NLTE are intertwined and can not be studied individually. A complete 3D NLTE treatment of the radiation field thus seems to be necessary in order to accurately derive stellar parameters, specifically for Fe-peak elements in metal-poor and/or red giant stars (Asplund et al. 1999; Bergemann et al. 2019).

Studies exploring 3D NLTE effects for certain species in stellar samples of a few 100 stars exist (e.g. Storm et al. 2025), but computational restrictions often limit them to either an average 3D (<3D>) analysis or interpolation within a grid of 3D NLTE−1D LTE abundance corrections. The former accurately represents the average differences between 3D and 1D model atmospheres but fails to address temperature inhomogeneities and the full velocity distributions (e.g. Holzreuter & Solanki 2013; Amarsi et al. 2016). The latter captures the complete 3D atmospheric nature but depends on spectral line equivalent widths rather than direct observation fitting, and is indirectly influenced by hyperparameters like microturbulence and mixing-length used to derive 1D LTE abundances. Both methods are limited by the sparse availability of current 3D model atmosphere grids. A robust 3D NLTE fit is the most reliable method for determining stellar abundances, which requires the resolution of computational issues when the objective is to apply 3D NLTE methods to millions of stars.

1.2 Galactic Archeology

It is precisely this analysis of stellar abundances across a broad, extensive population of stars that is needed for a comprehensive understanding of the Galactic chemical evolution (GCE) and the evolution of individual stellar populations (Matteucci 2003; Tornatore et al. 2007; Matteucci 2014). Studies of this kind offer constraints on different nucleosynthesis sites – such as core-collapse (CC, e.g. Woosley et al. 2002; Portinari et al. 1998; Kobayashi et al. 2006; Nomoto et al. 2006; Limongi & Chieffi 2018) and type-Ia (e.g. Fink et al. 2010; Seitenzahl et al. 2013a; Ruiter 2020) supernovae (SNe), asymptotic giant branch (AGB) feedback (e.g. Marigo 2001; Karakas 2010; Karakas & Lattanzio 2014), or neutron star (NS) mergers (e.g. Bauswein et al. 2013; Rosswog et al. 2014) – as well as the overall star formation histories and their environmental characteristics (Côté et al. 2017; Côté 2018). Using GCE models (Matteucci 2003), which simulate the chemical history of stellar populations over time, one can derive insights by comparing them with observed abundance patterns.

Although GCE models exist with increasing complexity – from classical models (Chiappini et al. 1997), over radial migration (Sellwood & Binney 2002; Schönrich & Binney 2009; Grand et al. 2015), galaxy mergers (Mihos & Hernquist 1996; Springel et al. 2005), Galactic winds driven by supernova feedback (Strickland & Heckman 2009; Smith et al. 2018), or halo formation (Heger & Woosley 2002, 2010; Hartwig et al. 2018; Magg et al. 2022a;

Klessen & Glover 2023; Hartwig et al. 2024), to cosmological zoom-in simulations (Grand et al. 2017, 2024; Pinna et al. 2024) – the frequency, specific explosion mechanisms, and yields of individual chemical production sites remain significant uncertainties when modeling current observables (Romano et al. 2010; Côté et al. 2016) and often require calibration to reflect Galactic abundance trends accurately (e.g. François et al. 2004; Palla 2021).

GCE models are furthermore commonly used to fit observed abundance distributions to obtain information about different processes in the Galaxy (e.g. Côté et al. 2017; Kobayashi et al. 2020b) Consequently, systematic offsets in stellar abundances, including 3D and NLTE effects, directly relate to misinterpretation and misjudgment of individual parameters, such as e.g. nucleosynthetic production sites. An important example in this regard are SNe Ia, which are assumed to have a uniform brightness allowing for their use as cosmological standard candles (Riess et al. 1998), although emerging evidence suggests multiple explosion mechanisms beyond the traditional model (e.g. Hillebrandt et al. 2013; Ruiter et al. 2013; Blondin et al. 2017; Kirby et al. 2019; Ruiter 2020; Eitner et al. 2020; de los Reyes et al. 2020; Flörs et al. 2020). Because there are multiple pathways possible that lead to a SNe Ia explosion (see Ruiter & Seitenzahl 2025, for a comprehensive overview) the signature they imprint on the Galactic chemical distribution is key to investigate which of these indeed appear in nature (Kobayashi et al. 2020a,b).

While SNe Ia influence the relatively metal-rich part of the Galactic distribution (Matteucci & Greggio 1986), abundance patterns found in the oldest, most metal-poor, stars in the Galaxy provide insights into their predecessors – the first, Population III (Pop III) stars – and early Galactic conditions (Spite et al. 2013). Largely, these stars exhibit unusually low levels of iron and other metals, while at the same time showing high levels of carbon, which lead to their classification as carbon-enhanced metal-poor (CEMP) stars (Beers et al. 1985; Christlieb et al. 2002; Beers & Christlieb 2005).

Of these, in particular, the CEMP-no subclass – which lacks s- or r-process elements – seems common in the early Galaxy, providing a window into Pop III nucleosynthesis (Yoon et al. 2018). However, their classification and analysis are largely based on abundance measurements of C from the molecular CH G-band, which potentially introduces biases from spectral modeling assumptions. Furthermore, increasing atmospheric 3D effects in metal-poor stars may significantly influence molecular abundances (Asplund et al. 1999; Collet et al. 2018; Gallagher et al. 2016, 2017), which suggests that a detailed 3D analysis of their spectra is needed.

1.3 GCE in 3D & NLTE – Thesis Outline

In this thesis, I analyze the influence of assumptions made in the process of generating synthetic stellar spectra – specifically the neglect of full 3D RHD models of stellar atmospheres and departures from LTE when solving the radiative transfer – on the measurements of stellar abundances and investigate to what extent they skew our understanding of the evolution of the Galaxy. With this purpose in mind, I present our newly developed 3D RHD code `M3DIS` within the `DISPATCH` framework (Nordlund et al. 2018) for generating grids of model atmospheres – with the corresponding NLTE spectra – on much shorter timescales than what is possible with current codes. I will show that the techniques developed in the course of this thesis will enable to bridge the gap between the full 3D NLTE analysis of individual stars and their application to large spectroscopic surveys, bringing the quality of stellar models in agreement with the quality of next-generation spectroscopic data sets.

The thesis is structured as follows; First, I will give an overview of the most important concepts, summarize the physical principles involved in modeling stellar atmospheres and spectra, and describe the theoretical background (Sec. 2). This will include a general description and numerical solution strategy for the equations of radiation-hydrodynamics, as well as the most important ideas involved in the synthesis of the NLTE spectrum (Sec. 2.1). In addition, I will outline the connection to the GCE and motivate why Fe-peak elements are the key to understanding the explosion mechanism behind SNe Ia (Sec. 2.2).

Next, I will apply these concepts to the derivation of NLTE [Ni/Fe] abundances in a sample of Galactic stars and analyze the results with respect to the role of different SNe Ia in Galactic chemical enrichment (Sec. 3). I will then take the step from 1D towards full 3D and introduce the `M3DIS` code (Sec. 4), describe its working principles and input physics. I will furthermore validate the code by comparing the `M3DIS` solar model with models computed using other 3D RHD codes, demonstrate its capabilities on a small sample of solar-like stars, and further introduce the corresponding 3D spectrum synthesis code `MULTI3D@DISPATCH` within the same numerical framework. Lastly, I will utilize the flexibility of `M3DIS` with respect to the chemical composition to create a collection of CEMP stars at different metallicities, from relatively metal-rich to extremely metal-poor, analyze the effects of 3D – paired with significant C-enhancement in the model atmosphere – on the CH G-band and the C abundances derived from it. I will again make the connection to the chemical history of the Galaxy by investigating the implications of changes in the CEMP-no fraction on Pop III nucleosynthesis (Sec. 5). I will close with a future outlook to highlight in what context `M3DIS` models are anticipated to be used in the near future, specifically for the science goals of the 4MOST and PLATO missions (Sec. 6), and a final summary (Sec. 7).

2 Fundamentals & Theoretical Background

2.1 Deciphering of Stellar Spectra

Analyzing the light from stars is crucial for understanding the formation, evolution, and current structure of the Galaxy. Stellar spectra are particularly important since they reveal the chemical makeup and history of their surroundings and make it accessible to present-day observers. Extracting information about the emitting star requires theoretical insights into its atmospheric structure, including temperature, density, and pressure in its outer layers, as well as the fundamentals of radiation transport.

The procedure thus requires computing model atmospheres that serve as the basis for simulating radiation transport, leading to the synthesis of the spectra we observe. It is crucial to note that photons traveling through the atmosphere are constantly absorbed and emitted by gas, affecting the energy balance and altering atmospheric structure, hence again impacting the radiation field (Nordlund 1982). This non-linearity – combined with the inherent complexity of radiative transfer calculations – renders the determination of stellar atmospheres, and thus stellar parameters and abundances, challenging and computationally intensive. A common method is to separate the computation of stellar model atmospheres, using a simplified radiation approach, from the detailed spectrum synthesis, which is conducted on a static atmospheric background.

The construction of models of stellar atmospheres has been a challenge since the first models of late-type stars have been published (Carbon & Gingerich 1969) and have been continuously developed to improve physical consistency (e.g. Nordlund 1982; Plez et al. 1992; Grupp 2004; Gustafsson et al. 2008; Nordlund et al. 2009; Freytag et al. 2012; Magic et al. 2013a). Due to the numerical complexity, it is mostly 1D models, describing the atmosphere as a function of depth only, in HE that are widely used for the derivation of stellar parameters in the majority of large-scale stellar spectroscopic surveys, such as e.g. Gaia-ESO (Gilmore et al. 2012), GALAH (Bland-Hawthorn et al. 2019), APOGEE (Majewski et al. 2017), or LAMOST (Liu et al. 2020). Here, studies either interpolate between spectra synthesized for

a precomputed sample of 1D HE model atmospheres, such as the MARCS (Gustafsson et al. 2008), ATLAS (Kurucz 1979; Castelli & Kurucz 2003; Kurucz 2013), or MAFAGS (Grupp 2004) grids, or interpolate the 1D model structures directly. Understanding how these 1D HE models are constructed in terms of underlying principles – the physical domain in which these models are applicable, what the shortcomings are and how they translate to stellar observables – is of high relevance, as these models build the foundation of countless studies in modern astronomy that make use of synthetic stellar spectra.

2.1.1 1D Hydrostatic Models of Stellar Atmospheres

A model of the stellar atmosphere essentially constitutes a description of the properties of the gas within the outer layers of stars, as these are crucial for the emerging radiation. Specifically, it is essential to accurately model the optical surface – a region where gas density and opacity decrease so that radiation can escape – to obtain a physically realistic temperature and density profile. Under the assumption that the atmospheric material is at rest, the fundamental equation of hydrostatics may be written as (following the description by Gustafsson et al. 2008)

$$\nabla P_{\rm tot} = -\rho \frac{GM}{r^2}\,\hat{\mathbf{r}} \equiv \rho\ \mathbf{g}(r), \tag{2.1}$$

where $\nabla P_{\rm tot}$ is the total pressure gradient, ρ the density of atmospheric gas, M the mass enclosed within the radius r (along the unit vector $\hat{\mathbf{r}}$), the Newtonian constant G, and the surface gravity $\mathbf{g}$. The total pressure itself contains the contribution from the gas pressure $P_{\rm g}$, the turbulent pressure $P_{\rm turb}$, and the radiation pressure $P_{\rm rad}$, that is,

$$\nabla P_{\rm tot} = \nabla P_{\rm g} + \nabla P_{\rm turb} + \nabla P_{\rm rad}. \tag{2.2}$$

Here, $P_{\rm turb}$ describes the force linked to the turbulent movement of the material and may be expressed in terms of the turbulent velocity $v_{\rm t}$, such that $P_{\rm turb} \approx \rho v_{\rm t}^2$. It is important to note that – because of the underlying hydrostatic assumption – the velocity field and, hence, also the turbulent velocity can not be derived self-consistently. It is therefore a free parameter that has a direct consequence for the atmospheric stratification; As demonstrated by Gustafsson et al. (2008), the influence of turbulent pressure on the model can be expressed in terms of an effective surface gravity ($g_{\rm eff}$),

$$g_{\rm eff} = g\left(\frac{1 - L/L_{\rm Edd,eff}}{1 + \gamma\,(v_{\rm t}/c_{\rm s})^2}\right), \tag{2.3}$$

with luminosity L, effective Eddington luminosity $L_{\rm Edd,eff}$, sound speed $c_{\rm s} = \sqrt{\gamma P_{\rm g}/\rho}$, and adiabatic index γ. This implies that altering $v_{\rm t}$ mimics changing surface gravity, directly impacting the atmospheric structure as per Eq. 2.1. Additionally, Eq. 2.3 indicates a similar effect for L, which relates to the radiative pressure – expressed by the radiative energy flux

$F_{\rm rad}$ – via the energy balance equation.

$$F_{\rm comv} + F_{\rm rad} = \frac{L}{4\pi r^2}. \tag{2.4}$$

In addition to $F_{\rm rad}$, Eq. 2.4 also considers energy transport by the gas itself through convection, which is a relevant mechanism in the atmospheres of FGK-type stars. Regions in the atmosphere that are unstable against convection can be identified using the Schwarzschild criterion (e.g. as formulated by Hubeny 2013)

$$\nabla_{\rm R} > \nabla_{\rm A}, \tag{2.5}$$

$$\nabla_{\rm R} \equiv \left(\frac{{\rm d}\ln T}{{\rm d}\ln P}\right)_{\rm R},\ \nabla_{\rm A} \equiv \left(\frac{{\rm d}\ln T}{{\rm d}\ln P}\right)_{\rm A} \tag{2.6}$$

where $\nabla_{\rm R}$ is the radiative temperature gradient, and $\nabla_{\rm A}$ is the adiabatic temperature gradient. In the stellar interior, densities are high and the opacity of the material large. In these conditions, energy transport via radiation is extremely inefficient, which causes the material to be convective. Towards the stellar surface the pressure, and hence density, drops (negative sign in Eq. 2.1). When the mean free path of photons becomes sufficiently large for radiative energy transport to be effective, the material stabilizes and convection stops (Gray 2005).

Again, it needs to be stressed that in hydrostatic equilibrium there is no derivation of the velocity field and hence no self-consistent way to estimate the convective energy flux. A common approximation is to resort to MLT (e.g. Prandtl 1925; Henyey et al. 1965; Joyce & Tayar 2023), which expresses $F_{\rm conv}$ with the help of additional free parameters, the most prominent being the mixing length parameter $\alpha_{\rm MLT}$ that describes the convective mean free path in units of pressure scale height ($H_{\rm p}$). Similarly to $v_{\rm t}$, also $\alpha_{\rm MLT}$ is directly linked to the atmospheric structure through Eq. 2.3 and 2.1. Despite their relevance for model atmosphere construction, constraining these parameters from first principles is not possible, as they require calibration based on observations of spectral lines themselves (e.g. Barklem et al. 2002), which introduces significant inconsistency in the derivation of stellar parameters.

The full system of equations is closed by an equation of state (EoS) that relates the gas pressure and density, which ultimately allows the solution of the radiative transfer and thus the computation of $F_{\rm rad}$. The full set of non-linear equations is solved iteratively. For this, an initial temperature stratification is used to solve Eq. 2.1 for gas pressure and density (together with the EoS), which is then used to compute the frequency-dependent radiative transfer and obtain $F_{\rm rad}$, which initially does not obey the radiative equilibrium equation,

$$\nabla \cdot \mathbf{F}_{\rm rad} = 0, \tag{2.7}$$

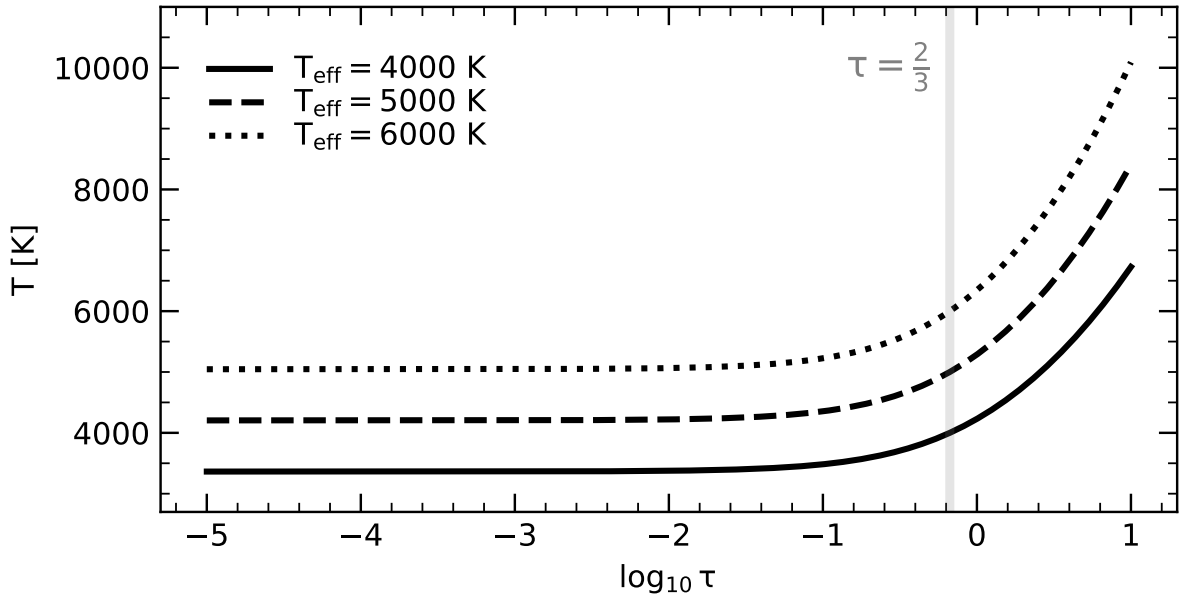

Figure 2.1: Example temperature against optical depth profiles of three grey, hydrostatic model atmospheres in radiative equilibrium, derived in the Eddington approximation. Black lines correspond to different effective temperatures.

and hence requires adjustments of the atmospheric structure until convergence (Hubeny & Mihalas 2014). Note that in plane-parallel atmospheres the radial dependence of $\mathbf{g}$ and $F_{\rm rad}$ can furthermore be neglected, because the atmospheric contribution in overall size and mass is assumed to be negligible compared to the remaining parts of the star. Radiative equilibrium in this case is equivalent to $F_{\rm rad} = \sigma_{\rm SB} T_{\rm eff}^4 = \text{const}$ (with Stefan-Boltzmann constant $\sigma_{\rm SB}$) in every layer of the atmosphere. The effective temperature $T_{\rm eff}$ therefore, together with surface gravity and chemical composition, is a defining input quantity of 1D HE codes and ultimately determines the atmospheric structure.

The radiative transfer is discussed in more detail in Sec. 2.1.3, however it is useful to mention an important special case: the 1D HE *gray* atmosphere. In the gray approximation (e.g. Gray 2005), the opacity of the medium is assumed to be frequency independent, allowing the atmospheric structure to be resolved on a frequency independent optical depth scale τ. Combined with the Eddington approximation, i.e. assuming a nearly isotropic radiation field, which allows for an approximate solution by relating the radiation pressure to the mean radiation intensity, the temperature structure can be expressed as a simple function of $T_{\rm eff}$ and τ,

$$T^4(\tau) = T_{\rm eff}^4 \frac{3}{4}\left(\tau + \frac{2}{3}\right). \tag{2.8}$$

A visual representation of the $T-\tau$ structure for different effective temperatures can also be found in Fig. 2.1. Despite its oversimplification, the Eddington solution of the atmospheric structure in the gray approximation provides two valuable order-of-magnitude estimates,

which are also relevant for the analysis of more complex models; the temperature at $\tau = 2/3$ matches the effective temperature ($T(2/3) = T_{\rm eff}$) reasonably well, and the temperature drop from this depth to the surface ($\tau = 0$) is modest, about 16% of $T_{\rm eff}$.

Motivated by the slow varying temperature in the upper layers, a very instructive example of a plane-parallel atmosphere in hydrostatic equilibrium is the isothermal, ideal gas. Neglecting radiative and turbulent pressure components in Eq. 2.2, the ideal gas EoS,

$$P_{\rm g} = \frac{\rho}{\mu m_{\rm p}} k_{\rm B} T, \tag{2.9}$$

with mean molecular weight μ, atomic mass unit $m_{\rm p}$ and Boltzmann constant $k_{\rm B}$, can be substituted directly into the 1D version of Eq. 2.1 (with height coordinate z), i.e.

$$\frac{{\rm d}P_{\rm g}}{{\rm d}z} = \frac{k_{\rm B}\ T}{\mu m_{\rm p}} \frac{{\rm d}\rho}{dz} = -\rho g \tag{2.10}$$

$$\Rightarrow \frac{{\rm d}\rho}{\rho} = -\frac{{\rm d}z}{H} \tag{2.11}$$

$$\Rightarrow \rho = \rho_0\ e^{-z/H}. \tag{2.12}$$

The density of an ideal isothermal gas in hydrostatic equilibrium thus drops exponentially with scale height $H = k_{\rm B}T/g\mu m_{\rm p}$, which in this case is equal to $H_{\rm p}$. Due to the proportionality in Eq. 2.9, the same is true for the gas pressure.

Although not entirely applicable for a realistic model of the entire stellar photosphere, especially toward the upper, radiation-dominated layers, where convective motions become less significant and the temperature gradient is small (as in Fig. 2.1), this simple model describes the density profile reasonably well and offers the opportunity to understand parts of physically more realistic – and significantly more complex – atmosphere models at least qualitatively. It specifically suggests that an exponentially dropping density at constant temperature is a suitable upper boundary condition in simulations of the stellar atmosphere.

Conversely, an exponential decrease of density paired with a constant temperature can be associated with a higher mean free path of photons, causing energy transport by radiation to be more efficient and providing stability against convection (Eq. 2.5) and initiating the transition from convection to radiation-dominated regimes within the photosphere.

2.1.2 3D Radiation Hydrodynamics Models of Stellar Atmospheres

Stars are not one-dimensional. Direct observations of the Sun make this clear immediately; it can be seen in observations by e.g. the Swedish Solar Telescope (Fig. 2.2, left panel) that the solar surface shows a rich, spatial substructure. A granular pattern can be observed, where rising bubbles of bright hot gas with spatial extension of $\sim 1000\,$km are surrounded

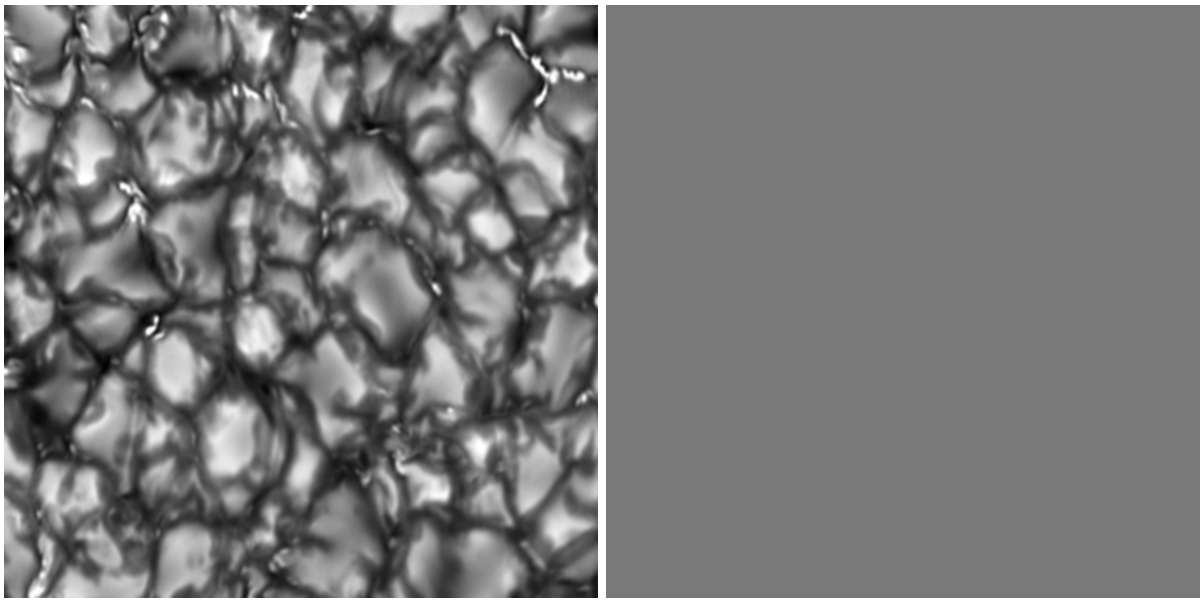

Figure 2.2: Left: High resolution solar granulation observation taken by the Swedish 1-m Solar Telescope (SST). Credit: Institute for Solar Physics, Sweden. Observer: Vasco Henriques, image processing: Vasco Henriques, date: 23 May 2010. Right: Solar surface flux expected from 1D HE models. In 1D HE, convection and hence granulation is not included. The surface would spatially show the identical temperature everywhere.

by dark and cool inter-granular regions of downflows.

Multi-epoch observations furthermore show that this pattern is not static[1]; convective cells are moving; they disappear and re-emerge as a function of time. It is clear that a 1D HE model, which by definition is static, in radiative equilibrium, and has a single constant effective temperature (and hence radiation flux) in space and time, is unable to reproduce the observed diversity (Fig. 2.2, right panel shows a schematic image).

Equations & Properties

Modeling a stellar atmosphere in full 3D, with realistic velocity fields, requires the solution of the Euler equations. Expressed as conservation of mass (continuity), momentum, and energy, they may be written as

$$\partial_t \rho + \nabla(\rho \mathbf{v}) = 0 \tag{2.13}$$

$$\partial_t (\rho \mathbf{v}) + \nabla(\rho \mathbf{v}\mathbf{v}) = -\nabla P + \rho \mathbf{g} \tag{2.14}$$

$$\partial_t e + \nabla((e+P)\mathbf{v}) = \rho \mathbf{v}\mathbf{g} + q_{\mathrm{rad}}, \tag{2.15}$$

with gas velocity $\mathbf{v}$, energy per unit volume e, and radiative heating q_{rad}. To close this system of radiation hydrodynamics (RHD), two more equations are required; the EoS, providing $P(\rho, e)$, and the radiative transfer equation to compute q_{rad}. More details can be found in

[1] https://www.isf.astro.su.se/data1/gallery/movies/2006/

Sec. 2.1.3 and 2.1.4. In conditions common in stellar atmospheres their solution requires numerical methods. The momentum and energy conservation Eq. 2.14 and 2.15 furthermore, strictly speaking, require the inclusion of a viscosity term. However, as demonstrated by Freytag et al. (2012), the intrinsic microscopic viscosity acts on scales of a few centimeters in the solar atmosphere, which is many orders of magnitude smaller than typical length scales (e.g. H_p), and hence numerically impossible to resolve. The numerical diffusion associated with the grid discretizations and numerical scheme are of greater significance.

Following the description by Toro (1997b); Dullemond (2011), the Euler equations mathematically can be viewed as first-order, hyperbolic, non-linear partial differential equations that advect the conserved quantities $\mathbf{Q}$ with the fluxes $\mathbf{F}_\mathrm{i}$ in every spatial dimension i,

$$\mathbf{Q} = \begin{pmatrix} \rho \\ \rho u \\ \rho v \\ \rho w \\ e \end{pmatrix}, \; \mathbf{F}_\mathrm{x} = \begin{pmatrix} \rho u \\ \rho u^2 + P \\ \rho v u \\ \rho w u \\ (e+P)u \end{pmatrix}, \; \mathbf{F}_\mathrm{y} = \begin{pmatrix} \rho v \\ \rho u v \\ \rho v^2 + P \\ \rho w v \\ (e+P)v \end{pmatrix}, \; \mathbf{F}_\mathrm{z} = \begin{pmatrix} \rho w \\ \rho u w \\ \rho v w \\ \rho w^2 + P \\ (e+P)w \end{pmatrix}, \tag{2.16}$$

with the velocity vector $\mathbf{v} = (u, v, w)^T$ in Cartesian coordinates x, y, and z. The Euler equations then read as

$$\partial_\mathrm{t}\mathbf{Q} + \partial_\mathrm{x}\mathbf{F}_\mathrm{x} + \partial_\mathrm{y}\mathbf{F}_\mathrm{y} + \partial_\mathrm{z}\mathbf{F}_\mathrm{z} = \mathbf{S}, \tag{2.17}$$

with the source term $\mathbf{S} = (0, 0, 0, -\rho g, -\rho w g + q_\mathrm{rad})^T$ on the right-hand side collecting the external gravitational force, as well as changes to the energy by radiative heating and release of potential energy.

In the regime of FGK-type stars with surface gravities between $1 \lesssim \log g \lesssim 5$, Gustafsson et al. (2008) estimate the effects of sphericity on the temperature stratification of the atmosphere to be smaller than 4% of the effective temperature in the optical depth regime relevant for spectral line formation. It is therefore common to simplify the computation of stellar atmospheres by simulating only local regions that are small compared to the size of the star and hence can be represented as Cartesian boxes, so-called *box-in-a-star* simulations (but see also Freytag & Höfner 2008, for *star-in-a-box* simulations of red supergiants), which are characterized by constant surface gravity in the entire atmosphere, $\mathbf{g} = (0, 0, -g)$. A reasonable order-of-magnitude estimate for the size of the atmosphere ΔR with respect to the stellar radius R may be obtained from an ideal gas in HE (Eq. 2.1) and with the assumption that $P_\mathrm{surface} = 0$, i.e.

$$\frac{\Delta P}{\Delta R} \sim \frac{-P}{\Delta R} \sim \frac{-\rho\, T}{\Delta R} \sim -\rho g \Rightarrow \frac{\Delta R}{R} \sim \frac{T}{Rg} \sim \frac{T}{\sqrt{Mg}}. \tag{2.18}$$

The plane-parallel assumption is a reasonable estimate in stars where the size of the atmosphere is negligible compared to the radius of the star, $\Delta R \ll R$. It is hence stars that are massive, cold or have a high surface gravity that are reasonably well described by box-in-a-star simulations. In the parameter space of FGK-type stars it may furthermore be noted that effective temperatures vary between $\sim 3500\,\mathrm{K}$ and $\sim 7000\,\mathrm{K}$, while on the other hand the surface gravity spans multiple orders of magnitude, $1 \lesssim \log g \lesssim 5$, making it the crucial factor in this regard. Nevertheless, it was found by e.g. Heiter & Eriksson (2006) that for giant stars with $\log g > 1.5$ the sphericity effect on Fe I abundances is $\lesssim 0.1\,\mathrm{dex}$ even for strong lines, and 0.04 dex for Fe II (their Fig. 6), suggesting that for the majority of observed Galactic stars plane-parallel geometry is sufficient.

Particular attention has to be paid to the size of the region in the atmosphere that is modeled. For the physical behavior of the gas to not be influenced by the boundary conditions at the edges of the simulation domain, it has to be ensured that a sufficient number of granular cells, which typically have an extent comparable to H_p (Magic et al. 2013a), are continuously evolving. Therefore, the size of the box is required to scale roughly with $H_\mathrm{p} \sim T/g$ (Eq. 2.10). Since g generally covers multiple orders of magnitude, it can also be viewed as the primary indicator for the size of the computation domain.

In contrast to 1D HE models, solving Eq. 2.17 yields the velocity field from first principles and hence replaces the need for any turbulence and mixing length parameters (Eq. 2.3). In 3D RHD the stellar atmosphere naturally develops a convective zone at the bottom of the simulation domain, and the inclusion of radiative heating initiates the transition to photospheric layers without the need of hyperparameters. Since there is also no assumption of radiative equilibrium, the final $T-\rho$ stratification of the model depends only on essentially three input parameters: The chemical composition, the surface gravity $\log g$, and the entropy at the bottom of the atmosphere. The reason why the bottom entropy is a particular important quantity that governs the state of the entire atmosphere lies already within the Euler equations and the first law of thermodynamics, i.e.

$$\mathrm{d}\hat{e}_\mathrm{int} = T\,\mathrm{d}\hat{s} + \frac{P}{\rho^2}\mathrm{d}\rho, \tag{2.19}$$

with the specific internal energy $\hat{e}_\mathrm{int}$ and the specific entropy $\hat{s}$. By introducing the *convective derivative* $\mathrm{D}_\mathrm{t} = \partial_\mathrm{t} + \mathbf{v}\nabla$, one can express Eq. 2.15 in terms of the specific internal energy $\hat{e}_\mathrm{int} = \hat{e} - v^2/2$ such that

$$\mathrm{D}_\mathrm{t}\hat{e}_\mathrm{int} = \frac{1}{\rho}\left(q_\mathrm{rad} - P\ \nabla\mathbf{v}\right), \tag{2.20}$$

which makes use of the momentum equation, $\mathrm{D}_\mathrm{t}\mathbf{v} = -1/\rho\ \nabla P + \mathbf{g}$, and the energy equation, $\mathrm{D}_\mathrm{t}\hat{e} = 1/\rho\ \left(q_\mathrm{rad} - \mathbf{v}\nabla P - P\nabla\mathbf{v}\right) + \mathbf{vg}$, expressed in convective form. Note that the potential energy contribution in the energy- and the gravity force term in the momentum equation

cancel out, as they appear in both terms of $\mathrm{D_t}\hat{e}_{\mathrm{int}} = \mathrm{D_t}\hat{e} - \mathbf{v}\mathrm{D_t}\mathbf{v}$. Combining both Eq. 2.19 and 2.20 then implies that

$$T\ \mathrm{D_t}\hat{s} = \frac{1}{\rho} q_{\mathrm{rad}}, \tag{2.21}$$

which finally makes use of the continuity equation in convective form, $\mathrm{D_t}\rho = -\rho\nabla\mathbf{v}$. This result is very instructive as it provides deep insight into the general atmospheric structure. Toward the bottom of the computation domain, where the density is high and the energy transport is dominated by convection, the radiative flux divergence – and hence the radiative heating contribution to the overall energy balance – is small, i.e. $q_{\mathrm{rad}} \to 0$. Eq. 2.21 implies that convective cells in these conditions rise adiabatically, $\mathrm{D_t}\hat{s} = 0$. Provided that the model atmosphere covers deep enough layers, a constant bottom entropy thus defines an isentropic upward flow of material. When q_{rad} becomes significantly large, deviations from the adiabatic structure arise (see also the description by Dullemond 2011).

Eq. 2.20 furthermore highlights the balance between radiation and the second, very important cooling mechanism: adiabatic cooling. The situation becomes even more instructive when the continuity equation is explicitly used to express the velocity divergence as $\nabla\mathbf{v} = -1/\rho \cdot \mathrm{D_t}\rho$ (or alternatively by inserting Eq. 2.21 back into 2.19),

$$\mathrm{D_t}\hat{e} = \frac{1}{\rho}\left(q_{\mathrm{rad}} + \frac{P}{\rho}\mathrm{D_t}\rho\right). \tag{2.22}$$

It becomes clear that the gas of the atmosphere can either cool by emitting photons, $q_{\mathrm{rad}} < 0$, or via the adiabatic cooling associated with rising fluid parcels, which expand, decrease their density and hence also contribute to the atmospheric energy balance, $\mathrm{D_t}\rho < 0$. Note that in hydrostatic equilibrium the velocity term in Eq. 2.20 is not included, which shows that this mechanism is missing in 1D HE models.

Solution Method

To outline the solution strategy of the RHD equations, it is important to realize that general advection equations in the form of Eq. 2.17 – for simplicity in 1D – can be expressed in terms of the flux derivative with respect to the conserved quantities (Toro 1997b), i.e.

$$\partial_{\mathrm{t}}\mathbf{Q} + \partial_{\mathrm{x}}\mathbf{F} = \partial_{\mathrm{t}}\mathbf{Q} + \frac{\partial\mathbf{F}}{\partial\mathbf{Q}}\partial_{\mathrm{x}}\mathbf{Q} = 0, \tag{2.23}$$

without the source term on the right-hand side. Here, $\mathbf{F} = \mathbf{F}(\mathbf{Q}(x))$ does not explicitly depend on x (as is the case for the hydrodynamic equations). The non-linearity is hereby introduced by the Jacobian matrix $\frac{\partial\mathbf{F}}{\partial\mathbf{Q}}$, which in general can be a function of $\mathbf{Q}$ itself. Mathematically, these equations can be solved using the *characteristics* method (e.g. Olver 2014; Arendt & Urban 2023). To understand the solution qualitatively, it is furthermore useful to look at the specific case of a scalar-valued state function $Q(x,t)$ and flux $F(Q)$, i.e. one

specific out of the five Euler equations,

$$\partial_t Q + \frac{\partial F}{\partial Q}\partial_x Q \equiv \partial_t Q + c(Q)\cdot\partial_x Q = 0, \tag{2.24}$$

with *advection speed* $c(Q)$. A comparison with the total differential of Q

$$\frac{\mathrm{d}Q}{\mathrm{d}t} = \partial_t Q + \frac{\mathrm{d}x}{\mathrm{d}t}\partial_x Q \tag{2.25}$$

reveals that along the so-called *characteristic curves* x, with $\mathrm{d}x/\mathrm{d}t = c(Q)$, the value of Q is conserved, $\mathrm{d}Q/\mathrm{d}t = 0$. The solution of the partial differential advection equation therefore reduces to the solution of an ordinary differential equation, which immediately provides the evolution of an initial configuration $Q_0(x) \equiv Q(x,0)$, i.e.

$$\frac{\mathrm{d}^2x}{\mathrm{d}t^2} = \frac{\mathrm{d}c(Q)}{\mathrm{d}t} = \frac{\mathrm{d}c(Q)}{\mathrm{d}Q}\frac{\mathrm{d}Q}{\mathrm{d}t} = 0 \tag{2.26}$$

$$\Rightarrow \frac{\mathrm{d}x}{\mathrm{d}t} = \mathrm{const} = c(Q) = c(Q_0(x_0)) \tag{2.27}$$

$$\Rightarrow x = c(Q_0(x_0))\cdot t + x_0 \tag{2.28}$$

$$Q(x,t) = Q_0(x_0) = Q(x - c(Q_0(x_0))\cdot t, 0). \tag{2.29}$$

Eq. 2.26 shows that the characteristic curves are straight lines in the (x,t) plane; however, their slope (Eq. 2.27) in the non-linear case depends on the initial state. Different characteristic curves hence necessarily cross at some point, after which no general analytic solution can be found, and only weak solutions with additional conditions to handle discontinuities are applicable. In the special, linear case with $c = \mathrm{const}$, the solution is simply $Q(x,t) = Q(x - ct, 0)$, that is, the initial profile becomes advected with the constant advection velocity c.

In the full HD system, $\mathbf{Q}$ and $\mathbf{F}$ are vector-valued functions, which means that the individual advection equations become coupled by multiplication with the Jacobian matrix. The solution of the complete set of equations thus involves diagonalizing the Jacobian, that is, computing eigenvalues λ_i and decomposing it locally into eigenvectors ($Q \to \hat{Q}$), both depending on Q itself, so that it can be brought into the same form as Eq. 2.24

$$\partial_t \hat{\mathbf{Q}} + \mathrm{diag}(\lambda_1, ..., \lambda_n)\partial_x \hat{\mathbf{Q}} = 0. \tag{2.30}$$

The Jacobian eigenvalues can therefore be interpreted as the characteristic velocities at which conserved quantities $\hat{\mathbf{Q}}$ are advected. In the case of the hydrodynamics equations as expressed in Eq. 2.17, the characteristics (e.g. in the x-direction) turn out to be u, $u - c_s$ and $u + c_s$, where the sound speed c_s depends on pressure and density. The u characteristics represent the motion of the fluid itself, while the $u - c_s$ and $u + c_s$ characteristics correspond

to sound waves. Note that the decomposition $\hat{\mathbf{Q}}$ cannot be done globally, because the Jacobian is not constant, and thus the corresponding transformation matrix cannot be pulled into the differential. Because the eigenvectors themselves furthermore depend on $\mathbf{Q}$, the locally decomposed state does not provide a decoupling of the equations, which requires the introduction of characteristic integral curves, along which only one state component varies on the basis of the eigenvectors. For more details, see Toro (1997b); Dullemond (2011).

Numerical Solution Techniques

Before numerically solving the Euler equations, a decision is to be made; one may notice that Eq. 2.13, 2.14 and 2.4 already take on an advective form, if the pressure-related terms in the momentum and energy equations are moved from the advection on the left-hand side to the source terms on the right-hand side. The result is that the entire system is advected by the material velocity itself, i.e. the characteristics for all equations are equal to u, v and w in the x, y, and z directions, respectively, which considerably simplifies the numerical advection scheme. However, when using this method the propagation of sound waves is entirely driven by the source term. This procedure is what is used in classical HD solvers.

On the other hand, there are multiple classes of so-called *approximate Riemann* solvers that do not rely on this splitting but include the pressure term in the advection scheme and thereby advect the conserved variables along the proper characteristics u, $u - c_s$ and $u + c_s$ (i.e. following Eq. 2.17). Because sound waves are propagated properly, Riemann solvers typically excel at capturing shocks and discontinuities. Classical solvers, on the other hand, have the advantage of better recognizing stable hydrostatic situations. Picking the right solver is hence situation- and priority-dependent (Roe 1986; LeVeque 1997).

Although complex in detail, the working principle of a Riemann solver can be outlined by investigating the basic working principle of the Harten, Lax, and van Leer approximate Godunov-type solver that includes the contact wave (HLLC, see e.g. Toro 1997a, for a comprehensive overview). Starting with the x-direction of Eq. 2.17, the numerical solution requires discretization of the Euler equations. For simplicity, one may consider the state vector $\mathbf{Q}_i^n$ in the grid cell i and the time-step n. In addition, one may assume that the size of the grid cell is Δx and that the time-step Δt is locally constant. To advance $\mathbf{Q}_i^n$ by one time-step, fluxes are required at the cell interfaces $\mathbf{F}_{i\pm1/2}$. The change of $\mathbf{Q}$ is hereby given by the difference between the flux entering and leaving the cell i, i.e.

$$\mathbf{Q}_i^{n+1} = \mathbf{Q}_i^n + \frac{\Delta t}{\Delta x}\left(\mathbf{F}_{i-1/2} - \mathbf{F}_{i+1/2}\right). \tag{2.31}$$

Precisely the computation of $\mathbf{F}_{i\pm1/2}$ is the duty of Riemann solvers. Each of the cell interfaces $x_{i\pm1/2}$ constitutes a jump between the state vectors left and right of the cell boundary, $\mathbf{Q}_L$ and $\mathbf{Q}_R$, which may be reconstructed from cell-centered variables using specific reconstruction

algorithms.

In the original HLL solver, there are three options to determine the flux across the cell interfaces $\mathbf{F}_{i\pm1/2}$ depending on the locally fastest signal velocities S_L and S_R, which, in the simplest case, are given by the characteristic velocities $S_L = u_L - c_{s,L}$, $S_R = u_R + c_{s,R}$ in the cells left and right of the respective interface. The interface flux is then set to $\mathbf{F}_L$ if material is crossing the interface from the left with $S_L > 0$ and $\mathbf{F}_R$ if it is crossing from the right with $S_R < 0$. In the region between, $S_L < 0 < S_R$ (also called the *star region*), the intermediate state $\mathbf{Q}_{i\pm1/2}$ is computed from the integral average (across the interface) of the exact solution by assuming constant $\mathbf{Q}_{R/L}$ states, and the corresponding $\mathbf{F}_{i\pm1/2}$ using the Rankine-Hugoniot condition (for the exact analytic expressions see Toro 1997a, their Eq. 10.13 and 10.19).

It is important to note that the domain splitting in $S_{R/L}$ includes the acoustic characteristics $u \pm c_s$ in the solution scheme, unlike in classical HD solvers. However, it does not properly reflect the signal propagating as contact waves corresponding to characteristic u. This flaw is removed in the HLLC Riemann solver, which extends the HLL scheme by additionally including the contact wave S^*, decomposing the cell interface flux in four states ($0 < S_L$, $S_L < 0 < S^*$, $S^* < 0 < S_R$, and $0 > S_R$) of constant $\mathbf{Q}$. For more details, see Toro (1997a). The final fluxes at both cell interfaces may then be used in Eq. 2.31 advance $\mathbf{Q}^n$ in time.

Special attention is hereby given to the time-step Δt, which in general can be $\Delta t(x,t)$. When computing the update $\mathbf{Q}_\mathbf{i}^{n+1}$ using cell interface fluxes, the description above is only valid if the local gas velocity does not transport material beyond the domain of a single spatial grid cell during the duration of this update. The consequence is that there exists an upper bound for Δt, which is given by the Courant-Friedrichs-Lewy condition (CFL) for the Courant number C,

$$C(x,t) = \frac{\Delta t(x,t)}{\Delta x(x,t)} \cdot u(x,t) \leq C_{\max}. \tag{2.32}$$

The exact value that grants stability may depend on the specific situation. Note that in theory Δx and Δt may depend on the location within the computational domain. The former is the case for *adaptive mesh refinement* methods with variable grid discretization, the latter may be referred to as *local time-stepping*.

In the specific case of radiation hydrodynamics, where the Euler equations are coupled with the radiative transfer equation through the q_{rad} term in the energy equation, there are additional constraints on the Courant number. Here, C furthermore needs to ensure that photons do not diffuse across multiple cells within a single time-step. The limiting velocity in the CFL condition therefore must not be smaller than the local radiative diffusion speed u_{dif}, i.e. $u_{\text{CFL}} = \max(u_{\text{dif}}, u)$. In regions around the optical surface the radiative timescale usually is significantly shorter than the dynamic timescale, meaning that the maximum time-step at which the simulation may evolve – and hence computational cost – is governed by the radiation field.

It is crucial to emphasize the significance of $q_{\max}$ in the energy equation beyond the general solution methods of the HD equation discussed here. In fact, the non-convective, photospheric layers of FGK stellar atmospheres are dominated by radiative energy transfer. Beyond eventually synthesizing the spectrum, it is thus essential for the temperature-density structure to understand the key concepts of radiation transport and compute the radiative flux as accurately as possible.

2.1.3 Radiative Transfer

In the context of stellar atmospheres, radiative transfer describes the interaction between the radiation field and the atmospheric material through the absorption and emission of photons. Considering a beam of light with specific intensity I_ν per frequency ν, traveling in the direction of the unit vector $\mathbf{n}$ under the angle $\mu = \cos(\theta)$ in a spherical coordinate system (r, θ, ϕ), the change of I_ν along its path can be expressed in terms of emission coefficients (j_ν) and absorption (χ_ν) coefficients (as in Hubeny 2013)

$$\mathbf{n} \cdot \nabla I_\nu = j_\nu - \chi_\nu I_\nu. \tag{2.33}$$

It is often useful to express the Eq. 2.33 in terms of the optical depth τ_ν, where an optical depth increment is defined through the increment ds along the propagation ray such that

$$\mathrm{d}\tau_\nu = -\chi_\nu \, \mathrm{d}s = -\rho\kappa_\nu \, \mathrm{d}s, \tag{2.34}$$

where κ_ν is another expression for the absorption coefficient, also called *opacity*, that expresses explicitly the density dependence of χ_ν. The radiative transfer equation can then be modified in such a way that

$$\frac{\mathrm{d}I_\nu}{\mathrm{d}\tau_\nu} = I_\nu - S_\nu, \tag{2.35}$$

with the *source function* $S_\nu = j_\nu/\chi_\nu$. While Eq. 2.35 appears straightforward, the real complexity lies in computing κ_ν and S_ν. The radiation intensity at frequency ν in the stellar atmosphere is influenced primarily by absorption, which weakens it, and by spontaneous or stimulated emission, which enhances it. These interactions occur through electronic transitions within atoms or molecules, creating spectral lines (bound-bound transitions, “bb”), ionization or recombination (bound-free transitions, “bf”), or free electrons (free-free transitions, “ff”). Additionally, photons may scatter off free electrons (Thomson scattering, “T”) or bound electrons (Rayleigh scattering, “R”). This distinction can be appreciated by splitting the scattering from the “true absorption” (see e.g. Hubeny 2013; Rutten 2003).

$$\chi_\nu = \chi_\nu^{\mathrm{bb}} + \chi_\nu^{\mathrm{bf}} + \chi_\nu^{\mathrm{ff}} + \chi_\nu^{\mathrm{T}} + \chi_\nu^{\mathrm{R}}, \tag{2.36}$$

As the true line absorption coefficient χ_ν^{bb} is linked directly to fundamental properties of the atmospheric gas, it is instructive to express it in terms of Einstein coefficients for spontaneous de-excitation (A_{ul}), excitation (B_{lu}), and induced de-excitation (B_{ul}), each describing the number of transitions from the upper energy state (u) to the lower energy state (l) and vice versa – per unit time and per particle in a given state. The coefficients B_{ul} and B_{lu} are usually expressed per unit of specific intensity.

For each spectral line, the difference between the associated energy levels $\Delta E = E_{\mathrm{u}} - E_{\mathrm{l}} = h\nu$ (on average) leads to a photon of frequency ν. Neglecting hyperfine and isotopic substructure and assuming isotropy, it is intuitive that the total fraction of absorbed intensity is given by the difference between the number of photons removed by absorption and added by emission. Following the description by Rutten (2003), this means that

$$\chi_\nu^{\mathrm{bb}} = \frac{h\nu}{4\pi}\left(n_{\mathrm{l}}B_{\mathrm{lu}} - n_{\mathrm{u}}B_{\mathrm{ul}}\right), \tag{2.37}$$

where n_{i} is the number density of participles in energy state i, which is also called atomic- or molecular *level population*. The Einstein coefficients are furthermore coupled by the statistical weights g_{i} of the corresponding energy levels,

$$A_{\mathrm{ul}} = \frac{2h\nu^3}{c^2}\, B_{\mathrm{ul}} \tag{2.38}$$

$$B_{\mathrm{ul}} = \frac{g_{\mathrm{l}}}{g_{\mathrm{u}}}\, B_{\mathrm{lu}}. \tag{2.39}$$

It is instructive to note that the Einstein coefficients are fundamentally linked to the electronic configuration, as they are directly proportional to the oscillator strength, $B_{\mathrm{lu}} \propto f_{\mathrm{lu}} \,/\, h\nu$, making them specific to each individual transition and most importantly part of the atomic data, and hence independent of the atmospheric structure (see e.g. Li et al. 2012; Tennyson et al. 2016, for more details on the determination of these parameters). Consequently, it is only the level populations in Eq. 2.37 that remain uncertain and require further investigation. Following the same line of reasoning, the emissivity can be expressed as a function of A_{ul} such that

$$j_\nu^{\mathrm{bb}} = \frac{h\nu}{4\pi} n_{\mathrm{u}} A_{\mathrm{ul}}, \tag{2.40}$$

which immediately leads to the expression for the line source function

$$S_\nu^{\mathrm{bb}} = \frac{n_{\mathrm{u}}A_{\mathrm{ul}}}{n_{\mathrm{l}}B_{\mathrm{lu}} - n_{\mathrm{u}}B_{\mathrm{ul}}}, \tag{2.41}$$

again, highlighting that the solution to the radiative transfer problem hinges on determining the level populations. Although being more complex in detail, the same is qualitatively true for the other opacity sources in Eq. 2.36. Generally speaking, the extinction coefficients follow the common form $\chi_\nu^{\mathrm{i}} = \sigma_\nu^{\mathrm{i}} \cdot n$, where σ_ν^{i} are the so-called *cross-sections* of

the respective source of opacity, and n represents the number density of participants in the interaction. In the case of Thomson scattering for example, σ_ν^{T} is given by the classical Thomson cross-section, and n represents the number density of electrons n_{e}.

If the stellar atmosphere is locally in thermodynamic equilibrium (LTE), the situation simplifies considerably. By definition, LTE implies that locally, thermodynamic equilibrium distributions hold as a description of the matter component (Rutten 2003). According to statistical physics, this implies that energy levels are populated as dictated by the Boltzmann distribution

$$\frac{n_{\mathrm{u}}}{n_{\mathrm{l}}} = \frac{g_{\mathrm{u}}}{g_{\mathrm{l}}} e^{-\Delta E / k_{\mathrm{B}} T} \,, \tag{2.42}$$

Similarly, the fraction of atoms in successive stages of ionization ($N_{\mathrm{I}+1}/N_{\mathrm{I}}$), separated by the ionization energy η_{I}, is given by the Saha equation,

$$\frac{N_{\mathrm{I}+1}}{N_{\mathrm{I}}} \propto \frac{1}{n_{\mathrm{e}}} \frac{2\,U_{\mathrm{I}+1}}{U_{\mathrm{I}}} \, T^{3/2} \, e^{-\eta_{\mathrm{I}}/k_{\mathrm{B}}T}, \tag{2.43}$$

with the partition functions $U_{\mathrm{I/I}+1}$. Particle velocities are furthermore assumed to follow the Maxwell distribution. The combination of Eq. 2.42 and 2.43 – together with the assumption of a fixed total chemical composition of the entire atmosphere that sets the total metal content – the radiative transfer equation can be solved directly. By substituting Eq. 2.42, 2.38, and 2.39 into the line source function equation (Eq. 2.41), one furthermore notices that in LTE the source function is equivalent to the Planck function B_ν, which (at a given frequency) is famously only a function of temperature,

$$S_\nu^{\mathrm{bb}} = \frac{2h\nu^3}{c^2} \frac{1}{\frac{g_{\mathrm{u}} n_{\mathrm{l}}}{g_{\mathrm{l}} n_{\mathrm{u}}} - 1} = \frac{2h\nu^3}{c^2} \frac{1}{e^{h\nu/k_{\mathrm{B}}T} - 1} = B_\nu(T). \tag{2.44}$$

In LTE, opacity and source function are therefore closely tied to the local state of the atmosphere and can be determined unambiguously for a given atmospheric chemical composition, temperature, and density, which significantly eases the computation. However, understanding the limitations of the LTE assumption requires considering the electronic transitions between different particle states and their influence on the local Saha-Boltzmann equilibrium. Two primary mechanisms cause these transitions: collisional and radiative.

Collisional transitions occur through the interaction of bound electrons with free electrons or ions. Collisions with free electrons are generally more significant because of the dependence of the mean velocity $\langle v \rangle \sim \sqrt{T/m}$ on the particle mass m (when Maxwell distributed), which causes much higher collision frequencies due to the low-mass of the electron (Rutten 2003). In general, collision rates are proportional to the flux of particles that participate in the interaction, such that the collision frequency is $\sim n \langle v \rangle$. Since velocities are in Maxwell equilibrium, collisional transitions preserve LTE. Radiative transitions, on the other hand,

involve interactions with photons, which means that their rate $R_{\rm lu}$ per particle directly depends on the mean intensity of radiation $\overline{J}_\nu$ itself, i.e.

$$n_l R_{\rm lu} = n_{\rm l} B_{\rm lu} \overline{J}_\nu \tag{2.45}$$

$$n_{\rm u} R_{\rm ul} = n_{\rm u} A_{\rm ul} + n_{\rm u} B_{\rm ul} \overline{J}_\nu, \tag{2.46}$$

where $\overline{J}_\nu$ is computed as angular- and frequency averaged intensity across the spectral line. It is strongly dependent on the mean free path of photons ($\sim 1/\chi_\nu$) by how far the light participating in the radiative transition has traveled and thus how different the atmospheric conditions are between the emitting and the absorbing regions. The radiation field is hence inherently non-local, which drives the system away from LTE.

The combination of all collisional and radiative rates (including bound-free transitions, which follow very similar principles as the bound-bound transitions discussed above) leads to a net upward or downward transition that has an immediate consequence for the respective level populations. In statistical equilibrium, level populations are assumed to be constant in time (Hubeny & Mihalas 2014), i.e.

$$\frac{{\rm d}n_{\rm i}}{{\rm dt}} = 0 = \sum_{j \neq i} n_{\rm j} P_{\rm ji} - n_i \sum_{j \neq i} P_{\rm ij}, \tag{2.47}$$

which implies that the number of particles leaving the energy state i (with a transition rate of $P_{\rm ij}$) is equivalent to the number of particles entering it from all other energy states j (with transition rates of $P_{\rm ji}$). When individual level populations $n_{\rm i}$ start to deviate from the predictions by the Boltzmann equation (Eq. 2.42) as a consequence of these transitions, the condition is known as non-local thermodynamic equilibrium (NLTE). In NLTE, hence, Eq. 2.42 and 2.43 can no longer be used to determine the individual $n_{\rm i}$, which means that the statistical equilibrium (Eq. 2.47) must be solved. To understand when departures from LTE populations occur, it is useful to express the net radiative rate of de-exitation $\mathfrak{R}_{\rm ul}$ (Eq. 2.45 – 2.46, also called the *net radiative bracket*) for a single transition between levels u and l,

$$\mathfrak{R}_{\rm ul} = n_{\rm u} R_{\rm ul} - n_{\rm l} R_{\rm lu} = \frac{4\pi}{h\nu} \chi_\nu^{\rm bb} \left(S_\nu^{\rm bb} - \overline{J}_\nu \right), \tag{2.48}$$

in terms of the so-called *departure coefficients* $b_{\rm i} = n_{\rm i}/n_{\rm i}^{\rm LTE}$. For a qualitative analysis, it is furthermore useful to investigate Eq. 2.48 in the Wien limit of high energies ($h\nu > k_{\rm B}T$), where

$$\chi_\nu^{\rm bb} \approx b_{\rm l}\, \chi_\nu^{\rm bb,\ LTE} \tag{2.49}$$

$$S_\nu^{\rm bb} \approx \frac{b_{\rm u}}{b_{\rm l}}\, B_\nu, \tag{2.50}$$

and thus

$$\Re_{\mathrm{ul}} \approx \frac{4\pi}{h\nu} b_{\mathrm{u}}\, \chi_{\nu}^{\mathrm{bb,\ LTE}} \left(B_{\nu} - \frac{b_{\mathrm{l}}}{b_{\mathrm{u}}} \overline{J}_{\nu} \right). \tag{2.51}$$

The above equation is strictly speaking only valid for bound-bound transitions. However, the corresponding bound-free net radiative recombination shows a very similar functional dependence on the radiation field, when the upper level u is replaced with the continuum (for more details see Rutten 2003).

From Eq. 2.51 it becomes obvious that in LTE, when $b_{\mathrm{l}} = b_{\mathrm{u}}$, there are no net radiative transitions if $B_{\nu} = \overline{J}_{\nu}$, which means that the levels populations are in strict detailed balance. Since in general $B_{\nu} \neq \overline{J}_{\nu}$, the equation further implies that even in LTE $\Re_{\mathrm{ul}} \neq 0$. Note that this does not necessarily mean NLTE conditions, since LTE only requires the populations to follow the Saha-Boltzmann equation, which may still be true e.g. if net collisional rates are dominant.

In general, it may be noted that a super-thermal radiation field, i.e. $\overline{J}_{\nu} > B_{\nu}$, leads to $\Re_{\mathrm{ul}} < 0$, which is equivalent to net over-excitation and over-population of the upper energy levels or over-ionization in continuum transitions. If radiative rates are significant compared to collisional rates, there can also be departures from the Saha-Boltzmann equilibrium, $b_{\mathrm{i}} \neq 1$. In this case, the effect of super-thermal over-exitation and ionization is enhanced if $b_{\mathrm{l}} > b_{\mathrm{u}}$, i.e. the lower level of a transition is stronger affected by departures from LTE than the upper level. The same is true for the opposite case; when $\overline{J}_{\nu} < B_{\nu}$ the radiation field is sub-thermal, providing overall less photons and hence net de-excitation, $\Re_{\mathrm{ul}} > 0$.

According to Eq. 2.37 and 2.41, both opacity and source function – and ultimately the radiation field via Eq. 2.35 – are functions of the level populations. This means to compute $\overline{J}_{\nu}$ one needs n_{i}, which in turn depends on $\overline{J}_{\nu}$ to determine $\Re_{\mathrm{ul}}$, R_{ul}, P_{ij}, and finally n_{i}. The consequence is that solving the NLTE problem requires an iterative method that solves Eq. 2.35 and 2.47 together.

The complexity of computations raises the question in what conditions LTE may still be valid – for spectrum synthesis and for structure calculations. In the convective layers below the photosphere, the gas density and temperature are higher than in the surface layers. Here, the electron flux is relatively high ($n \langle v \rangle \sim n\sqrt{T/m_e}$), leading to high collisional rates and a small photon mean-free-path due to high opacity, resulting in LTE conditions. In contrast, density and temperature decrease considerably in the outer layers, reducing opacity and increasing the photon mean-free-path, which affects the locality of the radiation field and causes photon loss at the stellar surface. Lower density and temperature furthermore reduce collisional rates, making radiative transitions more significant in the statistical equilibrium. Consequently, deviations from LTE are more likely under these conditions.

Departures from LTE level populations lead to differences in the connected spectral lines. From Eq. 2.50 it can be seen that, if $b_\mathrm{u} > b_\mathrm{l}$, then $S_\nu^\mathrm{bb} > B_\nu$, and vice versa. Over-population of the upper level and depletion of the lower level reduce the number of absorbers, which leads to weaker spectral lines. Thus, a super-thermal source function leads to weak NLTE absorption features. Conversely, a sub-thermal source function, $b_\mathrm{u} < b_\mathrm{l}$, strengthens the spectral lines compared to LTE. For more information, see Bergemann & Nordlander (2014).

A interesting implication of Eq. 2.48 especially in the context of RHD simulations of stellar atmospheres is the connection to the radiative heating rate q_rad (see Eq. 2.15 in Sec. 2.1.2). The net amount of energy that is taken from the gas by a specific spectral line is simply given by the net rate of radiative de-excitation (Rutten 2003), i.e.

$$q_\mathrm{rad}^\mathrm{bb} = -h\nu\, \mathfrak{R}_\mathrm{ul} = -h\nu (n_\mathrm{u} R_\mathrm{ul} - n_\mathrm{l} R_\mathrm{lu}) \tag{2.52}$$

In the case of $\mathfrak{R}_\mathrm{ul} > 0$, there is a net transition of electrons from levels $u \rightarrow l$, which means that there are more photons – carrying energy $h\nu$ on average – added to the radiation field than removed from it. Consequently, this excess energy is removed from the total energy of the gas, effectively causing net radiative cooling ($q_\mathrm{rad}^\mathrm{bb} < 0$).

If there is net-excitation ($\mathfrak{R}_\mathrm{ul} < 0$) on the other hand, the number of particles in upper energy states is increased, decreasing the photons in the radiation field and hence increasing the total energy of the gas. A similar argument can be made for the connection between net ionization or recombination and the continuum cooling. The right-hand side of Eq. 2.48 furthermore reveals that

$$q_\mathrm{rad}^\mathrm{bb} = -4\pi\chi_\nu^\mathrm{bb}\left(S_\nu^\mathrm{bb} - \bar{J}_\nu\right) \overset{\mathrm{LTE}}{=} -4\pi\chi_\nu^\mathrm{bb}\left(B_\nu - \bar{J}_\nu\right), \tag{2.53}$$

which makes the link between the radiative transfer equation and the Euler equations explicit. According to Eq. 2.53, the gas of the atmosphere cools if the radiation field is sub-thermal ($\bar{J}_\nu < B_\nu$ in LTE), i.e. the emission of Planck-source dominates the absorption of intensity. If the radiation field is super-thermal ($\bar{J}_\nu > B_\nu$) there is more absorption by the material than there is emission of Planck source, which causes the gas to heat up $q_\mathrm{rad}^\mathrm{bb} > 0$. Including all possible transitions, the total radiative cooling rate is given by the divergence of the radiation flux $\mathbf{F}_\mathrm{rad}$. Following Eq. 2.53, it may furthermore be shown that

$$q_\mathrm{rad} = -\nabla\cdot\mathbf{F} = 4\pi \int \chi_\nu (J_\nu - S_\nu)\ \mathrm{d}\nu \tag{2.54}$$

holds in general, where $\chi_\nu = \kappa_\nu \rho$ is the monochromatic opacity at frequency ν, representing all possible opacity sources and blends of different spectral lines.

2.1.4 Opacities

Extending the qualitative overview given in Sec. 2.1.3 to a system with multiple species, each having numerous energy levels linked by many spectral lines that influence opacity at specific frequencies, reveals the complexity of the statistical equilibrium. Overlapping, potentially asymmetric, lines require extending the equations for bound-bound opacity (Eq. 2.37) and emissivity (Eq. 2.40) with absorption and emission profiles, as these equations represent the absorption coefficient integrated over the spectral feature (Rutten 2003). Introducing a profile function, which accounts for the frequency variation of the absorption feature, ensures that the opacity summation includes all atomic transitions affecting the opacity at a given frequency via line cores, wings, or continua.

In LTE, the opacity can be calculated based only on the chemical composition, local temperature, and density, provided that atomic data is available, by using the Saha and Boltzmann equations. This calculation of opacity does not require prior knowledge of the radiation field, which would be influenced by the entire atmospheric structure. In 3D RHD stellar atmospheres, this point is crucial.

As radiative heating in Eq. 2.54 includes integration over the full spectrum, consisting of numerous overlapping spectral lines and continua, recalculating the opacity during the time-dependent hydrodynamic problem, which involves a changing atmospheric structure, is computationally very challenging. Therefore, it is beneficial and common practice to pretabulate opacities, which reduces the complexity to simple interpolation during the simulation (Ludwig 1992; Plez et al. 1992; Plez 2008).

Note that this is strictly speaking only possible in LTE, as in NLTE level populations do indeed depend on the radiation field, which means that a specific (T, ρ) combination corresponds to different opacities for different atmospheres. NLTE atmosphere models are thus much more computationally complex, which – with the current computational infrastructure – requires either using the 1D HE approximation (e.g. Werner et al. 2012) or significant compromises in terms of atomic structure, model- and time resolution (Sander 2017; Sander et al. 2017).

Eq. 2.54 hides another complexity; calculating the average radiation field J_ν involves solving the radiative transfer equation along multiple rays and at each frequency in the spectrum. Given that frequency (or wavelength $\lambda = c/\nu$) spans a wide range, from roughly 1000 Å in UV to approximately 100000 Å in infrared, with individual spectral lines as narrow as $\sim 1/100$ Å, the number of RT solutions needed per HD update becomes prohibitively computationally demanding, which is unfeasible for this work.

Given that Eq. 2.54 requires only the integrated heating, there are practical methods for approximating the integral while maintaining manageable computational costs. The leading technique is known as *opacity binning* (or *multi-group* approximation) and involves col-

lecting together and averaging opacities at different wavelengths. The radiative transfer equation is then solved only for a small number of opacity bins, assuming constant opacity within each bin (see Ludwig 1992, for a more in-depth analysis, see also Sec. 4.3.3). The binned opacity is generally computed using a combination of the Planck mean,

$$\kappa_{\text{planck}} = \frac{\int \kappa_\nu B_\nu \, \mathrm{d}\nu}{\int B_\nu \, \mathrm{d}\nu}, \tag{2.55}$$

and the Rosseland mean,

$$\kappa_{\text{ross}}^{-1} = \frac{\int \kappa_\nu^{-1} (\partial_T B_\nu) \, \mathrm{d}\nu}{\int (\partial_T B_\nu) \, \mathrm{d}\nu}. \tag{2.56}$$

The Rosseland opacity is directly linked to the diffusion limit of the RT equation and is hence generally a better approximation towards deeper layers of the star, where the mean free path of photons is rather small and the radiation field is comparably isotropic. The Planck mean, on the other hand, constitutes a weighted average in alignment with the source function (in LTE at least) and is hence more suitable in the upper, optically thin layers of the atmosphere. The Rosseland optical depth,

$$\tau_{\text{ross}} = -\int_{z_0}^{z} \rho \kappa_{\text{ross}} \, \mathrm{d}z' \tag{2.57}$$

In addition, it is commonly used as a general depth scale of the atmosphere, instead of the geometrical height z. It is instructive to consider the situation in which the monochromatic optical depth $\tau_\nu \approx 1$. At this depth, the photon mean free path $(1/\rho\kappa)$ is comparable to the thickness of the remaining material above. The result is that photons that are created (with frequency ν) at the Rosseland optical depth of $\tau_{\text{form}} = \tau_{\text{ross}}(\tau_\nu = 1)$ have a high probability of escaping the atmosphere. τ_{form} is hence also called the *formation depth*, as it expresses the (optical) depth where a given opacity source forms, i.e. starts to contribute significantly to the intensity of the emergent radiation.

It may be noted that this depth depends on the monochromatic opacity. For strong lines – where the opacity is high – the depth increment photons can travel is rather small. The line hence generally forms in the upper layers of the atmosphere. This is especially true for the line cores, where the opacity is the highest across the line profile. The line wings successively have a lower opacity, and hence form deeper within the atmosphere. The continuum then forms around the optical surface, where $\tau_{\text{ross}} = 1$.

This height dependence furthermore suggests that the grouping based on wavelength alone is suboptimal. In fact, neighboring points in the wavelength space may have very different opacities and thus form in vastly different regions of the atmosphere. A more robust technique is therefore a wavelength grouping based on formation depth, which has been shown to produce integrated heating rates in satisfactory agreement with the full monochromatic heating rate with as little as four opacity bins (Ludwig 1992; Vögler et al. 2004, 2005).

Here, some studies rely on 12 opacity bins, which are spread over the 2D wavelength vs. formation depth space (Freytag et al. 2012). In most cases, the bin edges are determined in complex iterative procedures that frequently regroup opacities in the course of the 3D simulation (Magic et al. 2013a). However, as recently shown by Perdomo García et al. (2023), there is no immediate correlation between the integrated heating error caused by the binning approximation and the number of bins, but more so with the precise selection of the bin limits. A balance needs to be found between the accuracy of the radiative transfer solution and the additional computational burden. More information and more practical considerations may be found in Sec. 4.

2.1.5 Spectrum Synthesis in 3D

In 3D, the velocity field is a function of space and time. Since different parts of the line form in different regions of the atmosphere, photons experience a different Doppler shift depending on their wavelength, causing line profiles to become naturally broadened and asymmetric. In classical 1D HE models, there is usually no depth dependent velocity field and spectral lines are assumed to be perfectly symmetric (e.g. Asplund et al. 2000). The following section will give a brief overview of important characteristics of 3D spectra, which are relevant for the remainder of this thesis.

Spatially Resolved Spectroscopy

Synthesizing spectra in 3D gives access to the domain of horizontal variations across the stellar disk. To demonstrate this, Fig. 2.3 shows the spatially resolved intensity at the disk-center of a solar 3D RHD model atmosphere in an arbitrary optical wavelength window – a zoom-in of the 4MOST (see Sec. 2.1.7) high-resolution window between 5330 Å and 5619 Å (HR10) in this example. Each (black) line in this figure corresponds to the spectrum emerging from a grid point at the models surface.

Because the atmospheric structure exhibits horizontal (and vertical) gradients in velocity, light that emerges from different parts of the stellar surface experiences convective blue- or red-shifts. Since uprising fluid parcels cover a larger area spatially, spectral lines generally experience net convective blue shifts on average. This is especially the case for weak lines or the wings of strong lines – as they form close to the basis of the photosphere, where there is still considerable convective flux – and less so for the cores of strong lines, which form further out past the convective overturn in radiation-dominated regions (Asplund et al. 1999).

Besides shifts in wavelength, it may furthermore be noticed that the absolute intensity is changing across the stellar disk. Through the connection between emitted radiation energy and temperature (Stefan-Boltzmann law $\sim T^4$ for frequency integrated-, Planck law as in Eq.

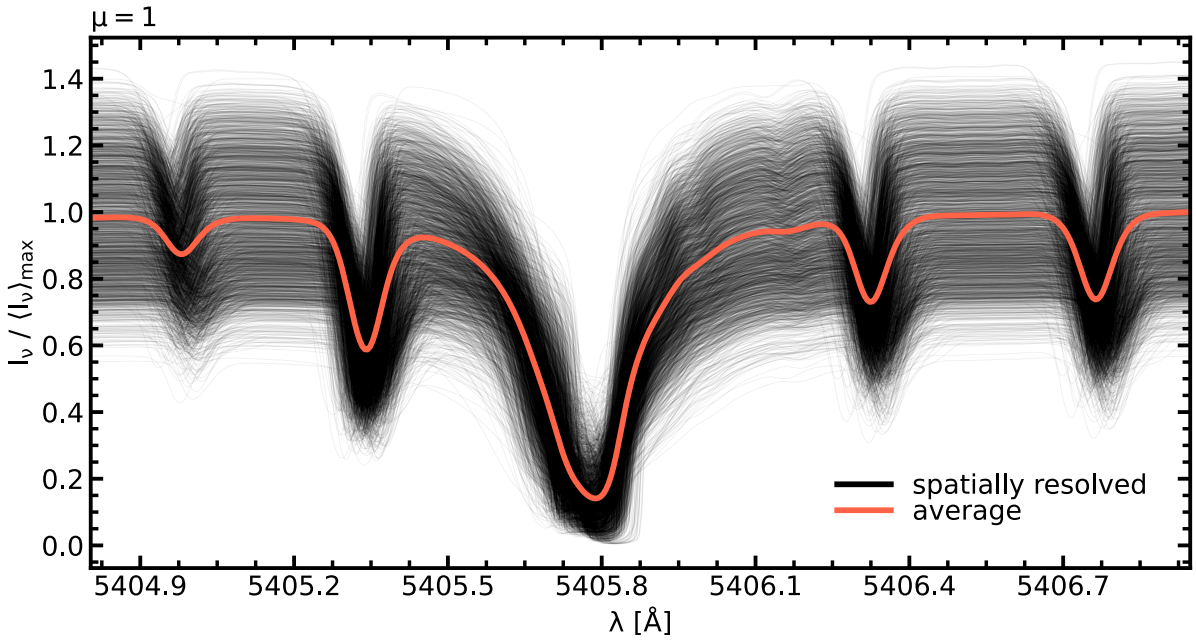

Figure 2.3: Spatially resolved disk-center ($\mu = 1$) radiation intensity I_ν, synthesized for an arbitrary optical spectral window in the 4MOST HR10 (see Sec. 2.1.7 below) using a solar 3D RHD model atmosphere. Grey lines in the background corresponds to the intensity emerging from a different horizontal grid point. The red, solid line represents the horizontally averaged spectrum. The intensity has been normalized to the maximum intensity level of the average spectrum.

2.44 for frequency depended) these differences can directly (at least in LTE) be attributed to atmospheric temperature variations in the line forming region. It is clear that any kind of resolved stellar spectroscopy – spatial or temporal – requires 3D models. Note that these horizontal variations also influence observations from distant stars, which generally are observed as point sources, as the final spectrum constitutes the integral across the disk.

Center-to-limb Variations

A qualitatively similar effect can be observed when viewing the star from different angles $\mu = \cos\theta$, where θ is considered the angle between the normal of the stellar surface and the direction towards the observer, such that the center and limb of the disk are given by $\theta = 0°$, $\mu = 1$ and $\theta = 90°$, $\mu = 0$, respectively. A schematic visualization across the observed solar surface can be found in the right panel of Fig. 2.4, where concentric rings of constant μ are shown in front of solar observations from Bridgman et al. (2021). For selected viewing angles from limb (top) to center (bottom), the left panel of Fig. 2.4 furthermore shows the solar spectrum in the same spectral window as in Fig. 2.3.

In both panels, the so-called *limb-darkening* is clearly visible; at the limb of the stellar disk, i.e. $\mu \to 0$, the star appears to be less bright. Similarly to the angle-integrated, horizontal shifts described above, the culprit is again a combination of optical depth and the tem-

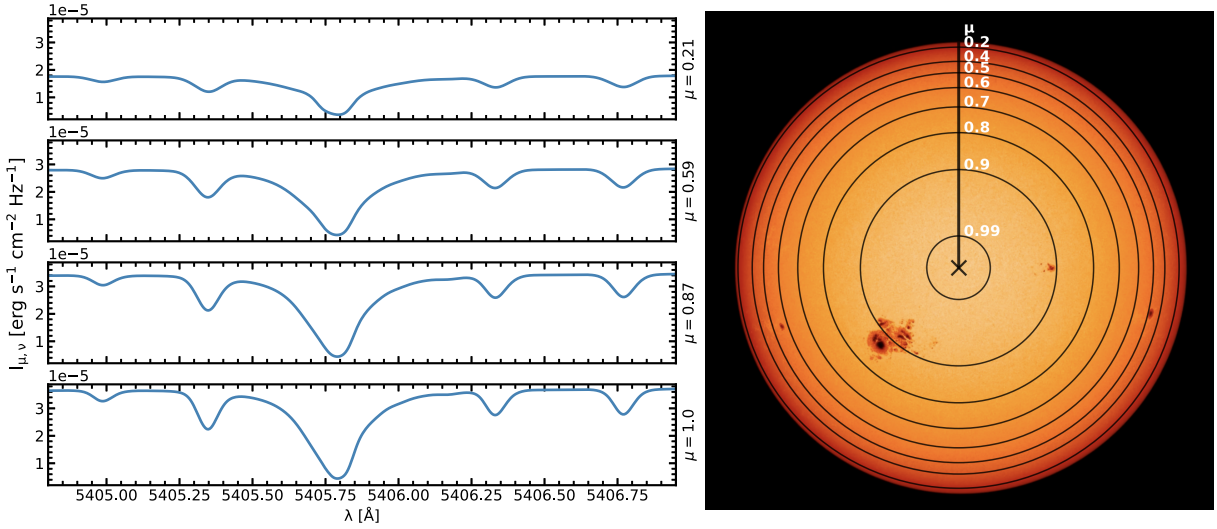

Figure 2.4: Schematic visualization of stellar center-to-limb variations. Left: Optical spectrum around 5405 Å at different viewing angles μ (see text). Right: Corresponding surfaces of equal μ across the solar disk. The image of the sun in the background was adopted from Bridgman et al. (2021).

perature structure. When viewing the star at an angle, optical depth of unity – i.e. the region from which light is able to escape the atmosphere and travel towards the observer – is reached in higher atmospheric layers, as less deep regions are penetrated due to the increased path length required to reach the same depth at angle μ (see Eq. 2.34, where $\mathrm{d}s = \mathrm{d}z/\mu$ in the 1D case, with height coordinate z).

Because the atmosphere exhibits a negative temperature gradient, it is significantly cooler and hence fainter when viewed at the limb as opposed to the disk center, where light from deeper and thus hotter layers is received (e.g. Rutten 2003; Lind & Amarsi 2024). This behavior manifests itself in the continuum displacement seen in the left panel of Fig. 2.4, where at $\mu = 0.21$ the absolute intensity is a factor of ~ 2 smaller than at $\mu = 1$.

It should be noted that limb-darkening can also be studied using 1D models, as they can be extended horizontally with the implicit assumption that there is no horizontal variability in the atmospheric structure. While providing useful estimates especially in the context of transiting exoplanets, where limb-darkening has a significant impact on the predicted light-curve and parameter uncertainties (Claret 2004; Southworth 2008), it was shown that inconsistencies found between limb-darkening measurements and model predictions for, e.g. α Centauri B (Bigot et al. 2006) or light-curves of exoplanet HD 209458 (Hayek et al. 2012) can mostly be attributed to the usage of 1D atmospheric models. Magic et al. (2015) furthermore compared limb-darkening coefficients for a range of 3D model atmospheres with 1D ATLAS models, and found that for most FGK-type stars the 3D − 1D differences are mostly noticeable towards the limb, where generally 1D models appear to be brighter.

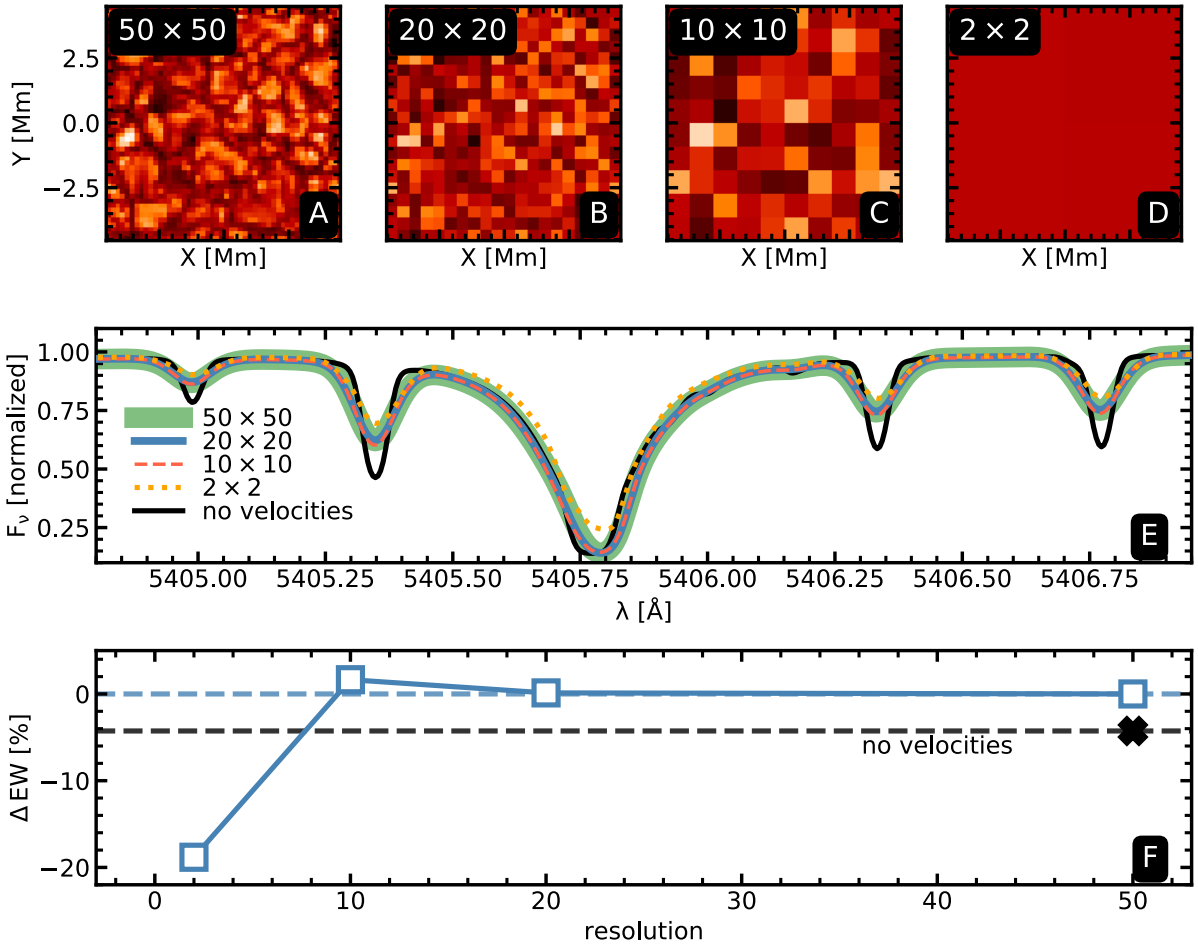

Figure 2.5: Influence of horizontal resolution in 3D models on spectra. Top: temperature at the optical surface for different number of points in the horizontal, as quoted in the figure inset. Middle: Comparison of the resulting horizontally averaged flux in an arbitrary optical wavelength window within the 4MOST HR10 (see Sec. 2.1.7 below). Black, solid line corresponds to a spectrum taken at 50×50 resolution, but with the velocity field set to 0 in the entire atmosphere. Bottom: compared to the spectrum with resolution 50×50 as a function of resolution. See text.

Self-consistent Broadening & Horizontal Downsampling

Considering all of the above, it becomes clear that the shape of spatially- and angular-integrated spectral lines is linked to temperature and density variations imposed by the granular pattern across the stellar atmosphere, which itself is highly non-static and variable with time. Not only that; the horizontal variation on planes of constant optical depth furthermore randomly samples the local velocity field, and hence naturally produces a line broadening that has a similar effect than the micro-turbulence hyperparameter that is required in 1D HE models. It is important to note that a statistical representation of horizontal fluctuations is often sufficient to describe spectral features to a satisfactory degree.

This statement is motivated by the content of Fig. 2.5, showing synthetic solar spectra, which are derived from the same 3D atmosphere model and subsequently subjected to hor-

izontal downsampling to 50×50, 20×20, 10×10, and 2×2 points in the post-processing. The corresponding horizontal temperature slices at the optical surface are shown in the top row. Although the original resolution of the solar simulation shown here is 180×180, all of the substructure and granular pattern is still visible in 50×50 (panel A) and to a large extent also in 20×20 (panel B), although their representations become more statistical. When the resolution is further reduced to 10×10 (panel C), granular and inter-granular cells become indistinguishable to the extent that they appear randomly sampled in the final atmosphere. With only 2×2 points (panel D) almost no horizontal variation is noticeable.

High spatial resolution – paired with a large number of points in the frequency domain – constitutes a severe computational challenge and significantly increases the consumption of time and memory resources. Since vertical atmospheric gradients are larger – and hence their resolution more important for the final spectrum – reducing the number of points in the horizontal directions is a common technique to limit resources spent on the spectrum synthesis, while still retaining physical accuracy. This can be seen qualitatively by comparing spectra from high- and low-resolution atmospheres in panel E of Fig. 2.5 – for the same spectral window as in Fig. 2.4 and 2.3 – and investigating how much they differ from each other.

In addition to the horizontally averaged spectra corresponding to models in panel A (green, thick, solid line), B (blue, solid line), C (red, dashed line), and D (orange, dotted line), I also include the spectrum emerging from the same atmosphere as panel A, but with the velocity field set to zero in the entire atmosphere (black, solid line). In addition, I show the corresponding difference in the equivalent width (EW, see Eq. 2.58 in Sec. 2.1.7 below for the definition) compared to the spectrum with resolution 50×50, i.e. $\Delta\mathrm{EW} = \mathrm{EW}_{\mathrm{X}\times\mathrm{X}}/\mathrm{EW}_{50\times50} - 1$ as a function of resolution X in panel F.

In the extreme case of 2×2, one may notice that the spectral lines generally become brighter. Here, the normalized flux in line wings, as well as cores, is notably overestimated with respect to high resolution, which causes a substantial difference from the high resolution EW of $\sim 20\%$. Increasing the resolution to 10×10 considerably improves the agreement ($\Delta\mathrm{EW} \sim 2\%$), with small differences still noticeable in weaker line cores. The spectrum 20×20 already is visually almost indistinguishable from the high resolution case ($\Delta\mathrm{EW} \sim 0.1\%$), indicating that the statistical representation of temperature and density stratification at this resolution is sufficient to capture the essence of 3D structural inhomogeneities. By comparison with the static spectrum it may furthermore be noticed that horizontal velocity fluctuations – even when only sampled statistically – naturally cause broadening of spectral lines. When removing velocities, the corresponding error in the EW is $\sim 5\%$, which is notably larger than the uncertainty associated with a rather rigorous downsampling to 10×10, stressing the importance of modeling the velocity field from first principles.

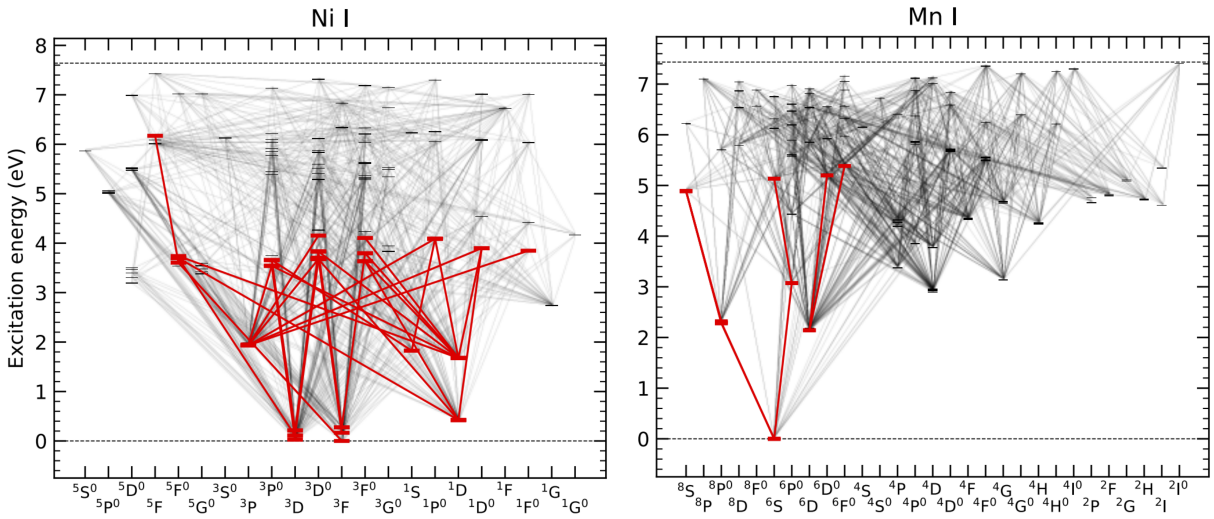

Figure 2.6: Grotian diagram showing bound-bound transitions between energy levels of Ni I (left) and Mn I (right). Highlighted in red are specific, diagnostic spectral lines that are used for abundance studies. Image taken from Storm et al. (2025).

To what extent spatial resolution influences the inferred stellar parameters and abundances remains to be investigated in more detail (see Sec. 4). However, it was found by Bergemann et al. (2021) that the O I solar flux was subject to deviations smaller than 2% and abundances smaller than 0.01 dex when relying on a horizontal resolution of 30×30. Nordlander et al. (2017) furthermore found that a downsampling from 240×240 to 60×60 introduces errors of 0.03 dex in EW, while Rodríguez Díaz et al. (2024) investigate comparably high resolution atmospheres of 80×80 and find only minimal deviations in abundances (< 0.007 dex) and normalized fluxes of (< 0.005) with respect to 240×240.

2.1.6 Statistical Equilibrium of Fe-peak elements

When thinking about Galactic Archaeology with the objective of studying Galactic chemical evolution, elements that are located close to the maximum in the binding energy per nucleon around Fe – i.e. Cr, Mn, Co, and Ni – are of special interest, as they are the end product of many stellar nucleosynthesis sites. Among these *Fe-peak* species, it is mainly Fe itself, which is commonly used as a proxy element for the overall metallicity of stars, Ni, which is produced in large quantities by massive stars as well as SNe Ia explosions (Nomoto et al. 2013), and Mn, which is very sensitive to different SNe Ia explosion mechanisms (Seitenzahl et al. 2013a), that are especially interesting to investigate.

In NLTE the level population number densities of a species are not governed by the Saha-Boltzmann equation, but one rather needs to solve the statistical equilibrium equation (Eq. 2.47). This requires detailed models for each atom or molecule, capturing energy levels and the transitions linking them. Such models include spectral lines, transition probabilities (oscillator strengths), line-broadening parameters, and possibly hyperfine structures or isotopic

shifts. For bound-free transitions, photoionization cross-sections are essential; while some employ quantum mechanical methods, such as R-matrix techniques (Burke 2011; Zatsarinny & Bartschat 2013; Bergemann et al. 2012b), simpler hydrogenic approximations may be sufficient for less influential levels (Bergemann et al. 2019). In addition to the inclusion of radiative transitions, it is important to consider collisional transitions as well, as they are of high relevance for the statistical equilibrium due to their thermalizing nature. Especially inelastic collisions with free electrons (van Regemorter 1962) and H interactions are considered, utilizing classical methods (Drawin 1968) or quantum mechanical approaches (Kaulakys 1991).

A visual representation that highlights the complexity of the resulting model atoms is shown in the so-called *Grotian* diagram for Mn and Ni (Fig. 2.6, adopted from Storm et al. 2025), where all bound-bound transitions included in the model are shown in black, while the few diagnostic transitions used for abundance analysis are highlighted in red. It is clear that the solution of the full system of level populations can not be obtained by omitting transitions that are not used for diagnostic purposes, as they nevertheless may influence the number densities of particles transitioning into or from a specific energy level, even though the lines themselves are not used to eventually derive parameters from spectra.

Model atoms are used within NLTE codes (such as e.g. the well-established `MULTI` code, Carlsson 1992; Leenaarts & Carlsson 2009, for 1D and 3D, respectively), where level populations for each energy level in the model atom are computed iteratively, while simultaneously solving the radiative transfer to keep the radiation field up-to-date for each point in a given stellar atmosphere. The influence of NLTE on each species then needs to be evaluated line-by-line and for each model with different stellar parameters and atmospheric structure separately.

The statistical equilibrium of Fe was analyzed in great detail by Bergemann et al. (2012a). Especially for neutral Fe I, which is a minority species in late-type stellar atmospheres and hence very sensitive to over-ionization (Bergemann & Nordlander 2014), it was found that level populations significantly depart from their LTE values due to a super-thermal UV continuum in the stars they analyzed. According to Eq. 2.50 this leads to underpopulated lower energy levels, $b_\mathrm{l} < b_\mathrm{u}$, which causes spectral lines to weaken in NLTE and hence generally leads to positive abundance corrections for Fe I.

The strength of NLTE corrections is furthermore very sensitive to stellar parameters and atmospheric models that are considered; for solar-like stars, Bergemann et al. (2012a) found only modest corrections ~ 0.02 dex. However, with decreasing metallicity they notice that the departures increase considerably and reach values ~ 0.15 dex for weak lines, and up to 0.5 dex for strong Fe I lines when using average 3D (<3D>) atmosphere models. Generally, Bergemann et al. notice that the cooler temperatures in the upper atmospheric layers

in metal-poor <3D> models amplify corrections due to the enhanced decoupling of the radiation field from the local temperature. They furthermore note that the situation is qualitatively different for the majority species Fe II, which appears to be thermalized and shows only negligible deviations from LTE.

The statistical equilibrium of Ni was investigated in Bergemann et al. (2021) in the context of accurately determining the solar O abundance, where the diagnostic forbidden O I line at 6300 Å is blended with a Ni I line at 6300.3 Å. As a species in the Fe group, they found that Ni I also behaves like a classical minority species and, as such, is subject to over-ionization, which consequently causes the underpopulation of lower energy levels. This again leads to weaker spectral lines and thus generally positive NLTE corrections. Specifically for the 6300.3 Å line, Bergemann et al. (2021) find that the corrections may exceed +0.15 dex (1D) and +0.2 dex (3D) already for the Sun, although they note that there is a significant uncertainty due to the computation of collisional rates using Drawin's recipe (Drawin 1968).

For Mn the situation is even more severe. As presented by Bergemann & Gehren (2008); Bergemann (2008) in 1D and later by Bergemann et al. (2019) in 3D, the minority species Mn I is again strongly influenced by super-thermal UV radiation, leading to significantly weaker spectral features in NLTE. Due to its large photoionization cross-sections, abundance corrections for solar-like stars are already above 0.22 dex (3D), and may climb up to $\sim$ 0.6 dex in red giants already at moderately low metallicities of $[\mathrm{Fe/H}] = -2$, where the low density in the atmosphere causes weakening of thermalization by less frequent collisional interactions.

Bergemann et al. (2019) furthermore note that there is also an NLTE effect seen in high-excitation Mn II lines, where at solar-metallicity dwarfs and giants the relevant energy levels experience photon loss, which causes them to be slightly overpopulated with respect to the upper levels, spectral lines to strengthen, and abundance corrections to be slightly negative. In very metal-poor stars $[\mathrm{Fe/H}] = -3$, Mn II lines become increasingly weak, and radiative pumping starts to cause positive corrections again. Bergemann et al. furthermore express the importance of the combined influence of 3D and NLTE on the statistical equilibrium, as they find that over-ionization is significantly enhanced within granules, due to stronger background radiation, which changes the abundance corrections between 3D NLTE and 1D NLTE by $\sim$ 0.2 dex in the case of the Sun.

The statistical equilibrium of Fe-peak elements underscores the need to overcome traditional 1D HE models and 1D LTE spectrum synthesis for the abundance analysis because they may introduce significant biases in resulting abundance distributions. Given that Fe-peak elements are key indicators of Galactic chemical evolution, it is crucial to quantify the errors caused by these simplified models.

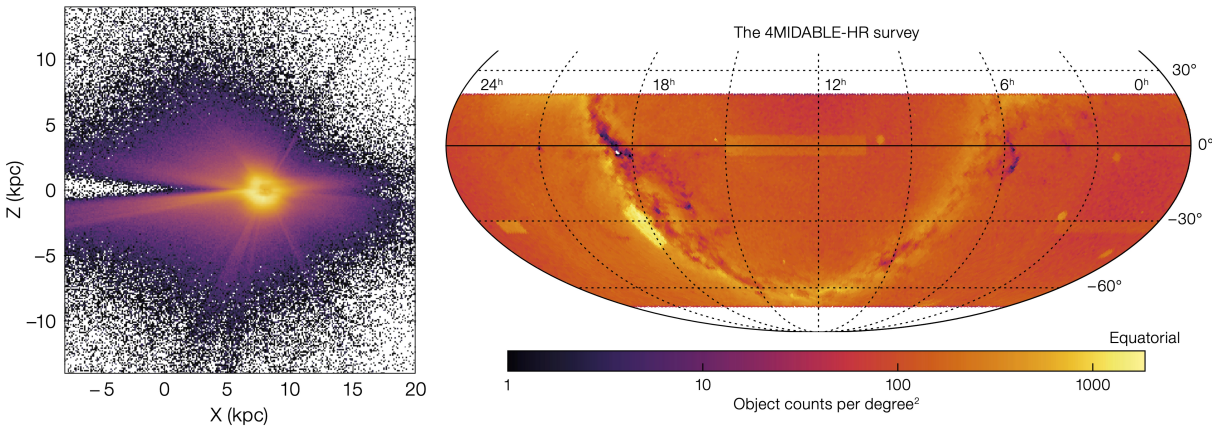

Figure 2.7: Location of the 4.1 million stellar targets of the 4MOST Milky Way Disc and Bulge High-Resolution Survey (4MIDABLE-HR) in Galactic coordinates (left) and all-sky (right). Figure taken from Bensby et al. (2019)

2.1.7 Deriving Stellar Parameters on Large Scales

With the advent of large spectroscopic surveys, the need for on-the-fly spectrum synthesis becomes increasingly pressing. The *4-metre multi-Object Spectroscopic Telescope* survey (4MOST, de Jong et al. 2019) for example is expected to provide $\sim$ 20 million stellar spectra, where the Milky Way Disc and Bulge High-Resolution (4MIDABLE-HR, Bensby et al. 2019, see also Fig. 2.7 for an overview over the spatial location of selected targets in the Galaxy) sub-survey specifically targets 4.1 million stars in the solar neighborhood, but also across the remaining Galactic disk and towards the Galactic center, which is expected to reveal the formation history and evolution of the Galaxy to an unprecedented degree.

Once in operation, the 4MOST optical spectroscopic instrument will be mounted on the 4-meter VISTA telescope at the Paranal Observatory, where light within a 2.5-degree field-of-view will be collected in 2436 fibers, out of which 812 will be fed into a high-resolution ($R \sim 18000-21000$) spectrograph. To reach scientific goals, 4MOST is designed to provide radial velocities for any Gaia source ($G_{\rm Vega} < 20.5$ mag) with a precision of 2 km/s or better, redshifts for galaxies and active galactic nuclei with $r_{\rm AB} < 22$ mag, as well as stellar parameters and abundances of up to 15 elements for stars with $G_{\rm Vega} < 15.5$ mag, and for selected key elements, even $G_{\rm Vega} < 18$ mag with an accuracy better than 0.15 dex (de Jong et al. 2019). Beyond that, other high-resolution spectroscopic surveys, such as APOGEE (Majewski et al. 2007), GALAH (Buder et al. 2021; Bland-Hawthorn et al. 2019; Buder et al. 2024), Gaia-ESO (Gilmore et al. 2012), SDSS-V, Milky Way Mapper (Wilson et al. 2019; Kollmeier et al. 2019), and WEAVE (Jin et al. 2024), also provided or will provide spectra for million stellar samples that require efficient, while still accurate analysis.

From Spectra to Stellar Parameters

The most intuitive strategy to determine stellar parameters and abundances from observations is the direct fitting of spectral lines. This involves using an initial guess of the stellar parameters and elemental abundances, also known as *labels*, to derive the atmospheric structure. The NLTE problem is then solved iteratively on the static atmospheric background. Comparison of the synthetic spectrum with observations can be done using, for example, the least-squares method, and stellar labels can be adjusted using a gradient descent algorithm.

To eliminate the most time-consuming part in the stellar label determination process (also called *pipeline* in the context of stellar surveys), the common solution is to compute extensive grids of precomputed models of stellar atmospheres with varying $T_{\rm eff}$, $\log g$ and [Fe/H]. The remaining chemical mixture is usually assumed to be scaled-solar, i.e. to decrease with the overall metallicity, while still retaining the solar abundance ratio (except for α-elements, which are usually scaled in agreement with the Galactic abundance trend, Kobayashi et al. 2006; Ruchti et al. 2011; Magic et al. 2013a). For the bulk distribution of stars observed in Galactic surveys, this assumption is reasonable since the mean opacity is dominated by the H^- continuum (Alexander & Ferguson 1994; Rutten 2003). Whether this is also valid especially for the most abundant species C, N, and O – and their molecules – and what the implications for stellar observables are remains to be investigated (Gustafsson et al. 1975; Perdomo García et al. 2023).

Based on precomputed atmosphere models, there are multiple options to obtain stellar labels with reasonable computational investment. In 1D, there are popular codes, such as `TURBOSPECTRUM` (Plez 2012), that are able to synthesize stellar spectra in LTE with minimal time investment ($\sim$ seconds), which means they may be used in real time to fit observations directly. Including NLTE for multiple species still requires additional time that significantly influences the performance of a stellar parameter pipeline, if done from scratch for every star.

A common procedure to overcome this issue is to pre-compute departure coefficients $b_{\rm i}$ for the energy levels of every atomic species that should be treated in NLTE, as a function of stellar parameters and thus temperature-density structure of the corresponding 1D model atmosphere. The departure coefficients are then interpolated for models in between grid nodes and applied to the LTE level populations, which allows the derivation of stellar parameters in NLTE without additional time investment during the fitting procedure (Gerber et al. 2023).

The solution of the statistical equilibrium is done by other codes, such as e.g. `MULTI` (Carlsson 1992) in the case of the public NLTE version of `TURBOSPECTRUM` v20[2] (Gerber et al.

[2] https://github.com/bertrandplez/Turbospectrum_NLTE

2023). Specifically for the NLTE version of TURBOSPECTRUM, Gerber et al. (2023) compute NLTE departure grids for 13 chemical elements and further rely on 1D and <3D> model interpolation within the MARCS and average STAGGER grids (see below). This leads to a key advantage of TURBOSPECTRUM, as this code philosophy enables the synthesis of NLTE spectra of multiple elements at the same time, which naturally allows the combined fitting of blended features or entire spectral bands. With the public release of TURBOSPECTRUM NLTE, the accompanying fitting tool TSFitPy is published (Gerber et al. 2023, later updated by Storm & Bergemann 2023). TSFitPy relies on the simplex method to fit a specific set of parameters (such as stellar parameters, specific abundance, micro- and macro-turbulence, rotation or radial velocity shifts) by minimizing the χ^2 between model and observed spectrum. Within this procedure, the speed of TURBOSPECTRUM allows for it to be called directly for each parameter configuration during the minimization process.

When moving towards a full 3D analysis and/or samples containing millions of stellar spectra across the entire Galaxy, the time investment of the direct fitting method above quickly becomes the bottleneck. For this purpose, it may be advantageous to additionally precompute stellar spectra with a variety of chemical compositions for each node in the model atmosphere grid, such that the expensive, repeated calls of the spectrum synthesis code can be replaced by a faster interpolation technique, at least in NLTE.

The interpolation method itself is then dependent on the specific use case; Besides simple, direct interpolation of synthetic spectra libraries, there are multiple stellar parameter pipelines in use (or preparation) that build upon machine-learning models for either spectral emulation or direct prediction of stellar labels. Notably, there are data-driven artificial neural networks (ANNs) such as the Canon (Ness et al. 2015), which are trained on reference labels and the corresponding observed spectra from a small sample of stars with known labels, model-driven ANNs such as the Payne (Ting et al. 2019), which are trained on grids of model spectra directly, and convolutional neural networks such as the CNN (Guiglion et al. 2024), which directly predict stellar labels from spectra as input and hence skip the χ^2–minimization procedure entirely. Note that Canon, as well as CNN, depend on atmosphere models and synthetic spectra no less than Payne, despite the fact that they may be trained on real spectra, through the derivation of reference labels.

Spectral emulators that generate spectra from labels may furthermore be included in more complex Bayesian pipelines that complement the spectroscopic probability distribution function (PDF) with additional constraints based on, e.g., Gaia (Gaia Collaboration et al. 2016, 2018), WISE (Lang et al. 2016) or 2MASS (Skrutskie et al. 2006) photometry, distances (Bailer-Jones et al. 2018, 2021), and asteroseismic information (e.g. Auvergne et al. 2009; Gilliland et al. 2010). One such example is the SAPP (Gent et al. 2022) – the stellar parameter pipeline that will be used in the context of the *PLAnetary Transits and Oscillations of stars* (PLATO Rauer et al. 2014) space mission – which builds its spectroscopy module

on a derivative of the `Payne` (Kovalev et al. 2019) to allow efficient on-the-fly spectrum synthesis, and furthermore makes use of stellar evolution models from `GARSTEC` (Weiss & Schlattl 2008). According to Gent et al. (2022), the stellar parameter within the PLATO core sample can be recovered with typical uncertainties of 27 K (systematic) ± 37 K (statistic) for $T_{\rm eff}$, 0.00 ± 0.01 dex for $\log g$ and 0.02 ± 0.02 dex for [Fe/H], highlighting the applicability of the procedure for large spectroscopic surveys.

Because the `SAPP` is an integral part of Sec. 3, its main working principle is briefly outlined here. In its standard operation mode, the `SAPP` derives stellar parameter and abundance estimates in a multi-step procedure. First, spectra are fitted by minimizing the χ^2 difference between model and observations. In addition to stellar labels, the placement of the continuum is also slightly adjusted during the fitting procedure by determining coefficients for linear combinations of the first ten Chebyshev polynomials (Kovalev et al. 2019). Radial velocity shifts are corrected by cross-correlating templates of model spectra.

As described by Gent et al. (2022), the astrometry module estimates the likelihood of the observed magnitudes in different filters by comparing them to predictions from stellar evolution models, which are subject to parameters such as $T_{\rm eff}$, $\log g$, mass, age, metallicity, and α-abundance. For this, apparent magnitude observations are de-reddened and converted to absolute magnitudes using the distance modulus. Here, the comparably large uncertainties of distance measurements (mostly from parallaxes) are most significant. To avoid double-counting them in different filters, they are treated as separate measurement and then marginalized over. The astrometric likelihood is constructed via the product of Normal distributions for each photometric band.

To obtain the desired posterior probability for model parameters $\mathbf{X}$, given the observations $\mathbf{Y}$, `SAPP` resorts to Bayes theorem, $p(\mathbf{X}|\mathbf{Y}) = p(\mathbf{Y}|\mathbf{X}) \cdot p(\mathbf{X}) \,/\, p(\mathbf{Y})$, which additionally allows for the inclusion of a prior $p(\mathbf{X})$ (to account for potential limitations of the models) and a normalization constant $p(\mathbf{Y})$ (which is independent of $\mathbf{X}$). To develop the probability distribution function (PDF), the astrometric likelihood is evaluated on a parameter grid of stellar evolution models. Additionally, `SAPP` computes a spectroscopic PDF on the same grid, again employing a Normal distribution.

After normalization, both PDFs are combined, and the result is evaluated to obtain the most likely set of parameters. Besides spectra, apparent magnitudes, and distances, `SAPP` also has the capability to make use of asteroseismic information $\Delta\nu$ and $\nu_{\rm max}$, if available. To increase the precision of effective temperature estimates, `SAPP` furthermore includes the *InfraRed Flux Method* (IRFM, Casagrande et al. 2006, 2010, 2020). This method relies on the weak temperature dependence of the IR-flux in the Rayleigh-Jeans limit, $F_{\rm IR,model} \sim T/\lambda^4$, and the Stefan-Boltzmann law, i.e. $\sigma_{\rm SB} T_{\rm eff}^4 = F_{\rm bol,obs}/F_{\rm IR,obs} \cdot F_{\rm IR,model}$, to provide a more robust, less model-dependent temperature estimate (Casagrande et al. 2020). Further information of

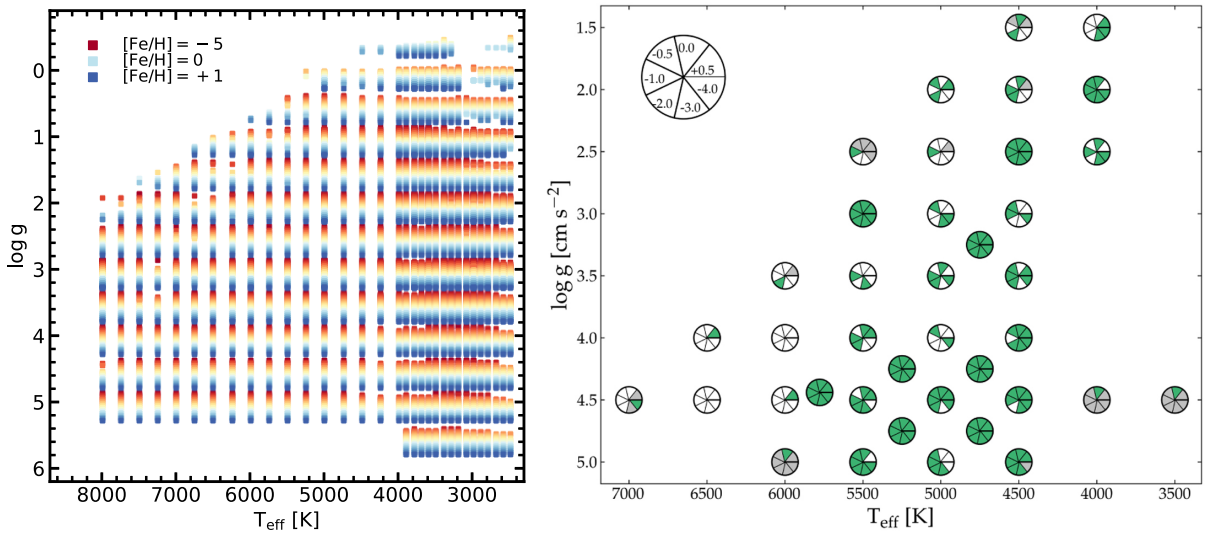

Figure 2.8: Comparison of the MARCS 1D HE (left) and 3D RHD STAGGER (right) model atmosphere grids in the $T_{\rm eff} - \log g$ plane. The left image shows the public, standard composition MARCS grid (Gustafsson et al. 2008), where different metallicities are shown in different colours with slight vertical offsets from the respective grid node. The right image was taken from Rodríguez Díaz et al. (2024).

about the SAPP can be found in Gent et al. (2022).

Model Atmosphere Grids

The quality of every stellar parameter retrieval pipeline however crucially depends on density and availability of the model spectra grid – and hence also on the grid of model atmospheres – in the parameter space for which it is built. For the analysis of FGK-type stars, most studies here rely either on the grid of MARCS models for a 1D analysis or on the STAGGER grid (Magic et al. 2013a; Rodríguez Díaz et al. 2024) in 3D. A comparison between models from both grids in the $T_{\rm eff} - \log g$ plane is shown in Fig. 2.8.

Especially in the region between 2500 K and 4000 K, the MARCS grid is sampled very densely with a temperature spacing of $\Delta T_{\rm eff} = 100$ K. Also in the regime of higher temperatures ≤ 8000 K the spacing is not larger than $\Delta T_{\rm eff} = 250$ K. The models are also placed with a surface gravity step $\Delta \log g = 0.5$ dex and provide for metallicities between −5 and +1 dex, where a good chemical coverage is ensured by varying the spacing between 1 dex and 0.25 dex for low and intermediate-to-high metallicities, respectively.

In 3D, the availability of models is comparably poor; until recently, there was no grid of 3D models available to the public. The STAGGER grid, originally created by Magic et al. (2013a), was released and refined by Rodríguez Díaz et al. (2024) to increase the model sampling in the dwarf star region in the PLATO core sample. With 243 STAGGER models in total (distributed between metallicities between −4 and +0.5 dex), the grid is significantly

more sparse (compared to the $\sim$ 52 000 MARCS models available[3]) due to the increased computational effort involved in creating these models. It may be noted that there are 77 CO^{5}BOLD models in addition, collected in the CIFIST grid (Ludwig et al. 2009a; Bonifacio et al. 2018; Kučinskas et al. 2018), which, however, is not publicly available.

According to tests by Kovalev et al. (2019), roughly 20 000 spectra are furthermore needed to train Payne and obtain a satisfactory spectrum emulation result, which in the case of 3D additionally involves a serious amount of CPU hours. It is still questionable to what extent the low $T_{\rm eff} - \log g$ resolution of the STAGGER grid is sufficient in this context. Currently, there is no machine learning algorithm based on a extensive grid of 3D spectra available that may be used to derive 3D LTE (or even NLTE) stellar labels for large spectroscopic surveys. Direct fitting in full 3D is thus currently computationally only possible for individual stars.

Abundance Corrections

One common technique to account for the error made by the modeling assumptions at least approximately are the so-called *abundance corrections*. Here, for a fixed set of stellar parameters, the abundance of a given species of interest is varied, and synthetic spectra are created for each chemical composition. The resulting *Equivalent-Width* (EW) is obtained by integrating the normalized flux $F_{\rm N}$ across each spectral line, i.e.

$$\mathrm{EW} = \int (1 - F_{\rm N})\, \mathrm{d}\lambda, \tag{2.58}$$

and then expressed as a function of to the abundance itself, which is also called *Curve-of-Growth (CoG)*. The CoG is then inverted to yield $A = A(\mathrm{EW})$, and compared between different model assumptions, e.g. LTE–NLTE or 1D–3D. The final abundance correction is computed with respect to a specific reference abundance $A_{\rm ref}$. NLTE abundance corrections for example are then defined as

$$\Delta A_{\rm NLTE} = A_{\rm NLTE}(\mathrm{EW}_{\rm LTE}) - A_{\rm LTE,ref}, \tag{2.59}$$

where the reference abundance is set to the LTE (or 1D in the case of 3D corrections) abundance for which one wishes to derive the correction. The corrected abundance is then given by simply adding the correction to the measurement.

There are several areas where caution has to be taken when applying abundance corrections. Higher abundances increase the opacity and hence formation height of lines, causing the departures from LTE and thus abundance corrections to depend on the abundance itself (e.g. Eitner et al. 2019; Popa et al. 2023). The NLTE effects furthermore depend on the electronic configuration of energy levels and characteristics of transitions between them,

[3] https://marcs.astro.uu.se/

which means that abundance corrections also vary between spectral lines.

Depending on the line, there are furthermore regions in abundance space where the line becomes saturated. If this is the case, a step in abundance is associated with small changes in EW, which can cause asymptotes in the inversion EW(A) $\rightarrow$ A(EW) (Rutten 2003). Since abundance corrections are often provided as averages over different spectral lines and for a single reference abundance, their blind application constitutes an additional source of uncertainty. Since in the case of 1D corrections the CoG is constructed from 1D spectra, it is furthermore important to realize that the abundance corrections are inherently dependent on all hyperparameters included in 1D spectrum synthesis, i.e. mixing length parameters and micro-turbulence. Nevertheless, while this method is generally inferior to the actual fitting of observations, it is a very useful tool to estimate the potential impact of modeling assumptions, especially for large stellar samples.

2.2 Galactic Archeology

Modeling assumptions are inherent to the procedures involved in the deciphering of stellar spectra and hence directly influence measured stellar parameters and especially chemical abundances. These abundance measurements – often done in 1D LTE when analyzing large stellar samples – are then considered the ground trough when they are further used to understand the formation and evolution history of the environment they reside in. The interpretation of the measured Galactic abundance trends is done with the help of so-call *Galactic Chemical Evolution* (GCE) models, which describe the evolution of the Galactic gas content and formation of metals, from a primordial composition to the present-day chemical diversity.

2.2.1 Galactic Chemical Evolution Models

There are countless variations of GCE models, with vastly different complexity involved in the detailed treatment of metal production sites, the dynamics of stars and gas in the gravitational potential of the Galaxy, and the interaction with the intergalactic medium or other near-by galaxies. Following the description by Matteucci (2001, 2003, 2016), the fundamental idea behind a GCE model is to understand how the mass of the Galactic gas $M(t)$ changes as time t passes. Generally speaking, there are two main processes that cause the gas mass to change: star formation and Galactic inflows and outflows of material. Considering the Galaxy as a single box of perfectly mixed gas (a so-called *one zone* model), the amount of gas that is removed from the Galactic gas mass reservoir to form stars per unit time is described by the star formation rate (SFR) $\psi(t)$. A common assumption in various GCE models is the validity of the Kennicutt-Schmidt law (Schmidt 1959; Kennicutt 1998), which imposes a proportionality between the SFR and the gas mass M, that is,

$$\psi(t) = \frac{\epsilon_\mathrm{s}}{\tau_\mathrm{s}} M(t), \tag{2.60}$$

with parameterization through the proportionality constants of the dimensionless star formation efficiency ϵ_s and the star formation timescale τ_s.

Stars have a finite lifespan t_m that is generally influenced by their initial mass m. Consequently, the gas mass at time t is reduced by currently forming stars but increased by stars that formed t_m time-units ago, returning some of their material to the Galactic reservoir. Using the initial mass function (IMF) $\phi(m)\mathrm{d}m$, which represents the stellar distribution per mass unit, the number of stars with masses between m and $m + \mathrm{d}m$ that will end their life – and thus return their mass to the Galactic gas at time t – can be described as $\psi(t - t_\mathrm{m})\phi(m)\mathrm{d}m$, under the assumption that the IMF is constant in time. Different stellar evolution paths are possible on the basis of initial mass, leading to remnants such as white

dwarfs (WD), neutron stars (NS), or black holes (BH). Therefore, an additional factor $f(m)$ is necessary to specify the mass returned to the Galaxy upon the death of stars, excluding the mass locked in remnants and removed from the gas reservoir. Often, $f(m)$ can be defined as $m - m_{\mathrm{remnant}}$. Combining the creation and destruction of stars, the fundamental equation of GCE may be written as the time derivative of the gas mass $\mathrm{d}_t M$,

$$\mathrm{d}_t M(t) = -\psi(t) + \int_{m_\mathrm{l}}^{m_\mathrm{u}} f(m)\ \psi(t - t_\mathrm{m})\phi(m)\ \mathrm{d}m, \tag{2.61}$$

where the integration needs to be executed from a lower mass limit m_l, below which stars are assumed to live longer than the age of the galaxy (typically $\sim 0.8\,\mathrm{M}_\odot$) and hence do not contribute to the chemical enrichment, to a upper limit m_u, above which stars are assumed to leave behind nothing but a black hole (typically $\sim 30\,\mathrm{M}_\odot$ for disk models, see e.g. Matteucci 2001, 2003; Nomoto et al. 2013; Côté et al. 2019).

Neglecting the stellar lifetimes entirely, one may notice that the SFR can be moved in front of the integral in Eq. 2.61. In this *instantaneous recycling* approximation, the remaining equation can be solved analytically by an exponentially decaying gas density. Eq. 2.61 furthermore lacks completeness regarding the mass entering or exiting the simulation domain, hence it is known as the *closed box* approximation. To modify this, inflow and outflow rates can be incorporated on the right-hand side. A prominent example of such a GCE model is the *two-infall-model*, which characterizes the formation of the Galaxy through two intervals of primordial gas inflow, each enhancing the SFR as per Eq. 2.60. The initial inflow, which forms the halo and bulge, occurs rapidly, whereas the second inflow that forms the Galactic disk(s) takes place over a longer period (Chiappini et al. 1997; Chiappini 2001; François et al. 2004). Outflows are generally considered to result from stellar feedback, proportional to the SFR, such that the outflow rate is given by $\eta\ \psi(t)$, where the proportionality constant η, known as the *mass-loading factor*, is a variable parameter (Côté et al. 2017).

Although the evolution of the gas mass is noteworthy, it is even more intriguing to realize that the gas returned by stars differs chemically from the gas they originated from. Thus, analyzing the evolution of the metal fraction $X_\mathrm{i}(t)$ for each species i is of particular interest. Following Eq. 2.61, it is clear that

$$\mathrm{d}_t\,(MX_\mathrm{i}) = M\ \mathrm{d}_t(X_\mathrm{i}) + X_\mathrm{i}\ \mathrm{d}_t(M) = -\psi X_\mathrm{i} + \int_{m_\mathrm{l}}^{m_\mathrm{u}} f_i(m,t)\ \psi(t - t_\mathrm{m})\phi(m)\ \mathrm{d}m, \tag{2.62}$$

where the freed mass of species i is given by the amount of metals that are freshly produced by the star, plus those that are merely ejected and hence remain present in the abundance they had when the star was created, i.e.

$$f_\mathrm{i}(m,t) = y_i(m,t) + X_\mathrm{i}(t - t_\mathrm{m})f(m). \tag{2.63}$$

The crucial part in this equation is $y_i(m,t)/m$, the stellar *yield* of species i, which in general may be a function of overall metallicity and hence Galactic time. Much of the complexity in GCE modeling revolves around the determination of yields for the different chemical production sites for stars of different mass.

2.2.2 Formation of Elements: Early Universe

Throughout the formation and evolution of the Galaxy, various sites for element production emerge, affecting the chemical makeup of the Galactic gas to different extents. Due to the distinct physical environments where nucleosynthesis occurs, the chemical composition of the ejecta – and hence the overall metal content of the Galaxy – experiences continuous change. Interestingly, low-mass stars have lifespans comparable to the age of the Galaxy (e.g. Kippenhahn & Weigert 1990; Matteucci 2001; Kippenhahn et al. 2012), allowing one to deduce early universe conditions from their chemical abundances. Initially, before stellar feedback enriches metals, *Big Bang Nucleosynthesis* (BBN) determines the baseline gas metallicity.

In the classical Friedmann–Lemaître–Robertson–Walker ΛCDM cosmological picture, the BBN is confined to the first minutes of the universe, where temperatures are high enough for the formation of ^{4}He, but also already low enough such that deuterium (^{2}H) is not immediately photo-disintegrated. Small fractions of ^{4}He are further processed to ^{6}Li and ^{7}Li. In general, the net composition of the gas after BBN is completely dominated by H (75%) and ^{4}He ($\sim$ 25%), with only trace amounts of ^{2}H/H $\sim 2\times10^{-5}$, ^{3}He/H $\sim 10^{-5}$, ^{7}Li/H $\sim 5\times10^{-10}$, and ^{6}Li/H $\sim 10^{-14}$. The synthesis of heavier, further nuclei is prohibited by the lack of stable isotopes with mass numbers of 5 or 8, and the increasingly high Coulomb barrier that needs to be overcome in a rapidly expanding and cooling universe (e.g. Wagoner et al. 1967; Yang et al. 1984; Cyburt et al. 2016).

It is interesting to note that present-day measurements of abundances from various astrophysical sites may be used to test the predicted composition and hence the understanding of the early universe directly. In particular, the observation of primordial high redshift gas clouds – which are illuminated by the light of distant quasars – may be used to measure ^{2}H/H, which in turn is closely related to the baryonic fraction during BBN. Through this connection, it has been shown (see e.g Cooke et al. 2018) that the measured ^{2}H abundances, and the subsequent BBN prediction of the baryonic fraction, are in excellent agreement with estimates obtained from Planck observations of the *Cosmic Microwave Background* (CMB, Planck Collaboration et al. 2016). Investigating He I emission lines emerging from metal-poor extragalactic H II regions furthermore allows the determination of the primordial helium abundance. Also, here, there is generally good agreement between observations, BBN predictions, and CMB measurements (e.g. Aver et al. 2013; Izotov et al. 2014).

Despite the success of ΛCDM cosmology, there are still a number of open questions that challenge the cosmological standard model (Perivolaropoulos & Skara 2022; Abdalla et al. 2022). One major discrepancy is found in metal-poor Galactic halo stars; Multiple stellar observations of the ^{7}Li abundance (e.g. Spite & Spite 1982a,b; Sbordone et al. 2010) have found values that are significantly lower than the BBN prediction. Although, to this day, there is no definitive answer to this *cosmological lithium problem*, explanations involving nuclear physics, physics beyond the Standard Model, as well as astrophysical solutions – such as a depletion of ^{7}Li in the upper layers of stars due to atomic diffusion, stellar rotation, and convection – have been proposed (see Abdalla et al. 2022, and references therein).

Another disagreement is the so-called *Hubble-tension*, which concerns the current expansion rate H_0. The Hubble tension arises because the H_0 values predicted from CMB observations – when interpreted through the standard ΛCDM cosmological model – are significantly lower than the H_0 values obtained from direct measurements in the local universe; SNe Ia in particular are central to this issue, as they function as standard candles, i.e. they are used as distance indicators. H_0 values derived using SNe Ia are consistently higher ($\sim 4\sigma$) than those predicted from the CMB data (Riess et al. 2021b).

To resolve this tension, several theoretical considerations are discussed (Perivolaropoulos & Skara 2022). One possible solution is altering the sound horizon r_s, i.e. the maximum distance sound waves could have traveled in the early universe, whose predicted size directly influences the H_0 calculation from CMB data. Another approach is a modification of the Hubble expansion rate H(z) as a function of redshift z, suggesting that the rate of cosmic expansion in the recent cosmic history might differ from what the standard model assumes.

Lastly, Perivolaropoulos & Skara (2022) also consider a transition or recalibration of the SNe Ia absolute luminosity itself, i.e. the intrinsic brightness of SNe Ia might not be constant over cosmic time. Potentially, it could have changed because of evolving fundamental physical laws, such as a variation of the gravitational constant. Additionally, there is uncertainty in the metallicity measurements of Cepheid stars – which are crucial for calibrating SNe Ia distances via their Period-Luminosity (PL) relationship (Riess et al. 2018) – as metal-rich Cepheids seem inherently brighter (Gieren et al. 2018). However, the question to what degree SNe Ia are suitable standard candles in the first place remains to be answered (Taubenberger 2017).

2.2.3 Formation of Elements: Supernovae

Supernovae of Type Ia

In general, SNe Ia are understood as the thermonuclear disruption of a WD, which accretes material (from a giant companion in a binary system) until it reaches the Chandrasekhar

mass ($M_{Ch} \approx 1.4\,M_{\odot}$) and explodes (Ruiter 2020). Due to this uniformity in their mass, SNe Ia are assumed to produce consistent amounts of ^{56}Ni, which is radioactive. Because photons emitted in the process of its decay to ^{56}Fe produce the observed light-curve, it is expected that all SNe Ia exhibit the same intrinsic brightness, which makes them a powerful cosmological standard candle to derive distances (Riess et al. 1995).

However, it was already realized by Phillips (1993) and Perlmutter et al. (1997) that there is an unexpected diversity in the absolute peak brightness of observed events at low redshift, where independent distance measurements are available to check this assumption. Despite their apparent diversity, it was found that there is a correlation between the absolute magnitude at the peak of their light-curve and the rate at which it declines, i.e. the light-curves of brighter SNe Ia are wider. The resulting so-called *Phillips relation* (Phillips 1993) is found empirically and may then be used to calibrate target light-curves from high redshift observations such that a measurement of their decline rate and peak apparent magnitude provides the distance modulus directly. The physical reason for this observed variety of SNe Ia (Benetti et al. 2004, 2005) however is still not fully understood (Sim 2007; Hillebrandt et al. 2013). This standardization procedure furthermore rests on the assumption, that the Phillips relation is universally true – i.e. also at high redshift – which may in fact not be true for some observed peculiar SNe Ia (Taubenberger 2017).

Current theoretical SNe Ia modeling frameworks explore two distinct pathways for the mass of the primary exploding WD; those that reach the Chandrasekhar mass (M_{Ch} models) and those that explode at a lower mass (sub-M_{Ch} models). Within these categories, the nature of the mass-donating companion star – either another WD in a *double-degenerate* system or a non-degenerate star in a *single-degenerate* system – introduces further variety of possible explosion scenarios. The leading mechanism for M_{Ch} and sub-M_{Ch} SNe Ia are discussed in detail in Sec. 3.

In general, SNe Ia ejecta are rich in Fe-peak elements, since the temperatures in the core region of the exploding C-O white dwarfs are high enough for nuclear statistical equilibrium (NSE) to hold, preferentially causing the formation of the most stable nuclei by burning complete C and O up to ^{56}Ni, which eventually decays to ^{56}Co and ^{56}Fe (Matteucci 2001, 2003; Seitenzahl et al. 2013a). When it comes to the nucleosynthetic differences between M_{Ch} and sub-M_{Ch} expositions, variations in the chemical mixture of the ejecta SNe Ia arise mainly due to differences in the core density and temperature of the primary WD. One very interesting species in this context is Mn; its production chain may be easily followed as it has only one stable isotope, ^{55}Mn. Its parent nucleus ^{55}Co – which is unstable and decays to ^{55}Fe with a half-life of ~ 17 h, and then eventually to ^{55}Mn – is synthesized in NSE during the initial phases of the explosion. Its abundance, as the material rapidly expands and cools, is tightly linked to the abundance of Mn in the final ejecta (Seitenzahl et al. 2013b).

In M_{Ch} SNe Ia, initial burning occurs at higher temperatures and is more efficient, resulting in fewer α-particles when NSE reactions stop. Consequently, significant amounts of ^{55}Co and therefore ^{55}Mn persist. Conversely, in sub-M_{Ch} explosions, the initial burning is less complete, leaving more α-particles at freeze-out. As a result, ^{55}Co is more likely to be destroyed, and SNe Ia generate significantly less Mn overall (Seitenzahl et al. 2013b; Lach et al. 2020; Sanders et al. 2021), which is why Mn abundances of Galactic stars provide insight into the role of sub-M_{Ch} explosions in the chemical evolution of the Galaxy.

Although Ni production is generally more complicated, since there are multiple pathways for the formation of different isotopes, the differences between sub-M_{Ch} and M_{Ch} are qualitatively comparable. More details are provided in Sec. 3. Ni is not only produced in different SNe Ia, but it is also synthesized in CC-SNe in large quantities. Besides the radiative isotope ^{56}Ni, which is the end product of Si-burning due to its high binding energy per nucleon and its favorable location in the α-chain (^{52}Fe+^{4}He$\rightarrow^{56}$Ni, Matteucci 2001), the most abundant stable isotopes are ^{58}Ni, which is mainly produced in NSE during a SNe Ia (Seitenzahl et al. 2013a) and in explosive Si-burning in the deepest layers ejected from CC-SNe (Jerkstrand et al. 2015; Perego et al. 2015), and ^{60}Ni, which additionally has contributions from neutron capture during He burning or later burning stages (Woosley & Weaver 1995).

Independent of the formation channels, the explosion of SNe Ia requires a binary system with at least one WD present. As WDs are remnants of low to intermediate mass stars with $M < 8\,M_{\odot}$, the earliest occurrence of SNe Ia in the Galactic evolution is determined by the lifetime of $8\,M_{\odot}$ stars ($\sim 30\,$Myr, Matteucci 2014). Moreover, if the system is single-degenerate the secondary star is required to be significantly less evolved as it still has to have a H- or He-rich envelop for the companion to accrete. The time-delay associated with these events is thus even longer ($\sim 0.5 - 1\,$Gyr) because the secondary star must have a lower mass than the primary $< 8\,M_{\odot}$.

The rate at which SNe Ia events occur over time is characterized by the *Delay-Time Distribution* (DTD). The DTD for a specific SNe Ia pathway is determined by several factors, such as the mass range of possible progenitors of the respective SNe Ia channel, the binary fraction, and the IMF (Matteucci et al. 2006; Ruiter & Seitenzahl 2025). However, in general this means SNe Ia are not responsible for the chemical composition of older stars in the Galaxy, such as those residing in thick disk or halo.

Core-Collapse Supernovae

Before SNe Ia begin to appear, the chemical evolution of galaxies is mainly influenced by massive stars with $M \gtrsim 8\,M_{\odot}$ exploding. These stars produce heavier elements up to ^{56}Fe as they evolve, starting with He in their cores through either p-p-chain or CNO processes, followed by triple-α He-burning and progressing through the α-chain, i.e. ^{16}O, ^{20}Ne, ^{24}Mg,

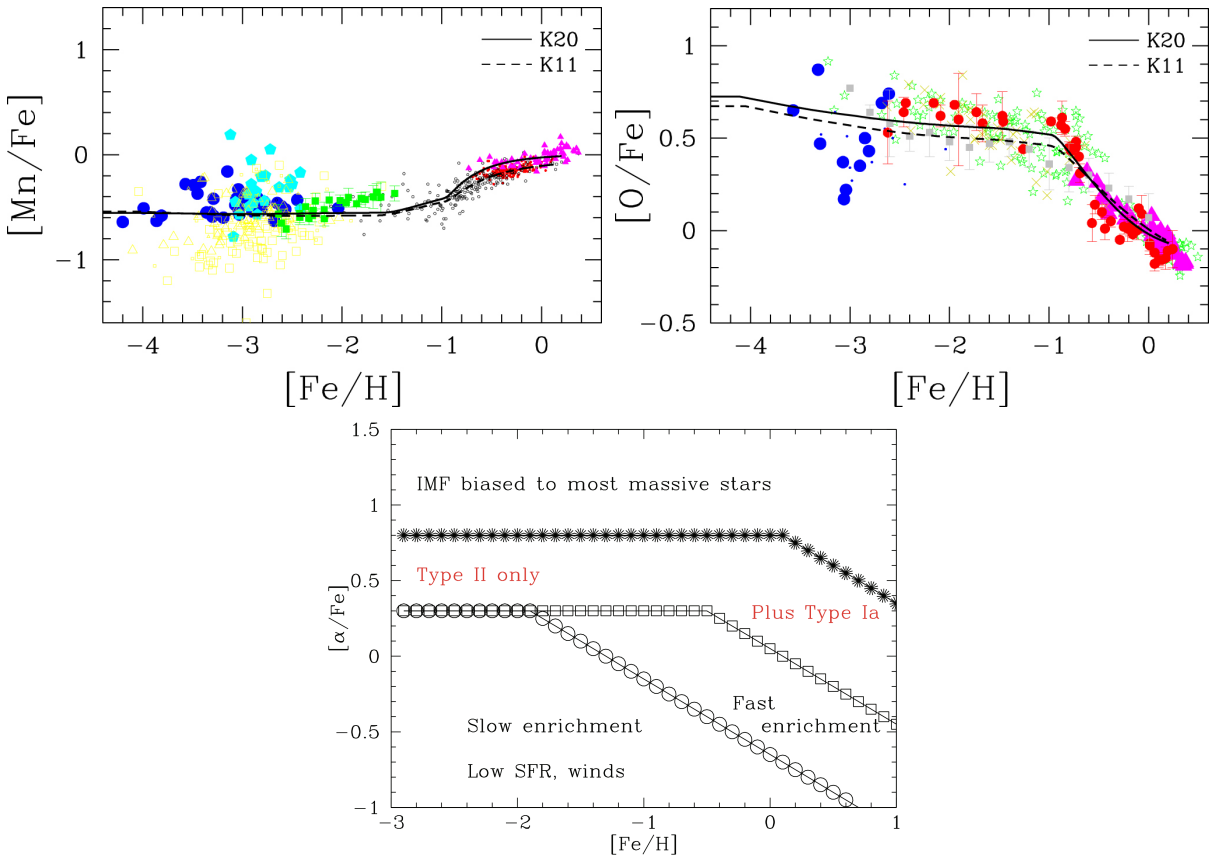

Figure 2.9: Schematic overview of Galactic chemical evolution model predictions for Fe-peak and α-elements. Top: LTE abundances of [Mn/Fe] (left) and [O/Fe] (right) against [Fe/H] from observations, over-plotted with GCE model predictions from Kobayashi et al. (2011) and Kobayashi et al. (2020b). Both figures are taken from Kobayashi et al. (2020b). Bottom: Illustration of the expected pattern of α-element abundances for a self-enriching, well-mixed star-forming system. Figure taken from Wyse (2016).

^{28}Si, ^{32}S, and ^{40}Ca, via C, Ne, O, and Si burning processes (Nomoto et al. 2013; Matteucci 2014). Their explosive ends as CC-SNe make them the main producers of α-, and also substantial Fe-peak elements. The yields of different Fe-peak elements relative to Fe is strongly dependent on the electron fraction Y_e in explosive Si-burning layers. If Y_e is small there is an increased neutron-excess, which means the yields for neutron-rich isotopes such as ^{58}Ni, ^{59}Co, and ^{63}Cu are higher. At the same time, the production of ^{56}Ni – and thus ^{56}Fe – is smaller, which means [(Ni, Co, Cu)/Fe] increase, while [Cr/Fe] stays constant. The same is true for [Mn/Fe], although it is produced in incomplete Si-burning (Nomoto et al. 2013).

Prompt enrichment by CC-SNe is fundamental in explaining the elemental abundance patterns observed in stellar populations of different ages and metallicities. To illustrate this quantitatively, Fig. 2.9 shows the comparison between predictions from the widely adopted GCE models by Kobayashi et al. (2011) and Kobayashi et al. (2020b), with a collection of Galactic LTE observations (top panels, both adopted from Kobayashi et al. 2020b). The detailed assumptions and differences between the models are not significant, as they serve to

highlight the qualitative GCE in this context here.

Early in the evolution of the Galaxy, when the first stars form, the Galactic gas has minimal metallicity since primordial gas enrichment via stellar feedback was not yet significant. As more stars form and the gas gets recycled, the metallicity rises, making [Fe/H] an age indicator (Matteucci 2003). This correlation is not entirely accurate, as it depends e.g. on the local star-formation history (Bergemann et al. 2014), but it suffices to understand the Galactic trend. The $[(\alpha, \mathrm{Mn})/\mathrm{Fe}]$ ratio in these old, metal-poor stars directly reflects massive star explosion yields (Nomoto et al. 2006). As time progresses, and [Fe/H] rises, SNe Ia start to imprint their signature on the Galactic average composition by producing substantial Fe-peak elements, which lead to a notable increase of [Mn/Fe] and decrease of [O/Fe] for stars with higher metallicity around $[\mathrm{Fe/H}] \sim 1$ up to the solar value. The distributions observed in the upper panels of Fig. 2.9 are hence the consequence of the time-delay between CC and type-Ia supernovae (Matteucci & Greggio 1986).

The location of this *α-knee* in the metallicity space is furthermore characteristic for the environment these stars formed in. This is illustrated by the image in the bottom row of Fig. 2.9 (adopted from Wyse 2016), where a schematic $[\alpha/\mathrm{Fe}]$ trend is shown for different self-enriching and well mixed stellar systems. In systems, where the overall gas density (and hence SFR) is low – such as dwarf galaxies, small satellites or irregular galaxies – there is only very little Fe build-up in the overall metal-budget. After the time-delay of SNe Ia has passed, the mean [Fe/H] is hence still low compared to the Galaxy. As a consequence, the α-knee is shifted towards lower metallicities. The opposite is true in regions of violent star formation with a high SFR or star formation efficiency, where the α-knee is shifted to higher metallicities because of the fast enrichment from CC-SNe. The IMF itself also has an effect on the $[\alpha/\mathrm{Fe}]$ trend, as the value of the low metallicity plateau is determined by the fraction of high-mass stars. Increasing their relative number in a top-heavy IMF also increases the yields of $[\alpha/\mathrm{Fe}]$ due to the dependence of the CC-SNe yields on the progenitor mass (Wyse 2016).

2.2.4 The First Stars

The first (Pop III) stars, likely formed from the collapse of nearly metal-free gas in dark matter mini-halos post-BBN and generally are thought to be more massive than the present-day IMF suggests (Bromm et al. 2002; Frebel et al. 2007, but see also Klessen & Glover 2023 suggesting a broader, while still top-heavy distribution). The nucleosynthetic contributions from Pop III stars are diverse and dictated primarily by their initial mass and the nature of their explosion (e.g. Heger & Woosley 2002; Nomoto et al. 2013). Stars with initial masses $10\,\mathrm{M}_\odot \lesssim \mathrm{M} \lesssim 40\,\mathrm{M}_\odot$ typically end as CC-SNe, ejecting α-elements alongside Fe-peak elements; the precise yields are sensitive to explosion energy and the material fallback onto

the remnant NS or BH. *Faint* supernovae within this category experience significant fallback and are thus expected to have expelled C-rich but Fe-poor ejecta due to their onion-like structure – a consequence from high-mass stellar nucleosynthesis – and the resulting Fe-core. More energetic *hypernovae* from Pop III progenitors produce distinct elemental signatures, including enhanced ratios of [(Zn, Co, V, Ti)/Fe] and small [(Mn, Cr)/Fe] (Nomoto et al. 2006; Tominaga et al. 2007).

In contrast, very massive Pop III stars, with initial masses $140\,M_\odot \lesssim M \lesssim 260\,M_\odot$, potentially explode as *pair-instability supernovae* (PISNe), which completely disintegrated the star, leaving no remnant behind and hence ejecting vast quantities of elements such as O, Si, and significant amounts of ^{56}Ni, while showing a strong odd-even effect with a depletion of odd-Z elements (Heger & Woosley 2002). Intermediate Pop III mass ranges, $40\,M_\odot \lesssim M \lesssim 140\,M_\odot$, as well as extremely high-mass stars above $\sim 260\,M_\odot$, likely result in direct collapse to BHs and thus contribute minimally to the chemical enrichment of the early universe (Heger & Woosley 2002; Ohkubo et al. 2006).

To this day, there has been no detection of true Pop III stars without any metals other than primordial traces of Li. However, it was first discovered by Beers et al. (1985) that the most metal-poor stars found in the Galactic halo show a peculiar chemical pattern. Beers et al. (1985, 1992) systematically detect stars within their HK-survey – targeted at the search and identification of stars with weak Ca II H & K lines, which indicates low metallicity – that display unusually strong lines associated with the CH molecule (the CH G-band in particular) in their spectra, which suggests unusual high C abundances. Spectroscopic follow-ups of these metal-poor candidates found that a significant fraction indeed shows strong C features, leading to their classification as *carbon-enhanced metal-poor* (CEMP) stars.

The Hamburg/ESO Survey (HES, Reimers 1990; Wisotzki et al. 2000; Christlieb et al. 2001, 2002) here also played an important role. As described by Christlieb et al. (2008), the HES utilizes approximately 12 million spectra from 379 photographic plates, captured with the 1 m ESO Schmidt telescope, covering 6726 square degrees. HES spectra range from 3200 Å to 5300 Å with a resolution of $\Delta\lambda \sim 10$ Å at 3934 Å. Using this instrumental setup, Christlieb et al. (2008) compile a catalog of about 20 000 metal-poor candidate stars based on criteria like the KP color index – centered on the Ca II K line – as a function of the de-reddened B−V and J − K 2MASS (Skrutskie et al. 2006) magnitude, as well as a non-detection of the Ca II K line in emission or absorption. Medium- and high-resolution follow-ups of HK and HES targets (e.g. Frebel et al. 2006; Placco et al. 2010; Sbordone et al. 2010; Masseron et al. 2012; Roederer et al. 2014; Hansen et al. 2015) have later led to the detection of some of the most metal-poor stars known, such as HE 0107–5240 (Christlieb et al. 2002), HE 1327–2326 (Frebel et al. 2005), and HE 0557–4840 (Norris et al. 2007). Furthermore, HES assesses the strength of the CH G-band using the GP color index, which allows Christlieb et al. (2008) to estimate [C/Fe], helping to identify CEMP candidates. Large-scale spectroscopic surveys

like SEGUE (Yanny et al. 2009), LAMOST (Deng et al. 2012), and RAVE (Steinmetz et al. 2020; Shank et al. 2022), along with photometric surveys such as SkyMapper (Keller et al. 2007) and Pristine (Starkenburg et al. 2017), follow the work of HK and HES surveys and expand the search for metal-poor stars, offering additional data for analysis.

It was found by e.g. Placco et al. (2014); Yoon et al. (2018) that below a certain metallicity ([Fe/H] ~ -4.5) all stars observed seem to be enhanced in C significantly enough to qualify as CEMP. This is in general agreement with theoretical considerations by Frebel et al. (2007), who note that the first low-mass stars at these metallicities require enhancement in either O or C in order to be sufficiently enriched to exhibit efficient atomic fine-structure cooling (although see potential Si-dust cooling Ji et al. 2014, and Ji et al. in prep.). The formal CEMP defining criteria of [C/Fe] > 1.0 was established by Beers & Christlieb (2005), who also noticed that some CEMP stars show hints of s- and/or r-process elements in their spectra, while others do not, which leads to a further sub-division into CEMP-s, CEMP-r, CEMP-r/s, and CEMP-no stars. Beers & Christlieb (2005) based the s- and r-process classifications on Ba and Eu abundances, respectively, and defined CEMP-r stars as having [Eu/Fe] > 1.0, CEMP-s as [Ba/Fe] > 1.0 in combination with [Ba/Eu] > 0.5, CEMP-r/s as $0.5 <$ [Ba/Eu] < 1.0, and CEMP-no stars [Ba/Fe] < 0. Based on new Subaru HDS spectral data for 26 metal-poor stars – selected from HK and HES – that showed strong CH G-bands and [Fe/H] < 2, the CEMP definition was later revised by Aoki et al. (2007) to [C/Fe] > 0.7.

Out of these different CEMP categories, it is especially CEMP-no stars that are generally found to be the most metal-poor stars in the Galaxy, making the chemical makeup of these second-generation stars the ideal laboratory for understanding Pop III nucleosynthesis. Due to their high [C/Fe] yield, it is especially the class of faint CC-SNe that are considered predecessors of CEMP-no stars, while the r- and s-process contribution visible in CEMP-r and -s stars may already indicate pollution by another generation of stars, before the CEMP-r and -s stars were created out of their remains (Yoon et al. 2016, 2019). Besides faint SNe, other potential progenitors of CEMP-no stars are the so-called *spinstars*, which are rapidly rotating massive stars that enrich their surroundings with C, N, and O through strong stellar winds (Meynet et al. 2006).

CEMP-s stars, on the other hand, are thought to obtain their super-solar [C/Fe] and [Ba/Fe] ratios from a low to intermediate mass companion, which synthesizes these elements during the AGB phase and transfers the material to their companion (e.g. Suda et al. 2004; Herwig 2005; Starkenburg et al. 2014, see also Yoon et al. 2016, and references therein).

The origin of CEMP-r/s stars, which are enriched in both s- and r-process elements, poses an additional challenge as these processes require neutron densities that differ by multiple orders of magnitude, which is why they are thought to occur in entirely different nucleosynthetic production sites (Hampel et al. 2016). The most plausible explanations for the

observed abundance pattern of these stars include binary mass transfer of C and s-process enriched material onto a primary star, which was born from a gas cloud enriched in r-process elements (e.g. Jonsell et al. 2006; Gull et al. 2018) either from jet-like explosions of magnetorotational CC-SNe (e.g. Nishimura et al. 2015) or neutron star mergers (e.g. Ji et al. 2016; Gull et al. 2018). Alternatively, the entirely different neutron capture pathway of the *i-process* is considered, which happens at neutron densities in between s- and r-process (conditions which are potentially met within AGB stars or rapidly accreting WDs) and yet produces enhanced [X/Fe] ratios of elements that are produced by both (such as Ba and Eu, Mashonkina et al. 2023, and references therein).

By analyzing the morphology of CEMP stars in the C abundance A(C)[4] against [Fe/H] space (also called *Yoon-Beers diagram*) it was found that CEMP-s and CEMP-r/s stars generally occupy a different region than CEMP-no stars. This originally lead to the separation of the sample in *high-C* and *low-C* bands (Spite et al. 2013), where only stars in the *high-C* band show hints of s- and r-process elements. This picture was later adjusted by Yoon et al. (2016), who find a rich substructure and introduce a splitting of the sample in CEMP Groups I, II, and III, where Group III occupies the region in between the original bands. Each of the different groups was later associated with a different formation history by Yoon et al. (2019), who identify Group III CEMP-no stars as direct descendants of Pop III stars – forming out of gas enriched by a single faint SNe – while Group II stars are formed from gas enriched by multiple normal CC-SNe of Pop II stars (their table 1).

It is important to note that the decision whether or not a star is classified as CEMP depends on the measured [C/Fe] and hence is again subject to assumptions made when creating model atmospheres and synthesizing their spectra. It is thus possible to mistake a star as C-enhanced only because of approximations made when the observed spectra were interpreted, which then translates to a wrong astrophysical interpretation of the early stages of the Galactic evolution when done for many stars. This again underlines the importance of analyzing (and removing) these potential biases, which is precisely what is the objective of this thesis.

[4] $A(X) = \log(N_X/N_H) + 12$

3 NLTE Abundances of Galactic Stars: Sub-Chandrasekhar SNe Ia in the Chemical Evolution of the Galaxy

As elaborated in Sec. 2.2, understanding the Galactic history largely relies on the interpretation of chemical abundance patterns observed in the spectra of stars in large Galactic stellar samples. One of the biggest open questions is hereby the explosion mechanism behind SNe Ia (Ruiter & Seitenzahl 2025). Despite that they are of very high significance in the cosmological context, due to their integration as standard candles in the cosmic distance latter, their origin is not fully understood. Major interest here lies in the mass of the primary WD upon explosion, which in the classical picture is always assumed to disrupt at the same mass – the Chandrasekhar mass M_{Ch} – which leads to the identical intrinsic brightness in every occurrence and hence allows a measure of distance (see Sec. 2.2.3).

Doubts about this assumption have increased, driven by substantial evidence that a significant fraction of sub-M_{Ch}SNe Ia contribute to Galactic chemical enrichment (see Sec. 3.7 below for a discussion). Nevertheless, it was until recently that especially the Galactic abundance of [Mn/Fe] provided compelling evidence for a significant contribution from classical M_{Ch} SNe Ia, as observations of extremely metal-poor Galactic dwarf and giants stars (e.g. Bonifacio et al. 2009; Mishenina et al. 2015) suggest a very low [Mn/Fe] abundance ratio, which requires a large number of M_{Ch} SNe Ia over-producing Mn significantly after they start to contribute beyond [Fe/H] ~ -1 (e.g. Kobayashi et al. 2006, 2020b). However, significant departures from LTE were noted due to a strong ionization imbalance observed, i.e. abundance differences obtained from the investigation of Mn II and I lines (Bergemann & Gehren 2008; Bergemann 2008; Spite et al. 2013), as well as abundance differences seen in turn-off and red giants stars of the same population (Bonifacio et al. 2009).

Later, Eitner et al. (2020) investigated how departures from LTE affect the overall Galactic [Mn/Fe] trend and consequently re-evaluated the fraction of sub-M_{Ch} SNe Ia that is consistent with this updated abundance distribution. An overview of their findings is shown in Fig. 3.1. By compiling a broad sample of stars between $-4 \lesssim$ [Fe/H] $\lesssim 0$ and computing

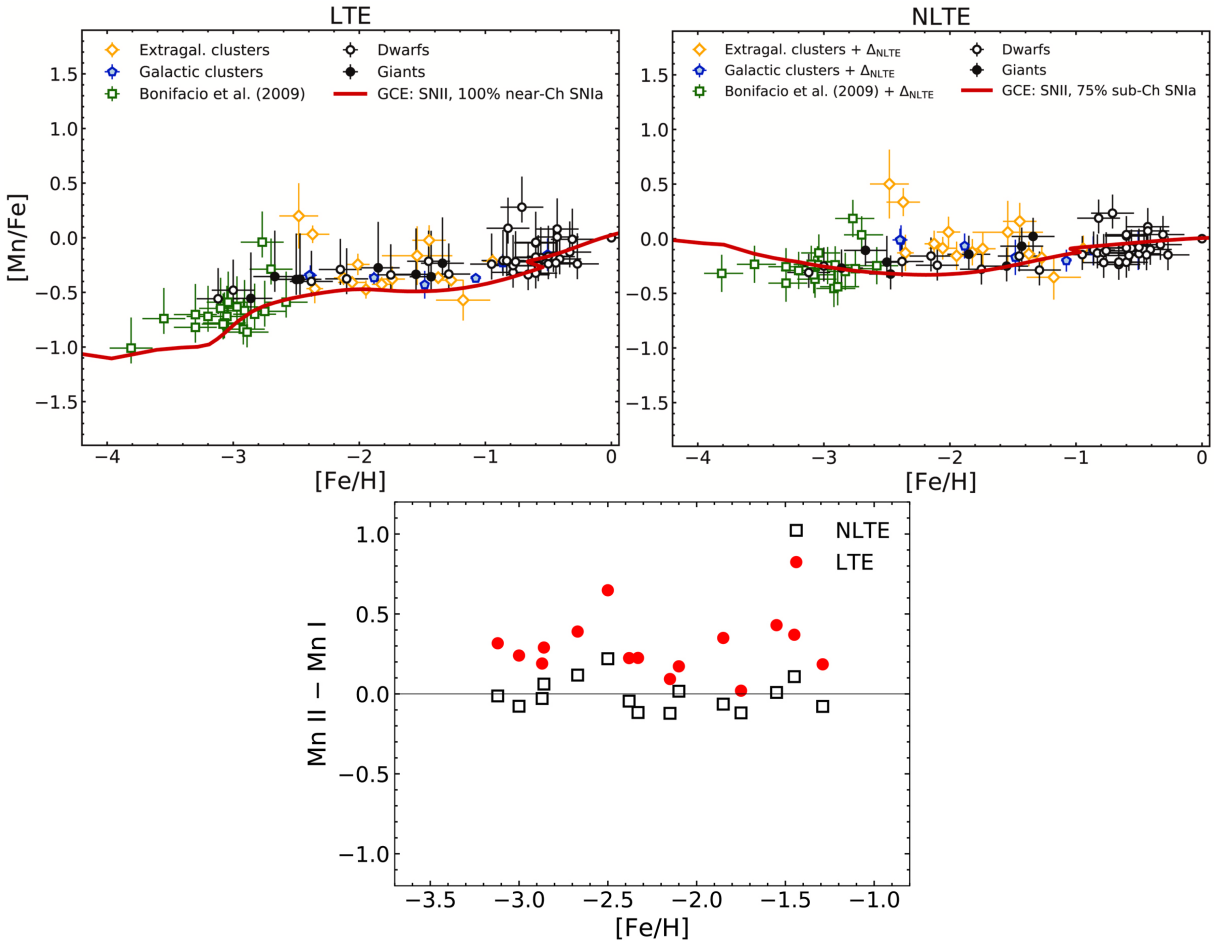

Figure 3.1: Top: Comparison of LTE (left) and NLTE (right) [Mn/Fe] abundances as a function of [Fe/H] of Galactic stars and Extragalactic clusters with GCE models from Cescutti et al. (2008), including variable contribution from sub-M_{Ch} SNe Ia. Bottom: Ionization imbalance between abundances derived from Mn I and II lines in LTE and NLTE. All three images taken from Eitner et al. (2020).

NLTE abundance corrections based on the EW of individual Mn lines (building upon results by Bergemann et al. 2019), Eitner et al. (2020) found that in NLTE the ionization imbalance between Mn I and II lines is reduced significantly (Fig. 3.1, bottom panel).

They then proceed to compare the two-infall chemical evolution model of Cescutti et al. (2008) with their sample of LTE (Fig. 3.1, top left panel) and NLTE corrected abundances (top right panel), where a strong differential effect with metallicity is noticeable; While at solar metallicity, only marginal departures between LTE and NLTE were found, the corrections increase significantly up to $\sim +0.5$ dex at [Fe/H] ~ -4. As expected, Eitner et al. (2020) find – similar to what was concluded by Kobayashi et al. (2006) – that the LTE data are in prefect agreement with a GCE that includes yields from classical M_{Ch} SNe Ia alone. However, in NLTE the low metallicity tail of the distribution is shifted towards much higher, almost solar, Mn abundances, which results is a flat [Mn/Fe] evolution with [Fe/H]. These findings contradict a large contribution from M_{Ch} SNe Ia, as the characteristic upturn at

[Fe/H] ~ -1 is no more visible in the data. Eitner et al. rather find that 75% sub-M_{Ch} SNe Ia are capable of reproducing the NLTE abundances instead, adding yet another piece of evidence hinting towards the dominance of non-classical SNe Ia explosion mechanisms.

Motivated by these findings, we expand the analysis by Eitner et al. (2020) qualitatively and quantitatively by carefully investigating yet another Fe-peak element, Ni, which – similar to Mn – is produced in SNe Ia in large quantities and shows a high sensitivity to different SNe Ia channels. We furthermore include a more diverse set of possible SNe Ia explosion scenarios and explicitly respect their different delay-times in the chemical enrichment. In addition, we employ a more sophisticated, Markov chain Monte Carlo (MCMC) based algorithm to sample the posterior probability distribution of different SNe Ia channels – given the agreement of corresponding GCE [Ni/Fe] vs. [Fe/H] tracks with observations – in order to estimate the most likely fraction of sub-M_{Ch} in the Galactic history and thereby determine the bias associated with improper modelling of stellar spectra.

The content of the remaining chapter has been published in Eitner et al. (2023) under the title ***"Observational constraints on the origin of the elements. V. NLTE abundance ratios of [Ni/Fe] in Galactic stars and enrichment by sub-Chandrasekhar mass supernovae"****. Minor modifications to format and text have been made in the context of this thesis. As the work presented here is a collaborative effort, I use the plural pronoun "we" instead of "I".*

- ***Title:*** *Observational constraints on the origin of the elements. V. NLTE abundance ratios of [Ni/Fe] in Galactic stars and enrichment by sub-Chandrasekhar mass supernovae*
- ***Authors:*** *Eitner, P. ; Bergemann, M. ; Ruiter, A. J. ; Avril, O. ; Seitenzahl, I. R. ; Gent, M. R. ; Côté, B.*
- ***Publication:*** *Astronomy & Astrophysics, Volume 677, id.A151, 10 pp.*
- ***Publication Date****: September 2023*
- ***DOI****: 10.1051/0004-6361/202244286*

The main scientific work of this paper was carried out by me, with invaluable contributions from all co-authors. Stellar parameters and Ni abundances were derived in close collaboration with O. Avril and E. Magg. The outcome of the `StarTrack` *simulation was provided by A. Ruiter.*

3.1 Abstract

We constrain the role of different SNe Ia channels in the chemical enrichment of the Galaxy by studying the abundances of Ni in Galactic stars. We investigate four different SNe Ia sub-classes, including the classical single-degenerate M_{Ch} SNe Ia, the fainter SN Iax systems

associated with He accretion from the companion, as well as two sub-M_{Ch} SNe Ia channels. The latter include the double-detonation of a white dwarf accreting helium-rich matter and violent white dwarf mergers.

The chemical abundances in Galactic stars are determined using Gaia eDR3 astrometry and photometry and high-resolution optical spectra. NLTE models of Fe and Ni are used in the abundance analysis. We include new DTDs arising from the different SNe Ia channels in models of the Galactic chemical evolution, as well as recent yields for CC-SNe and AGB stars. The data-model comparison is performed using a Markov chain Monte Carlo (MCMC) framework that allows us to explore the entire parameter space spanned by the diversity of explosion mechanisms and the Galactic SN Ia rate, taking the uncertainties of the observed data into account.

We show that NLTE effects have a non-negligible impact on the observed [Ni/Fe] ratios in the Galactic stars. The NLTE corrections for Ni abundances are moderate, but strictly positive, lifting the [Ni/Fe] ratios by $\sim +0.15$ dex at [Fe/H] -2. We find that the distributions of [Ni/Fe] in LTE and in NLTE are very tight, with a scatter of $\lesssim 0.1$ dex at all metallicities. This supports earlier work. In LTE, most stars have scaled solar Ni abundances, [Ni/Fe] ≈ 0, with a slight tendency for sub-solar [Ni/Fe] ratios at lower [Fe/H]. In NLTE, however, we find a mild anti-correlation between [Ni/Fe] and metallicity, and slightly elevated [Ni/Fe] ratios at [Fe/H] $\lesssim -1.0$. The NLTE data can be explained by models of the Galactic chemical evolution that are calculated with a substantial fraction, $\sim 80\,\%$, of sub-M_{Ch} SN Ia.

3.2 Introduction

SNe Ia systems are of critical significance in modern astrophysics because they play a key role in extragalactic distance measurements (e.g. Phillips 1993; Riess et al. 1998, 2021a), they contribute to chemical enrichment of stellar populations with Fe-peak elements (e.g. Timmes et al. 1995; Kobayashi et al. 2020b), and they are sources of kinetic energy in galaxies. Recent studies (see e.g. Taubenberger 2017; Ruiter 2020) uncovered a great diversity of SNe Ia types, associated with different explosions and progenitors of WDs (Iben et al. 1987). These include canonical single-degenerate M_{Ch} explosions caused by mass transfer onto a WD in a binary system, double-degenerate explosions associated with a violent merger of two WDs resulting in a prompt detonation (e.g. Pakmor et al. 2012), and scenarios in which He mass transfer from the companion leads to a surface He detonation triggering detonation in the C-O core (e.g. Livne 1990; Fink et al. 2010; Shen et al. 2018; Goldstein & Kasen 2018). Additionally, head-on collisions in triples through the Lidov-Kozai mechanism are being explored (e.g. Antognini & Thompson 2016; Toonen et al. 2018).

However, constraining the progenitor and explosion types by direct observations is difficult

because their spectroscopic and photometric properties are similar (Branch 1998; Hillebrandt et al. 2013). Independent constraints can be obtained through studies of the integrated chemical enrichment of stellar populations that probe a range of ages and metallicities, that is, by combining observed abundances and models of GCE (e.g. Timmes et al. 1995; Kobayashi et al. 2020b). This approach is particularly valuable in the studies of the properties of sub-M_{Ch} explosions (Seitenzahl et al. 2013b) because their associated integrated yields for Ni, Co, and Mn (e.g. Gronow et al. 2021; Boos et al. 2021) and delay-times are in stark contrast to those of the classical M_{Ch}-SNe Ia models (e.g. Ruiter et al. 2011; Goldstein & Kasen 2018). Recent studies of sub-M_{Ch} SNe fractions in the chemical evolution of the Milky Way and dwarf galaxies include Seitenzahl et al. (2013b), McWilliam et al. (2018), Kirby et al. (2019), Kobayashi et al. (2020b), Eitner et al. (2020), de los Reyes et al. (2020), Lach et al. (2020), and Sanders et al. (2021). Except for Eitner et al. (2020) and McWilliam et al. (2018), most other studies rely either on LTE calculations of stellar photospheric abundances or on mixed LTE and NLTE estimates. They combine, for instance, NLTE measurements of Fe abundances with LTE estimates of Ni abundances (as in Sanders et al. 2021).

In this work, we use a new data sets for [Ni/Fe] to study the role of sub-M_{Ch} SNe Ia channels in the chemical enrichment of the Galaxy. The Ni abundances are derived in NLTE for the first time for these Galactic stars. Starting with a summary of the observational sample in Sec. 3.3, we provide details on the methods for deriving and modeling explosion channels as well as abundance tracks in Sec. 3.4. The results are then presented in Sec. 3.5 and discussed in the light of similar studies in Sec. 3.6. We close with conclusions and a future outlook in Sec. 3.7.

3.3 Observations and Stellar Parameters

3.3.1 Main Stellar Sample

We use public spectra obtained from within the Gaia-ESO[1] survey data (Gilmore et al. 2022; Randich et al. 2022). One of the biggest science goals of the Gaia-ESO collaboration is to understand the Galactic structure and evolution, which is why it is designed to comprehensively cover stars in the Galactic disk, halo, and stellar clusters. The survey was executed on the Very Large Telescope (VLT) from 2013 to 2018. In this work, we rely on the high-resolution R$\sim$ 47 000 spectra taken in the UVES 580 setting ($\lambda \sim 480$ to 680 nm), and limit the analysis to data with a high signal-to-noise ratio (S/N) with S/N > 60 for stars in the metallicity range above -0.7, which offers a reasonable trade-off between the number of stars over a representative metallicity range and the quality of the spectra.

[1] http://archive.eso.org/programmatic/#TAP

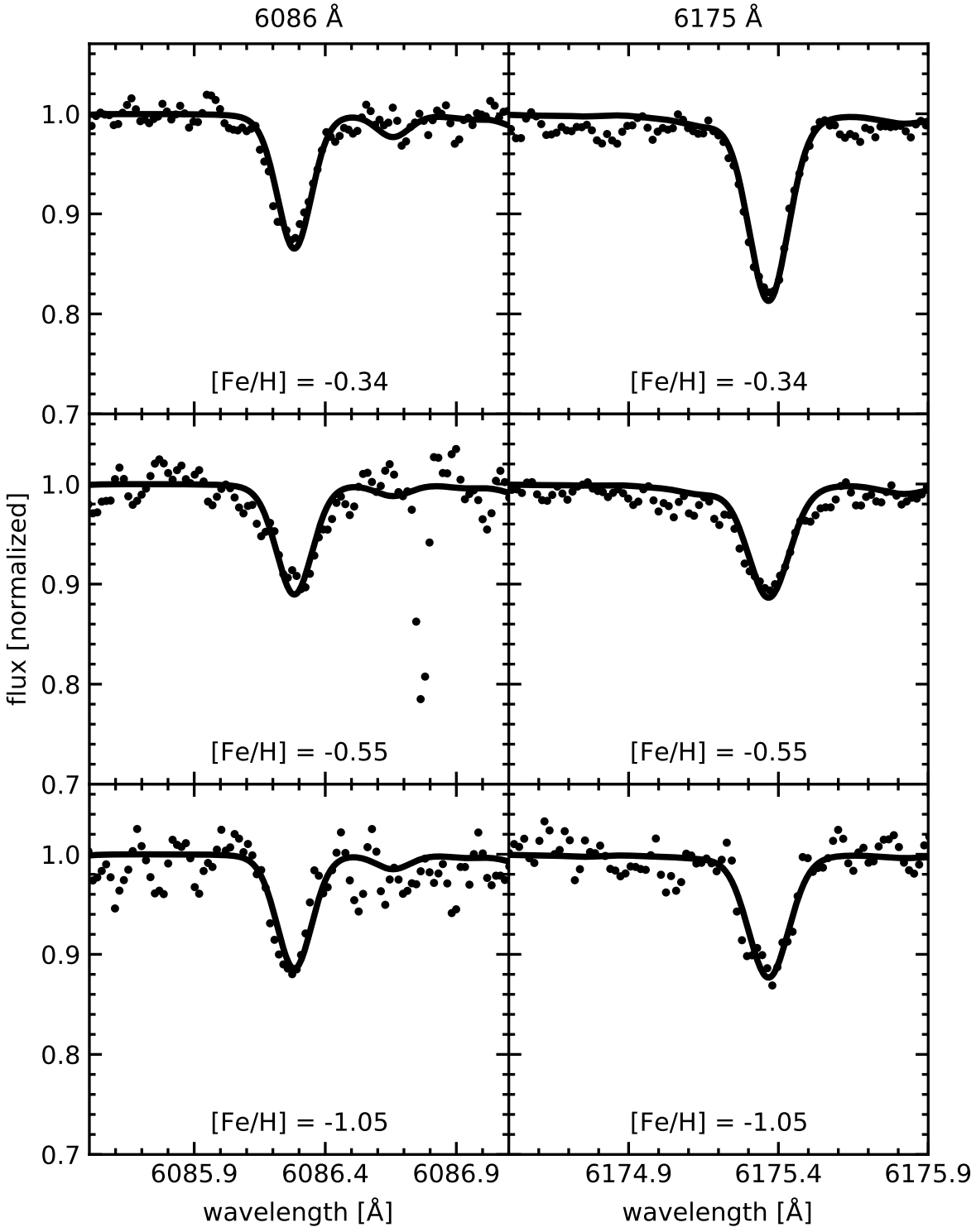

Figure 3.2: Best-fit line profiles for two diagnostic lines of Ni for three representative stars at metallicities [Fe/H] = −0.34, −0.55, and −1.05.

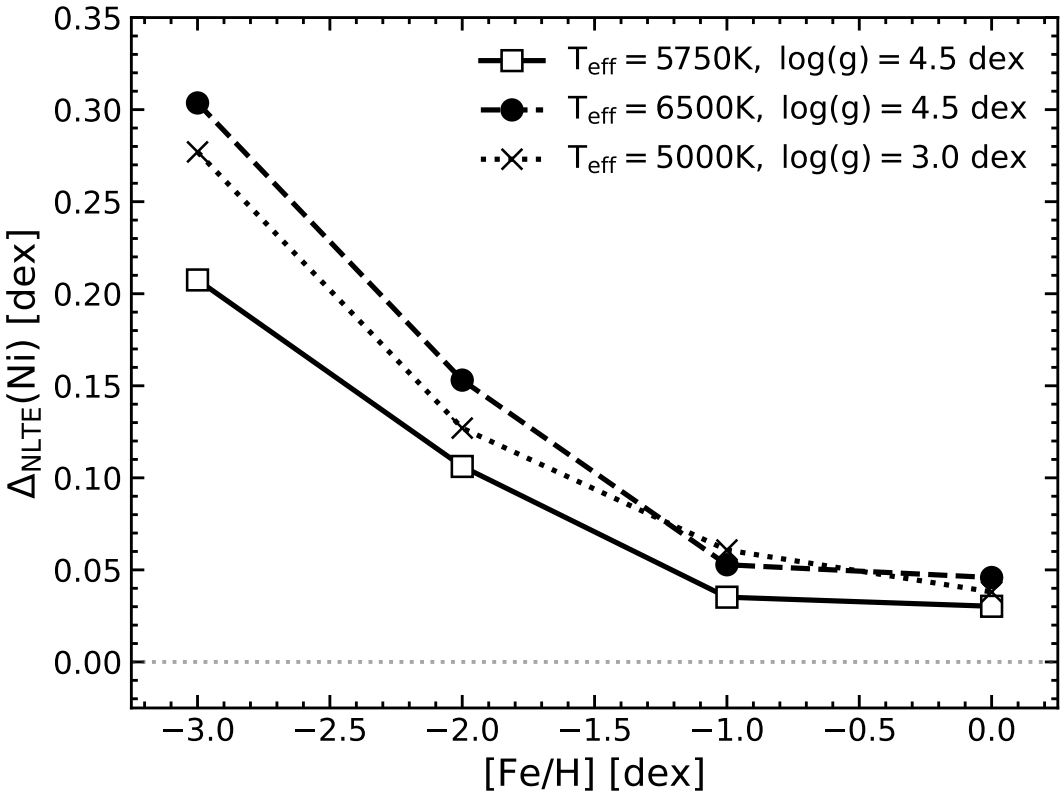

Figure 3.3: Ni NLTE corrections as a function of metallicity for three representative stellar model atmospheres averaged over diagnostic lines of Ni I in the optical wavelength range.

The analysis of stellar parameters is carried out using the SAPP pipeline (Gent et al. 2022), which combines different types of observational information, including photometry, spectra, and parallaxes in the full Bayesian framework to provide estimates of $T_{\rm eff}$, $\log g$, and [Fe/H] (see Sec. 2.1.7 for a brief description). The photometric magnitudes are adopted from the third data release (eDR3) of the Gaia catalog (Gaia Collaboration et al. 2020, 2021). The characteristic photometric errors range from 0.3 mmag to 6 mmag. Distances are adopted from the Bailer-Jones et al. (2021) catalog. As recommended by these authors, we use their photo-geometric data set.

To improve the quality of abundance diagnostics, Ni abundances are derived by a line-by-line analysis using the NLTE spectrum synthesis code `TURBOSPECTRUM` within the fitting framework `TSFitPy` (Gerber et al. 2023, see also Sec. 2.1.7), along with grids of NLTE departure coefficients calculated with the `MULTI2.3` code (Carlsson 1992) using updated NLTE atomic models of Fe (Semenova et al. 2020) and Ni (Bergemann et al. 2021; Magg et al. 2022b). We note that in the latter model, the transition rates associated with charge-exchange reactions Ni+H are calculated using new quantum-mechanical data from Voronov et al. (2022). Fig. 3.2 shows some examples of the observed spectra and the best fits for Ni I 6086 Å and 6175 Å. Our final high-quality stellar sample consists of 264 stars with Ni abundances.

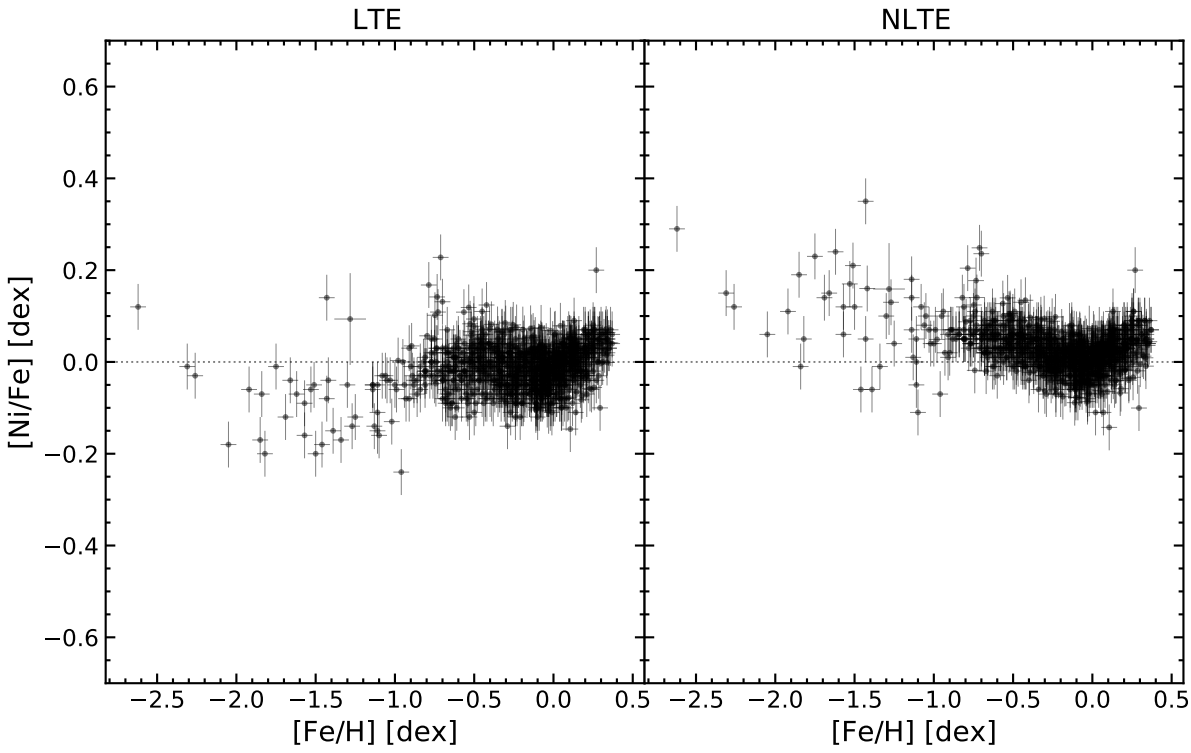

Figure 3.4: Trends of [Ni/Fe] against metallicity [Fe/H], calculated in LTE (left) and NLTE (right).

3.3.2 Additional Samples

For comparison, we also include additional data sets. Specifically, we add the abundances from Bensby et al. (2014), who employ high-quality optical spectra taken from different facilities and with a resolving power in the range from $R \sim 47\,000$ to $\sim 110\,000$. Fe abundances are corrected for NLTE effects based on the model atom and corrections from Bergemann et al. (2012a) and Lind et al. (2012). The LTE Ni abundances of stars in this sample are furthermore NLTE corrected (see also Magg 2023) using the direct line-to-line abundances kindly provided to us by T. Bensby (priv. comm.).

As guidance, we present the NLTE Ni I corrections for three models with representative stellar parameters in Fig. 3.3. The NLTE effect on Ni abundances is rather modest but non-negligible at solar metallicity. However, especially at metallicities [Fe/H] $\lesssim -2$, NLTE corrections for Ni increase and may reach +0.3 dex depending on the evolutionary stage of the star, which implies that NLTE abundances of Ni have to be used for reliable chemical evolution modeling. The Galactic [Fe/H] vs. [Ni/Fe] distributions from the combined sample are shown in Fig. 3.4. Our NLTE [Ni/Fe] results are higher than those of the LTE measurements, especially at low metallicity. This is fully expected given the NLTE effects in diagnostic lines, which are primarily associated with over-excitation and over-ionization in Ni I (Bergemann & Nordlander 2014; Bergemann et al. 2021; Magg et al. 2022b, see also Sec. 2.1.6 for an overview).

3.4 Methods

3.4.1 Chemical Evolution Model

We use the two-zone GCE model `OMEGA+`[2] (Côté et al. 2017; Côté & Ritter 2018), which was chosen for its high flexibility regarding the treatment of chemical enrichment sources. The model is conceptually similar to other widely used analytical GCE models (e.g. Tinsley 1980; Matteucci & Greggio 1986; Matteucci 2004; Chiappini et al. 1997; Kobayashi et al. 2000; Gibson et al. 2003; Prantzos 2008; Yates et al. 2013; Rybizki et al. 2017; Weinberg et al. 2017). In what follows, we provide a compact summary of the basic ingredients of the model.

At the core of `OMEGA+` lies an "inner region", representing the galaxy at the center of a dark matter halo, modeled using the one-zone GCE code `OMEGA` (Côté et al. 2017). Additionally, OMEGA+ includes in- and outflows from a halo gas reservoir encompassing the well-mixed core. The initial mass function is assumed to follow the Kroupa (2001) prescription, and the SFR is obtained via the Kennicutt-Schmidt law (Kennicutt 1998, see also Eq. 2.60). The version of the GCE model we adopt in this work uses Heger & Woosley (2010) yields for Pop III stars, in combination with yields from AGB and massive stars presented in Sec. 3.4.2, and SNe Ia yields described in detail in Sec. 3.4.3.

We model gas exchange with the circumgalactic medium using the two-infall model (Chiappini et al. 1997), featuring two phases of exponential gas inflow. Initially, a starburst occurs over about 0.7 Gyr, forming the Galactic thick disk. Subsequently, a 7 Gyr long, thin disk forming period of inflow begins after 1 Gyr, as recommended by Côté et al. (2019). In addition, we select all other free parameters of the GCE model in line with the best-fit Milky Way model from Côté et al. (2019), which they find to reproduce the observed, present-day Galactic metallicity, SFR, and gas mass.

The influence of model parameters was investigated in previous studies and is not repeated here. Specifically, SFR, mass loading factor, inflows, and outflows were discussed and explored in Côté et al. (2017) and Côté et al. (2018). In the former study, this was done against observational constraints and in the latter using hydrodynamical simulations of galaxy formation.

3.4.2 Asymptotic Giant Branch and Core-collapse Explosions

We consider two sets of CC-SN yields that are commonly used in the literature, Nomoto et al. (2013) and Limongi & Chieffi (2018). We also investigate two widely used sets of AGB yields from Karakas (2010) and Cristallo et al. (2015).

[2]Publicly available at `https://github.com/becot85/JINAPyCEE`

The tables in Nomoto et al. (2013) comprise yield data from Nomoto et al. (2006), Kobayashi et al. (2006), Kobayashi et al. (2011), and Tominaga et al. (2007), who examined masses between 13 and 40 $M_\odot$ and metallicities Z from 0.001 to 0.05. These models use the mixing and fallback approach by Umeda & Nomoto (2002). The yields were aligned with the observed spectra and light curves of CC-SNe based on progenitor mass, explosion energy, and ^{56}Ni production. Hypernovae are excluded from this work because their role in the Galactic chemical evolution is still debated (see the discussion in Eitner et al. 2020). The massive star yields from Nomoto et al. (2013) are augmented by the AGB yields of Cristallo et al. (2015).

Limongi & Chieffi (2018) investigate how rotational mixing affects the evolution and explosion physics of massive stars. They provide yield estimates for stars with masses from $13-120\,M_\odot$ and metallicities $[Fe/H] = 0, -1, -2, -3$. The mixing-fallback is included only for stars under $25\,M_\odot$. In their proposed model, stellar winds alone are suggested to enrich the environment chemically beyond this mass range due to full BH collapse. We utilize their models calculated with metallicity-dependent average rotation velocities from Prantzos et al. (2018). Increased rotation enhances continuous mixing during central He-burning, which boosts neutron sources and facilitates the production of heavy elements, thereby increasing Ni and Mn abundances at low metallicities. Yields from these massive stars are supplemented by AGB star contributions from Karakas (2010).

In Figure 3.5 we compare the average yields from Nomoto et al. (2013) (N13) and Limongi & Chieffi (2018) (LC18) as a function of mass (left panel) and metallicity (right panel). The LC18 yields show significantly more Ni than Fe throughout the entire metallicity and mass range compared to the N13 yields, except for solar and super-solar metallicities, where they are comparably large. Especially at low metallicities, the differences between the yields of LC18 and N13 are the most striking, where LC18 predict ~ 0.6 dex higher [Ni/Fe] ratios.

N13 yields, on the other hand, experience a strong metallicity gradient, increasing from ~ -0.6 dex at $[Fe/H] = -3$ to $+0.1$ dex above $[Fe/H] = 0$, while LC18 shows no notable variation. Both sets show a similar mass dependence in the metallicity-averaged yields, however, also here there is a systematic offset of about 0.4 dex visible. This difference has strong implications for the Galactic evolution of [Ni/Fe], which is explored in detail in Sec. 3.5.2.

3.4.3 Supernova Ia Scenarios

In this work, we include four of the most common SNe Ia scenarios that are discussed in the literature. Of these, two resemble explosions in which the primary WD explodes when reaching M_{Ch}, and two in which the disruption occurs below this limit, as described in detail below. Different explosion mechanisms were assumed for different scenarios. For each of

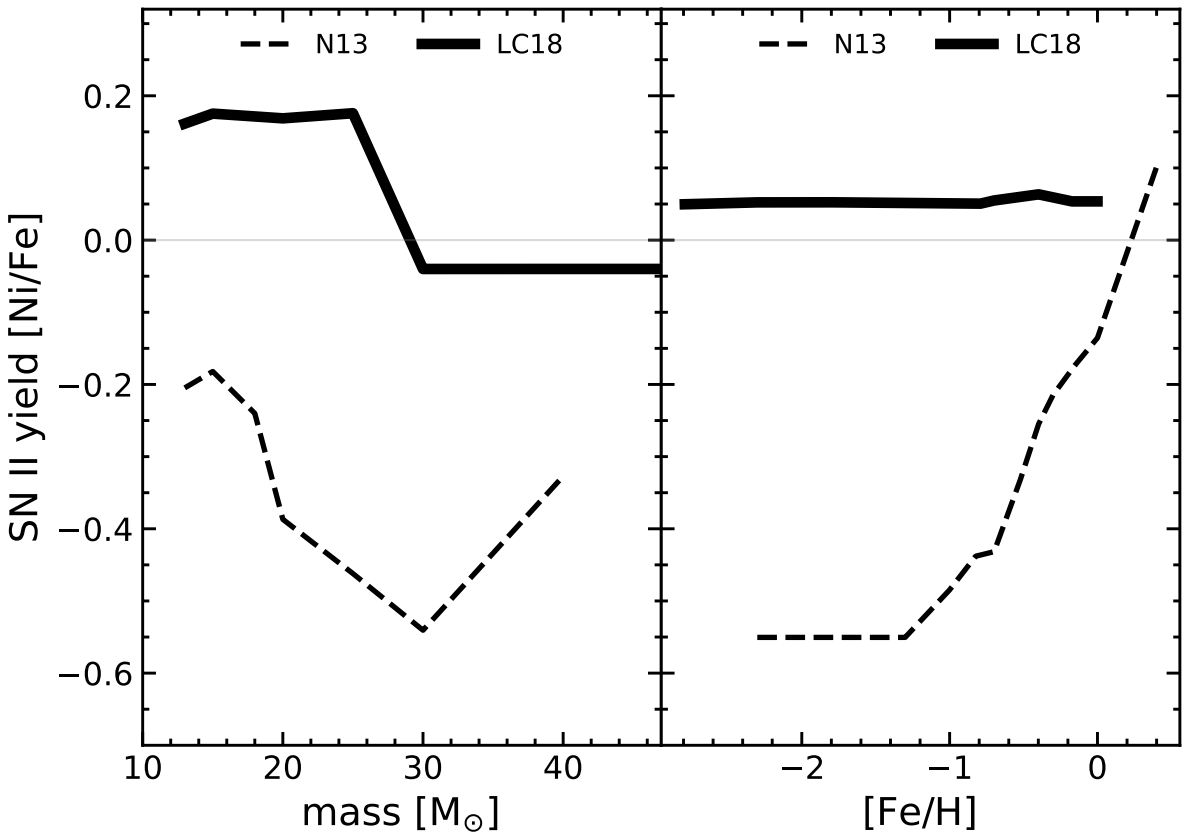

Figure 3.5: Comparison of the integrated yields from CC SNe from Limongi & Chieffi (2018) and Nomoto et al. (2013). Left: Yields as a function of stellar mass, averaged over metallicity. Right: Mass-averaged yields as a function of metallicity.

these models, the yield tables were adopted from the Heidelberg Supernova Model Archive (HESMA[3], Kromer et al. 2017).

Yields

First, we consider the standard model of a single-degenerate WD, in which the primary WD possesses a mass approaching M_{Ch}. For this analysis, we use the three-dimensional M_{Ch} SNe Ia delayed-detonation $N100$ model as developed by Seitenzahl et al. (2013a). In this model, hydrogen-rich material from a non-degenerate donor companion is transferred to the primary WD through Roche-lobe overflow (Khokhlov 1991). According to the description in Röpke et al. (2012), this simulation initiates the explosive event through a deflagration process, which is activated by 100 ignition sparks that partially overlap, being randomly positioned within a radius of 150 km from the core. The transition from deflagration to detonation occurs in regions where the density ranges between 6×10^6 and 7×10^6 g/cm^3. The progression of this theoretical model was traced until 100 s following the detonation event.

[3] https://hesma.h-its.org

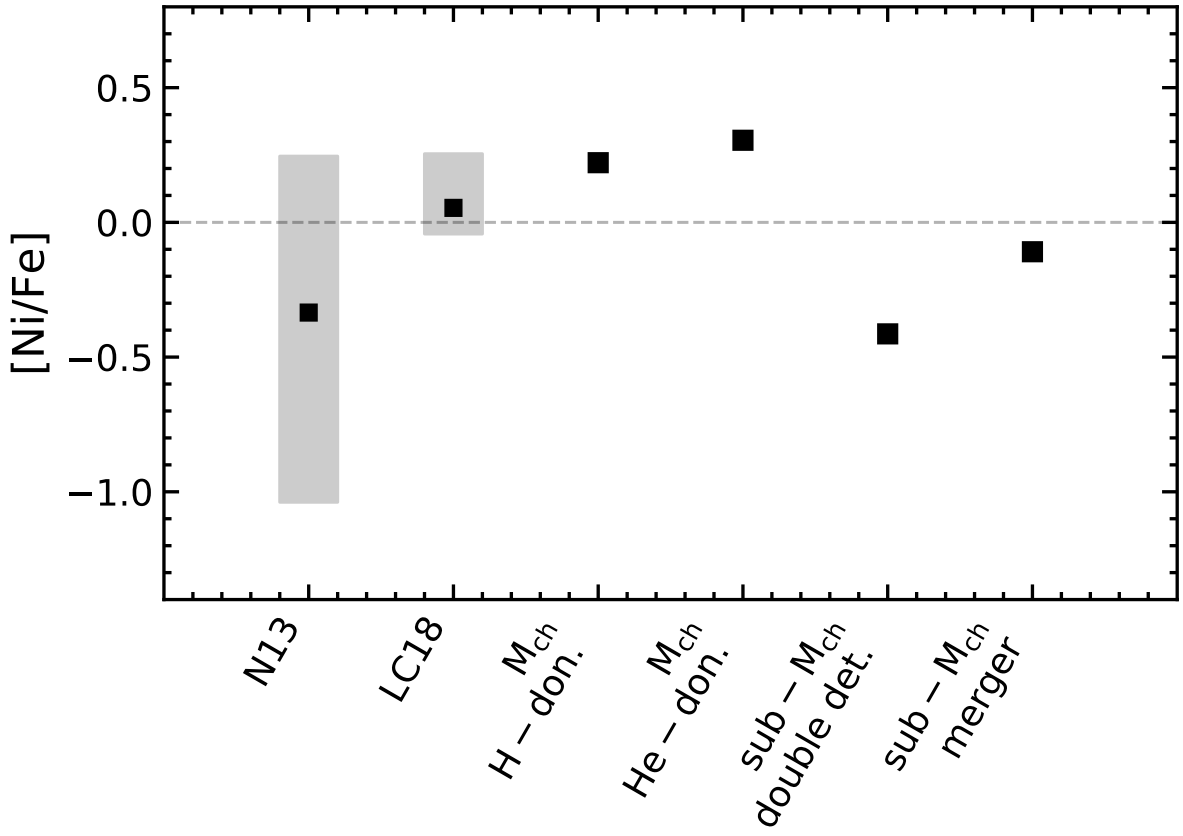

Figure 3.6: Comparison of yields from CC SNe and SNe Ia. The mean, maximum, and minimum yields are shown for the N13 and LC18 models.

The initial C-O WD is assumed to be in HE, with a central density of $\sim 2.9 \times 10^9 \mathrm{g/cm^3}$. According to Röpke et al. (2012), this causes significant parts of the nucleosynthesis to takes place at peak densities exceeding $\sim 2 \times 10^8 \mathrm{g/cm^3}$, which influences neutronization due to electron-capture processes and causes comparably large abundances of Fe-peak isotopes such as ^{54}Fe, ^{56}Fe, ^{58}Ni. However, Seitenzahl et al. (2013a) note that the yields for slightly neutron-rich isotopes – such as ^{58}Ni and ^{55}Mn – depend only weakly on the central density among different SNe Ia models of the same category, as long as it is not much higher. Because of these high core-densities, NSE reactions in classical M_{Ch} delayed-detonation models are efficient, which causes the material to be "normal" – as opposed to α-rich – during their freeze-out. This generally favors the synthesis of e.g. ^{55}Mn due to the decreased destruction probability of ^{55}Co (Bravo & Martínez-Pinedo 2012).

The second near-M_{Ch} channel investigated in this work represents the fainter SN type known as Iax (e.g. Foley et al. 2013; Jha 2017). The mechanism responsible for these systems is not yet fully understood. Jordan et al. (2012) and Kromer et al. (2013a) propose a failed detonation, near-M_{Ch} C-O WD event as the primary mechanism to form SN Iax. In this work, we rely on the *def_2015_N5def* model from Kromer et al. (2013b) and Fink et al. (2014), which is characterized by five asymmetric ignition sites, leading to a weak deflagration flame

that lacks the energy to unbind the remnant fully. This results in faint SNe with synthetic observables that match typical Ia SN 2002cx-like events, particularly SN 2005hk (Kromer et al. 2013b).

For sub-M_{Ch} SNe Ia, we consider two different binary star configurations. The first sub-M_{Ch} scenario is the double-detonation (hereafter, double-det.) of a C-O WD with a mass below M_{Ch}, but above $\sim 0.8\ M_{\odot}$ (Sim et al. 2010). As suggested by their name, these events are characterized by the disruption of the primary WD in a secondary detonation.

In these events, the final explosion is proceeded by an initial detonation in the He-rich shell that is accreted through stable Roche-lobe overflow from a He-rich companion, which can be either another WD (double-degenerate) or a star in a different evolutionary state (single-degenerate). The outer shell of the companion star is, furthermore, not required to be He-rich upon accretion by the primary, as H-rich material is burned to He and thus likewise results in the accumulation of a massive He-shell around the WD (Sim et al. 2010). In their hydrodynamical simulation of double-det. WDs Gronow et al. (2020) investigate the influence of core-shell mixing during the accretion phase and different ignition mechanisms. They note that their model *M2a* produces a near-maximum spectrum – and especially blue-wavelength absorption from intermediate-mass elements – in reasonable agreement with SN 2016jhr (Jiang et al. 2017), which is why we adopt it in this work.

Finally, we include a violent merger sub-M_{Ch} SNe Ia channel using the yields from Pakmor et al. (2012). Specifically, we use the model `merger_2012_11+09`, which is a three-dimensional simulation of a WD merger with a rather massive ($\gtrsim 1\,M_{\odot}$) primary, that includes nucleosynthesis contributions from NSE. In their simulation, the explosion of the primary WD is triggered by a qualitatively similar mechanism as described by Sim et al. (2010) for double-detonations; By evolving the binary system of C-O WDs with masses of $1.1\,M_{\odot}$ (primary) and $0.9\,M_{\odot}$ (secondary), Pakmor et al. (2012) find that after $\sim 600\,s$ and 15 orbits the secondary star gets unstable and disrupts on the timescales of one orbit. Its material then becomes violently accreted by the primary, which causes the more massive WD to compress and thus finally triggers the SNe Ia explosion. Pakmor et al. note that the mass of the primary WD is the decisive quantity that determines the brightness of the event, while secondary mass and metallicity of both objects is of secondary importance. They furthermore find that their WD merger models reproduces observational data of normal SNe Ia reasonably well.

Figure 3.6 shows the [Ni/Fe] yield ratios from different SN Ia channels compared to the massive star yields described in Sec. 3.4.2. Overall, the sub-M_{Ch} channels produce less Ni relative to Fe compared to M_{Ch} channels. Especially the double-det. SNe Ia events yield $[Ni/Fe] \sim -0.5$. Hydrogen and helium donor M_{Ch} SNe, on the other hand, produce super-solar amounts of Ni above the observed mean [Ni/Fe] abundance at low and high [Fe/H].

The reason for the large differences in Ni yields between M_{Ch} and sub-M_{Ch} explosion is the higher density of the M_{Ch} WDs upon explosion and the resulting electron fraction Y_e. The electron capture in M_{Ch} WDs during NSE is significantly more frequent than in sub-M_{Ch} WDs, which leads to a decrease in Y_e and hence the preferential synthesis of stable, neutron-rich Ni isotopes. The timescale of the following freeze-out is shorter and the α abundance is lower (normal freeze-out) for the more massive WDs, which causes the Ni abundances to stay close to their NSE values. For sub-M_{Ch} WDs, and hence lower peak densities, on the other hand, the freeze-out is α-rich and slower, which can cause the yields to diverge significantly from NSE. During freeze-out, Y_e stays constant, which means that sub-M_{Ch} synthesis occurs at rather high Y_e, which corresponds to low production rates of the main stable isotope ^{58}Ni (see Blondin et al. 2022).

Delay-time Distributions

Each of the considered SNe Ia channels is associated with a different evolutionary path and mass configuration of the progenitor binary system. Accordingly, each explosion scenario is subject to a different delay-time, and hence obeys a different DTD. We use this parameter to describe the number of SNe Ia events per year and per solar mass as a function of time. A DTD thus contains information about the time interval between formation and explosion, which is associated with the evolution of the individual binary components. It also contains information about the temporal distribution of all considered plausible candidates. For each SNe Ia scenario that may be associated with the individual yields introduced in Sec. 3.4.3, we construct the corresponding DTDs as described below. The resulting distributions, i.e. the normalized number of events in each channel as a function of delay-time, are shown in Fig. 3.7 and are briefly discussed below.

To study the DTDs, we use the `StarTrack` population synthesis code (e.g., Belczynski et al. 2008; Ruiter et al. 2009, 2014), which simulates a stellar population starting from the zero-age main sequence (ZAMS) and tracks potential SNe Ia events through different channels. From this population, converting about $4 \cdot 10^7\,M_\odot$ of gas into stars, we observe a $\sim 1\,\%$ occurrence of SNe Iax compared to 99 % classical SNe Ia among M_{Ch} explosion, as well as $\sim 72\,\%$ of sub-M_{Ch} in double-detonation and $\sim 28\,\%$ in double-degenerate mergers. For WD mergers, we consider all binary C-O WDs merging within a Hubble time, excluding those with primary WDs under $0.9\,M_\odot$, as these are thought to merge without supernovae (see also Pakmor et al. 2021).

For the single-degenerate scenario with H-rich donors (Fig. 3.7, panel A), the donor star is typically in the Hertzsprung gap or is a red giant star. The evolutionary timescale of the donor is most important in setting the lower limit for the DTD. The ZAMS masses for these progenitors are generally rather low, $\sim 1.7 - 2.6\,M_\odot$. This sets the timescale for the corresponding DTD because systems that have higher donor masses in our model would

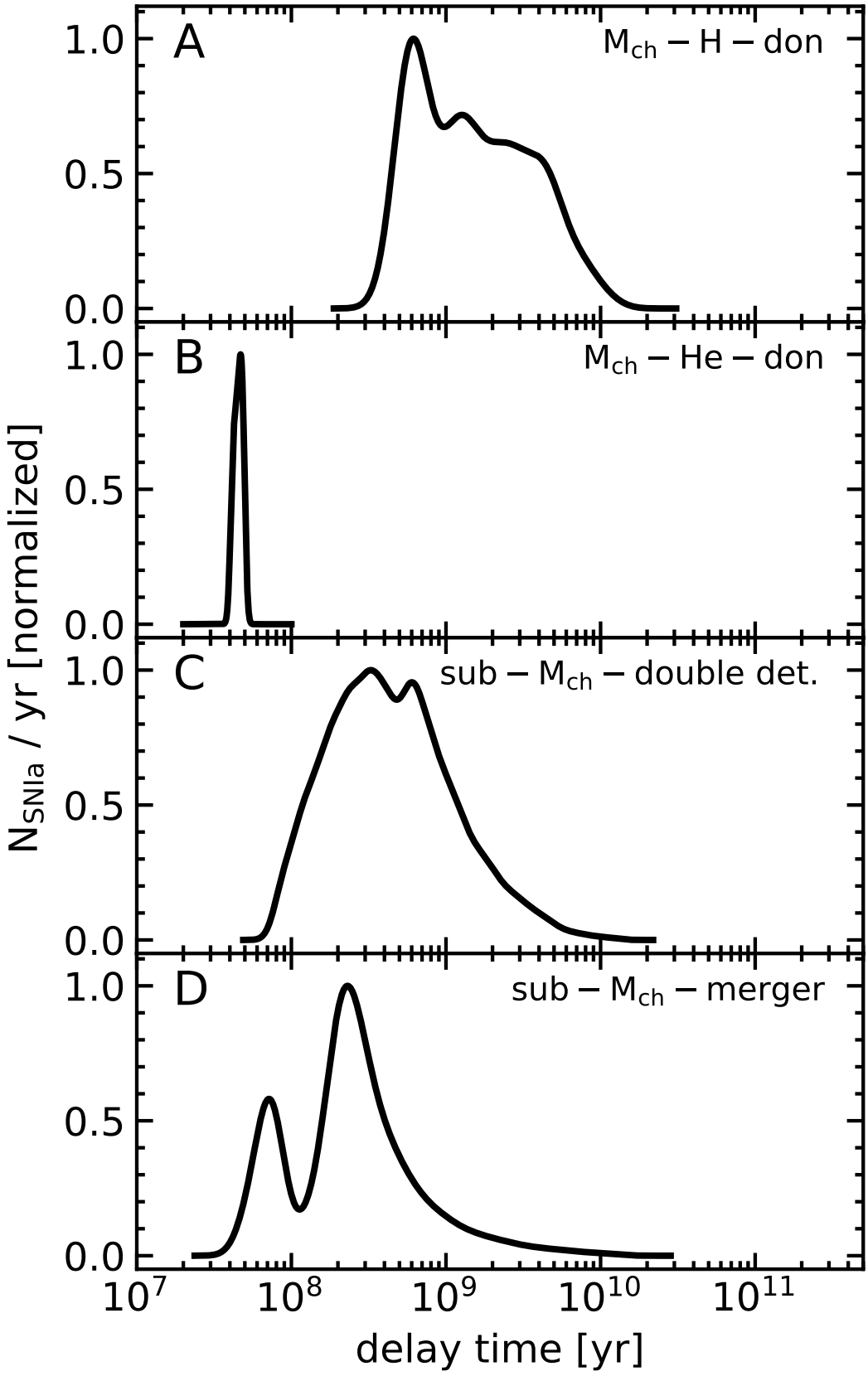

Figure 3.7: DTDs for four different types of SNe Ia as obtained from `StarTrack`.

drop out of this progenitor channel and evolve into something else, with the shortest delay-time occurring after $\sim 400\,\mathrm{Myr}$. In our binary population synthesis models, this only occurs in a rather narrow region of the $M_{WD} - M_{\odot}$ parameter space, although we allow for steady H-burning. It is therefore rather difficult to build up toward the M_{Ch} mass limit for a large number of accreting WDs (Ruiter et al. 2009).

The He-rich donor systems involving M_{Ch} mass WD exploders (Fig. 3.7, panel B) have short delay-times and arise from H-stripped He-burning stars that are relatively massive ($\sim 4-6\,M_{\odot}$) on the ZAMS. They form SNe Ia progenitors rather quickly after star formation (see Kromer et al. 2015, for details concerning the binary evolution calculations and delay-times). In general, these systems are currently a favored scenario for explaining SN Iax events (Jha 2017).

The evolution of binary systems leading to sub-M_{Ch} double-det. events (Fig. 3.7, panel C) differs from that of C-O WD binaries that lead to violent mergers. In the former, two common envelope events occur frequently (note the steeper power-law distribution; Ruiter et al. 2011), and the final mass transfer RLOF phase is dynamically stable. For these systems, which are assumed to undergo a double-det. SNe Ia, donors are He-rich WDs (either He or hybrid He-C-O WDs), or H-stripped He-burning stars with masses $< 1\,M_{\odot}$. Binaries with WD donors typically have rather low ZAMS masses for the secondary star ($\lesssim 2\,M_{\odot}$), and so the progenitor configuration is not realized until $> 500\,\mathrm{Myr}$ after star formation, leading to the second peak seen in panel C.

The first peak is attributed to double-det. occurring in binaries with He-burning stars, which generally derive from more massive progenitors in terms of the secondary star. The amount of He-rich material that is allowed to accumulate on the surface of the C-O white dwarf before the He-shell detonation is dependent on the white dwarf mass but is usually on the order of a few hundredths of a solar mass. Details are described in Ruiter et al. (2014) (model P-MDS). The timescale associated with stable mass transfer is minuscule compared to the evolutionary timescale of the binary. When RLOF starts, the explosion will occur within $\lesssim 10\,\mathrm{Myr}$.

Violent mergers of two C-O WDs (Fig. 3.7, panel D) have a DTD that roughly follows a power law $\propto t^{-1}$, which is to be expected because the main physical mechanism leading to decreasing orbital size in double WD mergers is set by emission of gravitational waves (see Ruiter et al. 2009, for details). A merging WD system is assumed to produce a SNe Ia if (i) both WDs are of C-O type and (ii) at least one of the WDs is above some mass threshold, in this case $0.9\,M_{\odot}$, because lower masses will not produce enough ^{56}Ni to produce an explosion whose light curve reflects that of a typical SNe Ia, including sub-luminous 91bg-like SNe Ia (Ruiter et al. 2013; Shen et al. 2018; Pakmor et al. 2022, see figures 4, 14 and 5, respectively).

The criteria that determine the stability of mass transfer, that is, whether a WD pair will merge or undergo stable mass transfer when one of the WDs fills its Roche lobe, are defined by the properties of the individual binary. We refer to Belczynski et al. (2008). On average, we find that most mergers undergo only one common envelope event, each of which drastically decreases the orbital separation by up to ~ 2 orders of magnitude. However, one particular formation scenario of double WD mergers leads to mergers occurring 100 Myr, or less, after star formation. These are the so-called ultra-prompt mergers (Ruiter et al. 2013). In these mergers, the same star loses its envelope twice; once while it is a regular giant-like star, and later when it is a He giant-like star. These merger progenitors, with their unique evolutionary channel, do not follow the canonical power-law distribution.

3.4.4 Model-data Comparison

We compare the generated model GCE curves with the observed data by calculating a goodness-of-fit statistic. This is done using the quadratic distance of each observation to the model track, weighted by the combined, projected uncertainties in [Ni/Fe] and metallicity. The fitting process utilizes the `emcee` ensemble sampler (Foreman-Mackey et al. 2013), a Markov chain Monte Carlo (MCMC) framework that efficiently explores the input parameter space with the help of *walkers*. The primary parameter relevant for this study is N_i, which represents the total number of SNe Ia events that occur in channel i per solar mass formed in the GCE simulation. A flat prior is applied to constrain N_i between 10^3 and 10^7 in each channel, allowing variability across the full relevant parameter space.

To ensure that the chemical evolution model is physically realistic, we furthermore require that it reaches solar metallicity around the birth time of the Sun, which effectively limits the total number of SNe from all channels combined and ensures a present-day [Fe/H] in agreement with expectations within the solar neighborhood. To enforce this constraint we include it in the evaluation of the likelihood, which is possible because the `OMEGA+` GCE model predicts the Galactic chemical mixture as a function of time directly. We find that a Normal distribution of the model solar metallicity – linear interpolated to the birth time of the sun ~ 4.6 Gyr ago – around $[\mathrm{Fe/H}] = 0$ produces a satisfactory agreement with the observed metallicity distribution and effectively disregards corner cases in the sampled SNe Ia parameter space that lead to un-physical models.

Following the same strategy, we furthermore apply an additional observational requirement, which enforces that the present-day SNe Ia rate is consistent with observations. By again applying a Normal distribution, we impose a rate within $0.4 \cdot 10^{-2} \pm 0.2 \cdot 10^{-2}\,\mathrm{yr}^{-1}$ (e.g. Prantzos et al. 2011). Initially, the walkers were evenly distributed within the bounds set by their prior to ensure that no bias was introduced by pre-selection.

The sampling is then executed for 10 000 burn-in iterations, followed by 40 000 regular

iterations from which the final chains are constructed. We include a pool of in total 700 walkers, which means that the GCE model was evaluated 7 000 000 times during burn-in and 28 000 000 times during sampling. We ensure that the chosen number of walkers, as well as burn-in and sampling iterations, has no significant influence on the results because we obtain identical results for significantly longer chains.

In the context of this work, it is sufficient to estimate the ratio of all sub-M_{Ch} type explosions relative to the M_{Ch} models, because the actual contribution of each type of progenitor is not known. Moreover, there is evidence that binary evolution population synthesis studies of the rates of SNe Ia characteristically under-predict the SNe Ia rate, in particular when compared against extra-galactic rates of SNe Ia (Ruiter et al. 2011, Fig. 1). We therefore refrain from restricting ourselves to the `StarTrack` binary population synthesis model rate output alone. Nevertheless, we utilize the population synthesis predictions to reduce the dimensionality of the parameter space by only fitting M_{Ch}-H-donor, sub-M_{Ch} double-det. events, as well as sub-M_{Ch} mergers to the data, whereas the M_{Ch}-He donor systems were modeled by requiring the inter-channel ratios obtained at the end of the `StarTrack` simulations[4].

We recall that our methodological approach assumes that the four specific formation channels used for our binary population synthesis model (and the associated DTDs) correspond to specific nucleosynthetic yields obtained for a set of four explosion models, as discussed in Sec. 3.4.3. The explosion models used are chosen to feasibly match a scenario that can be obtained naturally from binary evolution. We acknowledge that other plausible SNe Ia formation scenarios and DTDs might also contribute, but for this study, we only paired a set of four models (explosion model and binary evolution model) that we consider to be well-matched.

The likelihood of the GCE model track [Ni/Fe] against [Fe/H] is only evaluated in the metallicity range $[\mathrm{Fe/H}] \gtrsim -2.0$ dex. Stars with metallicities lower than the limit have a negligible constraining power for all considered SNe Ia channels (see the next section for a detailed analysis). We furthermore bin the stars in metallicity. The uncertainties in each bin were calculated from the individual abundance errors and the standard deviation. We note that this binning causes the MCMC sampling process to yield more robust posterior distributions, as the influence of the large scatter in observations is reduced. The simple, two-zone GCE model applied in this work can not be expected to reproduce small scale variations seen in the Galactic abundance trend, which is why we prefer to evaluate its likelihood only based on the binned Galactic average.

[4]During the fitting process, we hence assume that $\log \mathrm{N}_{\mathrm{He-don}} = \log \mathrm{N}_{\mathrm{H-don}} - 2.053$.

3.5 Results

3.5.1 Galactic Chemical Evolution Tracks

The predictions of OMEGA+ for a range of different SNe Ia channel weights are presented in Fig. 3.8. Here we show the models calculated with CC-SNe yields from the set LC18 (Limongi & Chieffi 2018), but we note that the behavior of the distributions is very similar in the N13 set. In each panel, N_i is varied from 10^3 to 10^6 (while the other channels are kept fixed), and the fraction relative to the total number of SNe is shown as color. The main common attribute independent of the weight of each SNe Ia channel is that there is no contribution at very low metallicities below ~ -2, which simply reflects the time delay imposed by their DTDs. However, each of the four SNe Ia channels clearly has a unique signature in the [Ni/Fe] ratios.

The classical M_{Ch} channel (panel A) sets in rather late, at [Fe/H]~ -1 dex, in the metallicity range corresponding to the transition between thick and thin disk stars (e.g. Feltzing et al. 2003; Ruchti et al. 2011; Bensby et al. 2014; Bergemann & Nordlander 2014). Decreasing the fraction of such events causes a stronger (more negative) slope towards solar [Ni/Fe] because the production of Fe is increased compared to Ni as the relative contribution from sub-M_{Ch} channels increases. The second M_{Ch} channel (panel B), representing M_{Ch}-He-donor type SNe Ia (SN Iax), sets in very early (mainly $-3 \lesssim$ [Fe/H] $\lesssim -0.5$). Even though the M_{Ch} He-donor type explosions produce a high [Ni/Fe] ratio, the absolute yield is too low to influence the Galactic trend significantly enough compared to the other SNe Ia channels.

The strongest effect is seen for the double-detonation sub-M_{Ch} channel (panel C). Because of their more extended DTDs, they contribute earlier, which is reflected in the lower metallicity departure from the CC plateau. With increasing double-detonation sub-M_{Ch} fraction, the ratio of [Ni/Fe] at a given metallicity decreases. The same trend is seen for the sub-M_{Ch} merger scenario (panel D). Similarly to SNe Iax, WD mergers contribute at lower metallicity, $-2 \lesssim$ [Fe/H] $\lesssim -0.5$, where they act to decrease the [Ni/Fe] ratio. Hence, the contribution from WD mergers is especially interesting for the study of very low-metallicity stars.

The differences between the double-det. and merger model tracks primarily lie in the minimum predicted Ni abundance. Due to their lower [Ni/Fe] yields, numerous double-det. SNe Ia combined with the CC yields of LC18 lead to a Galactic [Ni/Fe] ratio drop to about ~ -0.3 dex at [Fe/H] $= 0$. The merger models in this study, associated with slightly higher [Ni/Fe] yields, cause a smaller drop of about ~ -0.1 dex at solar metallicity. The extent to which the Galactic abundance trend aligns more closely with the steeper double-det. SNe Ia slope – beginning slightly later in Galactic history – or an earlier, more gradual slope, crucially depends on the [Ni/Fe] of the most metal-poor stars, which builds the base line from which the decline begins.

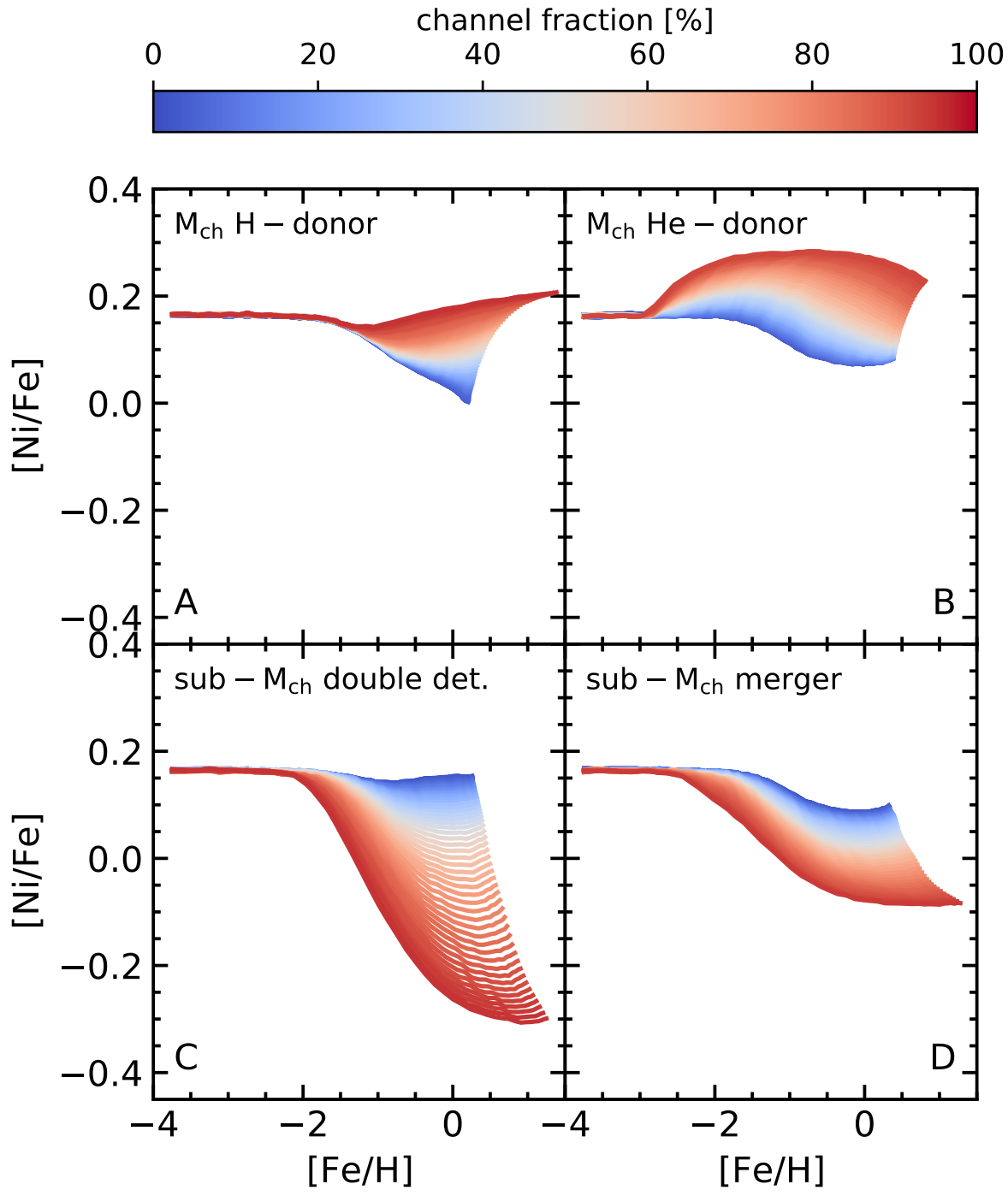

Figure 3.8: Effects of different numbers of SNe Ia on the synthetic abundance curves of [Ni/Fe]. In each panel, N_i is varied from 10^3 to 10^6 for the respective channel, while the contributions from the remaining three channels are kept fixed.

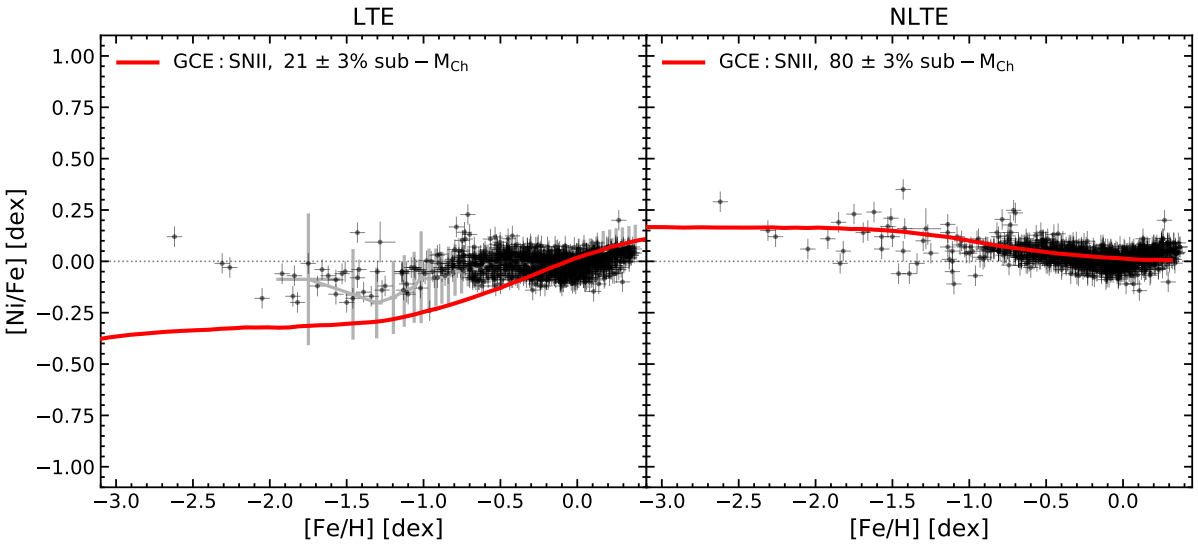

Figure 3.9: Observed distributions of [Ni/Fe] in LTE and NLTE against [Fe/H] compared to the best-fit GCE models. The solid gray lines correspond to mean GALAH abundances. See text.

3.5.2 Supernova Ia Fractions

Following the procedure outlined in Sec. 3.4.4, we determine the sub-M_{Ch} SNe Ia fractions from the posterior probability distribution constructed by fitting the observed [Ni/Fe] trend against [Fe/H] with a series of GCE models. In the procedure, we account for the individual abundance uncertainties of stars in the sample.

The best-fit GCE models are compared with observations in Fig. 3.9. In addition to our own data, we here also include the average trends based on the LTE [Ni/Fe] values from the GALAH survey[5] (Buder et al. 2021) in order to aid the statistics at low metallicity. Clearly, assuming LTE or NLTE has a strong influence on the best-fit models and consequently on the resulting sub-M_{Ch} SNe Ia fractions.

In LTE (Fig. 3.9, left panel), the observations can only be described by the GCE model calculated using the CC yields from Nomoto et al. (2013). This GCE model predicts a systematically decreasing [Ni/Fe] ratio with decreasing metallicity, which is qualitatively consistent with the LTE data. However, the models produce less [Ni/Fe] compared to what we see in our data at [Fe/H] $\lesssim -0.5$. The mean pattern observed in the GALAH data (indicated in gray, including the standard deviation) aligns well with our data. In particular, when accounting for the scatter in the low metallicity GALAH data, GCE model predictions fall within one standard deviation, although consistently below their average trend as well.

In order to reach solar [Ni/Fe] ratios, a significant contribution from classical M_{Ch} SNe Ia is required, and as a result, the best-fit fraction of sub-M_{Ch} SNe Ia (relative to the total number

[5]This survey did not provide NLTE abundances of Ni.

of SNe Ia) we derive for this data set does not exceed $\sim 21 \pm 3\,\%$. This is consistent with previous studies, in which the LTE abundances of Ni were used to interpret the enrichment due to different SNe Ia channels, specifically in Kobayashi et al. (2020b).

Interestingly, the NLTE abundance ratios of [Ni/Fe] as a function of [Fe/H] (Fig. 3.9, right panel) investigated in this work can only be explained by the GCE models that are based on the CC models of Limongi & Chieffi (2018). The slightly elevated [Ni/Fe] fraction in the low-metallicity regime, as well as the mildly decreasing [Ni/Fe] trend around [Fe/H] ~ -1, agrees excellently with the NLTE abundance measurements. As emphasized in Sec. 3.4 and 3.5.1, the slight over-production of Ni (compared to Fe) at low [Fe/H] can be balanced by sub-solar [Ni/Fe] fractions in sub-M_{Ch} SN Ia channels.

Consequently, a very substantial fraction, $80 \pm 3\,\%$, of sub-M_{Ch} SNe Ia is needed to account for the NLTE [Ni/Fe] distribution. Conversely, large fractions of M_{Ch} SNe Ia would fail to describe the [Ni/Fe] abundance in solar-like stars, as it would require the average observed [Ni/Fe] ratios to be ~ 0.2 dex higher, according to Fig. 3.8.

We note that the flatness of [Ni/Fe] with metallicity has been firmly established in other observational studies of the Galactic disc (Nissen & Schuster 1997; Chen et al. 2000; Adibekyan et al. 2012; Bensby et al. 2014; Hawkins et al. 2016; Jönsson et al. 2020). These studies report a tight zero-slope [Ni/Fe] trend in the disc, with a dispersion of $\lesssim 0.1$ dex that is fully consistent with our present findings based on the Gaia-ESO UVES spectra. However, as we show in this work, the NLTE corrections to Ni, although not large, are strictly positive at all metallicities. Hence, taking the NLTE effects into account would also lead to mildly super-solar [Ni/Fe] ratios in other observational data sets, as we show here using the data from Bensby et al. (2014), as well as our own LTE and NLTE analysis of [Ni/Fe] abundance ratios in stellar populations of the Milky Way.

3.6 Discussion

Our analysis of the chemical enrichment of the Galaxy suggests that a significant fraction of sub-M_{Ch} SNe Ia, $\sim 80\,\%$, is needed to explain the evolution of [Ni/Fe] abundance ratios in the Milky Way. This fraction is fully consistent with our earlier results (Eitner et al. 2020, 75 %), although the GCE model is different and we used a more comprehensive set of yields and delay-time distributions in this work.

Our study supports the conclusions presented by Palla (2021), who indicate that a significant contribution ($\gtrsim 50\,\%$) sub-M_{Ch} SNe Ia provides the most accurate description of the Galactic [Ni/Fe] evolution. Moreover, they emphasize that such a substantial fraction is in agreement with [Mn/Fe] ratios when NLTE corrections are applied. Additionally, we confirm the findings of Kobayashi et al. (2020b). By using the yields from massive stars as presented

in Nomoto et al. (2013), which closely resemble those reported by Kobayashi et al. (2011), together with LTE abundances for Fe-group elements, it appears there is minimal demand for sub-M_{Ch} SNe Ia. This is because the combination of extremely low yields from CC events and traditional H-donor SNe Ia can sufficiently account for the Galactic evolution of LTE [Ni/Fe] and [Mn/Fe] ratios across varying metallicities.

Evidence supporting a key role of sub-M_{Ch} SNe Ia in the chemical enrichment of galaxies has also been presented through studies of extragalactic stellar populations. de los Reyes et al. (2020) determine the Mn yield of SNe Ia in the Sculptor dwarf galaxy and, by comparing it with theoretical models, conclude that approximately 80% of the observed chemical pattern is due to sub-M_{Ch} SNe Ia. They also highlight environmental factors, noting that dwarf spheroidals with prolonged star formation histories often exhibit elevated [Mn/Fe] with varying [Fe/H]. This agrees with Childress et al. (2014), who find a notable SNe Ia-age correlation with host-galaxy mass.

In their study, Sanders et al. (2021) explore systems with a varying metallicity distribution and star formation histories, such as the MW Bulge and the Magellanic Clouds. They conclude that – to account for Fe-peak abundances – metallicity-dependent SNe Ia yields are essential. Notably, only substantial contributions from sub-M_{Ch} SNe can achieve this dependency, as [Mn/Fe] production from incomplete Si-burning is more metallicity-sensitive than synthesis in M_{Ch} models via normal freeze-out from NSE (Sanders et al. 2021; Gronow et al. 2021). Furthermore, Sanders et al. (2021) argue that low [Ni/Fe] SNe Ia yields (approximately -0.3 dex) are required to explain the high metallicity abundance pattern ([Fe/H] ~ -1.4) observed in the Gaia Sausage, suggesting a dominant sub-M_{Ch} SNe Ia contribution of 60–100 %.

Recent investigations of metal-poor extragalactic globular clusters by Larsen et al. (2022) further underscore the relevance of sub-M_{Ch} SNe Ia. Larsen et al. examine metallicities from -1 to -3 dex in globular clusters within the Local Group, revealing super-solar [Ni/Fe] ratios ($\gtrsim +0.2$ dex) after applying integrated-light NLTE corrections (Eitner et al. 2019), consistent with our Galactic star findings. Additionally, they report substantially elevated [Mn/Fe] ratios (~ -0.2 dex) at the lowest metallicities, further indicating a substantial sub-M_{Ch} SNe Ia contribution.

Direct studies of SN light curves and spectra also offer insights into SNe Ia progenitors. Goldstein & Kasen (2018) conducted simulations of time-dependent radiation transport, demonstrating that the variation in observed width-luminosity relations of SNe Ia is consistently explained by sub-M_{Ch} models, while traditional M_{Ch} explosions only account for brighter events. Moreover, Shen et al. (2021b) used multidimensional radiative transfer computations to derive light curves and spectra for double-det. WDs, presenting evidence that most observed SNe Ia occur below M_{Ch}.

Cikota et al. (2019) conduct an analysis of the polarization and line velocities of the Si II 6355 Å line using multi-epoch spectra. They discover a polarization dichotomy between sub-M_{Ch} and M_{Ch} SNe, revealing many supernovae with distinct sub-M_{Ch} signatures. Their findings align with the peak polarization predictions of the M_{Ch} model by Seitenzahl et al. (2013b) and the sub-M_{Ch} double-detonation model by Fink et al. (2010).

Theoretical studies by Ruiter et al. (2009) furthermore indicate that sub-M_{Ch} pathways of double-degenerate systems align more closely with observed SN rates. Additionally, the expected X-ray emissions from WDs accreting material prior to a M_{Ch} explosion appear to be insufficiently observed (Gilfanov & Bogdán 2010). Conversely, direct observational evidence exists for sub-M_{Ch} SNe Ia, as for example the early-time light curve of certain SNe aligns more closely with sub-M_{Ch} explosion models (Shappee et al. 2013). Further support comes from the analysis of the late-time nebular phase of these explosions, where Kuuttila et al. (2019) searched for nebulae ionized by the progenitor in SNe Ia remnants, which they claim should be visible up to 105 years post-explosion. Their findings of no such nebulae imply further evidence against the traditional SNe Ia model. Seitenzahl et al. (2019) examined the spatially resolved Fe XIV 5303 Å emission from three young SNe Ia, identifying one as an M_{Ch} event and another as an energetic sub-M_{Ch} explosion. Sub-M_{Ch} explosions are also supported by late-type SNe spectra studies. For instance, Flörs et al. (2020) conducted optical and near-IR spectroscopy on large SNe Ia samples, revealing [Ni/Fe] ratios that align with 85% sub-M_{Ch} explosions, and only about 11% can be attributed to M_{Ch} models.

3.7 Conclusions

Our objective is to assess the significance of varying M_{Ch} and sub-M_{Ch} SNe Ia channels by aligning Galactic chemical evolution models with newly obtained NLTE [Ni/Fe] abundance ratios in Galactic stars. Using an atomic model for Ni (Bergemann et al. 2021; Magg et al. 2022b), which incorporates quantum-mechanical Ni+H collision data from Voronov et al. (2022), we calculate the NLTE Ni abundances for 264 stars with high-resolution optical spectra (R= 47 000) from the Gaia-ESO survey. The GCE models are based on current yield data from AGB stars, core-collapse SNe, SNe Ia, and up-to-date delay-time distributions. We specifically examine four M_{Ch} and sub-M_{Ch} SNe Ia scenarios; the standard single-degenerate M_{Ch} SNe Ia, SN Iax, sub-M_{Ch} double-det., and double-degenerate violent mergers of C-O WDs.

First, we find that the [Ni/Fe] abundance ratios in our stellar sample show a very tight dispersion, both in LTE and in NLTE. In LTE, the trend of [Ni/Fe] is very close to solar at all metallicities probed by this work ($-2.5 \gtrsim$ [Fe/H] $\gtrsim 0.5$). In NLTE, the [Ni/Fe] ratios are mildly super-solar at low metallicity, but the trend flattens to zero at [Fe/H] ≈ -1. Our LTE results are fully consistent with the Galactic [Ni/Fe] measurements in earlier studies

(e.g. Nissen & Schuster 1997; Chen et al. 2000; Adibekyan et al. 2012; Bensby et al. 2014; Hawkins et al. 2016; Jönsson et al. 2020). However, our work is the first attempt to explore the effects of NLTE on the [Ni/Fe] over the entire metallicity range probed by the disk.

Comparing the predictions of GCE models with our LTE and NLTE data, we find that the GCE models based on the massive star yields from Limongi & Chieffi (2018) agree well with the NLTE [Ni/Fe] pattern. These models predict slightly super-solar [Ni/Fe] at low [Fe/H] and a mild decline toward the solar metallicity, as observed in the NLTE abundance ratios. The corresponding sub-M_{Ch} SNe Ia fraction is 80 %, which is consistent with our earlier constraints (Eitner et al. 2020). The GCE models based on the massive stars yields from Nomoto et al. (2013) do not yield a fully satisfactory agreement with Ni abundance patterns. Their [Ni/Fe] ratios are significantly lower than in LTE and NLTE data.

We emphasize that there are other SNe Ia models in the literature that are not included in this study (e.g. hybrid-disruption models for sub-M_{Ch} SNe Ia that produce explosions at low WD masses Perets et al. 2019). The exploration of the other scenarios is interesting and would merit a detailed investigation in future work. Detecting pairs of WD binaries not transferring matter is often difficult in the electromagnetic spectrum, and determining their physical properties poses additional challenges. The upcoming Laser Interferometer Space Antenna (LISA) is expected to identify numerous detached WD binaries in our Galaxy (Nelemans et al. 2001; Ruiter et al. 2010), including potential SNe Ia progenitors via the double WD merger channel discussed here. While observing a nearby double WD merging event from the start would be remarkable, it would require luck. However, future collaborations between LISA surveys like Gaia and the LSST will provide an unprecedented understanding of the properties of WD binary systems before they merge (Korol et al. 2017). This will be an important future step toward constraining SNe Ia progenitor models.

4 M3DIS – 3D RHD Stellar Atmospheres: Procedure, Validation & The Sun

The 1D NLTE analysis of Ni in Sec. 3 made abundantly clear that the improper modeling of stellar spectra can lead to significant biases when trying to understand the formation and evolution of astrophysical systems. In Sec. 2.1 and Sec. 2.2 it was highlighted that, in addition to the statistical equilibrium of trace elements, there is also major uncertainty associated with the assumption that stellar atmospheres are 1D and in HE when deriving stellar abundances. Ignoring 3D RHD, like neglecting NLTE, may result in the misinterpretation of Galactic abundance trends, if done so for stars across the entire distribution. However, it was furthermore noted that the significant computation time of 3D RHD atmosphere models and the following high-resolution spectrum synthesis make spectral fitting in 3D NLTE currently infeasible, which shows the need for large, extended, and dense grids of model atmospheres and synthetic spectra (Sec. 2.1.7).

The computation of these grids is, besides the physical and numerical challenge, obstructed by the fact that the computer codes developed for this task are not publicly available and slow – i.e. not optimized for mass production – resulting in a realistic computation time of weeks for a single MS model atmosphere. Furthermore, there are multiple codes and a significant amount of human interaction involved when considering the entire pipeline, starting from generating opacity and EoS tables, over opacity binning, the RHD simulation, the solution of the NLTE problem in 3D, and finally the 3D spectrum synthesis. This considerably slows down the process of generating grids.

Motivated by this, we decided to develop our own machinery that is specifically tailored to the computation of large grids of 3D stellar spectra – with flexible chemical composition – by minimizing the computation and human effort involved in the entire procedure. For this purpose, we develop the two main building blocks of this pipeline – a code that is capable of computing 3D RHD models of stellar atmospheres and a code that solves the statistical equilibrium, before it also synthesizes the resulting spectrum – within the high-performance computation framework for astrophysical applications `DISPATCH` (Nordlund et al. 2018).

*The content of the remaining chapter has been published in Eitner et al. (2024) under the title **"M3DIS – A grid of 3D radiation-hydrodynamics stellar atmosphere models for stellar surveys. I. Procedure, Validation & The Sun"**. Equations that are already mentioned in "Fundamentals & Theoretical Background" (Sec. 2) are replaced by the appropriate references. Minor modifications to format and text have been made in the context of this thesis. As the work presented here is a collaborative effort, I use the plural pronoun "we" instead of "I".*

- ***Title:*** *M3DIS – A grid of 3D radiation-hydrodynamics stellar atmosphere models for stellar surveys. I. Procedure, Validation & The Sun*
- ***Authors:*** *Eitner, P. ; Bergemann, M. ; Hoppe, R. ; Nordlund, Å. ; Plez, B. ; Klevas, J.*
- ***Publication:*** *Astronomy & Astrophysics, Volume 688, id.A52, 20 pp.*
- ***Publication Date:*** *August 2024*
- ***DOI:*** *10.1051/0004-6361/202348448*

The main scientific work was conducted by myself, with the invaluable contribution of all co-authors. The development of the `M3DIS` *radiation-hydrodynamic code for stellar atmospheres within* `DISPATCH` *was led by me and executed in close collaboration with Å. Nordlund, R. Hoppe, and A. Popovas. In addition, I contributed to the development of the* `MULTI3D` *@DISPATCH NLTE spectrum synthesis code in the same framework, which was led by R. Hoppe and used to generate the spectra presented in this work. This study greatly benefited from the spectrum synthesis expertise of M. Bergemann and R. Hoppe. All* `M3DIS` *model atmospheres presented in this work – including the corresponding opacity and EoS tables in collaboration with B. Plez – were computed by myself.*

4.1 Abstract

Large-scale stellar surveys, such as SDSS-V, 4MOST, WEAVE, and PLATO, require accurate atmospheric models and synthetic spectra of stars for accurate analyses of fundamental stellar parameters and chemical abundances. The primary goal of our work is to develop a new approach to solving 3D RHD and to generate model stellar spectra in a self-consistent and highly efficient framework.

We build upon the Copenhagen legacy RHD code, the `MULTI3D` NLTE code, and the `DISPATCH` high-performance framework. The new approach allows us to calculate 3D RHD models of stellar atmospheres on timescales of a few thousand CPU hours and to perform subsequent spectrum synthesis in LTE or NLTE for the desired physical conditions within the parameter space of FGK-type stars.

We compare the 3D RHD solar model with other available models and validate its perfor-

mance against solar observations, including the center-to-limb variation of intensities and key solar diagnostic lines of H and Fe. We show that the performance of the new code allows us to overcome the main bottleneck in 3D NLTE spectroscopy and enables calculations of multi-dimensional grids of synthetic stellar observables for comparison with modern astronomical observations.

4.2 Introduction

Energy transfer below the optical surface of atmospheres of late A- and FGKM-type stars is dominated by convection (Chandrasekhar 1939; Schwarzschild 1958). Convection defines the inner properties of stars, but it also has a direct coupling to the physical structure and dynamical evolution of their atmospheric layers, thereby having a major impact on observable electromagnetic spectra, their photometric magnitudes, and light curves, thus setting a fundamental scale for the characterization of the surface and interior structure of stars via spectroscopy, photometry, and asteroseismology techniques (e.g. Nordlund et al. 2009; Ludwig & Steffen 2016; Bonifacio et al. 2018; Mosumgaard et al. 2020; Lind & Amarsi 2024).

Most studies of stellar atmospheres have traditionally been carried out using one-dimensional models in HE and LTE (e.g. Kurucz 1979; Grupp 2004; Gustafsson et al. 2008). These strong approximations allow for rather simple and computationally affordable models, yet at the expense of physical accuracy. Convection is an inherently three-dimensional phenomenon and is therefore highly approximate in such models, as convective flux is represented by parameters based on the MLT or its variants (Böhm-Vitense 1958; Canuto & Mazzitelli 1991) and motions on small and large scales by ad hoc parameters of micro- and macro-turbulence (Gray 1992), respectively.

Codes for 3D RHD calculations exist, for example `STAGGER` (Nordlund 1982; Nordlund & Galsgaard 1995; Collet et al. 2011), `MURaM` (Vögler et al. 2004, 2005) and `CO5BOLD` (Freytag et al. 2012). However, 1D HE models have a tremendous computational advantage over 3D RHD-based models. In comparison with the former models that can be computed on timescales of approximately a few CPU minutes on a laptop, the latter need of the order 1 000 (low spatial resolution) to 10 000 (high resolution) CPU hours to achieve a robust relaxed local model of the solar outer layers, whereby realistic local models of metal-poor red giants may require up to a few 100 000 CPU hours (priv. comm. H.-G. Ludwig, C. Lagae) or more, around 1 000 000 CPU hours, for global models of AGB stars or red supergiants (priv. comm. B. Freytag, S. Höfner). Furthermore, the total number of CPU hours depends highly on different properties, such as the number and distribution of opacity bins, geometric extent of the box and step size, number of rays for the angular resolution of the radiation, desired precision of the output parameters (such as $T_{\rm eff}$) and the length of the time series.

In NLTE, other complexities arise also, including the convergence criteria, completeness of atomic models, and energy discretizations of all radiative quantities in the equations (Bergemann & Hoppe in prep). Although the physical aspects of the problem can be addressed with codes like MULTI3D (Leenaarts & Carlsson 2009) and NLTE3D (Sbordone et al. 2010), only studies of the chemical composition of the Sun (e.g. Asplund et al. 2009; Caffau et al. 2011a; Bergemann et al. 2021) and of a handful of individual stars (e.g. Caffau et al. 2011b; Nordlander et al. 2017; Lagae et al. 2023) were carried out in the 3D NLTE framework. Simply put, to compute a 3D NLTE grid of model spectra with similar properties to those that are presently employed in surveys, as for APOGEE (Mészáros et al. 2012), one would need approximately 10^{11} CPU hours, to be compared to 10^5 CPU hours for a 1D HE model grid (which is doable on a medium-size cluster within a month), which explains why 1D LTE models are still widely and exclusively used in the analysis of million star datasets from large-scale stellar surveys.

In this work, we attempt to overcome one of the main bottlenecks that has limited progress in this area. Specifically we focus on developing a set of codes, within the scope of the DISPATCH high-performance computing framework (Nordlund et al. 2018), in order to enable fast and efficient 3D simulations of stellar atmospheres and subsequent physical modeling of high-resolution stellar spectra within the same consistent approach, flexible as to handling of chemical mixture, opacities, resolution, but also resulting synthetic observables as required by modern spectral analysis methods, both classic (Schönrich & Bergemann 2014) and machine learning based (e.g. Gent et al. 2022).

Two grids of 3D RHD atmospheric models were computed by other groups (Ludwig et al. 2009a; Magic et al. 2013a). However, these grids are currently not publicly available and therefore cannot be readily used by the community for testing and scientific exploitation. In addition, the grids were computed with given assumptions on microphysics. For example, the range of chemical composition in the CIFIST grid (Ludwig et al. 2009a) is limited to four metallicity values, the STAGGER grid to seven (Magic et al. 2013a). Our approach, as outlined in this paper, is flexible and potentially allows the development of a robust diagnostic approach for large-scale stellar analyses as required by next-generation spectroscopic surveys, particularly 4MOST and high-resolution spectroscopic survey of the Galactic disc & bulge stars, which we are co-leading (Bensby et al. 2019) and which provides a strong incentive for the effort presented here.

The work is structured as follows. Sec. 4.3 presents the RHD problem, covering microphysics, opacities, the binning scheme, and initial conditions, and provides an overview of the synthetic spectra calculation method. In Sec. 4.4, we describe the simulations of solar sub-surface convection and include validation tests on numerical resolution, abundances, and opacities. Finally, Sec. 4.5 discusses synthetic observables and model sensitivity, concluding with a summary and future directions.

4.3 Methods

4.3.1 Radiation-hydrodynamics

The 3D model atmospheres in this work are calculated within the high-performance simulation framework DISPATCH (Nordlund et al. 2018). DISPATCH incorporates existing solvers for RHD problems and significantly increases their speed with its efficient task-based parallelization scheme that provides vectorization, local time-stepping, and unlimited scaling with OpenMP and MPI.

The detailed physics and numerical methods of RHD problems have been described in many previous studies (e.g. Stein & Nordlund 1998; Fromang et al. 2006; Freytag et al. 2012). In the following, we will briefly summarize the main aspects that are relevant to this work. The set of equations that are solved to advance the simulation in time includes the continuity (Eq. 2.13), momentum (Eq. 2.14) and energy conservation equations (Eq. 2.15). The latter is coupled to radiation through the radiative heating term, which itself requires the solution of the radiative transfer (RT).

In practice, the fluxes occurring inside the right-hand-side divergence terms are evaluated with a Riemann solver, analogous to the one used in the RAMSES code (Fromang et al. 2006) or, alternatively, with solvers analogous to the ones used in the STAGGER and BIFROST (Gudiksen et al. 2011) codes. The radiative heating q_{rad} is defined in Eq. 2.54, which may be expressed in terms of wavelength λ,

$$q_{\mathrm{rad}} = 4\pi\rho \int \kappa_\lambda (J_\lambda - S_\lambda)\, \mathrm{d}\lambda \,, \tag{4.1}$$

i.e. the monochromatic absorption coefficient κ_λ-weighted difference between the mean intensity J_λ and the source function S_λ. Under the assumption of LTE, the source function is given by the Planck function B_λ, so $S_\lambda = B_\lambda$. In the following, all opacities are given per unit mass of material. The models presented in this work do not include magnetic fields, but several MHD solvers are available in DISPATCH, such as RAMSES/HLLD, STAGGER, and BIFROST, with a separate module allowing for non-ideal MHD corrections (Nordlund et al. 2018).

The solution of the RHD equations is performed by the DISPATCH implementation of the RAMSES Riemann-HLLC solver (Fromang et al. 2006, see also the more general solution strategy outline in Sec. 2.1.2), which itself is an extension of the MUSCL-Hancock scheme (e.g. van Leer 1977). In short: An update of the hydrodynamic (HD) variables in this scheme consists of several steps. First, the cell-centered, volume-averaged primitive variables are advanced a half time-step in a non-conservative way using a Taylor expansion of the Euler system and slope-limited finite-difference spatial derivatives. The slopes are furthermore

used to construct the cell-interface values of the primitive variables, which are then fed into the Riemann solver to compute the cell-interface fluxes. These fluxes are then used to advance the volume-averaged quantities in time.

A similar Riemann solver is also used in the CO^{5}BOLD code (with multiple options for the time integration scheme, Freytag et al. 2012). Other RHD codes, such as STAGGER, BIFROST and MURaM, rely on explicit finite-difference schemes for spatial derivatives and a Runge-Kutta method (Williamson 1980) as temporal scheme.

The main difference between a Riemann solver and a classical non-Riemann solver is the treatment of the pressure term in Eq. 2.14. In the classical case, the pressure gradient is included as a source term on the right-hand side, which means sound waves are not propagated using advection and the system evolves entirely with the gas velocity. In Riemann solvers this is not the case. Here, all characteristics of the system are advected consistently by including the pressure gradient in the to-be-advected system.

In practice, this enables typical Riemann solvers to excel at capturing shocks and discontinuities and provide a better conservation of physical quantities. At the same time, Riemann solvers generally are less capable of handling smooth, semi-static regions. In these situations gravity and pressure forces cancel numerically down to machine-precision in classical solvers, because they are both treated identically as external sources. This is very different from the strategy followed by Riemann solvers, where pressure terms are included in the advection, while gravity remains an external force (e.g. Roe 1986; LeVeque 1997; Dullemond 2011; Freytag et al. 2012). Whether one or the other is more appropriate depends on their specific implementation and the problem at hand.

The main advantage of DISPATCH over previous codes for simulating stellar spectra is its parallelization scheme and numerical design. In short, one of the main reasons for the improved performance is the use of local time-steps. Previous hydrodynamical codes for stellar atmospheres relied on synchronized advancement of time. The rate in stellar atmospheres is dominated by the radiative time-step. For a relaxed model atmosphere it is usually at the boundary of the optical surface, but for a relaxing model atmosphere it can be anywhere. The core and unique ability of DISPATCH is to automatically devote additional resources to such areas to advance them at a lower time-step, while the rest of the model atmosphere can advance further in time using less resources.

In practice, to do so, DISPATCH divides the simulation domain in so-called *patches* that contain the local values of hydrodynamic or radiation variables based on their position in the atmosphere. Updating those variables by advancing them in time constitutes a *task*, which is executed by a task scheduler based on available computational resources and its status relative to its neighboring patches. For example: A task that solves the RT under a certain angle is required to wait for its upwind neighbors to reach the same (or a later) time

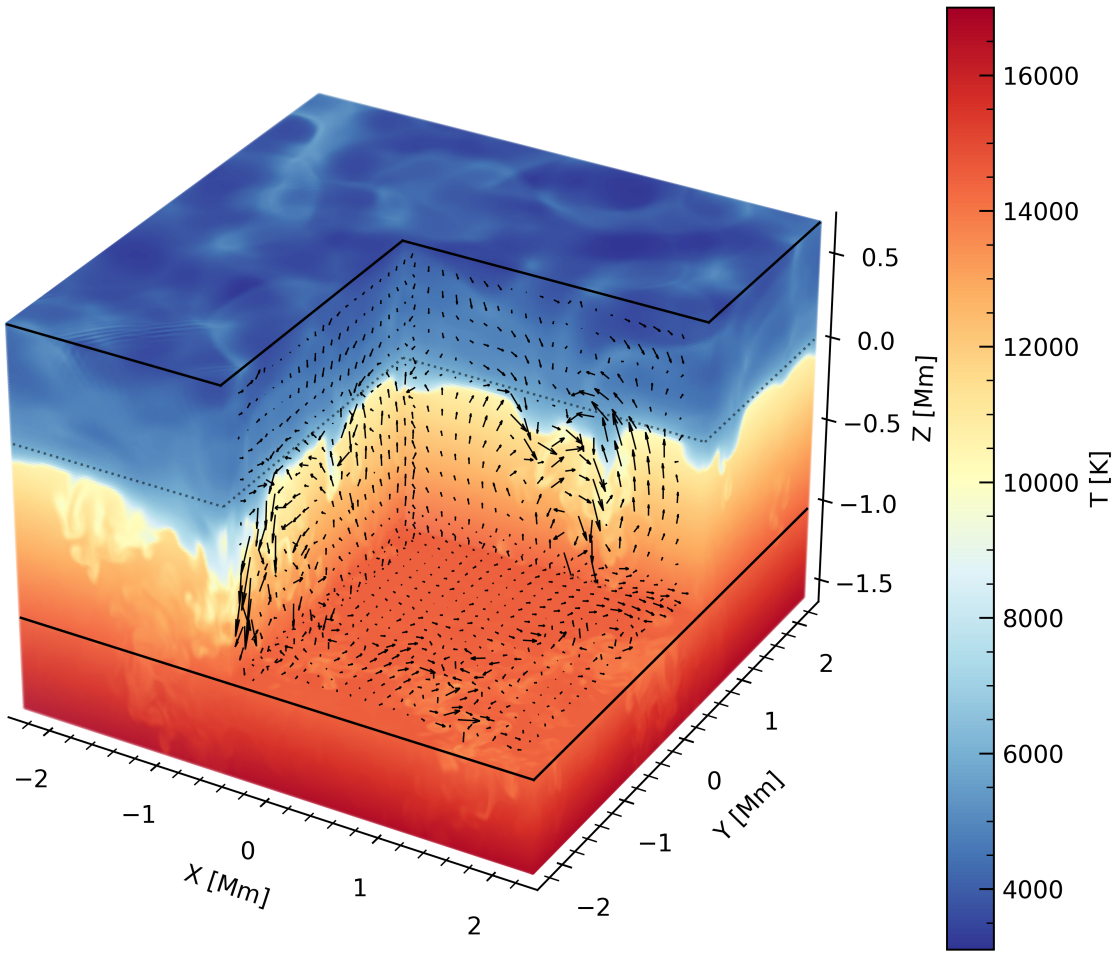

Figure 4.1: Temperature structure for our reference solar 3D RHD model. Black arrows indicate the local velocity field. The corresponding animation of the time evolution of the RHD simulation is available as supplementary material to the online version of the paper.

as the task itself, but not for tasks that are assigned to regions downwind. Likewise, the HD task is required to wait for the RT task to provide the current heating rate. A task hence only needs to check the time of its immediate neighbors before it can be queued for the next update, which then can be executed once a CPU thread is available. `DISPATCH` works best if there is an over-subscription of tasks compared to CPU threads, so that the CPU utilization is near 100 % at all times, thereby allowing a highly efficient use of available computational resources.

The implementation in OpenMP and MPI allows this scheduler to use all available threads on multiple nodes effectively by relying on shared memory within MPI ranks and virtual tasks in the transition region between different ranks for streamlined inter-node communication when needed. This design also incorporates local time-stepping naturally through the local time of each patch, which causes significant speed and stability improvements. The rate at which the stellar atmosphere is evolving in time is dominated by the radiative time-step, which in turn depends on the local hydrodynamic properties and radiation intensity through

the radiative Courant condition. Because of its design, DISPATCH is able to devote more computation resources to regions where the time-step is small, and hence minimize CPU idle times that would otherwise arise from non-synchronised time-steps. (Nordlund et al. 2018)

For illustration, in Fig. 4.1 we show the 3D distribution of temperature in the resulting solar simulation, which will be discussed in detail in Sec. 4.4. The full 3D animation cube can also be retrieved as supplementary material to the online version of the article.

4.3.2 Microphysics

To close the system of RHD equations, an EoS is required. In DISPATCH the EoS is provided in tabular form. It provides the gas pressure (P_g), electron density (N_e), and temperature (T) as a function of internal energy (e_{int}) and density. The internal energy is hereby linked to Eq. 2.15 though the subtraction of the kinetic energy,

$$e_{int} = e - \frac{1}{2}\,\rho\ \mathbf{vv}. \tag{4.2}$$

At a given density value, the internal energy depends on the temperature, chemical composition, as well as the ionization and molecular equilibrium. To avoid potential inconsistencies with opacities, it is hence advisable to compute the EoS and opacity tables simultaneously. The opacities themselves depend on the atomic and molecular level populations, which in LTE are functions of T and ρ only, and thus can be tabulated on the same grid as the EoS. Opacities are of utmost importance for the photospheric structure of stellar models; however, their accurate treatment is one of the major computational complexities involved. A dense sampling of an extended wavelength grid from the UV to the IR is needed to capture most spectral features. Depending on the resolution of the $T-\rho$ grid, this requires significant computation time.

The monochromatic opacities and EoS are computed using the MARCS (Gustafsson et al. 2008) as well as the TURBOSPECTRUM (TS) (Plez 2012; Gerber et al. 2023) codes. They include the same routines for the calculation of the chemical equilibrium and of continuum opacities. For line opacities, TS uses linelists, while MARCS interpolates in opacity sampling tables generated for a set of temperatures and pressures on a fixed wavelength set. They otherwise strictly use the same physical input data, for example partition functions, ionization potentials, and dissociation energies. The version of the chemical equilibrium we use includes 92 atoms and their first two or three ions, as well as more than 600 molecular species. A full description of the species included in the opacity package for continuum, atomic, and molecular lines is given in Gustafsson et al. (2008). Line opacities are computed assuming LTE. The opacities are provided at the wavelengths used by MARCS, with a resolution of $R = \lambda/\Delta\lambda = 20\,000$.

We sample a parameter space of 159×159 $T - \rho$ points, equally spaced in natural logarithm, where T ranges between 1 100 K and 550 000 K, and ρ between $10^{-15}\,\mathrm{g\,cm^{-3}}$ and $10^{-3}\,\mathrm{g\,cm^{-3}}$. These limits are motivated by the typical temperature and density extend of solar metallicity FGK-type stars; however, they are extended towards the low-density regime. This is necessary because of fluctuations, especially in the early phases of the simulation.

The internal energy is constructed from the temperature by the assumption of an ideal gas, $3/2\,k_\mathrm{B}T$, and is reduced by the properly weighted energy released by the formation of molecules and the recombination of ions. Following the procedure of `MARCS` (Gustafsson et al. 1975, 2008), only molecules containing H+, H2 and H2+ are considered for the summation of e_int.

The resulting table is then interpolated into a grid $e_\mathrm{int} - \rho$, which is chosen to be equally spaced in the natural logarithm. This final change of grids is necessary because of the appearance of the energy rather than the temperature in Eq. 2.15, which means that as the simulation advances energy and density in time, the temperature is a dependent variable and needs to be provided by the EoS rather than being an input parameter. We note, however, that due to non-linearities introduced by molecule formation and destruction, as well as ionization edges, the sampling of this final $e_\mathrm{int} - \rho$ table needs to be significantly higher to resolve step transitions in the $e_\mathrm{int} - T$ relation. We found that, specifically towards the surface layers of the Sun ($T \lesssim 7\,000\,\mathrm{K}$), the difference between opacities obtained from tables on the e_int and T grids reach values beyond 20 %. We avoid this issue by up-sampling the table to a resolution of 1024 points in e_int, which results in a deviation of $\lesssim 1\,\%$. Because interpolation in the EoS table does not contribute significantly to the overall computation time, this up-sampling has negligible impact on performance.

4.3.3 Opacity Binning

Procedure

Because monochromatic radiative transfer is a computationally expensive task, we follow the well-established strategy of opacity binning. Following the procedure presented in Nordlund (1982), which has been adopted as a basis for different RHD calculations (e.g. Magic et al. 2013a; Vögler et al. 2004), we sort a set of monochromatic opacities into bins the selection of which is described in more detail in the following section.

In each bin i we compute the mean opacity κ_i using a weighted transition from the Rosseland mean $\kappa_\mathrm{ross,i}$ (Eq. 2.56) in the interior to the Planck mean $\kappa_\mathrm{planck,i}$ (Eq. 2.55) in the optically thin layers (Nordlund 1982). We then interpolate between the two limits using the optical

thickness w_{thick} of the corresponding point in the table, i.e.

$$w_{\text{thick}} = 1 - e^{-2\,\tau_{\text{ross,i}}}, \tag{4.3}$$

$$\kappa_i = \kappa_{\text{planck,i}}\,(1 - w_{\text{thick}}) + \kappa_{\text{ross,i}}\,w_{\text{thick}}\,. \tag{4.4}$$

This formulation is similar to the expression used in Magic et al. (2013a), however, differs by using the Planck mean opacity instead of the intensity mean. The expression is also equivalent to the one developed in Ludwig (1992, their Eq. 3.51), defined as

$$\kappa_{\text{i}} = 2^{\frac{-\tau_i}{\tau_{1/2}}}\kappa_{\text{planck,i}} + \left(1 - 2^{\frac{-\tau_i}{\tau_{1/2}}}\right)\kappa_{\text{ross,i}}\,, \tag{4.5}$$

with $\tau_{1/2}$ defined as the turnover depth where Planck and Rosseland mean opacity are weighted equally. Whether one or the other is more relevant depends on whether absorption (of intensity) or emission (of Planck source) is the more important effect. But in practice it may make little difference, and the Planck mean is more convenient to compute. To compute the Rosseland optical depth $\tau_{\text{ross,i}}$ in Eq. 4.3 for each point in the table we follow the approximation from Ludwig (1992), that is

$$\tau_{\text{ross,i}} = \kappa_{\text{ross,i}} \cdot \frac{P}{g}\,, \tag{4.6}$$

which originates from the equation of hydrostatic balance (Eq. 2.1).

The radiative heating as given in Eq. 4.1 furthermore requires knowledge of the source function S_ν, which in LTE is given by the Planck function B_ν and hence depends only on the local temperature and frequency $\nu = c/\lambda$, where c is the speed of light. The integral in Eq. 4.1 can be divided into contributions from each bin as

$$q_{\text{rad}} = 4\pi\rho \sum_i \int_{\lambda(i)} \kappa_\lambda\,(J_\lambda - S_\lambda)\;\mathrm{d}\lambda\,. \tag{4.7}$$

In the approximation of opacity binning, the mean opacity of each bin is assumed for the whole set of wavelength points belonging to this bin and hence can be extracted from the integrand in Eq. 4.7 such that

$$q_{\text{rad}} = 4\pi\rho \sum_i \kappa_i \int_{\lambda(i)} (J_\lambda - S_\lambda)\;d\lambda \tag{4.8}$$

$$= 4\pi\rho \sum_i \kappa_i \left(\int_{\lambda(i)} J_\lambda\;\mathrm{d}\lambda - \int_{\lambda(i)} S_\lambda\;\mathrm{d}\lambda\right)\,. \tag{4.9}$$

The calculation of the mean intensity requires the solution of equations of the following

form, depending on the angle $\mu = \cos(\theta)$,

$$I_{\nu,\mu} = \int S_\nu e^{-\tau_\nu/\mu} \, \mathrm{d}\tau_\nu/\mu, \tag{4.10}$$

where $J_\nu = 1/(4\pi) \int_{4\pi} I_\nu \mathrm{d}\omega$ is the intensity I_ν averaged over the solid angle ω and $\mathrm{d}\tau_\nu = \rho\kappa_\nu \mathrm{d}z$ is the optical depth increment at frequency ν and geometrical depth increment $\mathrm{d}z$.

In this work, we rely on four ϕ (azimuthal) and two μ (polar) angles, and two additional angles with $\mu = \pm 1$, so in total ten different angles chosen in a Gauss-Radau quadrature. The selection of angles is equivalent to the STAGGER approach. In CO^{5}BOLD usually a higher number of angles is used (see e.g. Beeck et al. 2012), but it depends on the particular application of the code.

In the binning approximation the optical depth is computed from the binned opacity, and hence independent of λ, which means the optical depth terms in Eq. 4.10 can be pulled out of the λ integral in Eq. 4.9 such that

$$\int_{\lambda(i)} J_\lambda \, \mathrm{d}\lambda \sim \int_{\lambda(i)} \left(\iint S_\lambda e^{-\tau_i/\mu} \, \mathrm{d}\tau_i/\mu \, \mathrm{d}\omega \right) \mathrm{d}\lambda \tag{4.11}$$

$$\sim \iint e^{-\tau_i/\mu} \, \mathrm{d}\tau_i/\mu \, \mathrm{d}\omega \int_{\lambda(i)} S_\lambda \, \mathrm{d}\lambda. \tag{4.12}$$

The integration over wavelength points corresponding to bin i can hence be executed before the solution of the radiative transfer. The resulting binned source function

$$S_\mathrm{i} = \int_{\lambda(i)} S_\lambda \, \mathrm{d}\lambda, \tag{4.13}$$

can thus be pre-computed, included in the opacity table, and used together with the binned opacity to obtain the radiative heating during the simulation, which reduces the computational burden significantly.

Note that the monochromatic source function in NLTE would depend on the radiation field, which strictly speaking would require knowledge of the model atmosphere prior to its simulation. However, NLTE calculations for multiple species are extremely computationally expensive, especially in 3D, which is why all 3D RHD codes, including STAGGER, MURaM, and CO^{5}BOLD generally adopt the LTE approximation for structure calculations.

The effect of NLTE on the physical structure of models was investigated in other studies (e.g Short & Hauschildt 2005; Haberreiter et al. 2008; Young & Short 2014), based on 1D HE modeling. These studies showed that the effect is very small, in particular for the Sun not exceeding 50 to 100 K in the atmospheric layers $-3 \lesssim \log \tau_{500} \lesssim +0.5$ (Short & Hauschildt

2005), whereas outside these layers the presence of the chromosphere or convection is much more important. Including NLTE in structure computations would introduce additional dimensions to the opacity table and increase the complexity, which is why we for simplicity work in the LTE approximation. The spectrum synthesis in the relaxed 3D model atmosphere (see Sec. 4.3.7) however can be done in NLTE regardless.

Selection of opacity bins

Although there is no consensus among related studies on the exact number and positioning of opacity bins, there is a general understanding of the need to distribute bins to try to cover the regions most important for the energy balance. The STAGGER grid (Magic et al. 2013a) is computed using 12 opacity bins, which were defined depending on their wavelength and formation height on the Rosseland optical depth scale (τ_{ross}), that is, the Rosseland optical depth where their monochromatic optical depth equals unity. The computation of these optical depth scales requires some initial knowledge of the average atmospheric structure of the 3D model that is intended to be simulated.

For the STAGGER grid, an iterative procedure is involved at this stage, which adjusts the bin dimensions repeatedly as the simulation evolves in time. As a metric for the goodness of the binning, they furthermore compute the monochromatic heating rates and compare them to those of the binned result. They report typical differences of $\max\left|q_{\mathrm{rad}}^{\mathrm{bin}} - q_{\mathrm{rad}}^{\lambda}\right| / \max\left|q_{\mathrm{rad}}^{\lambda}\right| \sim 3\,\%$ for their solar model. However, they are able to improve this difference by further fine-tuning (Magic et al. 2013a). It remains to be tested how this translates to uncertainties of the 3D structure of the final model, and especially on the observables, for example, the stellar spectrum. In the case of our solar model, our binning method, as described in the following, achieves 2.8 % in the same metric.

A very similar binning is applied in the CO^{5}BOLD (e.g. Freytag et al. 2012; Ludwig et al. 2023) simulations, where, however, the bin selection involves less fine-tuning as they are placed in regular optical depth and wavelength intervals (Beeck et al. 2012). The MURaM solar model (Vögler et al. 2005) goes one step further and relies on only four opacity bins, which are wavelength independent and chosen based only on the monochromatic optical depth (as in Nordlund 1982). There is no further optimization procedure involved.

Despite their drastic differences in bin selection, it has been shown in Beeck et al. (2012) that the relaxed simulations of the solar photosphere are remarkably similar in terms of mean temperature and density stratification. The thermal structure of the solar models presented in Beeck et al. furthermore shows a good resemblance on the optical depth scale (see their Fig. 10, 11) with mean differences below 100 K in the regions relevant for spectral line formation, which suggests a rather small influence of the opacity binning procedure on the stellar spectrum.

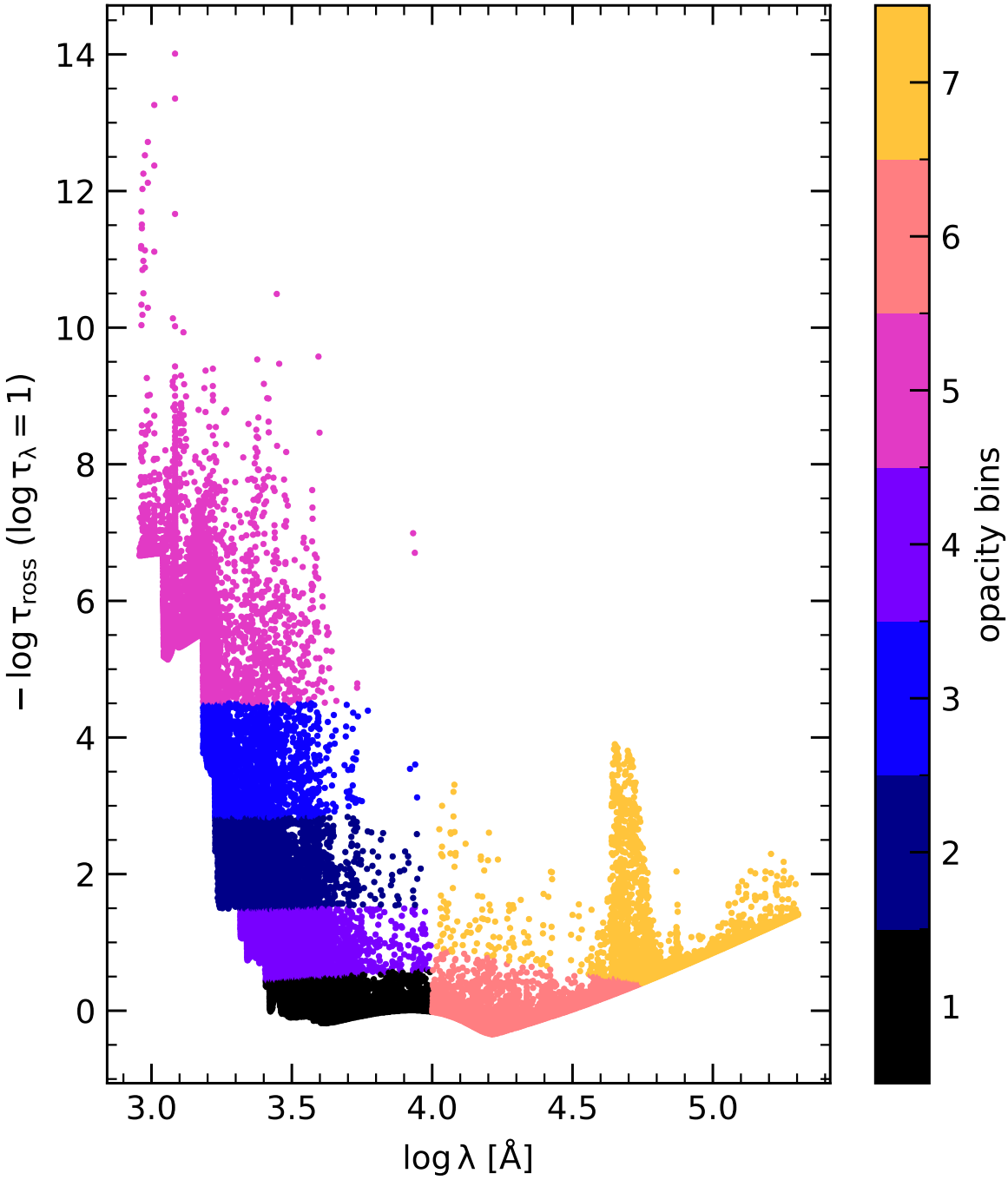

Figure 4.2: Formation height as a function of wavelength for monochromatic MARCS opacities, computed for an average 3D STAGGER solar snapshot.

4.3.3 OPACITY BINNING

In this work, we apply a simple, automatic binning procedure and do not alter the binning in the course of the simulation. We select seven opacity bins, which are distributed similarly to the bin distribution used by Magic et al. (2013a). The number of bins has been chosen as a compromise between accuracy and computational efficiency. In our simulations between 60 and 80 % of the entire computation time is spent solving the RT, a reduction of the opacity bins therefore has a very significant effect.

We first separate the strong lines at shorter wavelengths from the redder part of the spectrum. In the blue part, we furthermore specify an upper limit on formation height, beyond which we collect all wavelength points in a single, high-opacity bin in order to assure sufficient sampling in the regime closer to the continuum.

The formation height edges of the remaining blue bins are then automatically selected using a generic k-means clustering approach (e.g. Hartigan & Wong 1979). The red wavelength points are binned accordingly. Following this procedure, we split the most relevant opacity sources below the Rosseland formation depth of -4.5 in the blue part of the opacity table into four bins, leaving two bins for the red part of the spectrum and one bin collecting the remaining strong lines.

This procedure is deliberately designed to be as generic as possible, while at the same time producing consistent results for a variety of different stars without human intervention. It can be executed automatically prior to the simulation by using an initial 1D model (for example, a 1D HE model) and does not involve an iterative procedure. However, it captures the location of opacity nodes in the $\log\lambda - \log\tau_{\mathrm{ross}}$ diagram through clustering, and hence provides more bins where a higher resolution is required.

We have tested the approach by exploring the differences in the monochromatic heating rate with the heating calculated using four, five, seven, eight, and 12 bins with parameters similar to those chosen by other authors. We find that for all these combinations the differences relative to the cooling peak are at a sub-percent level. Therefore, we consider our chosen scheme as appropriate within the context of our work, as a compromise between very expensive fine-tuning (`STAGGER`, Magic et al. 2013a) and wavelength-independent (`MURaM`, Vögler et al. 2004, 2005) approaches.

For the solar model presented in this work, we bin tabulated opacities generated by the `MARCS` code using the chemical composition presented in Magg et al. (2022b). The formation height of each wavelength point in this table is computed using the average solar `STAGGER` model. The corresponding binning is presented in Fig. 4.2, where we show the formation height as a function of wavelength and indicate the bin assignment with colors.

4.3.4 Initial & Boundary Conditions

Every model simulated in this works relies on only three numbers that will determine its final state; the temperature and density at a single point within the atmosphere, as well as the surface gravity, $\log(g)$. This initial seed can be placed at any height z_0, which should be chosen such that the zero-point of the resulting z scale roughly coincides with the optical surface. From here, an initial 1D HE model is constructed by adiabatically integrating the initial seed upward and downward with a constant step in $\ln\rho$.

Considering a fluid parcel of constant mass, the change of its internal energy per unit mass e_{int} is given by the first law of thermodynamics (see also Eq. 2.19)

$$\mathrm{d}e_{\text{int}} = T\,\mathrm{d}S - p\,\mathrm{d}V = T\,\mathrm{d}S - pV\,\mathrm{d}\ln V = T\,\mathrm{d}S + \frac{p}{\rho}\,\mathrm{d}\ln\rho, \tag{4.14}$$

where S is the entropy per unit mass and V the volume of the fluid parcel. If the system is adiabatic, with $\mathrm{d}S = 0$, then the above equation links a change in log density directly to a change in internal energy per unit mass, through a pre-factor p/ρ that behaves similarly to the temperature T.

For a given step in $\ln\rho$ the internal energy per unit of mass can thus be computed iteratively, with a procedure that converges rapidly. The z-scale is constructed from hydrostatic balance (see also Eq. 2.1)

$$\mathrm{d}z = -\frac{p}{\rho g}\,\mathrm{d}\ln p. \tag{4.15}$$

Toward the surface, the adiabatic structure is terminated once a certain minimal energy is reached, which is kept fixed for the remaining integration. The resulting 1D structure is then interpolated onto the coordinate grid of the 3D simulation domain, assuming no variations in horizontal directions.

The velocity field at the start of the simulation is initialized as a Gaussian drop-off with distance from $z = 0$, including a random factor to kick-start convective motions. The entropy at the bottom of the atmosphere is kept fixed during the remaining parts of the simulation and serves as a bottom-boundary condition.

Alternatively, it is also possible to skip the adiabatic initialization and start directly from any 1D model atmosphere (either a 1D HE or a horizontally averaged 3D model), where the internal energy is computed consistently with the EoS that will be used in the simulation. This procedure is especially useful when a specific bottom boundary condition is required, for example, if a comparison with other simulations is desired. All models generated in this work are initialized using an average 3D (i.e. 1D) `STAGGER` model atmosphere to make the comparison more straightforward. We note, however, that also in this case only three numbers, density and temperature at the bottom of the initial model and surface gravity,

determine the ultimately emerging 3D structure.

The fixed entropy is enforced by requiring inflows to be isentropic while keeping outflows unchanged. At the top of the atmosphere, the energy per unit mass is kept constant, while the density is assumed to drop off exponentially with pressure scale height. The horizontal velocity field is furthermore decaying with the same factor, equivalent to a non-shear boundary, while the vertical velocity is dropped off on half a scale height. The radiation boundary, that is, the surface heating term, is estimated from the optical depth in the vertical, and zero in the horizontal. The surface gravity is furthermore kept fixed and is the same throughout the simulation domain.

4.3.5 Relaxation

The relaxation procedure consists of three stages, which are mainly characterized by the cooling sources and the presence of damping terms. The first phase starts from the initial model described in the previous section. In order to start convective motions quickly and reliably, the only source of cooling at this early stage of the simulation is the strong, artificial, so-called *Newton cooling*. It effectively removes (or adds) heat to the system so that its internal energy reaches a given value e_0 on a given time-scale δt_N at a given position s_0 on a scale of s_1. The resulting heating per unit volume q_N is given as

$$q_\mathrm{N} = (e_0 - e)\frac{f}{(1+f)\cdot \delta t_N}, \tag{4.16}$$

$$f = e^{-\frac{s-s_0}{s_1}}. \tag{4.17}$$

There is no radiative cooling at this stage. The average vertical component of the velocity field v_z is furthermore damped on the timescale δt_f via the addition of a friction term of magnitude $\rho\, v_\mathrm{z}/\delta t_\mathrm{f}$ to damp out artificial radial p-mode oscillations – excited by the rapidly changing thermal structure – that would otherwise survive for a long time.

Because of approximate conservation of wave mode energy, even weak wave modes initiated near the bottom boundary can grow in amplitude when traveling towards the surface and can ultimately even become disruptive. This initial procedure has emerged from countless tests and provides a reliable and fast pathway from the initial adiabatic cube to the first semi-realistic 3D model atmosphere that can evolve further in time in the following phases (e.g. Freytag et al. 2012). This intermediate model already has developed convective motions and displays a granular pattern towards the surface layers.

We note that the initial Newton cooling phase is strictly speaking not required, as the radiative transfer itself is capable of providing the relevant cooling to develop the radiative surface. However, the advantage of an initial Newton cooling phase is that (i) its strength is a hyperparameter that can be optimized to achieve a more realistic velocity field in a

shorter time, and (ii) it does not require the solution of the radiative transfer equation, which is expensive in terms of computation time and potentially unstable on an initially chaotic atmospheric background.

The particular choice of additional hyperparameters is irrelevant for the final structure of the model, but the numerical stability is enhanced if the cooling surface at e_0 lies close to the true optical surface that will emerge from the actual radiation field. However, the correct surface will emerge in the second phase regardless of the exact decision. We choose the hyperparameters e_0, s_0, s_1 and δt_N based on the 1D HE model that is used for initializing the 3D cube. After using the opacity table to compute the Rosseland optical depth scale of the initial 1D HE model, we place the upper boundary at $\log \tau_\mathrm{ross} \sim -5.5$. From here we pick the physical height, density, and temperature and use the EoS to compute the internal energy at this point in the atmosphere. This directly provides estimates for e_0 and s_0.

A qualitative investigation has shown that a scale of $s_1 = 0.1\,\mathrm{Mm}$ and a timescale of $\delta t_\mathrm{N} = 10\,\mathrm{s}$ produce adequate results in the solar case. For stars other than the Sun we scale those parameters according to changes in the physical dimensions of the star and the strength of their velocity field using the Courant condition.

This early atmosphere is advanced in time until a granular pattern has emerged. For the solar model, the duration of the first phase corresponds to roughly $30-40$ stellar minutes. After this, in the second phase, Newton cooling is gradually reduced and replaced by radiative cooling. Newton cooling is reduced by decreasing the cooling rate exponentially, with a decay time scale of two stellar minutes, until it reaches 1 % of its original value. After this, it is turned off entirely.

The switching of the cooling source is accompanied by additional, destabilizing oscillations, which is why the friction term remains present during this phase. We hence wait an additional ~ 20 stellar minutes (until 50 stellar minutes total simulation time) before we start to fade out the friction term in the same manner as described above, but with a longer characteristic time scale of 15 minutes.

`DISPATCH` uses local time-stepping, where the local time-step is derived according to the local CFL condition (Courant et al. 1967). During radiative transfer, this usually results in a time-step between 0.1 s and 0.4 s. The radiative heating rate is included in the Courant condition directly through the velocity $u = q_\mathrm{rad}/p \cdot \mathrm{d}s$, with grid spacing $\mathrm{d}s$.

4.3.6 Averaging of 3D RHD Cubes

For better visualization and comparison purposes we average the full 3D data cubes to averaged 1D vertical profiles. Since the absolute height scale in Cartesian coordinates bares no physical meaning, especially in the context of spectrum synthesis, the averaging of the data

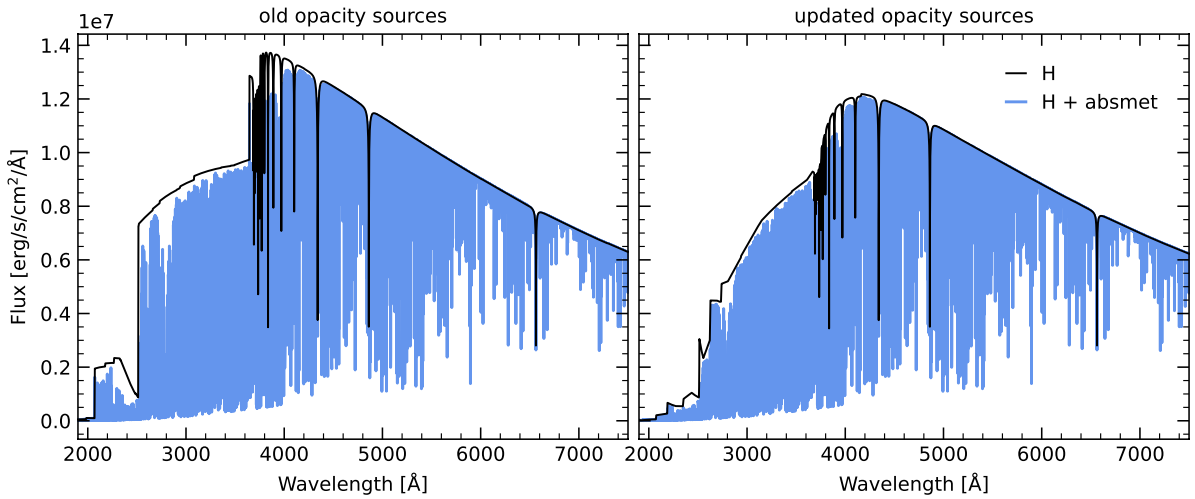

Figure 4.3: Model spectral energy distribution (SED) of the Sun computed using `MULTI3D@DISPATCH` and the solar `M3DIS` snapshot. Left and right panels show the SEDs computed with the old and our new updated background bound-free opacities. The occupation probability formalism (Dappen et al. 1987) is used in the updated opacities for H I bound-free transitions. The black line shows the result of running H lines in LTE on top of the LTE background bound-free opacities. The blue line shows the model flux when tabulated LTE opacities of bound-bound radiative transitions are included.

cubes is made on the Rosseland optical depth scale $\tau_{\rm ross}$. For this, we proceed as follows.

First, the Rosseland opacity for every point in the 3D cube is looked up in the EoS table. From this, $\tau_{\rm ross}$ is computed by column-wise integration. The entire cube is then interpolated to an optical depth scale equidistant in natural logarithm, again column-wise. The result is a 3D cube, where each horizontal plane corresponds to a common optical depth. The averaging of different quantities is then done per plane.

In order to be entirely consistent and avoid controversy originating from different opacities and integration limits of the Rosseland opacity, we also apply the same procedure to the reference models. This means that all models present in this work are on the same Rosseland height scale and consequently averaged in the same way. The average models are used for the sole purpose of comparisons and for gaining an intuitive understanding of the physical structure of models. We do not rely on averaged models for the calculations of synthetic observables.

4.3.7 Spectrum Synthesis

Calculations of high-resolution synthetic spectra presented in this work are carried out using the `MULTI3D` code (Leenaarts & Carlsson 2009), which we have also ported into the `DISPATCH` framework. For details of the code, we refer to Leenaarts & Carlsson and minor updates described in Gallagher et al. (2020) and Bergemann et al. (2019).

In summary, the code employs the method of short characteristics and accelerated lambda iteration (Rybicki & Hummer 1992) to solve the equations of radiation transfer and statistical equilibrium. After completing the final NLTE iteration, the outgoing flux is calculated with the method of long characteristics and the Lobatto quadrature. To enable detailed 3D spectrum synthesis, we have updated the code to include an extensive collection of tabulated bound-free and free-free cross-sections and partition functions for 92 elements. The partition functions are taken from Irwin (1981), while the sources of the continuous opacities are listed in Tab. 4.1. The occupation formalism is adopted for H I only, following the HBOP routine by Barklem & Piskunov (2003). This update ensures that the opacity sources of MULTI3D match those used in TURBOSPECTRUM (Plez 2012; Gerber et al. 2023).

As a result, MULTI3D can now incorporate bound-bound radiative opacities from comprehensive linelists provided in the TURBOSPECTRUM format. Alternatively, users can include pre-computed opacity tables to account for line blanketing. This allows for the use of fully self-consistent line opacities in both the 3D RHD modeling and the spectrum synthesis. A detailed description of all updates will be discussed in an upcoming paper (Hoppe, Bergemann in prep.).

In addition, we include the detailed linelist assembled by the Gaia-ESO Collaboration, as it provides carefully assessed atomic data for the diagnostic lines of the majority of chemical elements, including the transition probabilities and damping (Heiter et al. 2021). For H line profiles, we follow the HLINOP routine by Barklem & Piskunov (2003) which includes Stark broadening, natural broadening, and fine-structure splitting. Self-broadening is treated using the BPO theory in the case of the Balmer lines (Barklem et al. 2000) and using the theory of Ali & Griem (1965) in all other cases. In order to ensure backward compatibility with TURBOSPECTRUM we have implemented the same treatment of elastic H collisions (with four different options) as in the latter (see Gerber et al. 2023, and documentation to TURBOSPECTRUM v20[1]).

Fig. 4.3 shows the impact of the new (right panel) versus old (left panel) tabulated bound-free opacities, as well as the use of the occupation probability formalism. The latter explains the smooth transition in the flux continuum around 4000 Å, where there was a clear cut when classical Debye shielding was used instead. The updated continuous opacities are responsible for the depression in the UV where the flux has decreased noticeably. The slope of the continuum towards the infra-red has mostly been affected with the updated H^- opacities from McLaughlin et al. (2017).

Fig. 4.4 shows the center-to-limb variation (CLV) of one solar M3DIS snapshot compared to the observations by Neckel & Labs (1994). There is excellent agreement between the synthetic data and the observations at 611, 812 and 1099 nm, while slight differences are

[1]Publicly available at https://github.com/bertrandplez/Turbospectrum_NLTE

Table 4.1: Updated bound-free and free-free opacities and their respective sources. A subset of the MARCS and Turbospectrum opacities (Gustafsson et al. 2008; Plez 2012; Gerber et al. 2023).

Species	Type	Source
H	bf, ff	Karzas & Latter (1961)
H^-	bf	McLaughlin et al. (2017)
He, C, N, O, Mg	bf	TOPbase (Seaton et al. 1994)
Al, Si, Ca, Fe	bf	TOPbase (Seaton et al. 1994)
CH, OH	bf	Kurucz et al. (1987)
H^-	ff	Bell & Berrington (1987)
He, C, Mg, Si	ff	Peach (1970)
He^-	ff	John (1994)
H_2^-, O^-, CO^-, H_2O^-	ff	John (1975a,b)
H I + H I	ff	Doyle (1968)
H_2^+	ff	Mihalas (1965)

seen in the blue 402 nm. The same offset is seen in an alternative 3D RHD solar model from STAGGER which was also used in Bergemann et al. (2012a), hence it is unlikely due to the intrinsic properties of the 3D RHD models. Offsets of a very similar amplitude are also seen in 400 nm in other 3D RHD models, such as MURaM (Beeck et al. 2012, for a detailed comparison).

Compared with Pereira et al. (2013, their Fig. 3), we find that their 3D RHD models show very small yet discernible discrepancies around 402 nm, especially at larger angles $\mu = 0.5$ and 0.3, and, similarly to our results, the intensity ratios predicted by the 3D model are systematically higher compared to those of the observed data. This may indicate limitations of the observed data in the blue or the effects of a magnetic field and a chromosphere that are not included in standard 3D RHD simulations (Carlsson et al. 2019).

4.4 Results

4.4.1 Influence of Spatial Resolution on Atmospheric Structure

To allow the atmospheric models to converge towards a realistic thermodynamic structure the spatial resolution of the simulation domain, and especially the vertical resolution around the optical surface, are of utmost importance. In particular, the resolution adopted for the radiative solver is crucial to properly sample the cooling peak around the optical surface. We note that in this section the discussion will refer only to spatial resolution.

In order to investigate this effect, we compile a comparison between three models originating from identical initial conditions, but with varying spatial resolution. The HD grid spacing adopted is 25.6 km for the low- and intermediate-resolution models, and 15.4 km

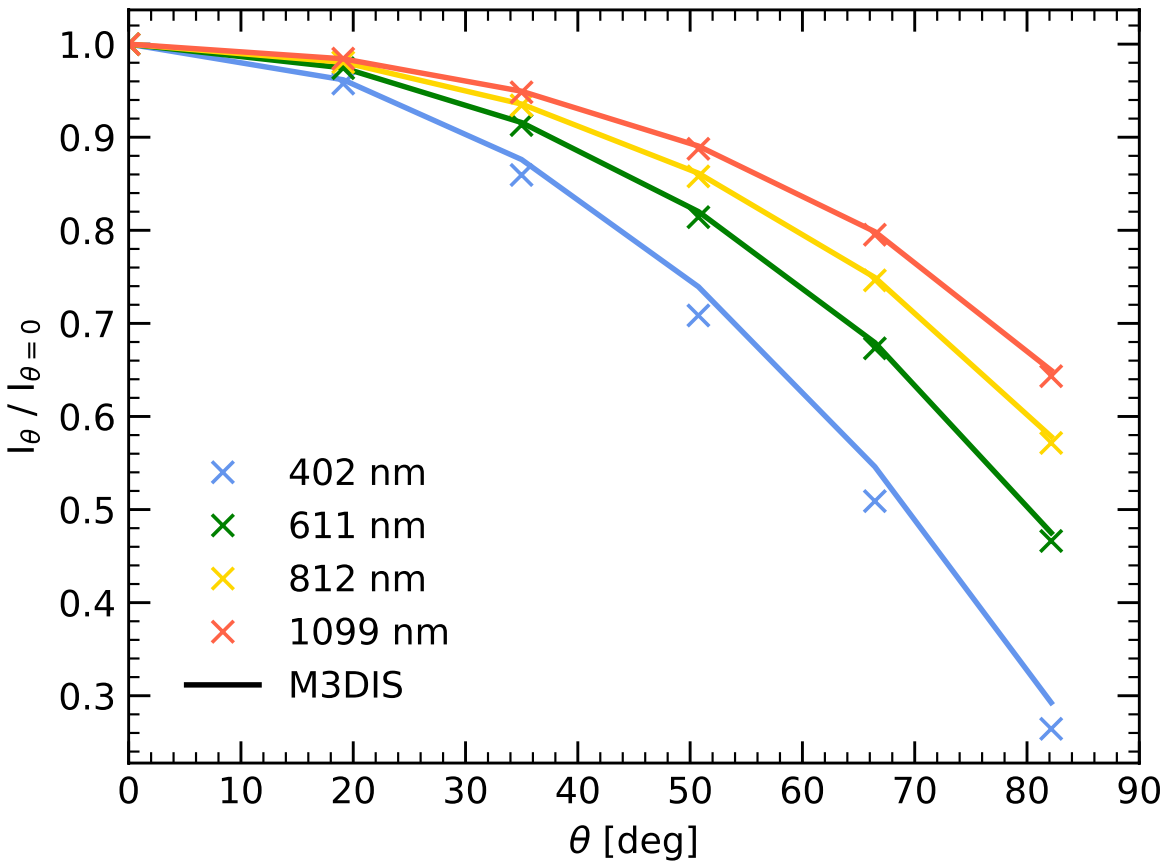

Figure 4.4: Angle dependent center-to-limb intensity variation of solar `M3DIS` snapshot at 4 discrete wavelengths. The solar spatially-resolved intensity data from Neckel & Labs (1994) are shown with crosses. We note that in the latter paper, only polynomial fits are available, here for didactic reasons we present them as discretized points.

for the high-resolution models. The vertical grid for the RT solver is denser by a factor 2 for intermediate and high-resolution models, with a spacing of 12.8 and 7.7 km, respectively. The low-resolution model has the same number of points in HD and RT. We summarize the different resolutions in Tab. 4.2.

Due to the modular nature of `DISPATCH`, it is straightforward to solve the radiative transfer on a grid different from the grid on which the underlying hydrodynamic solver operates. Tasks that are commissioned with solving Eq. 4.1 receive the necessary information about the current structure of the atmosphere, ρ and e_{int}, via linear interpolation from tasks that are responsible for solving Eq. 2.13–2.15. The final radiative heating rate q_{rad} is then interpolated back to the initial HD grid and added to the energy balance for the next update of variables.

The comparison between the resulting average profiles is shown in Fig. 4.5. The statistics is made on planes of constant Rosseland optical depth, as described in Sec. 4.3.6 and then averaged over nine snapshots to obtain a robust comparison. Snapshots are taken every

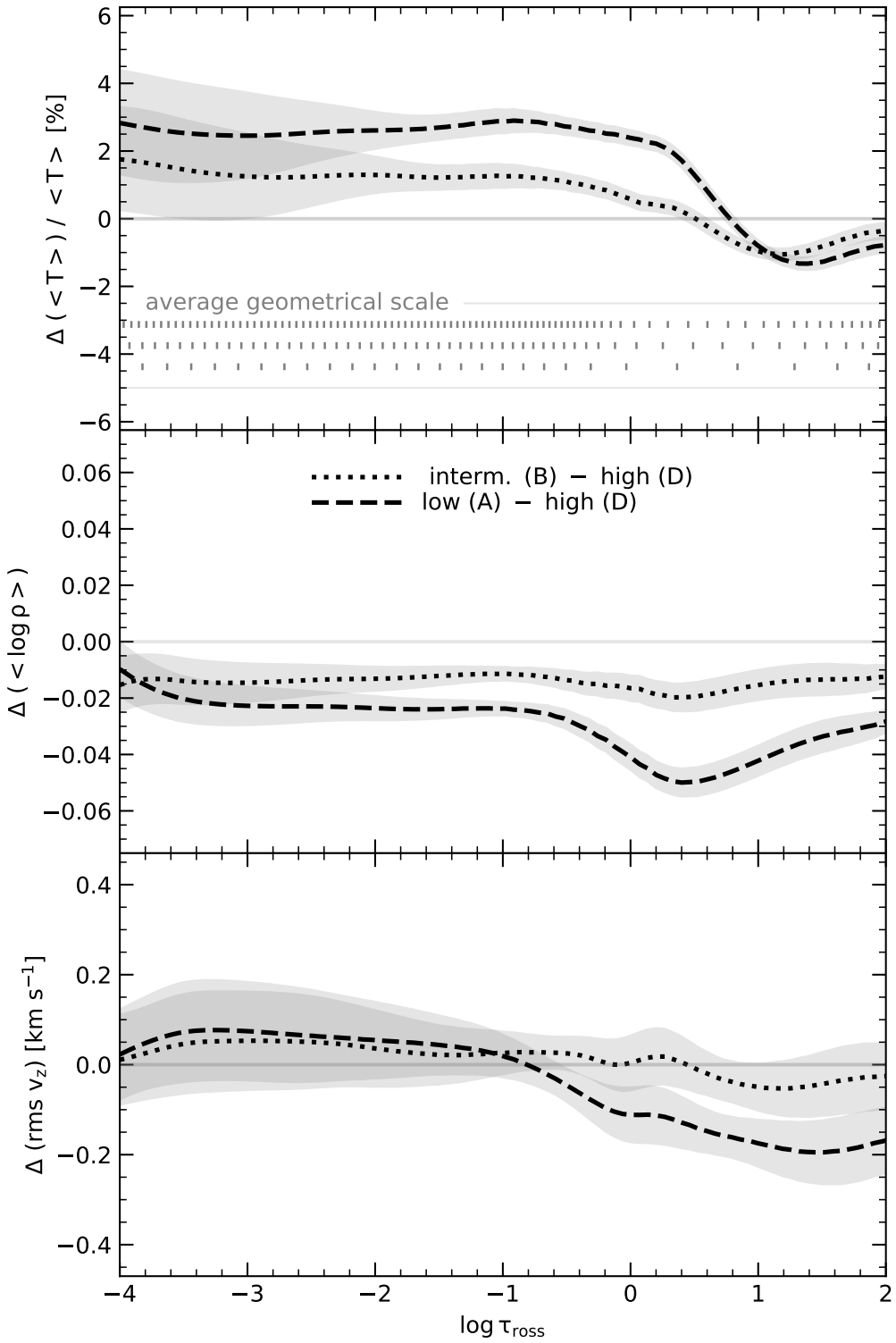

Figure 4.5: Average temperature (top) and density (middle) profiles, as well as rms vertical velocity (bottom) for models of different resolution. In each panel the difference to the highest resolution model ($\Delta z = 7.7$ km) is shown. Shading corresponds to the standard deviation between 9 different snapshots of the high resolution model. In the top panel we include the average geometrical depth scale of models A, B and D (from bottom to top) as vertical grey bars.

Table 4.2: Resolution overview of M3DIS solar models.

		$N_x \times N_y \times N_z$ (HD)	N_z (RT)	Δz (RT) km	N_{CPU} hours
A	low	180 × 180 × 90	90	25.6	226
B	interm.	180 × 180 × 90	180	12.8	576
C	very high*	390 × 390 × 195	390	5.9	15 206
D	high (ref.)	300 × 300 × 150	300	7.7	5 242

Notes. * Due to the high resolution of this model, the stellar time it evolved within 24h wall-clock time is reduced compared to models A, B, and D.
For all models, the number of grid points in each dimension (N_x, N_y, N_z), as well as the vertical grid spacing (Δz) and required CPU time (N_{CPU}), is shown. The physical size of the box in all simulations is $4.6 \times 4.6 \times 2.3$ Mm^3. The (x, y) resolution of the radiative transfer (RT) solver is the same as that for the hydrodynamic (HD) solver and is not shown here to avoid redundancy. See text.

200 s in time. Our time sequence thus covers at least one convective turnover time, which, at the bottom of our simulation, amounts roughly to $\sim$ 5 to 7 minutes. We note that the convective turnover time can be estimated locally using 1D HE models (kindly provided to us by H.-G. Ludwig) yielding estimates very similar to the ones above.

Each panel shows the difference $\Delta = \mathrm{av}_1 - \mathrm{av}_2$ between two average structures av_1 and av_2. Relative temperature differences in the upper panel are computed as $\Delta = (\mathrm{av}_1 - \mathrm{av}_2)/\mathrm{av}_2$. The shaded regions correspond to one standard deviation (std) between different snapshots of the highest resolution model, that is $\mathrm{av}_1 - (\mathrm{av}_2 \pm \mathrm{std}_2)$ for the upper and lower limit. In case of relative differences, $(\mathrm{av}_1 - (\mathrm{av}_2 \pm \mathrm{std}_2))/(\mathrm{av}_2 \pm \mathrm{std}_2)$ are the limits of the shaded region. By exploring the differences in the average temperature (top panel) and density profiles (middle panel), the effect of resolution becomes apparent mainly at the optical surface around $\log \tau_{\mathrm{ross}} \approx 0$ and towards the upper boundary of the star. In general, models with lower resolution are hotter and have a lower density in the upper layers. This behavior is expected and directly related to the poor sampling of the cooling peak. In the relevant layers, temperature and density change rapidly as a result of a sudden decrease in opacity. However, this transition region is spatially confined in the simulation domain and hence is only covered by a small number of grid points.

As a consequence, the linear interpolation on this sparse grid overestimates the heating rate, resulting in a shallower temperature decline and overall hotter upper atmosphere with lower densities. To illustrate optical depth sampling around the optical surface, we include the average optical depth derived from snapshots on the geometrical scale in the top panel of Fig. 4.5. Around $\log \tau_{\mathrm{ross}} \sim 0$ the step for low, intermediate, and high resolution models A, B, and D is 0.248, 0.113 and 0.062 dex, respectively. For comparison, the optical depth step in the MARCS models ranges between 0.1 and 0.2, depending on the location in the

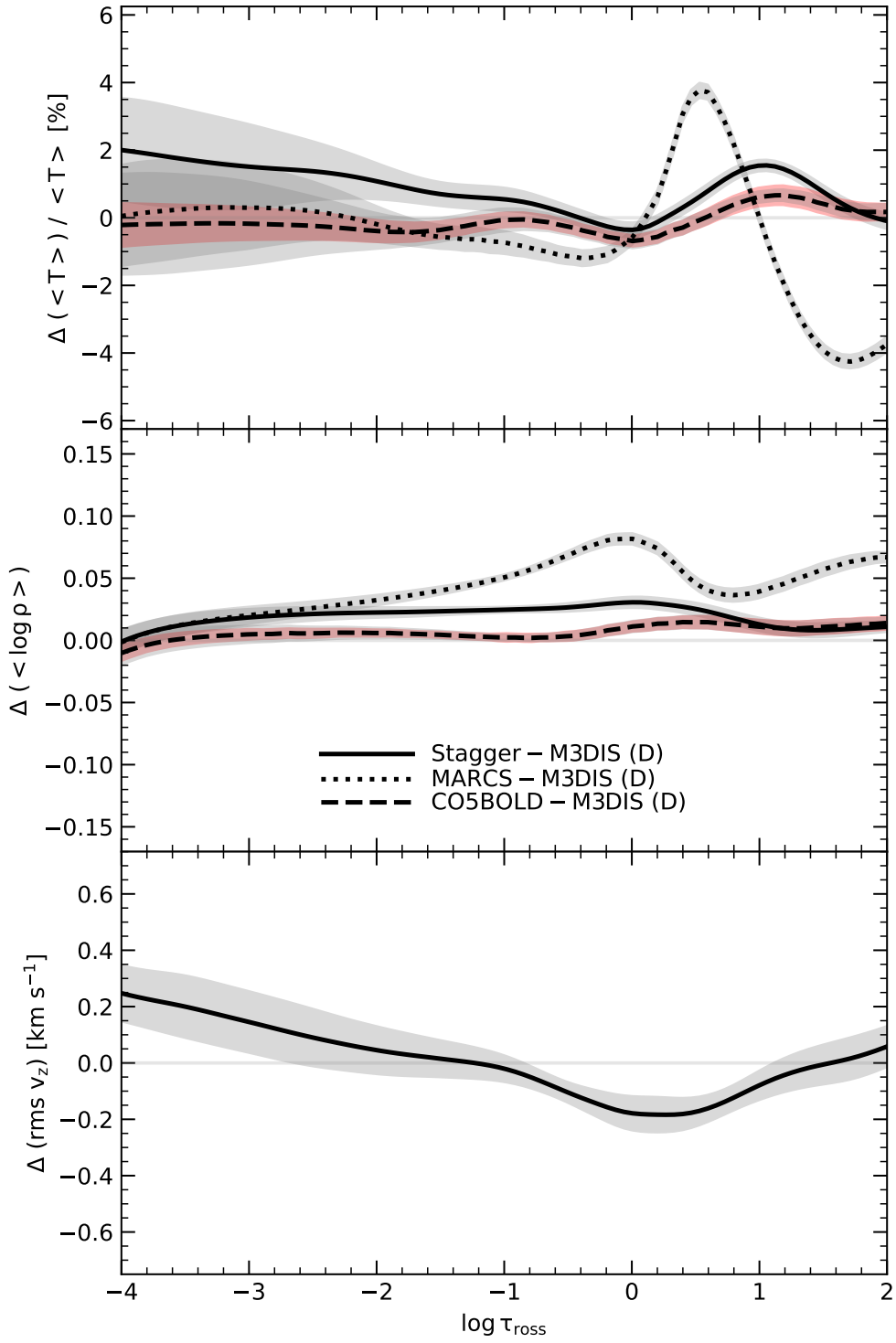

Figure 4.6: Differences in average 3D temperature (top), density (middle) and rms vertical velocity (bottom) structure as a function of Rosseland optical depth for our best solar model (M3DIS), STAGGER, CO^{5}BOLD and MARCS. We include the MARCS models, because they are among the most widely-used 1D hydrostatic model atmospheres for FGKM type stars analyses. The average M3DIS structure and the grey shading correspond to mean and standard deviation between 9 different snapshots of the high resolution model, respectively. For CO^{5}BOLD, the mean of 20 different snapshots was used. We also include the standard deviation between these snapshots in red as a reference.

atmosphere (Plez, priv. conv.).

Between A ($\Delta z = 26\,\mathrm{km}$) and D ($\Delta z = 7.7\,\mathrm{km}$) we estimate that the magnitude of this effect is of the order of 2.5 % on the average temperature stratification and between 0.02 dex and 0.06 dex for density. We furthermore note that the root-mean-square (rms) of the vertical velocity in the low-resolution case on average is higher in the interior compared to the high-resolution models. At the surface, the effect becomes minimal. We investigate in Sec. 4.4.4 how these differences in the atmospheric structure translate into observable quantities in the spectrum of the Sun.

For each resolution, we furthermore include the computation time necessary to compute the model in the last column of Tab. 4.2. Because solving radiative transfer is computationally expensive, the size of the RT grid has a significant impact on the overall computation time. However, due to the unique speed provided by DISPATCH all models presented here are obtained within 24 h[2] from start to end, using only 1D HE models as initial conditions, as outlined in Sect. 4.3.4. We emphasize that the comparisons performed here are made with fixed bottom boundary conditions, and as a consequence the temperature differences illustrated in Fig. 4.5 would also result in changes of the actual (as opposed to the "label") effective temperature. In a grid-of-models context, one would interpolate in the grid to the exact label effective temperature before computing synthetic spectra, which would most likely reduce the influence of resolution even further, since the changes shown in Fig. 4.5 do not vary much in the optically thin layers. It is thus likely that, in a grid context, the cost of modeling per grid point could be further reduced, relative to the results reported here. A summary of model properties and input physics is given in Tab. 4.3. Here we compute the effective temperature by using the binned opacity table presented in Sect. 4.3.3.

4.4.2 Solar Atmospheric Structure

In Fig. 4.6, we compare our reference 3D RHD solar model with models created by other groups. Specifically, we compare the mean vertical stratification of our best solar model with the solar STAGGER (Bergemann et al. 2012a; Magic et al. 2013a), CO^{5}BOLD (Freytag et al. 2012; Magg et al. 2022b), and the public version of the solar MARCS 1D hydrostatic model[3]. The averaging of all 3D cubes is performed on the Rosseland optical depth scale. In the case of CO^{5}BOLD average 3D models are used, and hence rms velocities are omitted. For STAGGER only the snapshot resembling the solar effective temperature closest was used.

Overall, the agreement between STAGGER, CO^{5}BOLD and our model is very good. The mean temperature structures (top panel) agree within 4 %. Throughout the optical depth range relevant to radiative energy transport (Grupp 2004), the structure of our model agrees

[2]Computations were performed on the HPC system Raven and Cobra at the Max Planck Computing and Data Facility

[3]https://marcs.astro.uu.se

to $\sim 2\,\%$ with STAGGER model, and below $\sim 1\,\%$ with the average CO^{5}BOLD model. The difference with CO^{5}BOLD reaches its maximum below the optical surface at $\log \tau_{\mathrm{ross}} \sim 1$ and falls in the sub-percent regime at $\log \tau_{\mathrm{ross}} \sim -4$.

In general, the STAGGER model is hotter across all optical depths, while the MARCS model transitions from cooler outer layers to a hotter optical surface and a cooler interior. No systematics can be identified for the CO^{5}BOLD model. As outlined in Sect. 4.4.1, the structural differences can primarily be attributed to the resolution of the cooling peak in the region of the steep temperature gradient.

In the inner layers, conditions closer to the diffusion approximation impose a rather narrow range of solutions, and hence the structures from different codes converge to similar values. However, in photospheric layers dominated by radiation loss, differences in the underlying treatment of microphysics, such as opacity data, abundances, EoS, and binning, can cause systematic differences in the average stratification. Specifically, the slight deviation in the outer temperature structure with the STAGGER model could be caused by differences in the line blanketing and specifically in the procedure used for the optimization of the group opacity bins.

In terms of density, the systematic difference of all 3D models with MARCS is the natural consequence of hydrodynamics. Convection provides additional turbulent pressure support to the atmosphere that implies, at a given temperature, lower pressures and densities compared to 1D hydrostatic models (Fig. 4.15 in Appendix), for a detailed discussion and analysis, see Stein & Nordlund (1998) and Rosenthal et al. (1999, their Fig. 7), which are also the mechanisms that change the properties of the resonant cavity of solar oscillations yielding systematic differences in the properties of oscillation frequencies compared to 1D hydrostatic models (see also e.g. Stein & Nordlund 2001; Samadi et al. 2003; Houdek et al. 2017).

The average density stratification, as well as the root-mean-square (rms) velocity distribution, are also in good agreement with STAGGER. On average, the density of our model is 0.02 dex lower, which corresponds to $\sim 5\,\%$. Especially on the surface, this is in line with the differences in the chemical composition between Magg et al. (2022b) and Asplund et al. (2009), of which the former predicts a higher bulk metallicity but also higher abundances of Fe, Mg, and Si, which are important electron donors under conditions of FGK-type atmospheres. Towards the deeper layers the resolution of the atmosphere again becomes more relevant. The MARCS model shows the same trend; however, the differences are more significant and exceed 0.1 dex below the surface.

Considering that the differences between the RHD models are relatively small, we decide that no further refinement, neither of the physical simulation domain nor in the opacity binning, is needed to obtain a realistic atmospheric model on reasonable time-scales. We

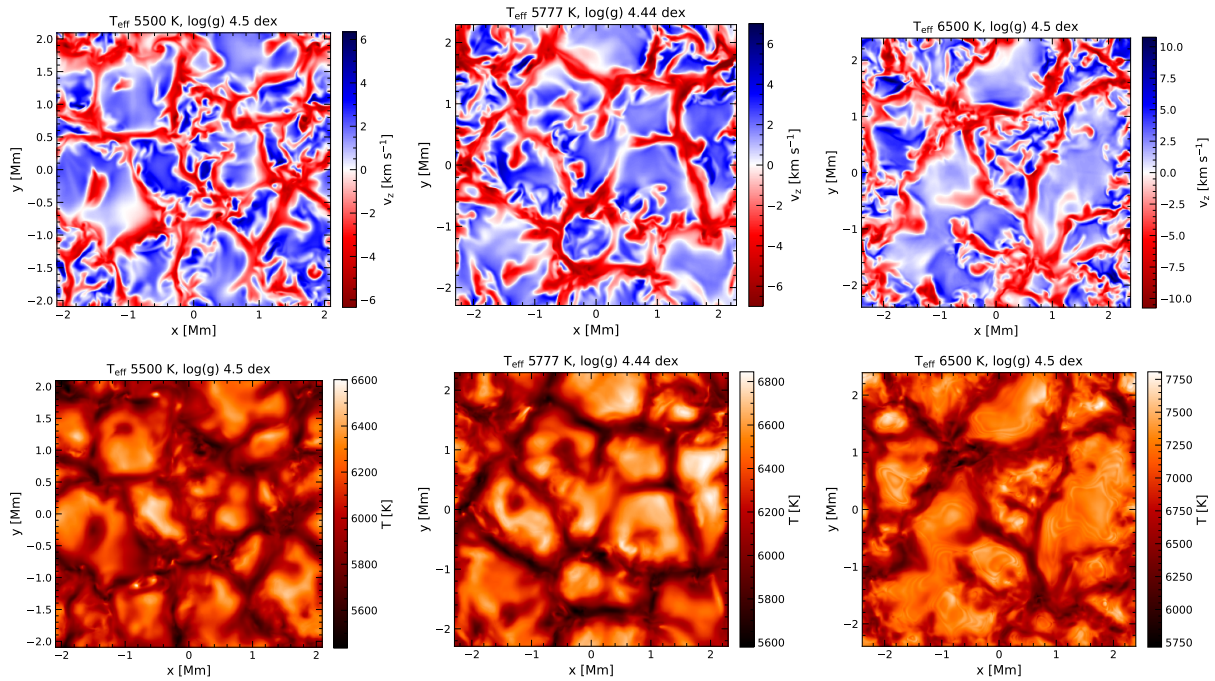

Figure 4.7: Vertical component of the velocity field (top) and temperature (bottom) at the optical surface for 3 selected solar-like simulations including our `M3DIS` solar model (D).

will further justify this decision in Sect. 4.4.4, where we test the validity of our solar model by producing observables that can be directly compared to solar observations.

4.4.3 Main Sequence Models

We compute several MS 3D RHD models with the same resolution as the solar model D. Specifically, we highlight models with $T_{\rm eff} = 5500$ and 6500 K, $\log g = 4.5$, and solar metallicity. In Fig. 4.7 we show horizontal slices of the vertical velocity component (top panels) and temperature (bottom panels) on the optical surface ($\log \tau_{\rm ross} = 0$) in order to illustrate the properties of the granulation pattern and its dependence on stellar parameters, specifically on $T_{\rm eff}$. We also include the solar model for comparison.

The size of the simulation domain is inspired by the corresponding `STAGGER` model and is set to 4.2, 4.6, and 4.8 Mm in x and y and 2.1, 2.3, and 2.4 Mm in the z direction, respectively. A representative horizontal extent of the box is important to simulate a sufficiently large number of granules, in order to establish realistic horizontal flows. In other words, the material in each granule must have enough room to spread sideways and sink back toward the interior when it reaches the optical surface. If it crosses the periodic border too quickly, the convective pattern can not be established without being significantly influenced by the boundary conditions. Magic et al. (2013a) typically choose approximately ten granules as a satisfactory condition, which is comparable to our results and suggests that the simulations shown in Fig. 4.7 are sufficiently large.

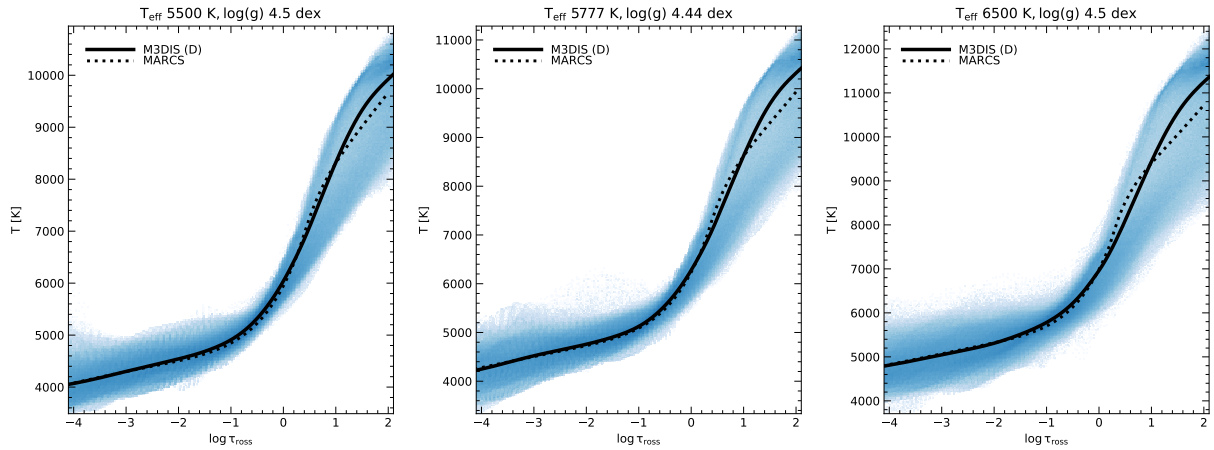

Figure 4.8: Full 3D temperature structure (blue contours) for 3 selected solar-like star simulations including our M3DIS solar model (D). Black solid lines correspond the the average temperature profile, dotted lines show the corresponding MARCS model.

For all models, we further show the full 3D temperature distribution as a function of $\log \tau_{\rm ross}$ in Fig. 4.8. We also include the T(τ) relationships of their respective horizontal averages and of the corresponding MARCS models with the same stellar parameters. We recall that the MARCS models are in HE, and convective flux transport is represented by the MLT (Henyey et al. 1965) with the mixing-length parameter α set to 1.5 (Gustafsson et al. 2008). A summary of the latter models is also provided in Gerber et al. (2023).

What has been established in Sect. 4.4.2 can also be observed when investigating 3D RHD models of different $T_{\rm eff}$. The agreement with 1D hydrostatic MARCS models is satisfactory towards the outer (optically thin) regions of the stellar atmospheres. This is simply because in these layers the structure of solar-metallicity models is close to the radiative equilibrium. We remark that this is not true for metal-poor model atmospheres, because of the prevalence of adiabatic cooling over radiative heating, as extensively discussed in the literature (e.g. Collet et al. 2007; Bergemann et al. 2012a).

Moving inwards, around $\log \tau_{\rm ross} \sim -2$ to -1, the MARCS models are slightly cooler than the average 3D model, and this behavior inverts in the deeper optically thick layers around $\log \tau_{\rm ross} \gtrsim +1$. At the bottom boundary, the MARCS models are always cooler than their 3D RHD counterparts. For the hottest models in our sample, $T_{\rm eff} = 6500\,$K, the difference between the 3D RHD model and the MARCS model amounts to $\sim 500\,$K, however, we remark that this difference can be reduced or amplified in principle using a different mixing-length parameter (e.g. Fuhrmann et al. 1993; Ludwig et al. 2009b). It is also interesting to point out that the extent of temperature inhomogeneities (at a given optical depth) varies significantly with $T_{\rm eff}$ of the 3D RHD model. As such, the cooler MS model with $T_{\rm eff} = 5500\,$K shows a reduced temperature spread at any $\log \tau_{\rm ross}$ compared to the hotter ($T_{\rm eff} = 6500\,$K) model, which is due to a more vigorous convection and consequently significantly larger velocity

amplitudes in the latter (see also Fig. 4.7).

Complementary to Fig. 4.7, we show vertical slices of the velocity field in Fig. 4.9 overlaid with colored contours of iso-temperature (top panels) and iso-optical depth (bottom panels). The direction of the flow is indicated with black streamlines; their width is proportional to the amplitude of velocity. For comparison, we show the exact structure and vertical extent of the equivalent 1D MARCS model to the left of each panel. Levels of temperature and $\log \tau_{\rm ross}$, as well as the vertical black line showing the extent of the 1D HE models, are placed at their respective geometrical height in comparison to the 3D model.

Firstly, it should be noted that the 1D HE models are much shallower than 3D RHD models that simulate convection and turbulent motions from first principle. Secondly, as already seen in 2D projections (Fig. 4.8), while the average structures are not too inconsistent between 1D HE and 3D RHD, the crucial difference between the two types of model atmospheres is in the presence of substantial horizontal inhomogeneities in all thermodynamic quantities (T, ρ, $P_{\rm gas}$, $\log \tau_{\rm ross}$, etc.) associated with horizontal and vertical mass motions. In all 3D models, multiple regions of pronounced downward motions are observed, with some extending across the entire vertical simulation domain. In between these regions, there are upflows of smaller vertical amplitude, however, typically much greater horizontal extent. These upflows pivot near the optical surface, which leads to the familiar granular pattern observed at the surface (e.g. Stein & Nordlund 1998; Nordlund et al. 2009).

Fig. 4.9 clearly shows that the flow pattern disrupts the iso-T and $\log \tau_{\rm ross}$ surfaces from the simple linear stratification seen in hydrostatic models, and these undulations in T and opacity are highly correlated. The curvature is especially pronounced in the hotter models (bottom panels in Fig. 4.9). The updrafts pull the hotter material along, bringing it closer to the surface, while the downdrafts mix cooler surface material deeper within the star.

This has significant implications for the opacity and consequently for the optical depth. Specifically, in the inter-granular lane the same optical depth is achieved at much larger geometric depths in the atmosphere, compared to the granule itself. In other words, one can see deeper into the inter-granular lanes than into the granules. For the 6500 K model, the (vertical) geometric extent of the iso-$\log \tau_{\rm ross}$ surface may exceed 400 km. By analogy, the vertical location of the isothermal surface changes by the same amount depending on the horizontal position. In the optically thin layers, also a very large difference is observed between the temperature of the granules and of the inter-granular lanes, leading to an approximately 1 000 K difference between these two main morphological components of the velocity field. In general, the inter-granular velocity field, its downward extent, and influence on atmospheric structure become more significant with increasing effective temperature and/or decreasing the surface gravity of the models (Magic et al. 2013a).

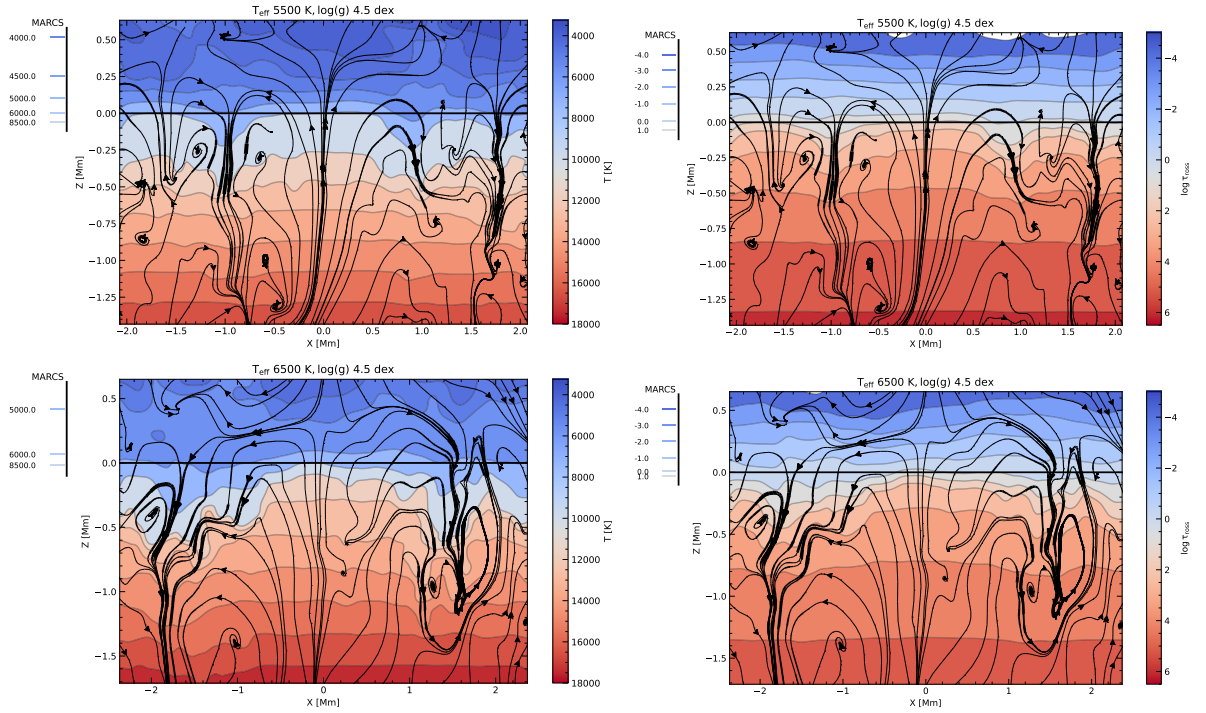

Figure 4.9: Vertical slice through the 3D RHD simulation domain for two selected MS stars (see Tab. 4.2) with solar metallicity, $\log g = 4.5$, and $T_{\rm eff} = 5500\,\mathrm{K}$ and $6500\,\mathrm{K}$. Note the differences in the vertical sizes of the boxes. Coloured contours corresponds to iso-temperature (left) and iso-$\log \tau_{\rm ross}$ surfaces (right). To the left of each panel, the geometric extension and respective profile of the corresponding 1D HE MARCS model, computed using the same stellar parameters ($T_{\rm eff}$, $\log g$, [Fe/H], and micro-turbulence of $1\,km\,s^{-1}$) is shown.

4.4.4 Solar Spectrum: Validation and Examples

The main aim of our work is to develop a self-consistent framework to compute model atmospheres and spectrum synthesis with detailed line formation in NLTE, with as far as possible consistent micro-physics. In this section, we present an analysis of synthetic line profiles for the Sun, computed using two approaches. In one approach, we test the influence of spatial resolution in 3D RHD simulations (Sec. 4.4.1) on the properties of spectral lines. This has already been explored earlier in the context of atmospheric structure.

In the second approach, we test the influence of the spatial resolution in the post-processing spectrum synthesis, which is carried out as described in Sec. 4.3.7. Two tests are performed to assess the needs in terms of precision of the thermodynamic structure of the M3DIS 3D RHD model, as well as in terms of spatial resolution in the post-processing spectrum synthesis calculations. The latter aspect was also addressed in Bergemann et al. (2019) for Mn I and in Bergemann et al. (2021) for O I lines. We use LTE line formation because it provides a more stringent test of the sensitivity of line formation to the local underlying atmospheric structure. In all cases presented here, the radiation transfer is computed in full 3D.

In Fig. 4.10 we show a simplified diagram of line formation in inhomogeneous atmospheres.

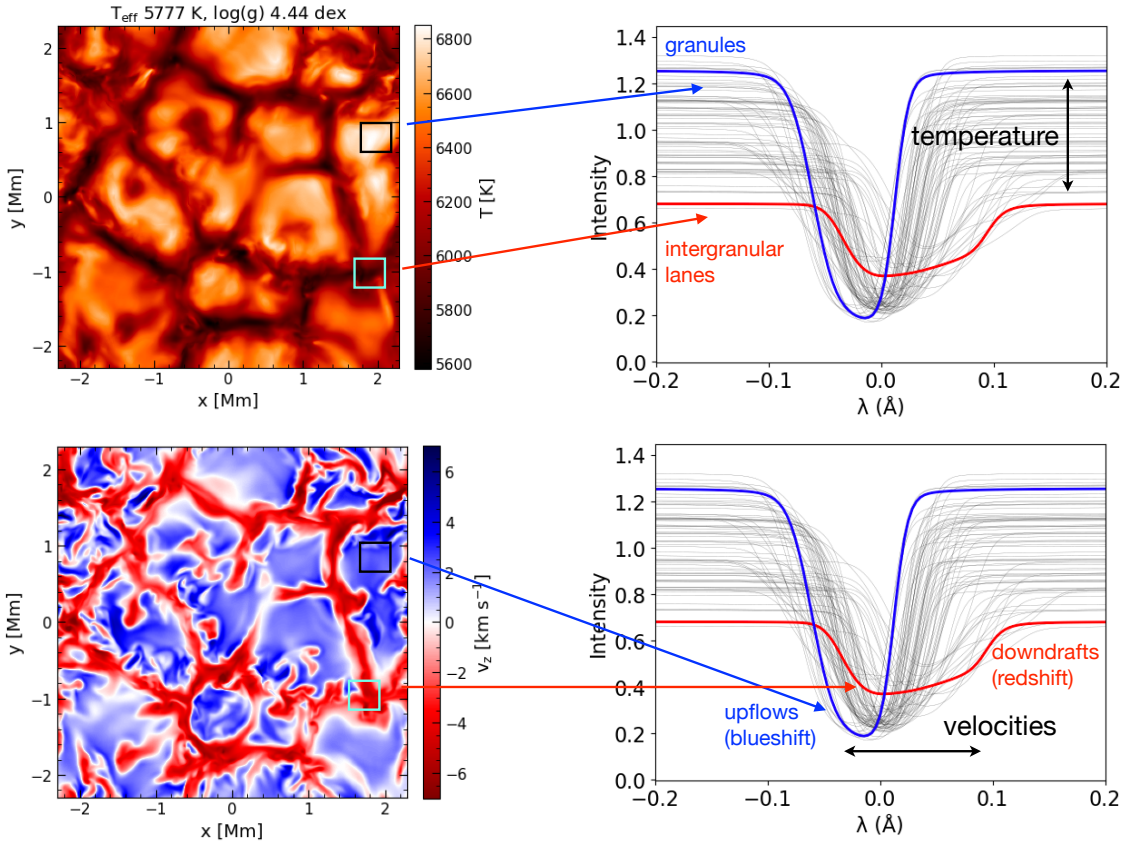

Figure 4.10: Simplified diagram of line formation in inhomogeneous atmospheres. Left panels: Temperature (top) and vertical velocity (bottom) slices at the optical surface. Right panels: Fe I 5432 Å line intensity emerging from different locations on the stellar surface.

This diagram helps to visualize the connection between the structural properties of 3D models, specifically, temperature, density, and convective velocity fields, and the observed quantities, that is, the emergent spectrum. We illustrate how the Fe I line at 5432 Å vary throughout the simulation cube and graphically identify the main features that follow from the complex temperature distribution and form the complex velocity structure within the granules and inter-granular lanes.

Linelist

For these two tests, we use the hydrogen Balmer H_α line and a set of diagnostic Fe I lines. The Fe I lines were carefully chosen from the atomic data compilations published by the University of Wisconsin group[4], the VALD database[5], and the Gaia-ESO linelist (Heiter et al. 2021). The line selection procedure was iterative and involved manual inspection of the line profiles in the observed solar spectra (to avoid blended features), lines with reliable $\log gf$ values (as, for example, given by the Y flag in the Gaia-ESO compilation) and relevance for

[4] https://github.com/vmplacco/linemake/tree/master/mooglists
[5] http://vald.astro.uu.se

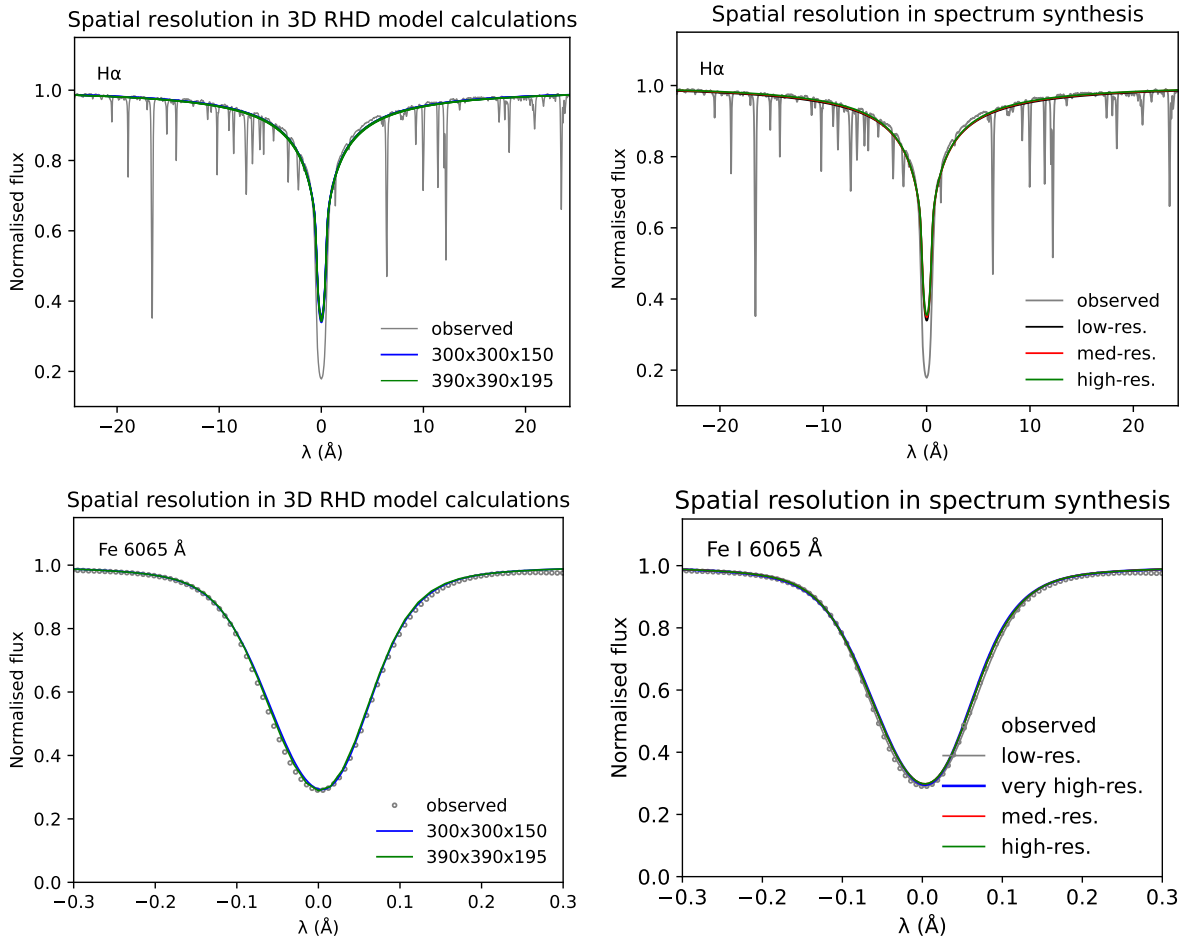

Figure 4.11: Comparison of H_α and Fe I line profiles computed with `M3DIS`, but with different spatial resolutions used in 3D RHD model calculations (left column) and in the post-processing spectrum synthesis (right column). For the results presented on the left-hand side, we adopt models C and D from Tab. 4.2, respectively, where D $(N_x \times N_y \times N_z) = (300, 300, 150)$ is our reference. For the results presented on the right-hand side, we use 3 characteristic spatial resolutions that differ only in horizontal resolution of $(N_x \times N_y) = (10, 10)$ (low − res.), $(30, 30)$ (med. − res.), and $(80, 80)$ (high − res.). For Fe I, we also show for comparison the profile computed a very high horizontal resolution of $(150, 150)$ in spectral synthesis. See text.

diagnostics of the Sun (based on Magg et al. 2022b) and for metal-poor stars as gauged by the availability in the University of Wisconsin compilation. We also aim to sample a range of strengths, excitation potentials, and wavelengths from 5000 to 9000 Å, the range that is used for optical spectroscopic surveys. With all these selection criteria, our final list includes 22 Fe I lines. Their parameters are provided in Table 4.4.

Influence of 3D RHD Model Resolution

In the left panels of Fig. 4.11 we compare the H_α and Fe I line profiles calculated using our reference `M3DIS` solar model D (Tab 4.2) with the profiles computed using the model with the highest vertical resolution of 5 km (C) which corresponds to (x,y)= $(390, 390, 390)$. We

stress that in this test (in contrast to the second test performed below), the model structure is different, whereas the resolution of spectrum synthesis is unchanged. The profiles correspond to the averages over four snapshots taken at time intervals of 100 s. The agreement of the line profiles is very good, especially for H_α, which has been traditionally used (e.g. Barklem et al. 2002; Mashonkina et al. 2008; Ruchti et al. 2013) as a diagnostic of the atmospheric structure of FGK-type stars and consequently represents an important $T_{\rm eff}$ indicator.

For H_β, we find small differences in the line wings, corresponding to the difference of order 20 to 50 K. Also, for the Fe I lines, the agreement between LTE profiles computed at different resolutions in the RHD calculations is excellent. This is further illustrated in Fig. 4.12, where we show the error incurred in the Fe abundance corresponding to the difference in structure between the high- and very high-resolution 3D RHD models. For most Fe I lines, the error is within 0.01 dex and there is no systematic trend with the line equivalent width. Lines with a slightly larger (positive) error of +0.015 dex are all near-IR lines with wavelengths $\gtrsim$ 8000 Å, while the features with the negative error are those towards the blue, at $\lambda \sim 5000$ Å. Overall, however, the impact of the resolution in RHD calculations appears to be modest, which suggests that our standard geometric setup (corresponding to that of model D in Tab. 4.2) can be reliably used for modeling MS FGK-type stars.

Influence of Spatial Resolution in Spectrum Synthesis

In the second test, we compare and test different spatial resolutions used in the post-processing spectrum synthesis, while using the same underlying 3D RHD model. This test is valuable because the motivation behind our work is the computationally expensive solution of the NLTE problem. In this context, decreasing the horizontal resolution during the calculations of departure coefficients offers a huge computational speed-up compared to solving coupled RT and statistical equilibrium equations at each iteration. Therefore, it is important for us to find a balance between the computational demands and the complexity of the approach. Such a horizontal down-sampling is among the most powerful means to achieve the speed-up, and we explore this approach in this section.

The model is re-sampled on the geometrical scale using linear interpolation. The number of vertical points is chosen to be 299, which is exactly twice the number of grid points in our best solar model (D), minus 1 point (see Tab. 4.2). This ensures that every second grid node coincides with the original grid of the snapshot to minimize interpolation errors, which is more relevant in the vertical direction. We find that the effect on spectral lines is small. In Fig. 4.11 (right panel), we illustrate the effect for the H_α line, as well as for one of the optical Fe I lines at 6065 Å. The comparison is performed for three models, each down-sampled to an effective spatial resolution of (x,y,z) = $(10, 10, 299)$, $(30, 30, 299)$, and $(80, 80, 299)$, respectively. Each profile corresponds to the average of a series of nine snapshots.

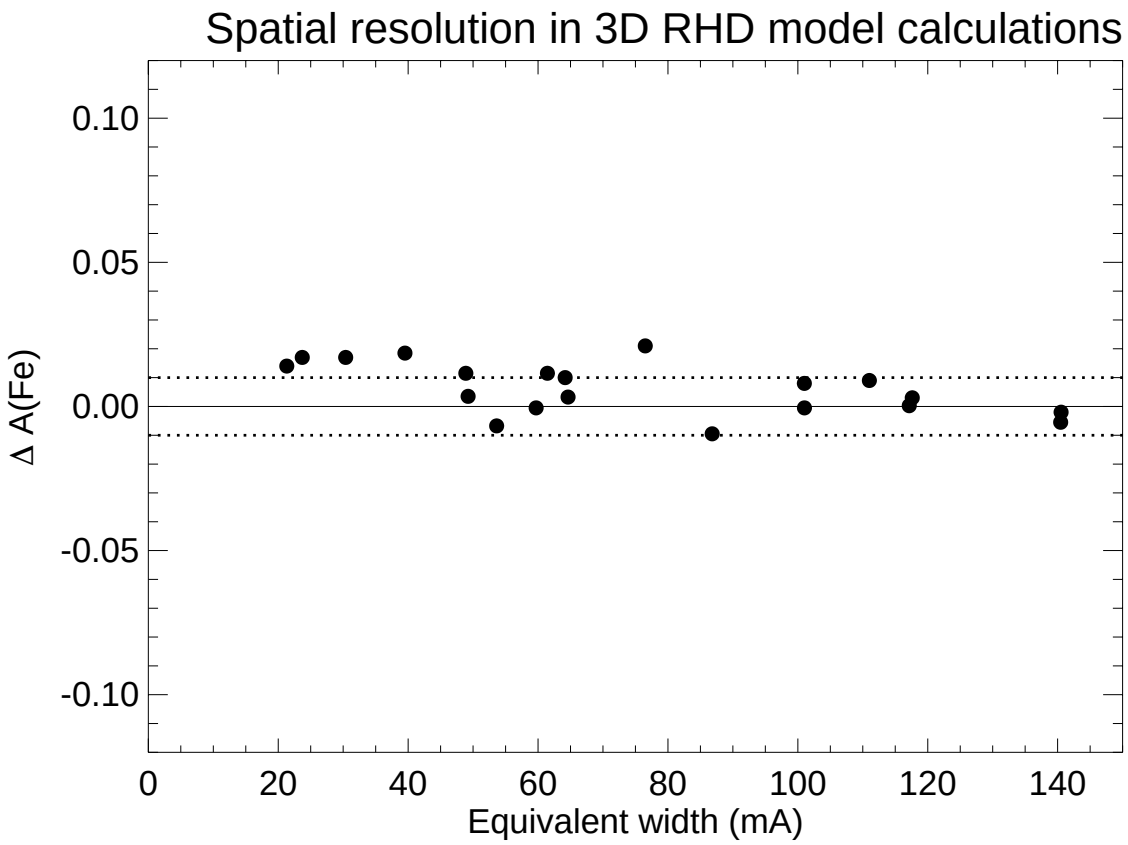

Figure 4.12: Error incurred in the Fe abundance as a function of equivalent line width corresponding to the difference between the high and very-high resolution models D and C, respectively. The horizontal lines show the 0.01 dex mark, to guide the eye. The ranges of y-axes are chosen deliberately to illustrate the typical error in abundances caused by the error of atomic data that, for diagnostic solar lines, ranges from 0.03 to 0.1 dex (Magg et al. 2022b).

As seen in the right panels of Fig. 4.11, for H_α, the synthetic profiles remain very close as long as the horizontal resolution in the spectrum synthesis calculations exceeds (x,y)= (10, 10). This is in agreement with our earlier studies (Bergemann et al. 2019), where we found a very small effect on the profiles of Mn lines.

For Fe I, we also show the effect of very high horizontal resolution, that is, (x, y) = (150, 150). Here, we find that the profiles computed with the model at (x, y) = (10, 10) are slightly stronger compared to the profiles computed at (x, y) = (30, 30), (x, y) = (80, 80), and (x, y) = (150, 150), whereas the latter three simulations are in excellent agreement. Comparing other line profiles, we find that the effect of low spatial resolution in spectrum synthesis slightly over-estimates the strength of line profiles and thus may under-estimate the Fe abundance by $\sim$ 0.02 to 0.05 dex. This is a typical uncertainty that shall be accounted for in abundances inferred through fits of LTE synthetic spectra, when low horizontal resolution is employed.

Such tests are vastly more time-consuming and require substantially more computational re-

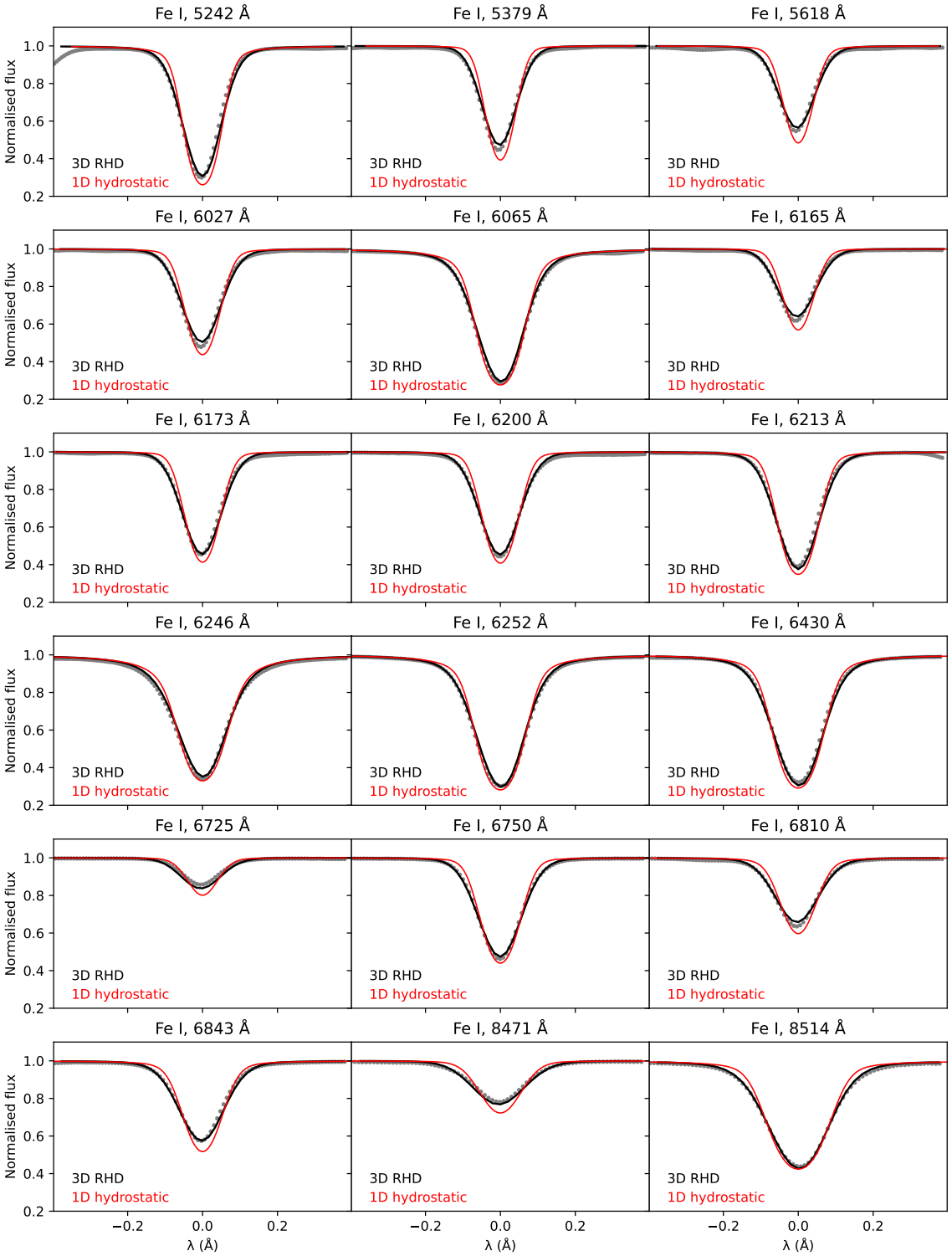

Figure 4.13: Comparison of the observed solar Fe I lines from the FTS KPNO flux atlas (Kurucz et al. 1984) with the synthetic line profiles computed using our 3D RHD Dispatch model (3D RHD) and the MARCS solar model (1D hydrostatic). For both models, the same iron abundance of A(Fe)= 7.50 was used. To compute the MARCS line profiles, we additionally include a microturbulence of $1\,\mathrm{km\,s^{-1}}$. Except the solar rotation, no other broadening was applied and the synthetic lines were not fit to the observations in any way.

sources in NLTE; however, in NLTE the effects are expected to be smaller. This is because the effects of differences in temperature and density are usually amplified in LTE calculations, due to the direct coupling of opacity and the source function to the local value of temperature. In contrast, in NLTE line opacity and source function are strongly influenced by the background non-local radiation field, especially in the blue and near-UV regimes, which form deeper in the atmosphere of FGK-type stars. This decoupling effectively eliminates the strong temperature dependence of the source function (Bergemann et al. 2012a).

While it may appear surprising at first that an under-sampling where horizontal structures are certainly severely degraded can still produce accurate results, it should be realized that, on the other hand, there is in some sense an over-representation of structures, with several granules providing samples at any one time and with several (here nine) samples in time.

Finally, in Fig. 4.13 we show the final line profiles of the Fe I lines compared to the very high-resolution solar flux observations from the KPNO FTS atlas (Kurucz et al. 1984). We overlay the results obtained from the radiation transfer calculations with our high-resolution reference M3DIS 3D RHD solar model (Tab. 4.2) and from the MARCS 1D HE solar model. In both cases, we use the same Fe abundance of A(Fe) = 7.50 and apply a broadening of $1.6\,\mathrm{km\,s^{-1}}$ to account for solar rotation. In the 1D HE case, we also include the standard microturbulence of $1\,\mathrm{km\,s^{-1}}$. No other velocities have been included as we want to avoid arbitrary fine-tuning of the models.

Clearly, the 3D RHD modeling leads to a much superior description of the asymmetric shapes of the observed line profiles compared to the 1D results. The latter, in virtue of the underlying assumptions of micro- and macro-turbulence, always predict perfectly symmetric profiles (note that this is distinct from the effects of isotopic structure or hyperfine splitting), thus failing to explain the deeper wings and shallower line cores. In addition, the 3D models successfully account for the characteristic blue-shifts of the lines. This reinforces the evidence that 3D RT modeling is indispensable for accurate and precise stellar spectroscopy to obtain realistic synthetic stellar fluxes and intensities, and consequently to derive accurate fundamental stellar parameters by comparing models with observations.

4.5 Conclusions

In this work, we present a new framework to solve radiation-hydrodynamics and detailed radiation transfer in LTE and NLTE, in order to model sub-surface stellar convection and calculate synthetic observables for FGK-type stars. We build upon the Copenhagen legacy RHD code, also known as the STAGGER code, the MULTI3D NLTE radiation transfer code, and the DISPATCH high performance computing framework (Nordlund et al. 2018). Here we outline the physical basis of the code, the key numerical properties, and updates to

Table 4.3: Model properties of M3DIS solar models.

Model	T_{eff}	log(g)	[Fe/H]	composition	HD solver	EoS	N_{bins}
M3DIS (A)	5923.5 ± 7.7 K	4.44	0.0	Magg et al. (2022b)	HLLC	Gerber et al. (2023)*	7
M3DIS (B)	5858.9 ± 14.8 K	4.44	0.0	Magg et al. (2022b)	HLLC	Gerber et al. (2023)*	7
M3DIS (C)	5786.0 ± 9.6 K	4.44	0.0	Magg et al. (2022b)	HLLC	Gerber et al. (2023)*	7
M3DIS (D)	5808.2 ± 14.8 K	4.44	0.0	Magg et al. (2022b)	HLLC	Gerber et al. (2023)*	7
Stagger	5768.51 K	4.44	0.0	Asplund et al. (2009)	Runge-Kutta	Mihalas et al. (1988)	12
CO5BOLD	5781 K	4.44	0.0	Grevesse & Sauval (1998)**	Roe Riemann	Wolf (1983)	12

Notes. For all models presented in this table the opacities from Gustafsson et al. (2008) were used.
* The EoS is computed using TURBOSPECTRUM v20, which is consistent with MARCS in terms of chemical equilibrium.
** except CNO

the input microphysics, and illustrate the gain in computational performance of the code, applying it to the simulations of sub-surface convection of the Sun and several stars on the MS.

Specifically, we show that with the new DISPATCH framework 3D RHD models with geometric and physical properties suitable for stellar spectroscopic modeling can now be computed – from scratch – on timescales of only a few thousand CPU hours, doable on medium-size computer clusters. Also, very high-resolution calculations, for example with vertical resolution of up to 6 km throughout the entire simulation domain, can be carried out conveniently with much more modest computations, compared to other available codes, permitting detailed systematic analysis of physical properties of the models at much smaller length scales.

We demonstrate how the updates to the code in terms of microphysics influence the basic observables for the Sun, specifically the bulk spectral energy distribution and the center-to-limb variation for the continuum, by comparing the model predictions with the data from Neckel & Labs (1994). We show that similarly to other models, such as STAGGER and CO5BOLD, our new models reproduce well the solar observations, with a minor difference in the blue and near-UV regimes, around $\lambda \lesssim 400$ nm. This difference manifests itself in slightly steeper center-to-limb intensity variations, but is common to other 3D RHD models (Beeck et al. 2012; Pereira et al. 2013). For the optical and near-IR, the CLV is in excellent agreement with the solar data.

Further, we perform an analysis of the influence of geometric resolution in 3D radiation-hydrodynamic simulations and in the post-processing spectrum synthesis. We show that low- and medium-resolution models are hotter at the surface and have slightly lower densities and velocities in the sub-photospheric layers. However, models with high- and very-high resolution show a high degree of consistency in their bulk thermodynamic properties, which results in very similar synthetic observables. For our purposes, which primarily aim to develop a method for characterization of stellar observations (such as spectra and photome-

Table 4.4: Diagnostic lines of Fe I adopted for tests presented in this work.

λ [Å]	state (low)	state (up)	$\log gf$
5242.491	a1I6	z1H5*	-0.830
5379.574	b1G4	z1H5*	-1.514
5618.632	z3P2*	e3D2	-1.250
6027.051	c3F4	v3G5*	-1.089
6065.482	b3F2	y3F2*	-1.529
6165.360	c3F3	v3G4*	-1.473
6173.334	a5P1	y5D0*	-2.880
6200.312	b3F2	y3F3*	-2.433
6213.429	a5P1	y5D1*	-2.481
6246.318	z5P3*	e5D3	-0.770
6252.555	a3H6	z3G5*	-1.699
6430.845	a5P3	y5D4*	-1.950
6725.356	y5D4*	e3F4	-2.100
6750.151	a3P1	z3P1*	-2.618
6810.262	y5P2*	e5P3	-0.986
6843.655	y3F4*	e3D3	-0.730
8471.743	x5D3*	g5D3	-0.910
8514.071	a5P2	z5P2*	-2.200
8621.601	b3G5	z3G5*	-2.320
8784.440	x5D3*	g5D4	-1.140
8905.991	x5F3*	e5P2	-1.220
8945.189	x5F4*	g5D3	-0.230

try), the spatial resolution of $(N_x \times N_y \times N_z) = (300, 300, 150)$ (in hydrodynamics, but double vertical resolution in radiation transfer) is appropriate to achieve the desired precision of the 3D structure.

In atmospheric layers above $\log \tau_{ross} \lesssim -3$, the vertical resolution has a systematic effect of decreasing surface temperature, which can impact the cores of strong lines that probe the outermost structure, such as H_α, and may bias the spectroscopic results if these are modeled in LTE. However, we show that the corresponding effect on abundance diagnostics does not exceed 0.01 to 0.02 dex for typical diagnostic lines with equivalent widths of 20 to 140 mÅ. We also find that – as a result of sampling several multi-structure snapshots in time – a spectrum synthesis horizontal resolution of $(N_x \times N_y) = (30, 30)$ is fully sufficient for precision diagnostics, as the corresponding error is smaller than the standard uncertainty of the input atomic and molecular data. We expect even lower resolutions to be suitable for NLTE calculations and encourage further studies of this kind.

This is the first work in the series that outlines the methodology, input physics, properties of the simulations, and presents basic validation tests. In subsequent papers, we aim to expand the parameter space of the simulations, probing the domain of more evolved stars, but also

cooler stars on the MS, to capture the entire parameter space of FGKM-type stars that are in the prime focus of upcoming large-scale stellar surveys, specifically the 4MOST high-resolution survey of the Galactic disc and bulge (de Jong et al. 2019; Bensby et al. 2019), the SDSS-V Milky Way Mapper (Kollmeier et al. 2017; Straumit et al. 2022), and PLATO (Rauer et al. 2014; Gent et al. 2022). As we develop the approach and methodology, we will put a substantial effort into developing an easily accessible and secure repository for public access, building on our experience with 1D HE model atmospheres and departure grids (Gerber et al. 2023) and NLTE abundance corrections[6]. The version of DISPATCH, on which the present code is built, is not publicly available yet. However, there are plans to also release the code in the near future. M3DIS stellar models will thus provide a qualitatively new basis for accurate and precise diagnostics of fundamental stellar parameters and the detailed chemical composition of stars.

4.6 Appendix – Supplementary Material

In Fig. 4.14, we show the horizontally averaged profiles of temperature (top), density (middle) and vertical velocity (bottom) against the Rosseland optical depth for three models of Sun-like stars computed using our new M3DIS code. The profiles show that the hotter model structures (corresponding to $T_{\rm eff} = 6500$ K) are characterized by lower densities and higher flow velocities, compared to the lower $T_{\rm eff}$ model atmospheres. This implies that the impact of convective motions and inhomogeneities on spectral lines is larger for hotter stars.

In Fig. 4.15, we compare the gas pressure versus temperature for the spatially averaged profiles of 3D RHD solar model atmospheres computed with different codes (M3DIS, STAGGER, and CO^{5}BOLD), with the corresponding profile of the standard 1D hydrostatic MARCS model atmosphere. The latter is characterized by systematically higher gas pressures and densities compared to the 3D models, with differences exceeding 10 % in the inner atmospheric layers at $\log \tau_{\rm ross} \gtrsim 0$.

In Fig. 4.16, we show the 3D synthetic profiles of remaining Fe I lines from Table 4.4 in comparison with the observed solar flux data. See Fig. 4.13 for more details.

[6] nlte.mpia.de

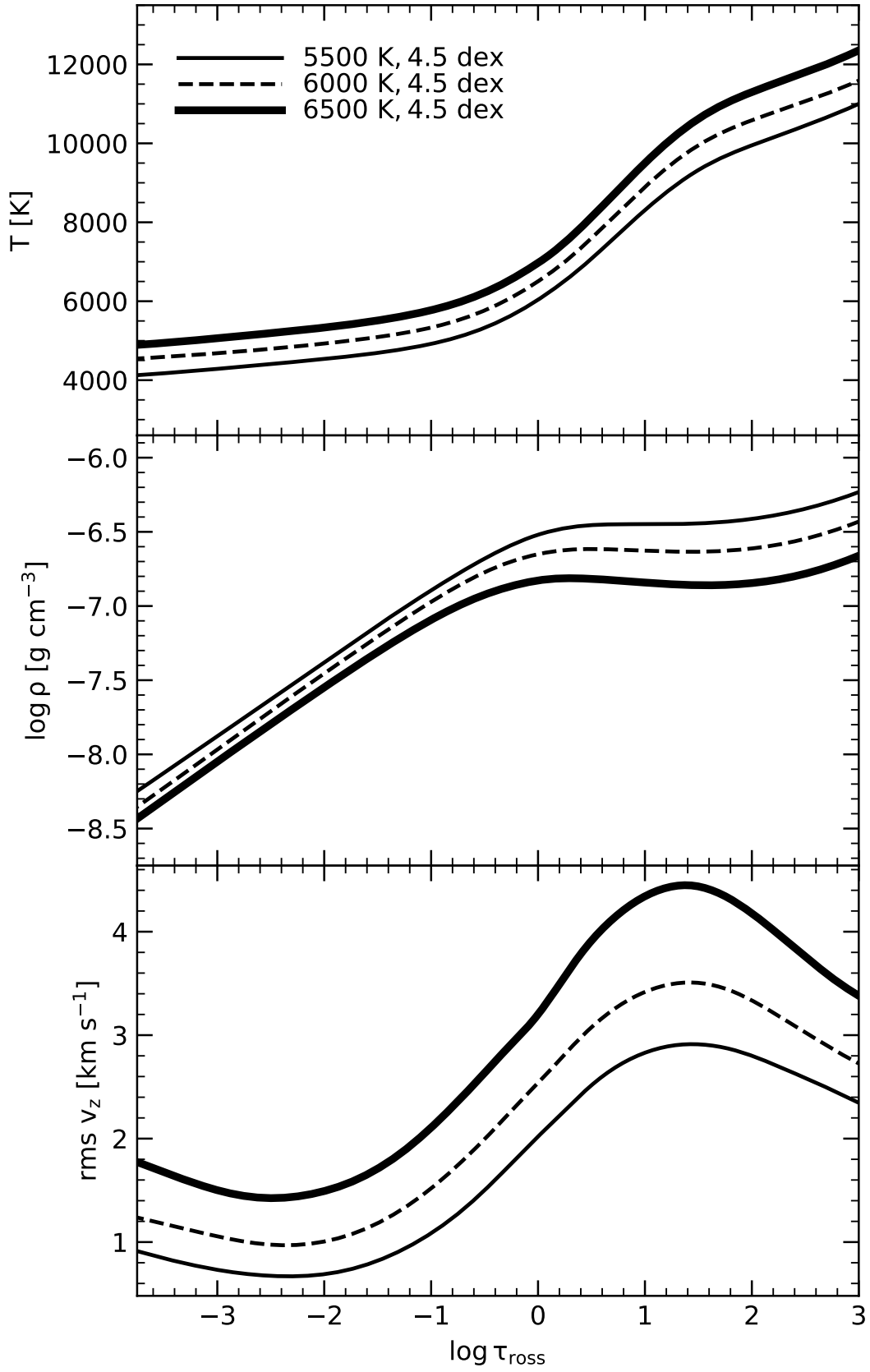

Figure 4.14: Average temperature and density profiles for three selected M3DIS models of solar-like stars.

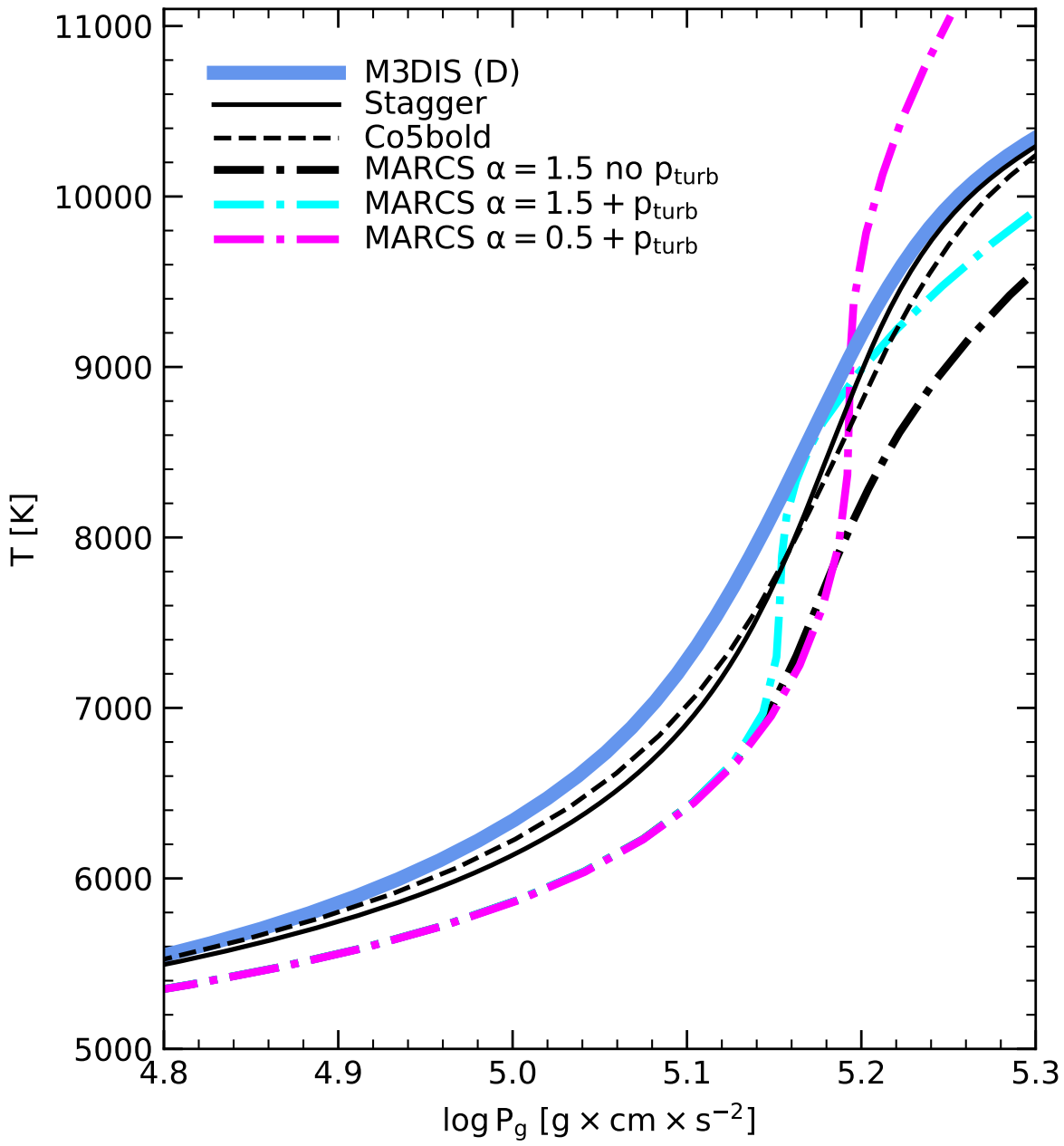

Figure 4.15: Comparison of average temperature and gas pressure profiles for M3DIS, STAGGER, CO^{5}BOLD, and MARCS solar model atmospheres. We also show different versions of the MARCS models, computed with and without turbulent pressure, and with different mixing length parameters α.

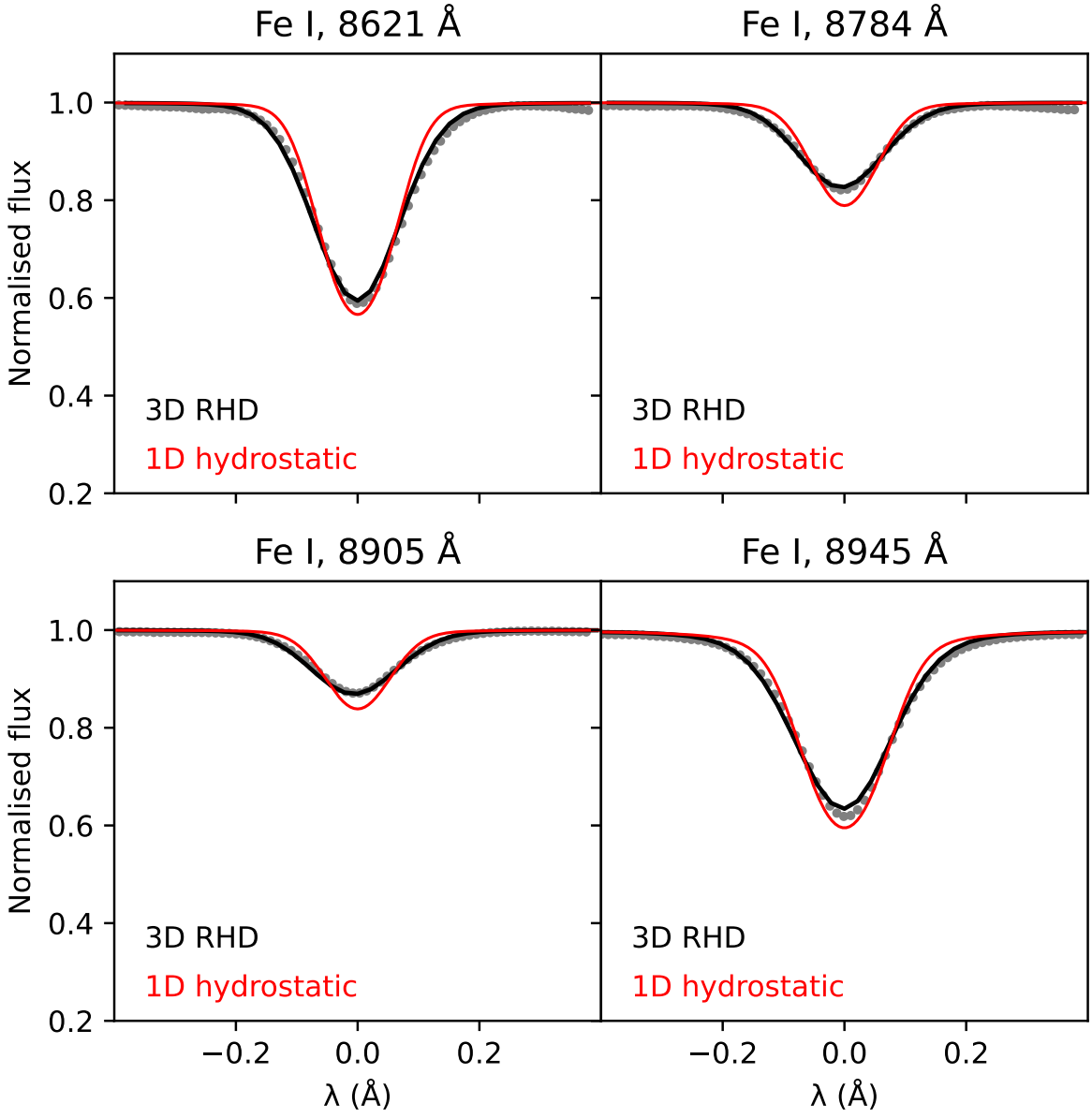

Figure 4.16: As Fig. 4.13, for the remaining Fe I lines from table 4.4.

5 M3DIS – 3D RHD Stellar Atmospheres: Carbon-enhanced Metal-poor Stars

There are countless applications of the newly created `DISPATCH` infrastructure, which was introduced and tested in Sec. 4. One major advantage is the consistency between microphysics included in EoS and opacities, which are used to determine the radiative heating during the simulation of the atmosphere and post-processing spectrum synthesis. The ability to generate monochromatic opacity tables using `MULTI3D@DISPATCH` furthermore makes the computation of chemically peculiar atmosphere models, which do not align with the common Galactic abundance trend, straightforward. One of the most interesting groups of stars in this context are CEMP stars, as they appear to contain highly non-solar C abundance fractions, while being generally very metal-poor at the same time.

Because C – and specifically its most abundant molecules CH, CN, and CO – contribute to the overall line opacity in the upper layers of FGK-type stellar atmospheres (e.g. Gustafsson et al. 1975; Alexander & Ferguson 1994), the question arises to what extent the atmospheric temperature and density stratification of CEMP stars is influenced by their highly non-standard composition. It was furthermore noted already by Asplund et al. (1999) that especially in metal-poor stars the atmospheric structure predicted by 1D HE models becomes increasingly un-physical due to the oversimplified energy transport, which means that large 3D − 1D departures are expected for abundances of specific elements.

It is unfortunate that C abundance measurements of Galactic stars mostly rely on the 1D HE synthesis of the CH G-band, where the number density of CH molecules is determined from the molecular equilibrium, which itself is highly sensitive to the temperature of the atmosphere (Eq. 2.43). Since it is explicitly the amount of [C/Fe] that is the responsible for the classification of CEMP stars, it becomes clear that – depending on the magnitude of the 3D − 1D effect – there may be a significant impact on the Galactic CEMP distribution and hence the understanding of early Galaxy formation and evolution. In total, this means that classical C abundance measurements of CEMP stars require urgent revision.

The content of the remaining chapter has been submitted as Eitner et al. (2025, subm.) under the title ***"M3DIS – A grid of 3D radiation-hydrodynamics stellar atmosphere models for stellar surveys. II. Carbon-enhanced metal-poor stars"****. The paper is currently still under review. Minor modifications to format and text have been made in the context of this thesis. As the work presented here is a collaborative effort, I use the plural pronoun "we" instead of "I".*

- ***Title:*** *M3DIS – A grid of 3D radiation-hydrodynamics stellar atmosphere models for stellar surveys. II. Carbon-enhanced metal-poor stars*
- ***Authors:*** *Eitner, P. ; Bergemann M. ; Hoppe, R. ; Storm, N. ; Lipatova, V. ; Glover, S. C. O. ; Klessen, R. S. ; Nordlund, Å. ; Popovas, A.*
- ***Submission to:*** *Astronomy & Astrophysics*
- ***Submission Date:*** *May 2025*

The main scientific work was conducted by me, with invaluable contribution of the co-authors. All model atmospheres, as well as spectra, and the corresponding analyses were done by me. In the process of the paper, significant updates were made to the radiative transfer solver and the overall code stability, which were implemented in close collaboration with R. Hoppe, Å. Nordlund, and A. Popovas. The paper greatly profited from the expertise of R. Klessen on understanding the first stars.

5.1 Abstract

Understanding the origin and evolution of CEMP stars is key to tracing the early chemical enrichment of the Galaxy. In this work, we investigate how physically realistic 3D RHD, carbon-enhanced model atmospheres affect the inferred carbon abundances in CEMP stars, and assess the implications for their classification and for GCE. We pay particular attention to the systematic biases introduced by traditional 1D HE models.

We use the `M3DIS` code to compute 3D RHD model atmospheres for MS and sub-giant stars spanning a wide range of metallicities and carbon enhancements. Synthetic spectra of the CH G-band are calculated using full 3D radiative transfer, and compared to spectra from classical 1D HE `MARCS` models. We derive abundance corrections and apply them to a large literature sample of metal-poor stars from the SAGA database to quantify systematic effects on the carbon abundance distribution and CEMP classification.

Our new 3D CEMP models predict significantly cooler upper atmospheric layers than those present in 1D HE models, resulting in stronger CH absorption and lower inferred carbon abundances by up to -0.9 dex at the lowest metallicities. Carbon enhancement in the atmosphere itself increases molecular opacities and leads to radiative re-heating, which partly offsets the adiabatic cooling in 3D models and reduces the magnitude of 3D $-$ 1D abun-

dance corrections. Applying these corrections lowers the CEMP fraction by up to 20 % below [Fe/H] = −3, and furthermore alters the relative contribution of CEMP sub-classes. In particular, the fraction of CEMP-no stars increases while the number of stars classified as CEMP-r/s decreases, owing to the downward revision of absolute carbon abundances. These changes bring the Galactic carbon abundance distribution into better agreement with GCE models that assume a contribution from faint supernovae of 20 %. Physically realistic model atmospheres are thus essential for reliable reconstruction of the early chemical enrichment history of the Galaxy.

5.2 Introduction

CEMP stars are of major interest in modern astrophysics. Chemical abundances measured in spectra of these stars are relevant for understanding the properties of type II supernovae events (SN II) in the early Galaxy, nucleosynthesis, formation and evolution of binary stars, the stellar initial mass function, the metallicity distribution function of the Galactic halo, and the production sites of neutron-capture elements (Beers & Christlieb 2005; Aoki et al. 2006; Hansen et al. 2018).

It is common to distinguish CEMP stars by categories based on the presence of elements synthesized in the slow- or rapid neutron-capture processes (s- and r-process, Hirschi et al. 2006). The categories include stars with enhancements in either of the two channels exclusively (CEMP-s and CEMP-r, respectively), both (CEMP-r/s), or none (CEMP-no), and each category is thought to probe a different formation environment (e.g. Masseron et al. 2010). CEMP-s stars are viewed as products of enrichment by a post-AGB companion in a binary system (McClure & Woodsworth 1990; Lucatello et al. 2005; Starkenburg et al. 2013; Hansen et al. 2016b), although some CEMP-s stars appear to be single, which might indicate that they formed from the ejecta of a massive, fast rotating source star with a late mixing event (Choplin 2017). In contrast, CEMP-r stars show strong enhancement of r-process elements, such as Eu (Sneden et al. 2003), and are thought to form from matter that became chemically polluted by either a CC supernova (electron-capture or magnetorotating), NS–NS, or NS–BH mergers (Frebel & Norris 2015; Côté et al. 2017; Hansen et al. 2018; Kobayashi et al. 2020b).

The formation history of CEMP-r/s and CEMP-no stars is less clear. Regarding CEMP-r/s, there is evidence of a contribution from the r-process (Aoki et al. 2006) from an SN II. Alternative explanations include enrichment of the s process by a thermally pulsating AGB companion (Masseron et al. 2006) and neutrino-driven winds from the accretion-induced collapse of an O-Ne-Mg WD (Cohen et al. 2003; Jonsell et al. 2006; Kobayashi et al. 2020b). CEMP-no stars are among the most metal-poor stars observed (Christlieb et al. 2002; Hansen et al. 2016a) and show no significant enrichment in the r- or s-process (Spite et al. 2013).

Table 5.1: Summary of M3DIS radiation-hydrodynamics code features.

Feature	Description
Code Name	M3DIS – **M**odels in **3**D @**DIS**PATCH (Eitner et al. 2024; Nordlund et al. 2018)
Dimensionality	Full 3D
Physics Included	Radiation and convection
Applications	FGKM stars; any $\log g$; any metallicity
Opacity Sources	92 elements; electron and Rayleigh scattering; molecules
Boundary Conditions	**Top:** Open, in-/outflows, exponential ρ drop, constant e/m; **Bottom:** Open, outflows free, inflows maintain entropy (via ghost zones)
Time Integration	Explicit; local CFL time step from gas velocity, radiative heating and radiative diffusion
Grid Type	Eulerian; uniform in all directions
Hydrodynamics Solver	HLLC Riemann solver (Fromang et al. 2006)
Radiative Transfer	Short-characteristics; conservative on staggered mesh; 8 frequency bins; 4 ϕ, 2 μ angles, plus disk-center rays

This can be interpreted in the framework of different scenarios, including nucleosynthesis in faint low-energy SNe (Umeda et al. 2005; Tominaga et al. 2007; Nomoto et al. 2013; Kobayashi et al. 2020b), hypernovae (Heger & Woosley 2002; Limongi et al. 2003; Nomoto et al. 2013), nucleosynthesis in C-rich winds of rotating massive stars (Hirschi et al. 2006; Meynet et al. 2006), and early-AGB stars (Masseron et al. 2010, and references therein).

The analysis of C abundances in the atmospheres of CEMP stars is primarily based on the spectroscopic diagnostic of the so-called G-band (e.g. Placco et al. 2016; Placco & Beers 2016; François et al. 2018; Norris & Yong 2019). The G-band represents the fundamental A-X transition of the CH molecule (Masseron et al. 2014; Popa et al. 2023) and is therefore highly sensitive to the abundance of C and the temperature gradient in stellar atmospheres. The G-band has been extensively studied using 1D LTE models (e.g. Lai et al. 2007; Roederer et al. 2014; Jacobson et al. 2015; Lee et al. 2013, see also Suda et al. 2008, 2017 and references therein), but recent analyses also explored the formation of the G-band in 3D RHD model atmospheres of metal-poor dwarfs and red giants (e.g. Collet et al. 2007; Bonifacio et al. 2013; Gallagher et al. 2016, 2017; Collet et al. 2018).

In this work, we investigate the effect of carbon enhancement on the structure of stellar atmospheres in realistic 3D RHD simulations introduced in our previous work (Eitner et al. 2024). We further study and quantify the impact of 3D convection on the diagnostics of C abundances from stellar spectra. We then analyze the results with respect to CEMP statistics in the Galaxy and discuss implications for the formation and evolution of CEMP stars.

This section is organized as follows. In Sec. 5.3, we briefly introduce the stellar observations used in this work, followed by a description of the M3DIS code and model parameters. In Sec. 5.4, we present our new 3D RHD model atmosphere calculations, including a comparison with 1D HE MARCS models, the spectrum synthesis of the CH G-band, and the analysis of CEMP abundances in 3D, along with a discussion of their implications for Galactic CEMP populations. Finally, in Sec. 5.5, we summarize our findings and discuss their implications for the study of CEMP stars and GCE.

5.3 Methods

5.3.1 Stellar Observations

In this work, we rely on stellar C abundances provided in the *Stellar Abundances for Galactic Archaeology* database[1] (SAGA, Suda et al. 2008, 2011, 2017). SAGA is a comprehensive source of abundances and stellar parameters for stars in the Milky Way and its satellites, with a particular focus on metal-poor stars. The data is based on published, peer-reviewed sources and has a particular focus on the homogeneity of the measurements, such that the abundances are derived from 1D LTE synthetic spectra (Suda et al. 2008).

This study concentrates on MS and sub-giant stars. We thus exclude stars with surface gravity $\log g < 2.7$ from the data set. We gather parameters for each star, including the effective temperature $T_{\rm eff}$, $\log g$, along with [Fe/H] and [C/Fe]. Given the limited data on Eu and Ba abundances, we do not demand measurements for our entire sample, as this would greatly reduce the number of targets. This makes it difficult to differentiate between CEMP-no, CEMP-s, and CEMP-r/s stars. However, according to Yoon et al. (2018), a classification into Groups I, II, and III based solely on [C/Fe] and [Fe/H] is feasible, enabling a rough differentiation of CEMP-no stars from those with increased n-capture elements.

In total, our sample contains 3 192 stars with sub-solar metallicities, [Fe/H] < 0, out of which 1 745 have a measured [C/Fe] abundance, with 541 exceeding [C/Fe] ≥ 0.7 and hence can be classified as CEMP (Yoon et al. 2018). References to individual datasets along with stellar parameters and abundances (original and 3D − corrected values) are provided as supplementary material via CDS.

5.3.2 Model Atmospheres

In this work, we rely on the M3DIS (Models in 3D@DISPATCH) code within the DISPATCH framework (Nordlund et al. 2018) for generating 3D RHD stellar atmospheres, which has been introduced and extensively tested by Eitner et al. (2024) (Sec. 4). In short: M3DISsolves

[1] http://sagadatabase.jp/

Table 5.2: Stellar parameters and carbon abundances of the 3D RHD M3DIS CEMP model atmospheres explored in this work. Here, N_i corresponds to the number of grid points in dimension i. In the last column, we quote the horizontal extend of the corresponding model atmosphere. Note that the vertical extend is half that number. For every CEMP model below we generated a scaled-solar ([C/Fe] = 0) counterpart. For each model, convergence was achieved in less than 3500 CPU-h.

T_{eff}	log(g)	[Fe/H]	[C/Fe]	A(C)	Resolution	Size
K	dex	dex	dex	dex	$N_x \times N_y \times N_z$	Mm
5750	4.5	-6	4	6.56	$240^2 \times 120$	5.2
5750	4.5	-5	3	6.56	$240^2 \times 120$	5.2
5750	4.5	-4	2	6.56	$240^2 \times 120$	5.1
5750	4.5	-3	1	6.56	$240^2 \times 120$	5.2
5750	4.5	-2	1	7.56	$240^2 \times 120$	5.4
5250	3.0	-6	4	6.56	$240^2 \times 120$	140
5250	3.0	-5	3	6.56	$240^2 \times 120$	140
5250	3.0	-4	2	6.56	$240^2 \times 120$	140
5250	3.0	-3	1	6.56	$240^2 \times 120$	150
5250	3.0	-2	1	7.56	$240^2 \times 120$	160

the HD equations together with the RT equation to calculate the radiative cooling, which in turn contributes to the energy balance of the atmosphere. The code relies on a HLLC Riemann solver for advancing the simulation in time (Fromang et al. 2006), and on short-characteristics radiative transfer in two μ (polar) and four ϕ (azimuthal) angles, plus upward and downward vertical rays, assembled in a Gauss-Radau quadrature. The main features of the models can be found in Table 5.1.

The RT is solved in the multi-group approximation (Nordlund 1982; Ludwig et al. 1990), such that monochromatic opacities and source functions are collected into eight bins based on wavelength and formation height within the respective atmosphere. The selection of opacity bin edges is done automatically using a k-means clustering approach. Monochromatic opacities are calculated together with internal energy and gas pressure, i.e. the EoS, on a grid of 151×151 $\log \rho - \log T$ points using the updated version of MULTI3D (Leenaarts & Carlsson 2009), also within the DISPATCH framework. Scattering due to free electrons and Rayleigh scattering (H I, H_2, He I) is treated as true absorption in the optically-thick part of the opacity table, and it is not excluded in the optically-thin regime. This is a common approach in 1D (Gerber et al. 2023) and 3D (Collet et al. 2011) calculations. Opacities and source functions are computed under the assumption of LTE in the context of computing surface cooling. For more details, see the description by Eitner et al. (2024) and Appendix 5.6.

In addition to its computation speed, the main advantages of M3DISare the highly flexible and consistent opacities and EoS, which make the simulation of stars with a non-solar chemical composition relatively straightforward. To investigate the impact of carbon abun-

dance on the atmospheric structure itself, we first compute scaled-solar [C/Fe] composition (relative to Magg et al. 2022b) opacity and EoS tables at [Fe/H] = −6, −5, −4, −3, and −2.

Second, we calculate carbon-enhanced opacity tables such that at [Fe/H] ≤ −3 we additionally have C-enhanced atmospheres with the same constant A(C) = 6.56, while at [Fe/H] = −2 we keep the C-enhancement fixed at [C/Fe] = 1, A(C) = 7.56 (in agreement with the Galactic CEMP abundance trend, e.g. as reported by Yoon et al. 2016, Fig. 1).

Because the computation of 3D RHD stellar atmosphere models is computationally expensive, previous studies relied mainly on a single representative set of stellar parameters (e.g. Gallagher et al. 2017; Collet et al. 2018). To minimize uncertainties originating in the variety of stellar parameters in the data sample, we create solar-like MS models at $T_{\rm eff} = 5750\,$K, $\log g = 4.5$, and cooler sub-giants at $T_{\rm eff} = 5250\,$K, $\log g = 3.0$ for all chemical compositions. The chosen parameters represent a compromise between spanning the full range of stellar parameters and accurately reflecting the bulk of the distribution.

To ensure a satisfactory resolution, the number of grid points has been set to 240×240×120. The physical size of the simulation domain has been limited between the average Rosseland optical depth of $\log \tau_{\rm ross} = -6$ and +6.5, which sets the geometric domain of the box. This is done to ensure that the models are deep enough to recover the adiabaticity at the bottom of the atmosphere and the relevant line-formation region of the CH G-band at the top. The resulting geometric domain ranges from approximately 2.5 Mm for the MS 3D models (vertically) to 80 Mm for the sub-giant models. Horizontally, the models are twice as extended as vertically. A summary of the model parameters can be found in Tab. 5.2.

For comparison, we use the classical 1D HE, scaled-solar, LTE model atmospheres from the `MARCS` grid (Gustafsson et al. 2008). To evaluate the effect of C-enhancement also in 1D hydrostatic models, we furthermore obtained a carbon-enhanced `MARCS` model with stellar parameters $T_{\rm eff} = 5750\,$K, $\log g = 4.5$, [Fe/H] = −5, [C/Fe] = +3.0 that we can include in the analysis (B. Plez, priv. conv.).

5.3.3 Spectrum Synthesis

Synthetic spectra in 1D and 3D are computed using the updated version of `MULTI3D` code (we refer to Eitner et al. 2024 and Sec. 4 for details). The code includes extensive tables of bound-free and free-free radiative cross-sections for 92 chemical elements and partition functions of Irwin (1981). The occupation formalism is adopted for H I, following the HBOP routine by Barklem & Piskunov (2003). The same code is used for calculations with `MARCS` and with `M3DIS` model atmospheres, to ensure consistency between results.

We synthesize the CH G-band in LTE between 4297 and 4303 Å with a wavelength spacing of 0.001 Å. In 3D, we down-sample the full cube horizontally to a resolution of 20×20 points

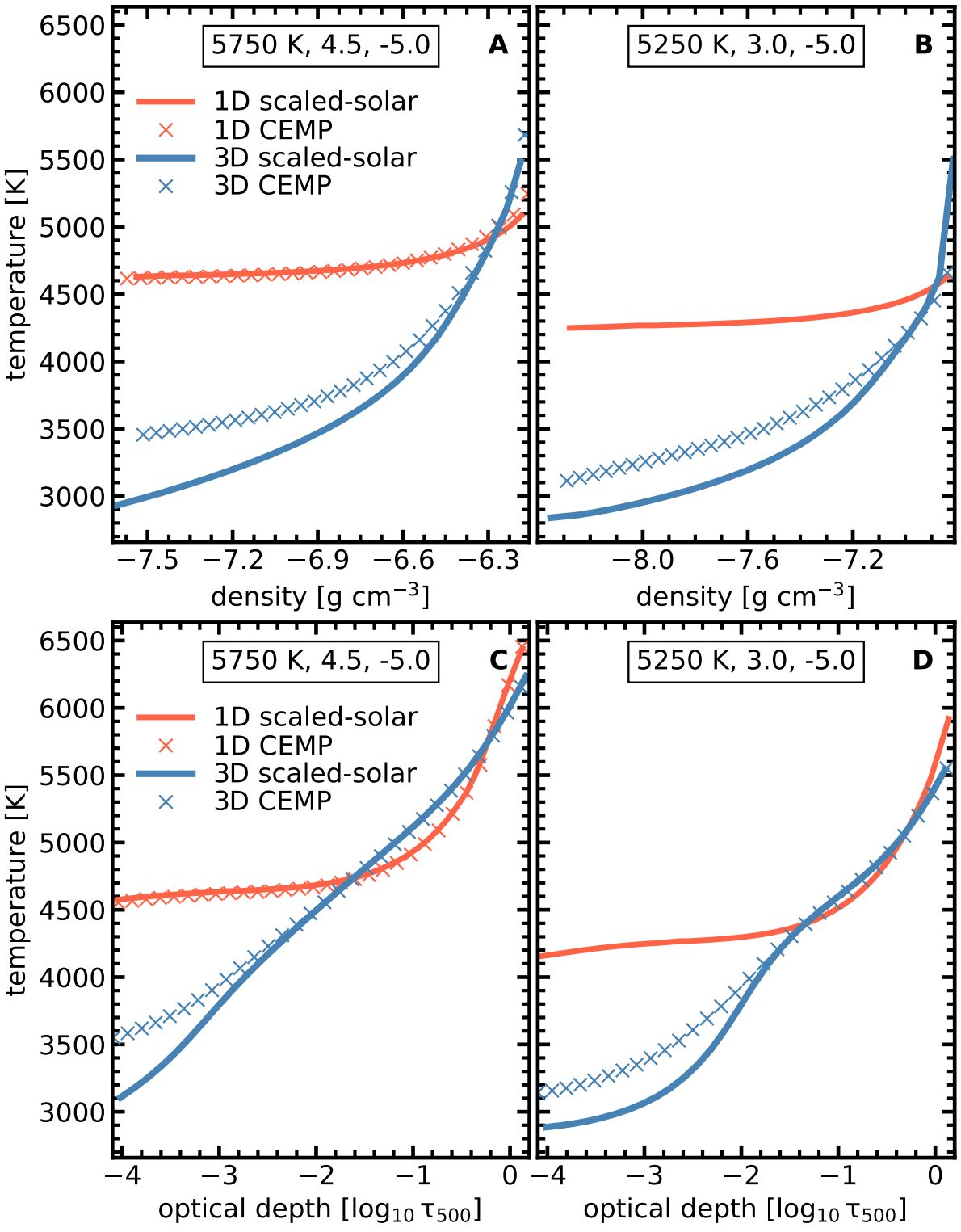

Figure 5.1: Comparison of the mean temperature stratification between 1D scaled-solar MARCS (red solid lines), 3D scaled-solar (blue solid lines), and 3D CEMP (blue crosses) models against mean density (top) and optical depth at 500 nm (bottom). Left: MS model. Right: sub-giant model. For the MS model in the left panels we furthermore include a CEMP MARCS model (provided by B. Plez, priv. conv., shown with red crosses)

.

using linear interpolation. This horizontal down-sampling is sufficient to provide reliable profiles of spectral lines with abundance errors within ~ 0.01 dex compared to simulations with a much higher horizontal resolution (Bergemann et al. 2019, 2021; Rodríguez Díaz et al. 2024; Eitner et al. 2024, and arguments outlined in Sec. 2.1.5). The vertical resolution is not down-sampled in the spectrum synthesis, but rather up-sampled to an adaptive grid in the optically thin layers to better resolve regions with large opacity gradients. For more information, see Hoppe et al. (in prep.). The final, re-sampled models have a resolution of $30 \times 30 \times 180$ points.

5.4 Results

5.4.1 3D Model Atmospheres

We begin with a qualitative discussion of the properties of 3D scaled-solar and 3D carbon-enhanced RHD model atmospheres in comparison to their 1D HE counterparts.

3D scaled-solar vs. 1D HE

First we compare the scaled-solar 3D RHD and 1D HE model atmospheres, computed using identical stellar parameters ($T_{\rm eff}$, $\log g$, metallicity). For simplicity and to highlight the main physical differences, we discuss the average temperature-density ($T-\rho$) profiles in this section, but we emphasize that all subsequent spectrum synthesis calculations are performed in full 3D using 3D cubes. In Fig. 5.1 we show the $T-\rho$ (top) and $T-\tau$ (bottom) structures, where τ is the optical depth of the MS (left, panels A and C) and of the sub-giant (right, panels B and D). As a representative case, we show both models at [Fe/H] $= -5$ to investigate their properties and illustrate the typical behavior observed across the full set of models. All panels illustrate the respective atmosphere between -4 and 0 in $\log \tau_{500}$.

Comparing the 3D structures with their 1D counterparts, the dominant differences are apparent towards the upper layers of the atmospheres. For the MS model (Fig. 5.1, panels A and C), the mean 3D temperature structure starts to deviate from that of the 1D HE model around optical depth $\log \tau_{500} \sim -2$. The 3D$-$1D difference reaches values of $\sim -1\,500$ K at $\log \tau_{500} = -4$. In those layers, the 3D RHD model is significantly and systematically cooler than the 1D MARCS model, which is well-established and was extensively discussed in earlier work on 3D models of very metal-poor (VMP) MS and red giant stars (Gallagher et al. 2016, 2017; Collet et al. 2018).

This difference is due to the fundamental property of convection, a process that is inherent to 3D RHD models, but is missing or parameterized by the MLT (Gustafsson et al. 2008) in 1D HE models. In metal-poor stars, the atmospheric structure is dominated by adiabatic cooling of rising, and hence expanding, fluid parcels of the gas. This is in stark contrast to stars with

solar-like metallicity; in such conditions, the high metallicity leads to significant radiative heating (Stein & Nordlund 1998), which counteracts the adiabatic cooling effect and implies that the average 3D structure remains nearly in radiative equilibrium (e.g. Nordlund et al. 2009; Freytag et al. 2012; Magic et al. 2013a,b).

A very similar behavior can be seen in the structure of the 3D model of the sub-giant star (Fig. 5.1, panels B and D). The 3D RHD model is over $\sim -1\,000$ K cooler compared to its MARCS counterpart in the layers with $\log \tau_{500} \lesssim -3$. Although the effect is very large, it is slightly less compared to that of the MS 3D model in the uppermost layers ($\log \tau_{500} \sim -4$). One would naively expect that a sub-giant 3D model, due to lower pressure, would show large deviations from the 1D HE model, compared to the MS case. However, there is another interesting effect. The cooler overall structure of this model favors the formation of different molecules, including CH, OH, and CO. Due to radiative re-heating, the temperature balance of the 3D model hence is slightly closer to that of 1D HE MARCS model. We emphasize that this difference is not a direct consequence of the C-enhancement – it is also present in models with scaled-solar composition – but of the overall absence of metal absorbers in the energy budget of the atmosphere.

3D CEMP vs. 3D scaled-solar

Comparing C-enhanced and scaled-solar 3D models directly (Fig. 5.1, blue crosses and blue, solid lines, respectively), we find that for the VMP MS star (panels A and C), the effect is modest compared to the 3D − 1D differences described above. At an optical depth of $\log \tau_{500} > -3$, there is no significant difference, while toward the upper limit of the atmosphere, the mean temperature of the CEMP model is ~ 400 K hotter at $\log \tau_{500} \sim -4$. In the sub-giant model (panels B and D), the same effect of C-enhancement is already noticeable at $\log \tau_{500} \sim -2$, with temperature differences of $\sim 200 - 300$ K throughout the entire optically thin part of the atmosphere. Overall, the effect on the main sequence model is ~ 100 K larger around $\log \tau_{500} \lesssim -4$ than on the sub-giant. However, towards deeper layers, $\log \tau_{500} \gtrsim -3$, the scaled-solar sub-giant remains consistently cooler than its CEMP counterpart, whereas the differences between the MS models are already negligible.

The reason for this additional heating in the CEMP models is found in the increased abundance of C, which implies increased molecular abundances of CH, CO, and CN, a higher molecular line opacity, and consequently more radiative heating of the upper atmospheric layers. Because O – as well as N – remain at their scaled-solar values, specifically the CH G-band is one of the main contributors to the line opacity beyond $\log \tau_{500} \sim -2$. In cooler atmospheres with very low [Fe/H], this effect is most noticeable. First, this is because, already in the scaled-solar approximation, C is an order of magnitude more abundant than Fe. Furthermore, the number densities of CH are higher in cooler systems, as chemical equilibrium favors a higher CH/C for lower T values.

The re-heating of the upper atmospheric layers induced by the C-enhancement hence produces the opposite of the 3D − 1D effect described in Sec. 5.4.1. We furthermore note that there is no such effect in 1D HE MARCS models. To highlight this, we include one example CEMP MARCS model with the same stellar parameters in panels A and C.

Due to its lower $\log g$, the sub-giant model overall has a lower density at the same temperature as the main sequence model. A consequence of this is that the formation height of spectral lines generally shifts towards deeper layers in terms of optical depth. This explains the larger departures (3D CEMP−scaled-solar models) at optical depth $\log \tau_{500} \gtrsim -3$ among the sub-giant models compared to the main sequence models (comparing the difference between blue lines and blue crosses in panel C with panel D) through the shift of the molecular line heating contribution to deeper atmospheric layers. It may be noted that decreasing the overall temperature causes the opposite effect, as the increase in molecular number densities increases the opacity and hence generally shifts the contribution function to a lower optical depth.

In 3D, there is an additional, interesting complexity; Increasing the effective temperature raises the overall temperature in the upper layers. However, the presence of a considerable temperature gradient in 3D results in layers just above the molecular-forming zones in cooler models now being more favorable to molecule formation, as they remain sufficiently cool. Consequently, in 3D, the molecular number densities in optically thinner layers increase, which moves the formation height toward the stellar surface, regardless of the fact that molecular lines overall weaken because of the higher overall temperature.

3D CEMP vs. 1D HE

Combining the results from Sec. 5.4.1 and Sec. 5.4.1, we now compare our M3DIS 3D CEMP model atmospheres with 1D HE scaled-solar MARCS models. The difference between these two model types is particularly important, as many studies rely on 1D scaled-solar MARCS models for spectral synthesis and abundance analysis. This raises the question of whether this simplifying assumption introduces systematic effects in the derived abundances.

To find the answer, we first show the full 3D temperature structure of both selected 3D CEMP models at $[\mathrm{Fe/H}] = -5$ in Fig. 5.2. For both models, MS (left-hand side) and sub-giant (right-hand side), we used the C-enhancement of $[\mathrm{C/Fe}] = +3$. The 1D MARCS models are shown with red lines. The full 3D structure is indicated by the blue shading. We furthermore show in the inset a horizontal slice of the same atmospheres, interpolated to the optical surface at $\log \tau_{\mathrm{ross}} = 0$. We note the very different scales and granular size between the MS (left panel) and the sub-giant (right panel) models. The model of the MS star is, because of much larger gravity, about 20 times smaller compared to that of a sub-giant simulation, the latter exceeding 100 Mm in size.

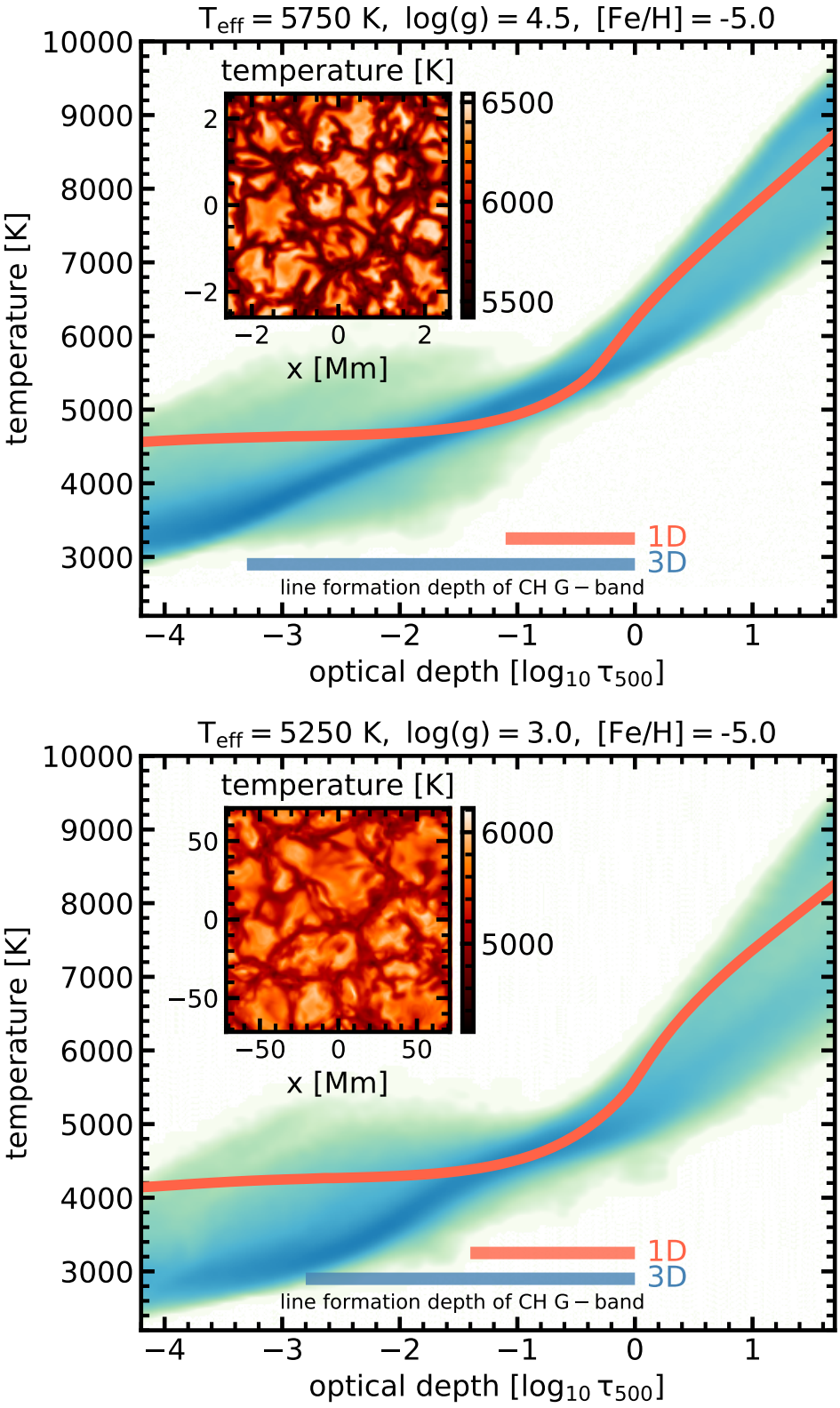

Figure 5.2: Comparison of mean temperature stratification between the DISPATCH 3D CEMP model and the 1D MARCS model on the optical depth scale. Top: $T_{\rm eff}$ = 5750 K, $\log g$ = 4.5, Bottom: $T_{\rm eff}$ = 5250 K, $\log g$ = 3.0. Horizontal bars at the bottom correspond to the approximate formation region of the G-band in 1D and 3D.

As described in the previous sections, the difference between 3D CEMP and 1D MARCS models is most striking in the optically thin layers of the atmosphere, where 3D CEMP models are still significantly cooler, even though the difference is reduced by the C-enhancement-induced re-heating. Both models converge towards the optical surface, the agreement is best in proximity to $\tau = 2/3$, indicating a very similar effective temperature of the 1D and 3D models.

Toward the bottom of Fig. 5.2 we furthermore include horizontal bars, indicating the formation region of the G-band. For this, we select a representative CH line, compute the contribution function in its core for each model atmosphere, and use the location of its peak as a proxy for the optical depth at which the G-band typically forms. We draw the horizontal lines until $\tau_{\mathrm{ross}} = 1$, which corresponds to the formation of weaker features, line wings, and the continuum. We emphasize that the computation of the G-band formation region does not affect the results or conclusions of this study; it is intended solely as a useful reference to aid in the analysis of model differences and to support their physical interpretation.

In Fig. 5.2, it may be noted that the G-band forms slightly deeper within the atmosphere of the sub-giant as compared to the MS model, which is a consequence of the significantly lower surface gravity and hence overall lower density. This shift happens despite the lower effective temperature of the 3D sub-giant model. In the 1D model the upper layers are strongly dominated by radiative equilibrium – and hence the effective temperature – which means the drop in temperature between the MS and sub-giant models is more significant, the opacity rises and the formation region of the G-band shifts in the opposite direction.

The evolution of the differences between the 3D CEMP and 1D MARCS models with metallicity can be investigated in Fig. 5.3. For clarity, we refrain from showing the differences between the full profiles as a function of optical depth for each metallicity. Instead, we present a representative 3D–1D difference for each metallicity, calculated from the atmospheric regions most relevant to the formation of the G-band. Accordingly, the data shown in this figure is evaluated at the G-band formation height in each respective atmosphere, as described in the previous paragraph.

In panel A of Fig. 5.3 the relative temperature difference is shown for the sub-giant models (red, solid lines) and for the MS models (blue, dashed lines). We find that 3D CEMP models are on average between 20 % and 25 % cooler than 1D HE models. At metallicities −6, −5, and −4, there is no significant variation in the 3D–1D difference. At [Fe/H] = −3 the differences begin to decrease and reach values around 5% at metallicity −2. In addition to forming in cooler parts of the atmosphere, the G-band also forms in regions of lower density (panel B), with $\log \rho_{\mathrm{3D}}/\rho_{\mathrm{1D}}$ between −0.6 dex in [Fe/H] = −6 and −0.3 dex at [Fe/H] = −2. Note that this is true despite the fact that metal-poor 1D HE models generally are less dense at the same optical depth (due to the hotter temperatures), and the data in panel B mostly

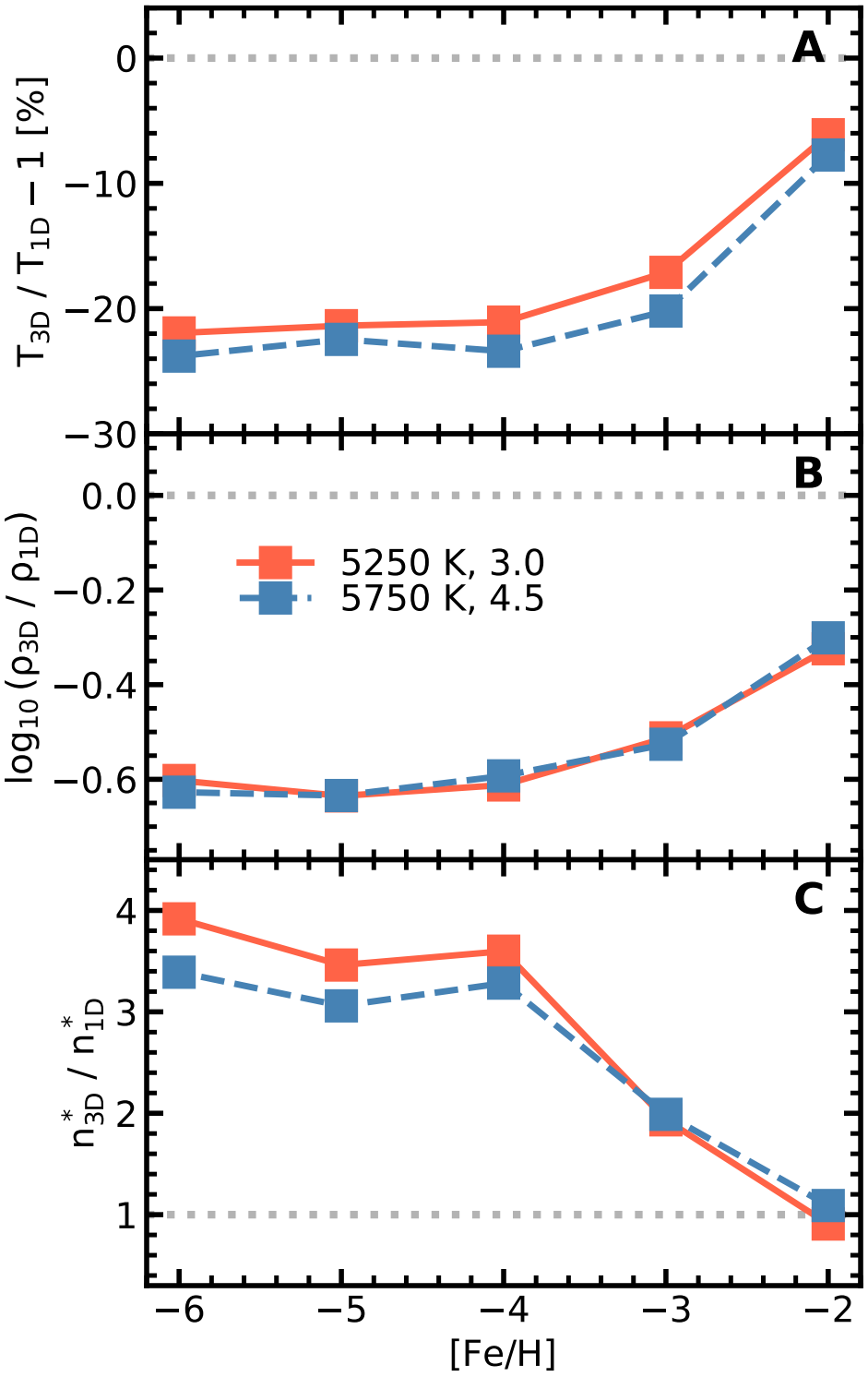

Figure 5.3: Difference between 3D CEMP and 1D MARCS models as a function of metallicity. Top: Relative temperature difference (percent). Middle: Logarithmic density differences (dex). Bottom: CH/H number density fraction, where $n^* = n_{\rm CH}/n_{\rm H}$ is the CH number density relative to the hydrogen number density. Blue, dashed lines correspond to $T_{eff} = 5750\,\mathrm{K}$, $\log g = 4.5$ models, red, solid curves to $T_{\rm eff} = 5250\,\mathrm{K}$, $\log g = 3.0$. The differences in each figure are computed at the representative formation height of the strong lines in the G-band. See Sec. 5.4.2 for more information.

reflects the differences in formation height through the exponential growth of density with depth.

Additionally, it may be noted that the MS models show 3D CEMP effects similar to – if not even slightly larger than – the sub-giant models, especially when considering the temperature differences (Fig. 5.3, panel A). However, at this stage, it is important to consider that the molecular equilibrium, which ultimately determines the CH number densities and hence directly influences the strength of the spectral lines in the G-band, is not a linear function of temperature and density, but rather exhibits a temperature and density dependence as dictated by the Saha equation (e.g. Carson 1992)

$$\frac{n_{\mathrm{C}} n_{\mathrm{H}}}{n_{\mathrm{CH}}} \propto \frac{z_{\mathrm{C}} z_{\mathrm{H}}}{z_{\mathrm{CH}}}\, T^{3/2}\, e^{\frac{-D_{\mathrm{CH}}}{k_{\mathrm{B}} T}}\,, \tag{5.1}$$

where n_{x} is the number density of species x, z_{x} the partition functions and D_{CH} the dissociation energy of the CH molecule, which is set to 3.47 eV (Popa et al. 2023; Storm et al. 2025, and references therein). To highlight this non-linear dependence, we include panel C showing the fraction of CH/H number densities $n^*_{\mathrm{3D}}/n^*_{\mathrm{1D}}$ – where $n^* = n_{\mathrm{CH}}/n_{\mathrm{H}}$ – in the same formation region as panels A and B. Here it becomes obvious that the number density of CH/H molecules in the sub-giants deviate by a factor of ~ 1.2 more between 3D and 1D than what is found in MS models. So, despite showing a slightly smaller 3D effect in temperature and density, the 3D effect is more prominent in the CH/H number density of sub-giants, which will ultimately be reflected in the G-band and [C/Fe] abundance corrections (see Sec. 5.5).

Overall, it may be noticed that with increasing [Fe/H] the differences in the structure between 3D CEMP and 1D HE models decrease noticeably. The reason is that with increasing metal content, radiative heating starts to dominate the overall energy budget of the photosphere. The consequence is that adiabatic cooling becomes less dominant in the outer layers, which ultimately closes the gap between the average 3D structure and 1D HE MARCS models, which do not include this cooling mechanism in the first place.

Our results are in a good agreement with work presented by Gallagher et al. (2016, 2017), although a different code (CO^{5}BOLD, Freytag et al. 2012) was used in that study and their choice of stellar parameters does not fully overlap with that of our models. Gallagher et al. (2017) furthermore note that if the abundance of O changes, this has an impact on the number densities of the CO molecule. Consequently, the amount of free C available to form CH is decreased. Whereas generally it would be of interest to test non-solar abundances of different elements, in this work we do not explore the dependence on the C/O ratio. First, because there is evidence for CEMP stars with only a very modest O enhancement (Bessell et al. 2004; Iwamoto et al. 2005). In addition, most diagnostic OH features that are suitable for O abundance measurements (Asplund & García Pérez 2001) are located in the UV range,

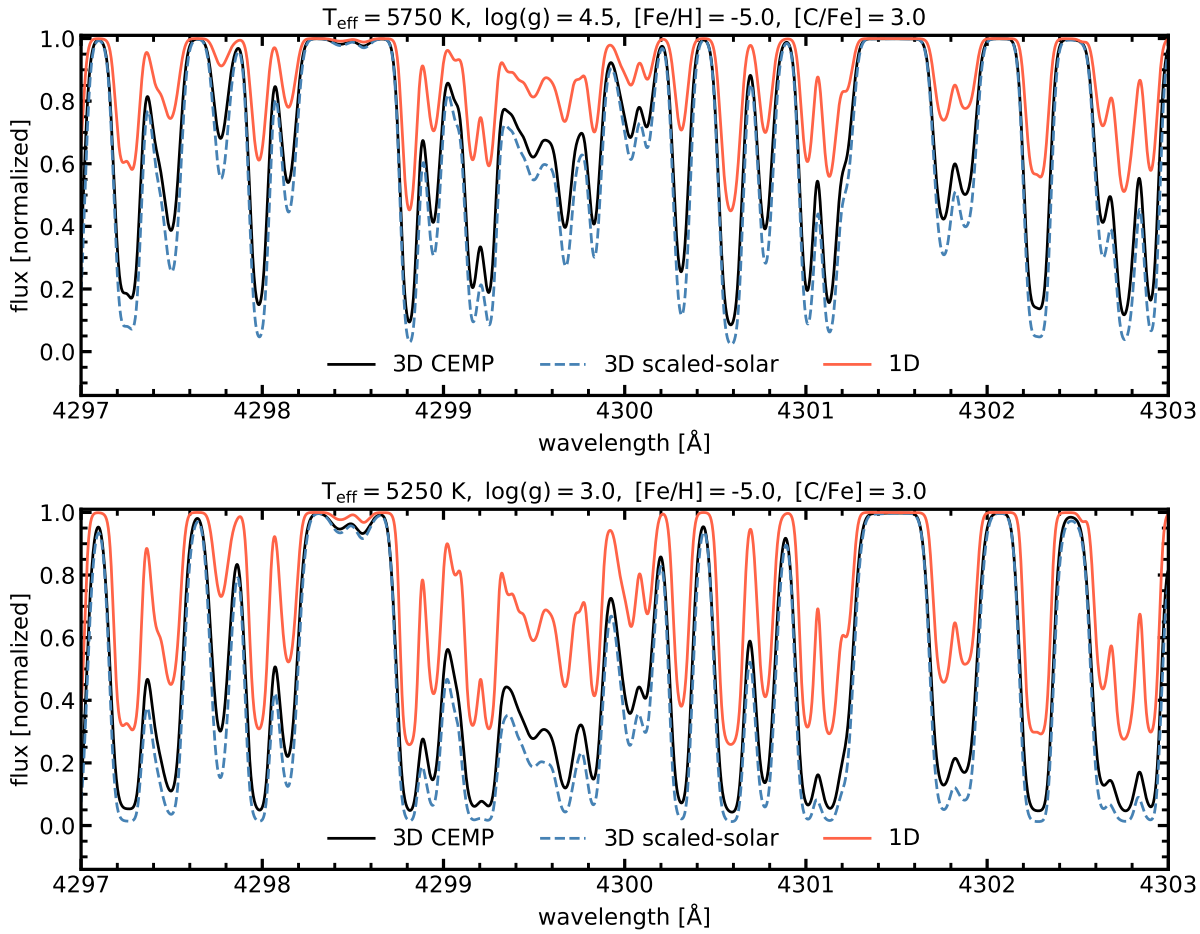

Figure 5.4: CH G-Band computed with M3DIS 3D and 1D MARCS model atmospheres. Black solid lines represent the CEMP 3D model, blue dashed lines the corresponding scaled-solar 3D model. Red solid lines show the 1D MARCS model with the same stellar parameters. Top: $T_{\rm eff} = 5750\,\mathrm{K},\ \log(g) = 4.5$, bottom: $T_{\rm eff} = 5250\,\mathrm{K},\ \log(g) = 3.0$.

which is extremely sensitive to NLTE effects in metal-poor stars (Bergemann & Nordlander 2014; Lind & Amarsi 2024). Furthermore, no 3D NLTE C/O ratios are available for CEMP stars (Collet et al. 2018).

We also note that Gallagher et al. (2017) focus on a hot sub-giant with metallicity −3, which leads to smaller differences between 1D and 3D models, partly because of the higher metallicity, and partly because of the lower CH/C ratio in both CEMP and non-CEMP models. We will explore the impact of different metallicities and stellar parameters on synthetic stellar spectra and C abundance determinations in the following sections.

5.4.2 Spectrum Synthesis of the CH G-band

We synthesize the CH G-band for all models listed in Tab. 5.2, including their scaled-solar counterpart, and for comparison, the respective 1D MARCS models with the same stellar parameters.

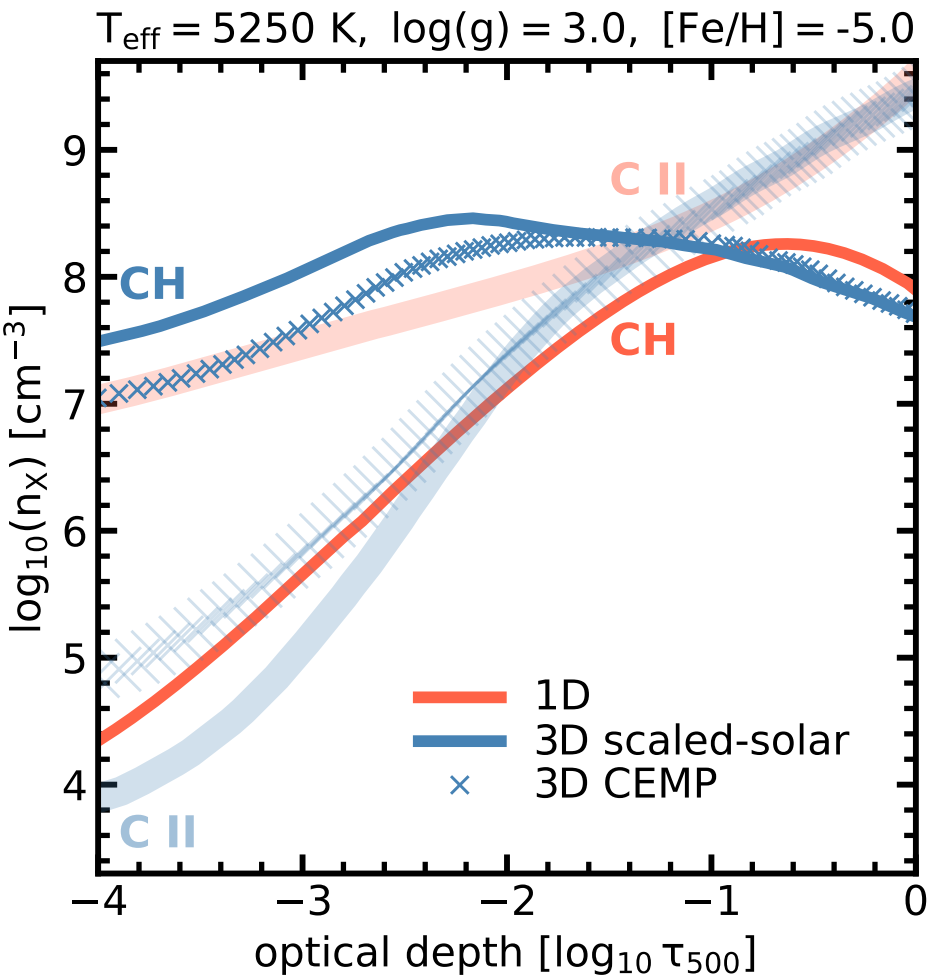

Figure 5.5: CH and C II number densities as a function of optical depth. Solid, blue lines correspond to the 3D scaled-solar model, blue crosses to the 3D CEMP model. The 1D MARCS model is shown with red, solid lines. For all models, CH number densities are shown as opaque lines, while C II number densities are shown as thick lines with higher transparency.

In Fig. 5.4 we show two representative synthetic G-band profiles for two model atmospheres, MS (top) and sub-giant (bottom), at [Fe/H] = −5 and [C/Fe] = +3. Independent of stellar parameters, it is evident that the 3D CEMP model (black, solid lines) leads to significantly stronger CH features than the 1D model (red, solid lines) at the same A(C). The 3D scaled-solar model (blue, dashed lines) on the other hand produces an even stronger stronger G-band as the 3D CEMP model (for the same $T_{\rm eff}$, $\log g$, and metallicity) and hence shows the largest departure from 1D HE. This is reflected in the equivalent width (EW).

These strong differences in the G-band strength are due to differences in the atmospheric structure. To explore this connection in more detail, we show the average CH number density, $\log n_{\rm CH}$, in the atmosphere of the sub-giant model at [Fe/H] = −5 as a function of the optical depth in Fig. 5.5. We also include the density of singly ionized carbon (C II). The CH number density can best be understood by linking their evolution with optical depth to the differences in atmospheric structures as presented in Fig. 5.1, panel D.

Below $\log \tau_{\rm ross} = -1$, the atmosphere is dropping sharply in temperature, in 3D and 1D, which favors the formation of CH molecules at the expense of C II, which is recombining with free electrons in a successively cooler and less dense environment. Towards the upper boundary the temperature in the 1D HE model stays roughly constant, while the density is dropping exponentially. In chemical equilibrium, the CH number density is proportional to $n_{\rm C}$ and $n_{\rm H}$ (Eq. 5.1) and hence $n_{\rm CH}$ drops proportional to ρ^2. This explains why the CH number density decreases significantly in the 1D model, despite the temperature staying constant. The C II number density, on the other hand, is only linearly dependent on density and is additionally affected by the balance of H^- and C II dissociation energies, which is why the trend is less obvious.

Although this proportionality is also true for the 3D model, the behavior in the atmosphere is entirely different. This is because the 3D model is not in radiative equilibrium – it is dominated by adiabatic cooling – which means that the temperature drops as a function of decreasing optical depth. In an increasingly colder environment the conditions for CH formation improve drastically, which is why $n_{\rm CH}$ increases in both 3D models and departures between 3D and 1D become significant.

When 3D CEMP (blue crosses) and 3D scaled-solar (blue solid lines) are compared, it may be noted that there are significantly more CH molecules present in the upper layers of the scaled-solar model, while there is only very little C II, compared to the CEMP model. Looking again at Fig. 5.1 this difference can be attributed to the additional heating induced by the C-enhancement in the CEMP atmosphere, which causes it to be hotter and hence less favorable for CH formation.

3D RHD models are much, up to −1000 K, colder in the atmospheric layers above $\log \tau_{500} \lesssim -2.5$. Due to strong C-enhancement, the cores of the strongest lines in the G-band form in regions around $\log \tau_{500} = -3.5$, as indicated by the horizontal lines in Fig. 5.2 and the $n_{\rm CH}$ extrema in Fig. 5.5. Due to much lower temperatures, the formation of molecules is more efficient, and due to larger molecular number densities, the absorption profiles are stronger (Uitenbroek & Criscuoli 2011). The final consequence is that the presence of strong G-band absorption in an observed spectrum is not necessarily related to a significant C-enhancement but can, in part, be associated with strong convection, as expected at low metallicities (Collet et al. 2011; Gallagher et al. 2017).

The larger differences seen in the synthetic spectra for the sub-giant (Fig. 5.4, bottom panel), as compared to the MS star, directly reflect the atmospheric structure distinctions discussed in Sec. 5.4.1. Specifically, while the 1D sub-giant model is colder (enhancing its G-band), the interplay of the non-linear dependence of CH formation on temperature and density, combined with the more pronounced C-enhancement-induced re-heating effect in the 3D sub-giant atmosphere, leads to the observed spectral differences relative to 1D.

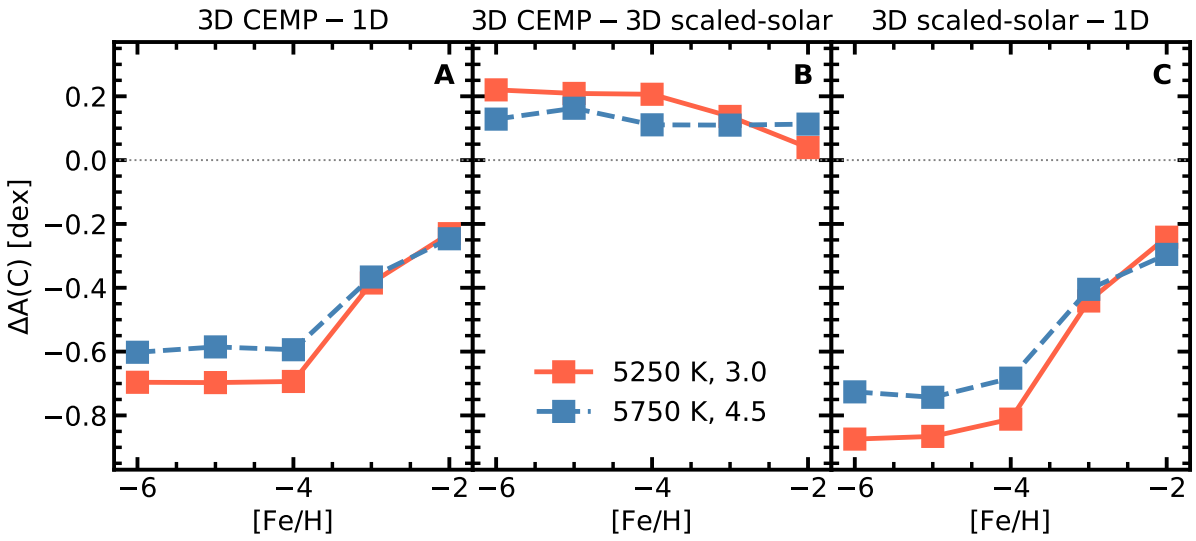

Figure 5.6: Abundance corrections to A(C) derived from the equivalent width of the CH G-band between 4297 and 4303 Å. Left (panel A): Final abundance correction $\Delta A(C) = A(C)_{\text{3D CEMP}} - A(C)_{\text{1D}}$ from 1D HE MARCS to 3D CEMP models. Centre (panel B): $A(C)_{\text{3D CEMP}} - A(C)_{\text{3D scaled-solar}}$. Right (panel C): $A(C)_{\text{3D scaled-solar}} - A(C)_{\text{1D}}$.

5.4.3 CEMP Abundances in 3D

In order to estimate the influence of carbon-enhanced CEMP 3D RHD models on synthetic observables, we perform the analysis as presented in the previous sections for stellar model atmospheres of different metallicities, from [Fe/H] = −2 up to [Fe/H] = −6. We compare the total EWs in the wavelength range of the G-band obtained in 3D with the corresponding 1D MARCS results, computed using a microturbulence of 1 km/s. By varying A(C) in the spectrum synthesis of the 3D RHD models we sample the full CoG and derive abundance corrections by matching the EWs within the integration limit of 4297 to 4303 Å. We emphasize that this EW integration of the G-band is not used to obtain abundances of observed spectra directly but only to quantify the corresponding overall effect on carbon abundances by comparing synthetic spectra. Other procedures, such as direct fitting of lines (Popa et al. 2023) can be used instead.

Our results for abundance corrections can be found in Fig. 5.6. We present the final correction $\Delta A(C) = A(C)_{\text{3D CEMP}} - A(C)_{\text{1D}}$ in panel A, the CEMP correction $A(C)_{\text{3D CEMP}} - A(C)_{\text{3D scaled-solar}}$ in panel B, and the $A(C)_{\text{3D scaled-solar}} - A(C)_{\text{1D}}$ correction in panel C for the MS and sub-giant model as a function of metallicity. We note that because we compare 3D CEMP to the 1D scaled-solar MARCS models, in panel A the effect of carbon enhancement on the correction is implicitly taken into account. We opt to use scaled-solar rather than C-enhanced MARCS models for our comparison, since scaled-solar models are more commonly employed in 1D studies of CEMP stars. However, panels A and C of Fig. 5.1 indicate that the differences between the two model types are negligible, making this distinction

ultimately unimportant.

As explained in the previous section, the 3D − 1D abundance corrections are larger (in modulus, or amplitude) for the sub-giant star. At [Fe/H] = −6 they are large and negative and reach up to −0.7 dex with C-enhancement in the atmosphere, and −0.9 dex without. Corrections decrease with increasing metallicity and are smaller, ΔA(C) ≈ −0.2 dex, at [Fe/H] = −2. The 3D CEMP − 1D corrections for the hotter MS star range from ∼ −0.6 dex at [Fe/H] = −6 to ∼ −0.2 dex at [Fe/H] = −2.

In contrast, the effect of carbon enhancement in 3D models is positive (panel B). At [Fe/H] = −2, the 3D scaled-solar and 3D CEMP G-band strengths in the sub-giant models are almost identical, which is why $A(C)_{\text{3D CEMP}} - A(C)_{\text{3D scaled-solar}} \lesssim 0.05$ dex. The differences increase with decreasing metallicity and decreasing surface gravity, so that $A(C)_{\text{3D CEMP}} - A(C)_{\text{3D scaled-solar}} = +0.2$ dex for the sub-giant model with [Fe/H] = −6. As discussed in Sec. 5.4.1, the effect of C-enhancement on the hotter MS model is generally smaller. The corrections are on the order of $\lesssim +0.1$ dex and show only a small deviation with metallicity. Compared to the significant 3D effect, the C-enhancement in hot, low-metallicity MS models is hence negligible.

It is interesting to analyze the impact of 3D CEMP models in the context of the observed CEMP distribution of Galactic stars. We therefore apply our corrections to a sample of MS and turn-off stars compiled from the SAGA database (Suda et al. 2008, 2011, 2017) to explore if 3D models have an impact on the statistics of CEMP stars in different Galactic metallicity regimes. We apply $A(C)_{\text{3D CEMP}} - A(C)_{\text{1D}}$ carbon abundance corrections to the observed data, based on the closest 3D model in terms of T_{eff} and $\log g$, and we interpolate linearly in metallicity. We then split the stellar sample into bins of ±0.5 dex in metallicity and compute mean and standard deviation in each of them. The result is shown in Fig. 5.7.

As expected, the differences between the 3D-corrected and 1D distributions increase with decreasing [Fe/H]. At [Fe/H] = −4 the mean [C/Fe] of CEMP stars is ≈ 1.1, 0.5 dex lower than the [C/Fe] ≈ 1.6 suggested by the 1D data. Toward [Fe/H] = −2, the differences decrease to ≈ 0.2 dex. We note that at metallicities above −5 the lower limit of the 1-σ interval already lies below the CEMP defining line of [C/Fe] = 0.7 (indicated by the gray dotted line) in 3D, which implies that there is a significant impact on the overall abundance distribution in this metallicity regime. Below [Fe/H] = −5 the corrections are larger; however, because of the overall higher [C/Fe] abundances found in these stars the impact on the distribution of CEMP stars is expected to be small.

To further investigate Galactic CEMP populations, we present the same data in the Yoon-Beers diagram (Yoon et al. 2016), which is shown in Fig. 5.8. In this figure, we present the uncorrected 1D (red points, top panel) and 3D CEMP corrected (blue points, bottom panel) data in the A(C) vs. [Fe/H] plane, and indicate the location of CEMP sub-groups I, II,

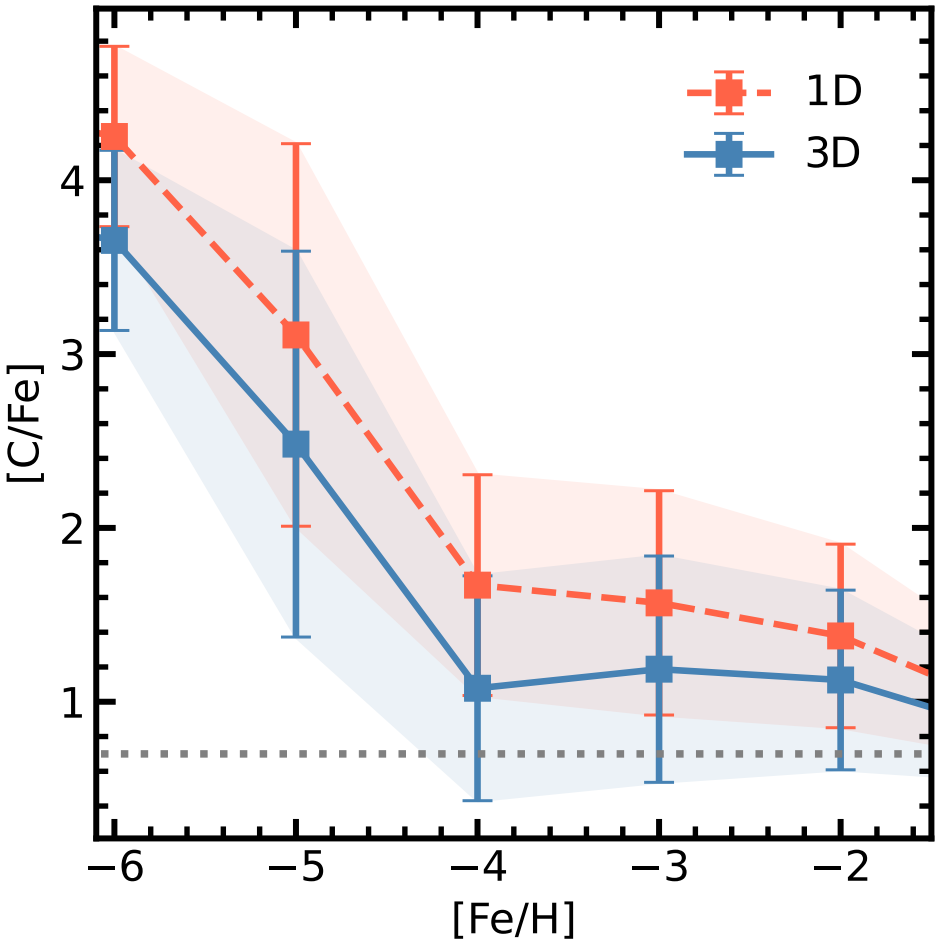

Figure 5.7: [C/Fe] against [Fe/H] for 3D CEMP and 1D measurements of Galactic stars from a MS and sub-giant sub-sample of the SAGA database (see text). The red, dashed line represents the mean, uncorrected 1D and the blue, solid line the 3D CEMP-corrected data. Shaded regions correspond to standard deviations of the observed sample in the respective metallicity bin ±0.5 dex. The grey dotted line represents the dividing CEMP classification abundance of [C/Fe] = 0.7.

and III – as defined by Yoon et al. (2016), see their Fig. 1 – as colored ellipses. In addition to the first identification of CEMP sub-groups, Yoon et al. furthermore showed that Group I is mostly populated by CEMP-r/s stars, while Group II and III contain mainly CEMP-no stars. Yoon et al. (2016) – and subsequently also Yoon et al. (2018); Chiaki et al. (2017) – furthermore identify different CEMP groups with different formation scenarios, indicating multiple progenitors for CEMP-no stars.

At lower metallicities, differences manifest as a systematic offset of ~ 0.6 dex, moving down the A(C) plateau (indicated by the horizontal orientation of the yellow ellipse in the 1D case) significantly. We note that as a consequence of this plateau, the carbon enhancement in the atmosphere, relative to iron, becomes more significant when even lower metallicities are considered. We do not expect that – at least in CEMP stars – G-bands from 3D and 1D models diverge even further at more extreme metallicities, mainly because the carbon

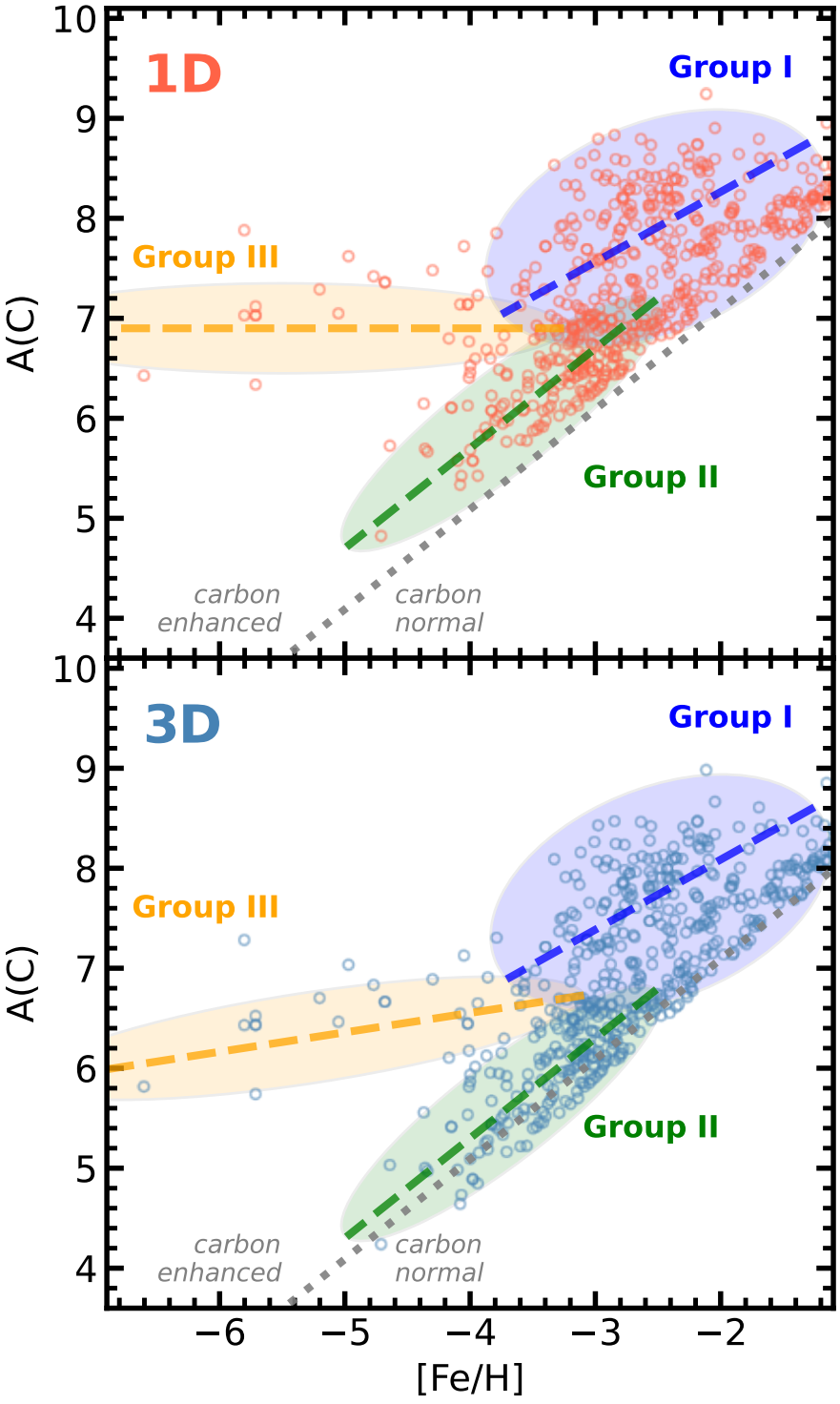

Figure 5.8: Yoon-Beers (Yoon et al. 2016) diagram, A(C) against [Fe/H] for the 3D-corrected and 1D measurements for Galactic stars from the literature (see text). Red circles represent uncorrected 1D, blue circles 3D CEMP-corrected data. The grey dashed line represents the dividing CEMP classification abundance of [C/Fe] = 0.7. Ellipses in 1D are drawn similar to Yoon et al. (2016), their Fig. 1.

enhancement itself will compensate for the loss of metals in exactly the right part of the atmosphere, as demonstrated in the previous sections. This compensation is noticeable as a decreasing metallicity gradient in panel A (compared to panel C) of Fig. 5.6 already between [Fe/H] = −4 and − 5.

One may be tempted to use scaled-solar, low metallicity, non-carbon-enhanced models for the analysis of these CEMP stars because of the time investment related to creating 3D models of stellar atmospheres. However, this would lead to an overestimation of the corrections and introduce an additional differential effect with metallicity that causes the A(C) plateau to be artificially tilted. When properly including C-enhancement in the atmosphere computation, this tilt is weaker, but still noticeable mostly due to differences in stellar parameters of individual targets. In Fig. 5.8 we find that an ellipse tilted by $\sim 10°$ with respect to the 1D case best represents our Group III sample in 3D.

Because 3D − 1D abundance corrections are negative, we find a significant number of stars in the SAGA sample that are – following the classical definition of Aoki et al. (2006) – no longer CEMP stars, as their [C/Fe] drops below 0.7. This is most noticeable in CEMP Group II, as these stars are located closest to the carbon-normal division in terms of A(C), while still experiencing a large abundance correction due to their relatively low metallicities.

Around the onset of the C-plateau at [Fe/H] = −4 we find that stars at higher [C/Fe] are systematically redistributed towards the abundance threshold, such that close to – and below – the dividing line we find significantly more stars in 3D than in 1D. Overall, there are significantly fewer stars with extreme carbon abundances above [C/Fe] = 1.5 (see Fig. 5.7, specifically for [Fe/H] ≥ −4). The consequence is that there is a migration of stars at the edges of Group I and III towards Group II, or even outside the CEMP category. In 3D, we find that Group II is best represented by an ellipse that is shifted down by 0.4 dex with respect to the 1D case.

5.4.4 Galactic CEMP Fraction in 3D

To quantify the consequences for Galactic fractions of CEMP-r/s and CEMP-no sub-groups, splitting the CEMP sample based on the neutron capture abundances is necessary. However, for a significant portion of the SAGA sample, no Ba or Eu measurements are available. This issue has been discussed by Yoon et al. (2016), who derived an alternative classification based on A(C) alone, for which they claim a success rate of 87 % for CEMP-r/s classification and 93 % for CEMP-no stars. In their method, stars are associated with the CEMP-r/s group, if a high absolute carbon abundance A(C) > 7.1 is measured, while CEMP-no stars consequently have A(C) ≤ 7.1.

The discussion of their approach goes beyond the boundaries of this work. We emphasize that their CEMP subgroup association is empirical, which means the systematic offsets pre-

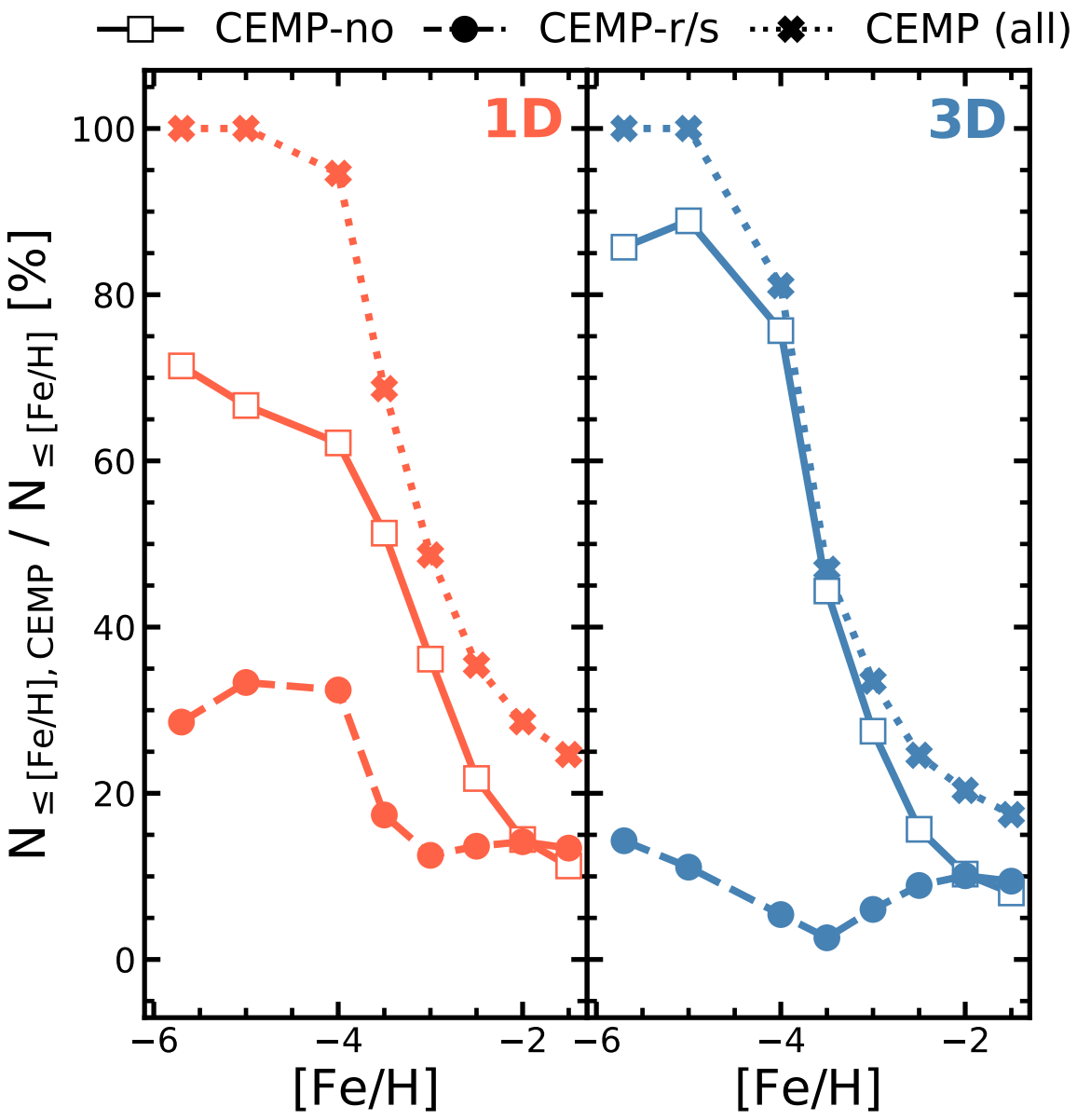

Figure 5.9: Cumulative fraction of CEMP-no (solid lines with squares) and CEMP-r/s (dashed lines with circles) stars in 1D (red, left panel) as well as 3D (blue, right panel). The dotted line with crosses shows the total cumulative fraction of CEMP stars in 1D (left) and 3D (right).

sented here will either lead to a re-classification of CEMP stars in the same system if the separation of Yoon et al. (2016) is still valid or require a change of the system through new A(C) limits based on new C abundances.

In the following, we use their method to classify our sample twice, in 1D and after the 3D CEMP abundance corrections have been applied. The resulting cumulative fractions can be found in Fig. 5.9. We show the cumulative fraction for CEMP-r/s (dashed lines) and CEMP-no (solid lines) stars separately – as well as for their sum (dotted lines) – for the 1D (red, left panel) and 3D (blue, right panel) case.

In 1D, there is a significant fraction of over 10 % CEMP-r/s stars across all metallicities; below [Fe/H] $= -4$ we find $\sim$ 30 % of all stars in our sample to be CEMP-r/s stars. The fraction of CEMP-no stars has a strong metallicity dependence. Below [Fe/H] $= -5$ all the stars in the sample are CEMP stars, with a share of 70 % CEMP-no and 30 % CEMP-r/s. Increasing metallicity decreases the contribution from CEMP-no stars, until [Fe/H] ≤ -2, where both contribute equally to the total number of CEMP stars ($\sim$ 15 % each).

However, in 3D, there are overall $\sim$ 10 % fewer CEMP stars below [Fe/H] $= -2$. Furthermore, the fraction of CEMP-r/s stars is significantly lower, which is due to the increasingly negative (with decreasing [Fe/H]) 3D abundance corrections and the resulting redistribution of Group I and III stars – where most of the CEMP-r/s stars reside – to the CEMP-no dominated Group II. CEMP-r/s stars are preferentially found at higher metallicities than CEMP-no stars, where the C-enhancement in [C/Fe] is less severe than at low metallicities; A large number of CEMP-r/s stars reside close to the defining boundary of [C/Fe] $= 0.7$. When 3D corrections to C abundances are taken into account, many stars originally classified as CEMP-r/s stars in reality have a lower C abundance, implying their identity as CEMP-no stars. The contribution from CEMP-no stars hence increases with respect to 1D, and climbs to above 90 % for all stars below [Fe/H] $= -5$, while it peaks around 70 % in 1D.

We remind the reader that it must still be explored, using large self-consistent stellar samples with 3D NLTE Ba and Eu abundances, whether or not the CEMP sub-group classification is still meaningful in 3D. Because the abundance corrections themselves depend on metallicity, it is not straightforward to assume that a separation based on a gap in 1D A(C) will still be present in 3D.

Integrating CEMP-r/s and CEMP-no distributions, we find that there are overall fewer CEMP stars in 3D. Below [Fe/H] $= -4$ our sample contains 95 % CEMP stars in 1D, while in 3D this number reduces to 81 %. Between [Fe/H] $= -3.5$ and [Fe/H] $= -3.0$ we consistently find a cumulative fraction that is $\sim$ 20 % lower in 3D than in 1D. Above [Fe/H] $= -3$ the 3D corrections in general are more modest, which is why we find that cumulative fractions agree to below 10 %.

If one considers CEMP fractions in metallicity bins rather than as cumulative sum of stars below a given metallicity, it is straightforward to estimate the misclassification of CEMP stars around a specific metallicity. For this purpose, we include Tab. 5.3 in the Appendix, listing the fraction of CEMP stars using the same binning as in Fig. 5.7. In total, we find that $\sim 30\,\%$ of the CEMP stars between $-4.5 < [\mathrm{Fe/H}] < -3.5$ are not carbon-enhanced enough to qualify as such. Between $-3.5 < [\mathrm{Fe/H}] < -2.5$ and $-5.5 < [\mathrm{Fe/H}] < -4.5$ the misclassification is still 15 % and 12 %, respectively.

In summary, we conclude that taking 3D CEMP effects on the C abundances into account reduces the observed CEMP fraction by $\sim 20\,\%$ in the metallicity regime below $[\mathrm{Fe/H}] = -3.0$. At the same time, the relative contribution of CEMP-no stars to CEMP-r/s stars increases. Below $[\mathrm{Fe/H}] \approx -4$ we find that, in 3D, more than 80 % of CEMP stars are CEMP-no stars.

5.4.5 Comparison with Literature

The total CEMP fractions derived using 3D models are in good agreement with CEMP fractions based on 1D models reported in Placco et al. (2014), but are somewhat lower in our distributions. Placco et al. (2014) find a fraction of 81 % CEMP stars with metallicities below $[\mathrm{Fe/H}] = -4$ and 100 % below -5, which is in good agreement with our findings. At $[\mathrm{Fe/H}] = -3.5$ and $[\mathrm{Fe/H}] = -3.0$, Placco et al. (2014) report a fraction of 60 % and 43 %, respectively. These values are based on MS, sub-giants, and giants (their Fig. 4). In our 3D-corrected [C/Fe] distributions based on MS and sub-giants, the fractions are $\approx 45\,\%$ at $[\mathrm{Fe/H}] = -3.5$ and $\approx 33\,\%$ at $[\mathrm{Fe/H}] = -3.0$, which results in a 3D CEMP effect similar to what we find in this study.

We note that Placco et al. also explored the impact of 3D on C abundances in giants. Using the 3D line formation calculations for CH by Collet et al. (2007), they estimate that negative 3D corrections, in giants with $\log g < 3$, of -0.3 for $-2.5 < [\mathrm{Fe/H}] < -2.0$, -0.5 for $-3.0 < [\mathrm{Fe/H}] < -2.5$, and -0.7 for $[\mathrm{Fe/H}] = -3.0$ may arise. These estimates are similar to our results; however, our analysis confirms that departures from 1D HE are also prominent in the CH G-band spectra of MS stars. We note that the effect of C-enhancement in the 3D RHD atmosphere itself was not taken into account by Collet et al. (2007) and, hence, it was not included in the 3D estimates by Placco et al. (2014). As we show in this work, 3D effects are relevant for stars in all evolutionary phases. They therefore can have a more significant impact on the overall distribution of CEMP stars across all metallicities than Placco et al. anticipated.

Since we find lower CEMP fractions at all metallicities, the question arises: What are the implications of lower CEMP occurrence rates in the early Galaxy? Hartwig et al. (2018) investigated the formation of the first generation of stars using a semi-analytical model[2]

[2] An early version of the A-SLOTH model; see Hartwig et al. (2022, 2024).

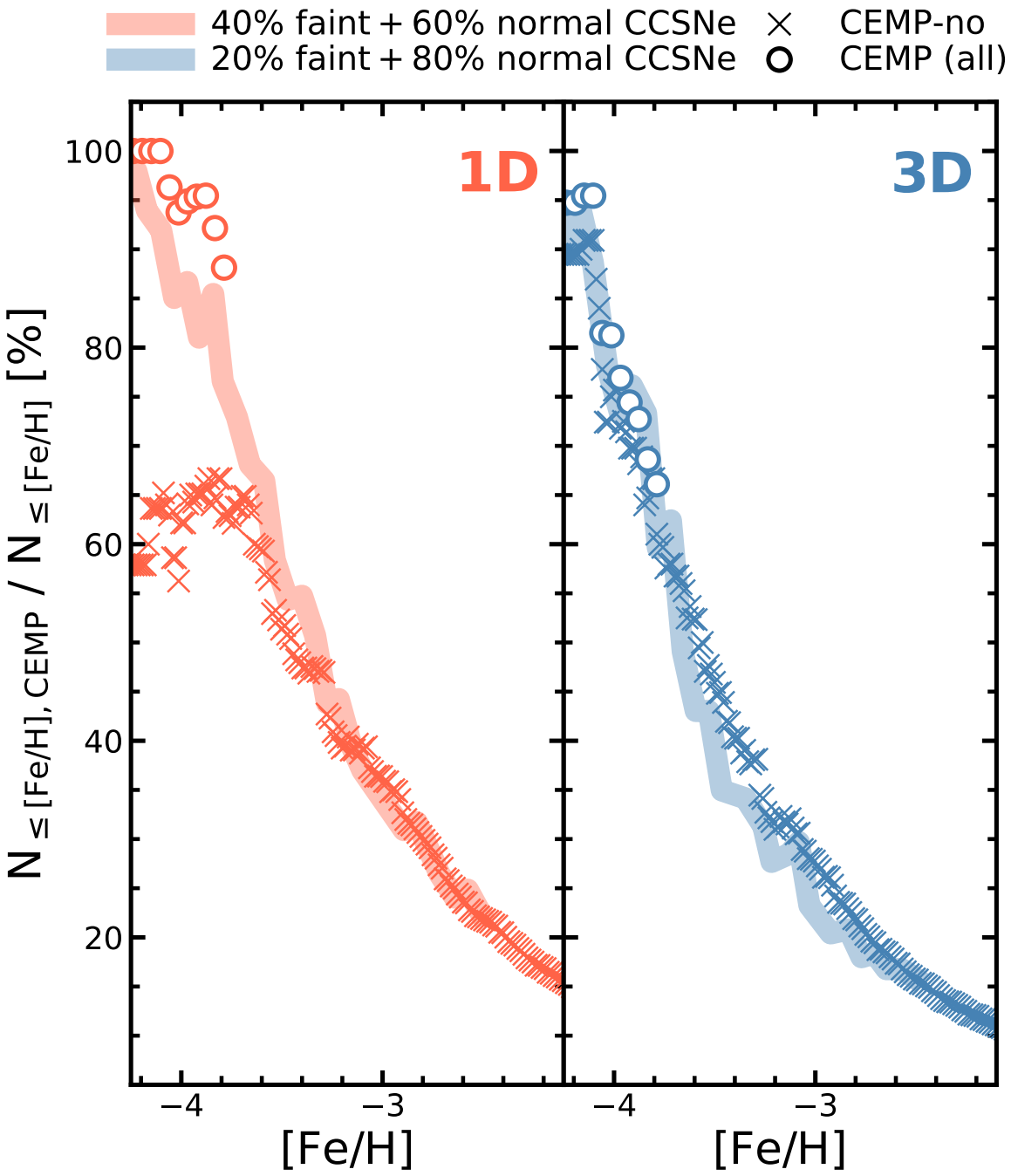

Figure 5.10: Cumulative CEMP-no fraction predictions from Hartwig et al. (2018), compared to our data. Below [Fe/H] < -3.75, the fraction of all CEMP stars in our sample are shown (circles). See text. 3D CEMP data is shown in blue (right panel), while 1D data is shown in red (left panel). The red line in the left panel corresponds to the fiducial model of Hartwig et al. (2018), which includes 40 % faint (from Ishigaki et al. 2014) and 60 % normal CCSNe (from Nomoto et al. 2013). The blue curve in the right panel corresponds to their 20 % faint, 80 % normal CCSNe model.

based on dark matter halo merger trees that yield MW-like halos. They investigated the influence of various input parameters on their simulations on the observed CEMP occurrence rate as a function of [Fe/H] and compared their predictions with the data of Placco et al. (2014).

Faint SNe were considered as the primary channel for the formation of CEMP-no stars (e.g. Klessen & Glover 2023, references therein). These objects, although they span the same mass range as normal CC-SNe, produce little ^{56}Ni due to low explosion energy and/or effects of geometry in the explosion (Tominaga et al. 2007). Faint Pop III SNe generally produces a higher ratio [C/Fe], because Fe peak elements fall back onto the remnant and are not ejected. In the fiducial model, which is tuned to reproduce the 1D CEMP data from Placco et al. (2014), Hartwig et al. (2018) include 40 % of faint (Ishigaki et al. 2014), and 60 % normal CCSNe (Nomoto et al. 2013).

In addition, Hartwig et al. (2018) provide CEMP fractions for a model that includes significantly fewer faint SNe (only 20 % instead of 40 %). A comparison of those two models specifically with the data presented in this work can be found in Fig. 5.10. We note that Hartwig et al. do not account for the r-process and s-process enrichment in their model and hence only provide predictions for the fraction of CEMP-no stars. As mentioned in Sec. 5.4.4, the CEMP-r/s or CEMP-no classification without s- and r-process abundance measurements is a relatively uncertain endeavor. At low metallicities, the rigid A(C) cut can especially lead to bias by wrongly assigning high [C/Fe] Group III stars as CEMP-r/s (see Fig. 5.8), even though Group III predominantly consists of CEMP-no stars (e.g. Yoon et al. 2016).

Motivated by Fig. 5.8, we choose to include all CEMP stars below [Fe/H] < -3.75 – corresponding to the low-metallicity end of the blue Group I ellipse – and only CEMP-no stars at higher metallicities in the comparison with Hartwig et al. (2018) shown in Fig. 5.10. This effectively assumes that Group III is composed exclusively of CEMP-no stars. We note that this assumption does not affect the overall conclusions, because we are focusing mainly on the shift between 3D CEMP and 1D and the metallicity region above -3.5. For a more detailed investigation, abundance measurements of s- and r-process elements are essential.

Remarkably, their model with a 20 % faint SNe fraction (blue, solid line) is in excellent agreement with our 3D-corrected CEMP fractions (blue crosses + circles), while their fiducial model is in good agreement with our 1D data (in red). We also note that the systematic offset between 3D CEMP and 1D data at metallicities above -3 resembles the systematic offset between the fiducial and 20 % faint SNe models Hartwig et al. very well. At intermediate to low metallicities the CEMP-r/s – CEMP-no classification becomes less precise because of the mixing of different CEMP groups. Nevertheless, because of the higher CEMP-no contribution in 3D, the agreement between model and observations is excellent also below [Fe/H] $= -3.75$, regardless of whether the assumption of nearly 100 % CEMP-no stars in

Group III holds.

In 1D, this is not the case; only after including all CEMP Group III stars the agreement is restored, indicating that the CEMP-no classification is the culprit here. However, independent of the agreement at low metallicity in 1D, Fig. 5.10 clearly shows that 3D-correction-induced shifts in the CEMP fraction can be met with a decrease in the contribution of faint SNe in GCE. Hartwig et al. (2018) furthermore note that the 20 % faint SNe model produces the approximately same metallicity distribution function for the halo as their fiducial model, and hence remains in good agreement with observations. An overestimation of the CEMP fraction thus leads to an overestimation of the contribution from faint SNe in the evolution of the early Galaxy.

This is very interesting, as faint SNe will also impact the chemical enrichment of other chemical elements and therefore large robust 3D NLTE abundance samples from next generation facilities, such as 4MOST (Bensby et al. 2019), will be in a position to constrain the contribution of faint SNe to the GCE. It will be particularly interesting to assess the connection to Fe-peak elements, such as Ni, Mn, and Co, as recent 3D NLTE studies show that their abundances are severely under-predicted in 1D LTE (Storm et al. 2025), which does not coincide with GCE predictions. A overall lower C abundance in metal-poor stars and thus fewer faint SNe, which are heavily dominated by the fallback of heavy elements and thus generally exhibit low Fe-peak yields (Nomoto et al. 2013), may thus qualitatively go into the right direction and improve the agreement with 3D NLTE measurements.

5.5 Conclusions

In this work, we show that physically realistic 3D RHD models of stellar atmospheres are crucial for the determination of accurate abundances of carbon in stars. We also show that these have a direct impact on understanding nucleosynthesis and Galactic chemical evolution (GCE).

We explore the effects of 3D convection on the critical diagnostic G-band in spectra of MS and sub-giant stars. The G-band arises as a result of absorption by the CH molecule and it provides the strongest observational constraint on C abundance and the [C/Fe] ratio in metal-poor stars. To compute 3D radiation-hydrodynamics simulations of stellar sub-surface convection, we use our new code `M3DIS` presented in Eitner et al. (2024). The uppermost parts of these models are used to calculate detailed 3D spectrum synthesis around the G-band and to derive a grid of 3D abundance corrections to [C/Fe] for the entire range of metallicities, $-6 \leq$ [Fe/H] ≤ -2, relevant for studies of GCE. The 3D models are computed for the first time using C-enhancement in line with low-metallicity observations. We compare the 3D synthetic spectra in the G-band with the equivalent simulations computed

using classical 1D HE models and quantify the amplitude of 3D effects on stellar [C/Fe] abundances.

We find that 3D effects on the G-band are substantial and lead to lower estimates of the carbon abundance. This effect arises due to the cooler outer temperature structures of 3D RHD models, compared to 1D HE structures. The formation of molecules is much more efficient in cooler 3D models, which implies that the spectral lines of CH are stronger. As a consequence, a *lower* abundance of C is required to fit a given observed spectrum, and the 3D corrections are negative. Interestingly, increasing C abundance in 3D models at the same metallicity (set by iron) yields the opposite effect: the G-band weakens. Physically, this is because increasing C (to levels observed in CEMP stars) implies higher radiative opacity in the models and leads to slightly hotter 3D models, compared to their scaled-solar counterparts. The 3D CEMP A(C) corrections for MS stars may exceed $A(C)_{3D\ CEMP} - A(C)_{1D} = -0.6$ dex at [Fe/H] $= -5$. For sub-giants, the 3D CEMP effects are on the order of ~ -0.7 dex, in good agreement with previous estimates in the literature (Collet et al. 2018; Gallagher et al. 2016, 2017). The differences between 3D and 1D A(C) decrease with increasing [Fe/H].

We apply 3D CEMP A(C) abundance corrections to a sample of metal-poor stars from the SAGA database to investigate the impact on the Galactic CEMP population. We find a significant fraction of CEMP stars across all metallicities that no longer classify as C-enhanced. In the range between $-4.5 <$ [Fe/H] < -3.5 we find $\sim 30\,\%$ fewer CEMP stars after applying the 3D abundance corrections, between $-3.5 <$ [Fe/H] < -2.5 the number is reduced by 15 %. In addition, we find that the cumulative CEMP fraction below [Fe/H] $= -3$ is $\sim 20\,\%$ lower in 3D than it appears in 1D. At lower metallicities, the distribution remains mostly unchanged, because the same A(C) corresponds to a higher [C/Fe]. As a consequence the A(C) plateau remains present in 3D, though it appears to be slightly tilted by 10°.

When considering the CEMP-no and CEMP-r/s sub-groups based on A(C) (Yoon et al. 2016), we find a reduction of the CEMP-r/s sample size in 3D, as a significant number of stars are either shifted below the CEMP limit of [C/Fe] $= 0.7$, or below the CEMP-r/s limit of A(C) $= 7.1$. Consequently, the use of 3D-corrected C abundances leads to a higher fraction of CEMP-no stars, as some stars previously classified as CEMP-r/s are re-classified. Despite their generally lower metallicities, CEMP-no stars retain a high A(C), ensuring that most remain classified as carbon-enhanced.

The fraction of CEMP stars as a function of metallicity is a tracer of the contribution of faint SNe to the GCE (Hartwig et al. 2018; Klessen & Glover 2023). Following the models of Hartwig et al. (2018), we find that a lower fraction (only 20 %) of faint SNe in the Pop III galaxy formation models can describe the 3D CEMP distributions. This is an interesting result that remains to be confirmed with detailed GCE models and other chemical elements,

Table 5.3: CEMP fractions in bins of Δ[Fe/H] = ±0.5 dex.

[Fe/H] dex	1D %	3D %
-6	100	100
-5	100	88
-4	83	53
-3	50	35
-2	26	19
-1	19	12

which are sensitive to the faint SNe contribution.

5.6 Appendix – Supplementary Material

We have found that the cost of computing accurate vertical temperature profiles at the surface can be significantly reduced, relative to Eitner et al. (2024), by modifying the centering of RT solutions in the short-characteristics solver. Instead of computing the radiation intensities $I_{\Omega,\nu}$ and source functions S_ν at cell centers, and computing the net radiative cooling from

$$q_{\rm rad} = \iint \mathrm{d}\Omega \, \mathrm{d}\nu \, \rho \kappa_\nu (S_\nu - I_{\Omega,\nu}), \tag{5.2}$$

one can instead compute the radiative intensities $I_{\Omega\nu}$ at cell interfaces, and from these compute the radiative fluxes $F_{\mathrm{i},\nu}$ in each direction i, which allows the cooling to be obtained from

$$q_{\rm rad} = \int \mathrm{d}\nu \nabla \, \mathbf{F}_\nu, \tag{5.3}$$

where the flux divergence is computed numerically as the differences between incoming and outgoing fluxes for each cell. This method is by construction *energy conserving*, in the sense that the cooling corresponds exactly to the increase in energy of the radiation field that leaves the cells, relative to the energy that was entering. Thus, while the previous method "samples" the cooling point-wise, the improved method computes the actual energy loss across cells. The improvement is illustrated in Fig. 5.11, which plots horizontally average cooling profiles for different vertical resolutions.

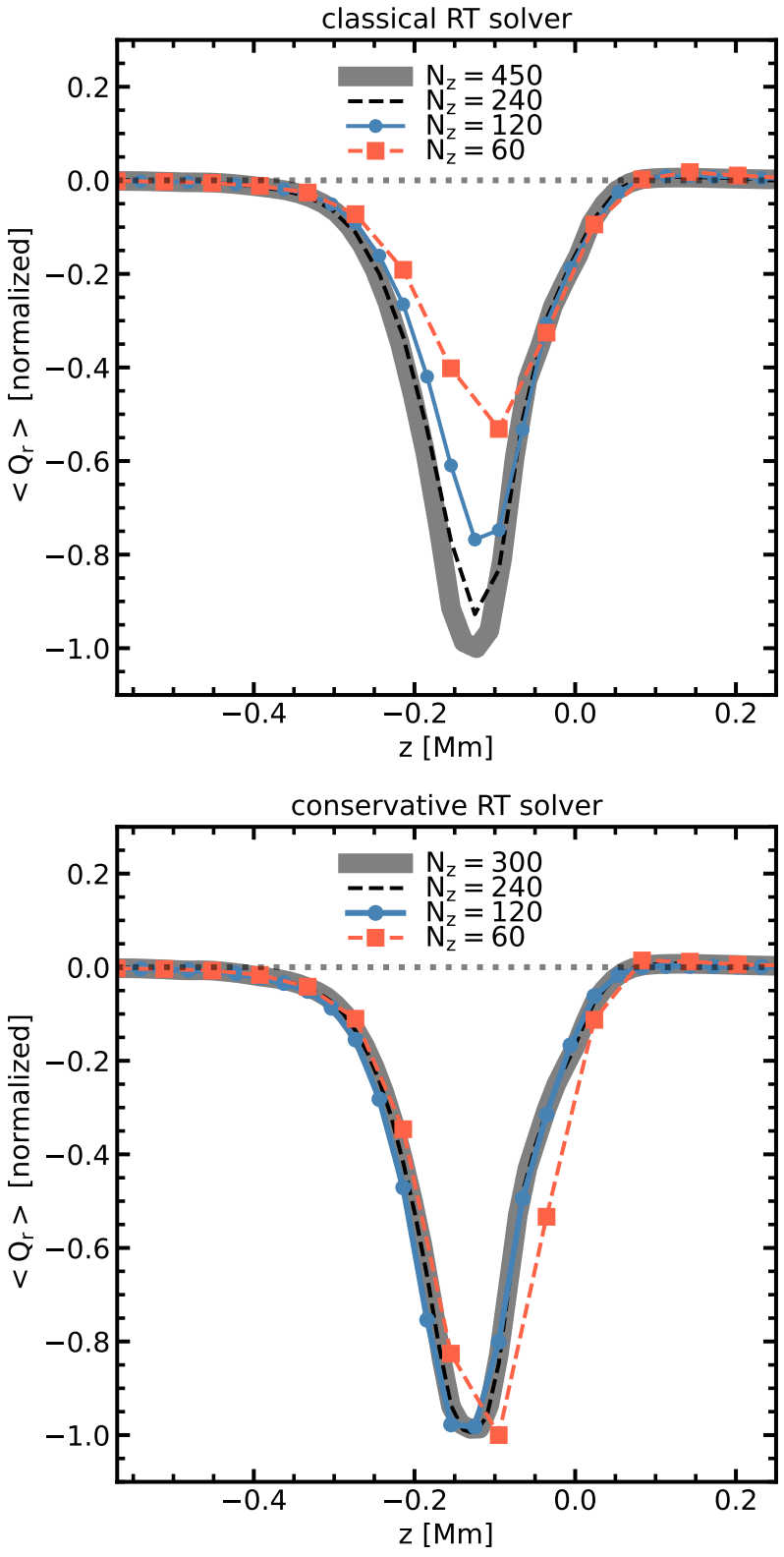

Figure 5.11: Comparison between the horizontally averaged radiative heating $q_{\rm rad}$, computed at different resolutions for the same model atmosphere using the old, classical RT solver (top) and new, conservative RT solver on a staggered grid (bottom). The new solver reproduces the cooling peak very well already at intermediate resolution, while the classical solver shows the typical under-sampling effect, which leads to artificial heating of the model.

6 Discussion & Future Outlook

In the previous sections we investigate the influence of 1D and LTE modeling assumptions on abundance measurements of Galactic stars. We show that there are significant departures between LTE and NLTE abundances of Fe-peak elements and find that in LTE specifically Galactic [(Ni, Mn)/Fe] ratios lead to a misinterpretation of SNe Ia explosion types. We furthermore develop an efficient 3D RHD stellar atmosphere framework, that is intended to relax the assumption of 1D for large stellar samples. Using this new `M3DIS` code, we find that there is a strong systematic bias on C abundance measurements of metal-poor stars, leading again to a misinterpretation of physical reality by wrongly interpreting strong CH-G band features in some stars as high [C/Fe] abundances, while it is merely a consequence of the limitations of the atmosphere models used.

In this section, I finally extend the detailed discussions of each individual research conducted in the context of this thesis, evaluate their combined significance, and explore promising avenues for future work that relies on results and methods presented in this work.

6.1 3D NLTE Galactic Archaeology

Fe-peak elements in 3D NLTE

A highlight in the context of Galactic Archaeology was recently published by Storm et al. (2025), who carefully derive line-by-line 3D NLTE abundance corrections for Fe-peak, as well as neutron-capture elements, for a relatively large sample of 746 Galactic stars. Due to the limited availability of densely-sampled 3D models – and hence 3D NLTE spectra – their analysis has to rely on a rather sparse sampling in the stellar parameter space and was limited to the technique of abundance corrections instead of employing direct fitting algorithms.

Depending on the lines, they find that especially Ni abundances are very sensitive to 3D effects, showing a positive correction of up to +0.3 dex in metal-poor MS stars with respect to 1D NLTE, and close to +0.6 dex compared to 1D LTE (see their Fig. 7). They furthermore confirm the strong positive 3D NLTE effect on Mn and, in addition, find that Co abundances

are influenced in a similar way, with the Galactic [Co/Fe] trend resembling the chemical evolution of [Ni/Fe].

Their findings further strengthen the conclusions drawn in Sec. 3 and in Eitner et al. (2020), and confirm that they also hold in 3D NLTE; Large [(Mn, Co, Ni)/Fe] ratios at low metallicities generally imply that there needs to be a lower production rate of these Fe-peak elements in the majority of SNe Ia, as otherwise the Galactic gas would not be diluted towards the solar ratio at solar metallicities.

Storm et al. (2025) conclude that these new 3D NLTE abundances reveal large discrepancies between observations and predictions from chemical evolution models, which they attribute to too low Fe-peak yields from CC-SNe. The authors note that especially the measured [Co/Fe] ratio at low metallicities can not be reproduced by standard GCE models (Kobayashi et al. 2020b) even in LTE. As possible solutions, the authors mention the fine-tuning of classical CC-SNe models with respect to electron excess, mixing-fallback, explosion energy (Kobayashi et al. 2006), multidimensional explosion modeling (e.g. Wang & Burrows 2024), as well as electron-capture SNe – CC-SNe of collapsing O–Ne–Mg cores with masses between 8 and 10 $M_{\odot}$, which do not ignite Ne burning but the explosion is triggered by electron-capture in the degenerate core (Janka et al. 2008; Wanajo et al. 2018).

It was recently pointed out by Kobayashi et al. (2020b) that elevated [Mn/Fe] NLTE abundances in metal-poor stars found by Eitner et al. (2020), and confirmed by Storm et al. (2025), are inconsistent with the Galactic observations of [Cr/Fe] ratios. Kobayashi et al. (2020b) base this statement on the fact that both elements are formed in incomplete Si-burning regions, which – according to them – means that higher Mn yields would also cause higher Cr yields.

It remains to be investigated to what extent [Cr/Fe] abundance trends are influenced by 3D NLTE. It was shown by Bergemann & Cescutti (2010) that NLTE abundance correction for Cr I lines are large in metal-poor stars (up to +0.5 dex). However, they generally find the influence on Cr II abundances to be negligible. According to the data presented in (Kobayashi et al. 2020b, their Fig. 25), this suggests that – in 1D at least – no significant change is expected from the NLTE Galactic [Cr II/Fe] distribution. Nevertheless, Kobayashi et al. (2020b) claim that the disagreement between Mn and Cr I abundances would be even more severe (see also Kobayashi et al. 2006, their Fig. 20 and 21), which can potentially be explained by the strong NLTE effects.

Regarding Cr II, it is interesting to consider that one of the possibilities to reconcile the yields of [(Mn, Ni, Co)/Fe] from CC-SNe with observations is a change in the electron-excess Y_e in Si-burning layers. As mentioned in Sec. 2.2.3, it was pointed out by Nomoto et al. (2013) that decreasing Y_e is equivalent to more neutrons, which causes the over-production of Fe-peak elements with stable neutron-rich isotopes such as Mn, Ni, Co, and Cu. At the same

time, the amount of neutron-poor isotopes such as ^{52}Fe, which eventually decays to ^{52}Cr, are decreased. Since [Cr II/Fe] yields and observations with current models seem to agree in the metal-poor regime, this appears indeed contradictory. However, Nomoto et al. (2013) further mention that decreasing Y_e also decreases the yields for ^{56}Ni, and thus ^{56}Fe, which means the [Cr/Fe] ratio stays roughly constant, while [(Mn, Ni, Co, Cu)/Fe] go up. It needs to be investigated in more detail if the magnitude of this effect is enough to bring models and observations into agreement. However, according to Nomoto et al. (2013), it appears that high Fe-peak abundances in metal-poor stars in combination with a steady [Cr/Fe] ratio are not contradictory per se.

A more comprehensive, detailed study using full 3D NLTE techniques to derive Fe-peak abundances for a large sample of metal-poor Galactic stars – such as will be provided by 4MOST – is needed to put reliable, quantitative constraints on the occurrence and working mechanism of these CC explosions.

On the Dominance of sub-M_{Ch} SNe Ia

Recently, there have been a number of studies published in support of the high sub-M_{Ch} fractions found by Eitner et al. (2020) and Sec. 3 (Eitner et al. 2023), but also a few that challenge these findings. Trueman et al. (2025) analyze the GCE of the α-elements O, Si, Ca, as well as the Fe-peak elements Ti, Cr, Mn, Co, and Ni using LTE and NLTE data. By using the same chemical evolution code as in Eitner et al. (2023), but with a different SNe Ia prescription, Trueman et al. find that their GCE model reproduces the Galactic O and Si abundance independent of the CC-SNe yields they assume. In agreement with the findings by Storm et al. (2025), they note that neither Co nor Ti can be reproduced by any combination of CC-SNe and SNe Ia. Using the NLTE Ni data from Eitner et al. (2023), they furthermore arrive at the same conclusion as I in Sec. 3.7; Using the same set of CC-yields from Limongi & Chieffi (2018), even with a simplified SNe Ia treatment, they derive a sub-M_{Ch} fraction of 85% and thus find that sub-M_{Ch} are dominating over classical SNe.

In agreement with our findings, they furthermore note that the result is sensitive to the set of CC-yields. This can be seen by looking at their results for Ni, as well as Mn, which use CC-yields from Nomoto et al. (2013). For both elements they find that the low metallicity part of the sample is not reproduced by any of their models. By fitting the sub-M_{Ch} contribution regardless, they obtain fractions of only $\sim$ 20%. Considering the [Mn/Fe] production from the different SNe Ia channels, this result is not surprising.

To support this statement I show in Fig. 6.1 the equivalent to Fig. 3.8, which sketches how the GCE [Ni/Fe] trend is influenced by the relative contribution of different SNe Ia, but for [Mn/Fe] instead. For simplicity, Fig. 6.1 only shows the most important channels, i.e. the canonical M_{Ch} SNe Ia (left), sub-M_{Ch} double-detonations (middle), and sub-

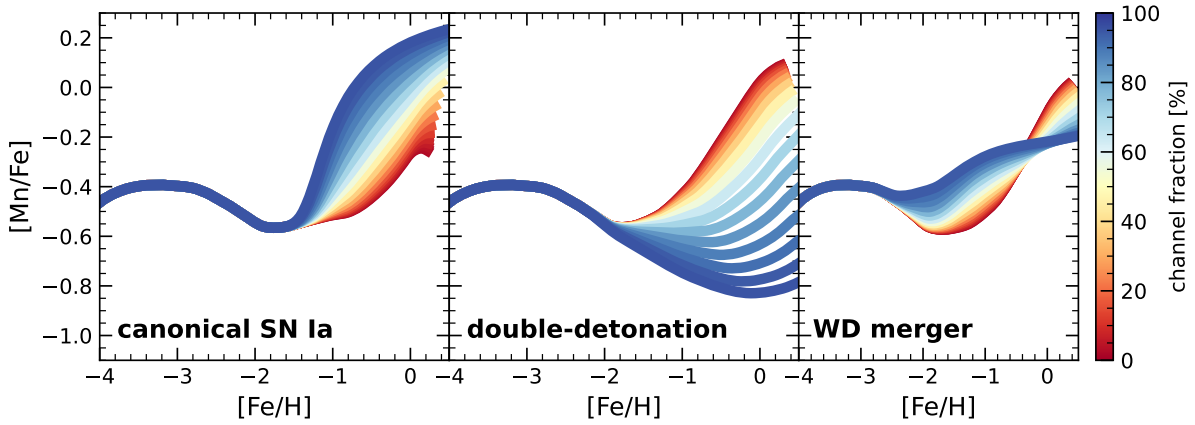

Figure 6.1: Contribution of different SNe Ia channels to the Galactic chemical enrichment. Same as Fig. 3.8, but for [Mn/Fe] and without the M_{Ch} He-donor channel for simplicity. Classical M_{Ch} SNe Ia (left) overproduce Mn relative Fe, while sub-M_{Ch} (middle + right) produce lower [Mn/Fe] ratios. See text.

M_{Ch} WD-mergers (right). In agreement with what was found in Eitner et al. (2020), who used an entirely different chemical evolution model, M_{Ch} SNe Ia support strong, positive [Mn/Fe] gradients above [Fe/H] ~ -1, while large sub-M_{Ch} fractions tend to flatten the [Mn/Fe] vs. [Fe/H] gradient.

By comparing NLTE and LTE data for Mn (Eitner et al. 2020, or Fig. 3.1, top row), one finds that there is a substantial offset at low metallicity between predictions from all CC-yields and the NLTE data, i.e. NLTE [Mn/Fe] abundances are higher than the models predict, the resulting abundance trend with metallicity is flat. If one does not correct this model offset manually (as deliberately not done by Trueman et al. 2025) the best-fitting model needs to exhibit strong gradients in order to reach the solar value. The result is that artificially inflated M_{Ch} are obtained, which is precisely what Trueman et al. find. If the CC-SNe would not systematically underproduce [Mn/Fe], the gradient would be flat and the trends again better represented by the right panels in Fig. 3.1.

A similar result was recently put forward by Alexander & Vincenzo (2025), who attempt to constrain SNe Ia progenitors from Fe-peak abundances in dwarf satellites. By using metallicity-dependent SNe Ia models and an inhomogeneous GCE model to fit the observed [(Mn, Ni)/Mg] abundance patterns and their spread to a sample of Sculptor and Leo I stars in LTE and NLTE, they find that there is no need to include large contributions from sub-M_{Ch} SNe Ia, as their M_{Ch} reproduces observations best. They furthermore find that sub-M_{Ch} SNe Ia in their models underproduce the [(Mn, Ni)/Mg]–[Fe/H] abundance evolution and stress the importance of accounting for inhomogeneous chemical enrichment and metallicity-dependent SNe Ia yields.

However, judging by their Fig. 8 and 9 the models of Alexander & Vincenzo are subject to

the same systematic offset of Mn CC-yields as described above; in NLTE their models fail to describe the low metallicity end of the distribution in both Sculptor and Leo I. The lack of low-metallicity targets in Leo I is unfortunate; however, in their Sculptor data (bottom left panel in their Fig. 8) it is clearly visible. Naturally, as explained above, they arrive at the misconception of high fractions of classical SNe Ia, because they do not correct for this offset. By visually investigating their sub-M_{Ch} model (black contours in the same figure), it appears that after correcting for the offset the model reproduces the observations well. In fact, abundance trend predictions from their complex inhomogeneous models do not appear to be significantly different from what a one-zone model predicts in terms of overall chemical evolution (Fig. 6.1), which is expected since they rely on the same stellar yield data.

In a different study, Nissen et al. (2024) investigate abundances of Fe-peak elements in accreted and in-situ Galactic halo stars. The authors use their sample of chemically well separated stars to derive empirical CC-SNe and SNe Ia yields, which they then compare to predictions from models to estimate how well they agree with their data-based estimates. By using 3D NLTE techniques for Mg, and 1D NLTE for Mn and other elements (Ni however in 1D LTE), Nissen et al. find that the agreement of all CC-yield sources with data is poor.

When investigating SNe Ia the authors find that their data suggests a significant contribution from sub-M_{Ch}, as classical SNe Ia predict too high [(Mn, Ni)/Fe] and too low [(Ca, Ti)/Fe], while double-detonations provide very good agreement. One may note that Nissen et al. arrive at this result without modifying CC-yields from models, which is expected because they derive their empirical SNe Ia yields based on NLTE abundance differences between their high-α and low-α sample directly.

Remarkably, Das et al. (2025) for the first time were able to identify a double-shell of highly ionized calcium in recent observations of the reverse shocked ejecta of SNR 0509–67.5 in the LMC. Using the MUSE optical integral-field spectrograph at VLT, they find two spatially separated Ca shells in the peak surface brightness of Ca XV. According to Das et al. (2025), the outer Ca shell originates from a helium detonation at the base of the progenitor WDs envelope, while the inner shell from the detonation of the C-O core, which is expected from theoretical HD explosion simulations of double-detonation sub-M_{Ch} SNe Ia. The authors interpret their findings as strong evidence for a double-detonation explosion, thus proving that sub-M_{Ch} explosions indeed exist in nature.

Implications for the Hubble-tension

It is not straight forward to interpret the implications of a high sub-M_{Ch} SNe Ia fraction in the context of the Hubble-tension. In the cosmic distance ladder, SNe Ia rely on being standardizable by applying the Phillips relation (Phillips 1993). While the origin of this

relation is not fully understood, it nevertheless allows to infer the absolute magnitude of high-redshift SNe Ia based on measurements of their decay-rate; By observing a sample of low-redshift SNe Ia with independent distance estimates – from e.g. Cepheid measurements (Leavitt & Pickering 1912) or the Tully-Fisher relation (Tully & Fisher 1977) – it is found that their brightness declines faster if they overall are less luminous, while the brightest SNe Ia appear to become fainter on longer timescales (Phillips 1993). Under the assumption that this connection is intrinsic to all SNe Ia and applicable at observations at all redshifts, it is thus possible to derive their absolute brightness by fitting their observed light-curves.

It is important to emphasize that the Phillips relation is empirical and does not inherently presume specifics about individual SNe Ia. According to Shen et al. (2021a), using NLTE radiative transfer simulations for double-detonation sub-M_{Ch} explosions, it was found that the observed Phillips relation aligns well with their model predictions. This suggests that variations in observed absolute brightness, which form the basis of the relation, may arise from different WD masses at explosion, thereby supporting a significant fraction of sub-M_{Ch} SNe Ia (see their Fig. 3). Thus, only systematic deviations from the Phillips relation impact distance estimates and H_0, and these deviations may not be solely attributed to the lower mass of WDs upon explosion.

While there is evidence that especially the faintest SNe deviate from the Phillips relation (Burns et al. 2014), a more detailed study of synthetic light curves of different SNe Ia channels is needed to pin-point those that are not standardizable. Woosley et al. (2007) investigate the influence of M_{Ch} SNe Ia model parameters on the resulting light-curves and find that different input scenarios indeed reproduce observations. However, they also note explicitly that most of their models do *not* follow the Phillips relation, as even models with the same ^{56}Ni mass exhibit different decline rates. Woosley et al. furthermore conclude that the observed scatter is related to the diversity of SNe Ia. It was furthermore found by Taubenberger (2017), that there are observations of peculiar SNe Ia which do not obey the Phillips relations, such as e.g. the faint and yet slowly declining “SN 02es-like” events.

This diversity may have implications for the Hubble-tension, if the corresponding events appear in large numbers and especially if there is an environmental effect, i.e. a change of SNe Ia morphology with redshift. As pointed out by Ruiter & Seitenzahl (2025), low metallicity AGB stars are expected to produce higher mass stellar cores – and thus a heavier WD – than solar metallicity AGB stars. Since the WD mass is an important measure of peak brightness (Ruiter et al. 2013), this implies that more luminous SNe emerging from heavier WD occur at higher redshift, in agreement with standardized observations of SNe Ia from galaxies of different morphological type (Pruzhinskaya et al. 2020).

Since host environment properties are different for galaxies at different redshifts – e.g. the binary fraction or SFR – it is not obvious to what extent frequent SNe Ia explosions in our

neighborhood, that may or may not follow the Phillips relation, also are dominating in high redshift galaxies, where potentially other SNe Ia with non-standard light-curves are more frequent. There is, for example, a potential bias associated with the differences between sub-M_{Ch} and M_{Ch} DTDs. Galaxies that are observed at high redshift in ΛCDM cosmology are younger (they potentially even formed only ∼ 500–700 Myr after the Big Bang in the most extreme cases, according to JWST observations, see Labbé et al. 2023; López-Corredoira et al. 2024). Due to the longer delay-time of M_{Ch} SNe Ia this potentially indicates that more rapid WD mergers or early double-detonation SNe Ia appear in higher frequency in Galaxies of higher redshift. However, this does not necessarily mean that there are systematic offsets in distance measurements, as these events may still be standardizable.

This suggests that a discrimination between sub-M_{Ch} and M_{Ch} SNe Ia alone might not be enough to accurately determine the validity of the SNe Ia standardization. Ideally, chemical signatures from specific SNe Ia sub classes – such as WD-WD mergers of different masses – are extracted from observations of stellar abundances directly, which again stresses the need for precise 3D NLTE abundances from large stellar samples.

6.2 Expanding Applicability of 3D Atmosphere Models

The methods developed for creating 3D atmosphere models presented in this work are applicable to the bulk distribution of FGK-type stellar spectra observed in Galactic surveys. Nevertheless, it is interesting to explore areas where either the current approach has its limitations, and may hence be improved, or where 3D models provide insight beyond what is discussed in this thesis.

Magnetic Fields

One extension of the models presented is the inclusion of magnetic fields. In addition to simulation of stellar chromospheres and/or coronae (Gudiksen et al. 2011; Wedemeyer et al. 2017; Carlsson et al. 2019; Przybylski et al. 2022), it was shown that even in quiet photospheric regions outside of magnetic activity there is magnetic flux caused by turbulent convective flows (Vögler & Schüssler 2007). These small-scale dynamo (SSD) interactions, as well as stronger global magnetic fields, directly influence the atmospheric temperature and density stratification, yielding overall hotter – from negligible differences below ∼ 0.1 % in high-metallicity FGK stars up to ∼ 100 K for lower metallicities or stronger magnetic fields – photospheric layers and potentially weaker cores of spectral lines that form in these regions (e.g. Fabbian et al. 2010; Bhatia et al. 2022; Witzke et al. 2023; Perdomo García et al. 2025).

This atmospheric heating can have a non-negligible influence especially on the molecular

equilibrium, molecular number densities, and the corresponding molecular features, such as e.g. the CH G-band. This may be critical for the study of CEMP stars, which are predominantly very metal-poor – especially in the interesting, CEMP-no dominated Group III – and SSD effects are expected to increase with decreasing metallicity (Witzke et al. 2023). Because these structural differences show a large variability with optical depth, there is possibly a strong interconnection with NLTE, which motivates a comprehensive 3D SSD NLTE study under these conditions. In the current version of `M3DIS`, there are no magnetic fields considered. However, the `DISPATCH` framework already hosts magnetized Riemann solvers, which makes their integration into stellar atmospheres straightforward.

Expanding the Parameter Space

It is furthermore desirable to extend the stellar parameter space of existing 3D model atmosphere grids, especially towards hotter A/B type stars and red giants. In the context of stellar surveys, a very useful first step in this direction is to densely cover the parameter space spanned by existing 1D `MARCS` models (Fig. 2.8) with 3D RHD `M3DIS` models.

A major challenge here is to estimate a suitable initial condition, which serves as the basis of the simulation setup. Due to the numerical efficiency of `M3DIS`, this initial condition can be a 1D `MARCS` model without significant computational time penalties. The precise initial atmospheric structure is not relevant for the resulting simulation. However, two aspects need to be considered; the opacity binning and the bottom boundary condition.

Within the parameter space of an existing 3D grid, such as the `Stagger` grid, a very useful initial condition is obtained from interpolating (e.g. via natural neighbor interpolation) the average structures on the optical depth scale (Sec. 4), from which the geometrical depth can be reconstructed. To explore conditions beyond these limits, an effective method is to extrapolate the entropy at the top and bottom boundaries and construct a semi-realistic atmospheric structure from the results.

One potential realization of such an initial condition extrapolation technique is presented in Fig. 6.2. In panels A to D, density and temperature values at the top (panels A and B) and bottom (C and D) of <3D> `Stagger` models at different metallicities are shown as a function of $\log g$ and $T_{\rm eff}$ (black squares). To allow extrapolation, a functional description is obtained by fitting a cubic regression model (Blaom et al. 2020) to the data in each panel, which enables the approximate computation of the bottom and top entropy for arbitrary $T_{\rm eff}$, $\log g$ and [Fe/H] values, as demonstrated by the application of the best-fit function to randomly selected points (red circles).

The output of the regression function is then used to construct the initial condition for the 3D simulation; an example is shown in panel E of Fig. 6.2 for a grid node of the `Stagger` grid ($T_{\rm eff} = 4500\,\mathrm{K}$, $\log g = 1.5$, $[\mathrm{Fe/H}] = -3$) to allow for a comparison. Starting with the

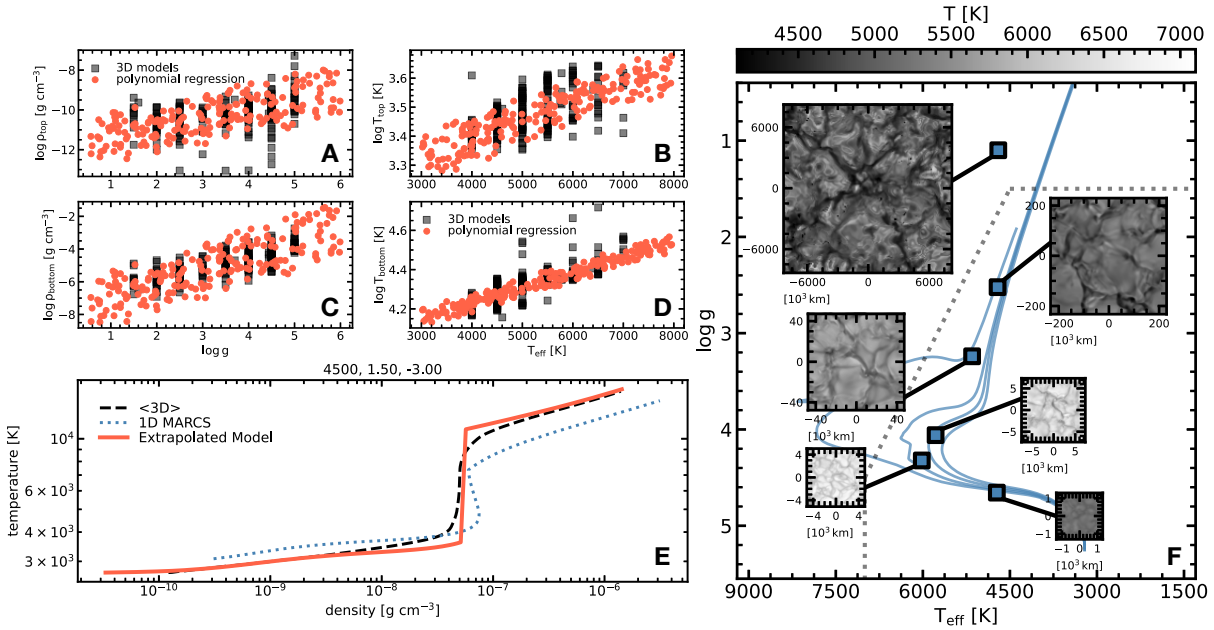

Figure 6.2: Extrapolation method for models outside the parameter space spanned by existing 3D models. Panels A to D: Average density and temperature in the top (panels A and B) and bottom (panels C and D) layers of 3D models in the `Stagger` grid (black) compared to randomly predicted values from a cubic polynomial regression fit (red). Panel E: Example of an initial model obtained from the regression fit (red) compared to a 1D `MARCS` (blue, dotted line) and <3D> `Stagger` (black, dashed line) models with $T_{\rm eff} = 4500\,\mathrm{K}$, $\log g = 1.5$, $[\mathrm{Fe/H}] = -3$. Panel F: Demonstration of an example use-case of the extrapolation method in the Kiel diagram. Blue squares correspond to `M3DIS` model atmospheres computed for stellar parameters along solar metallicity Dartmouth (Dotter et al. 2008) isochrones (blue lines in the background). For each point, the connected inset figures shows the temperature structure at the optical surface. Note the vastly different sizes of different models as indicated in the axis labels (image sizes are increased for increasing model size, however not to scale for visualization purposes). The model at the top of panel F with the lowest surface gravity ($T_{\rm eff} = 4700\,\mathrm{K}$, $\log g = 1.1$, $[\mathrm{Fe/H}] = -4.5$) was obtained from the extrapolation procedure, as it resides outside the `Stagger` grid (gray, dotted line indicates the grid boundaries).

bottom density and temperature obtained from the fit, the initial condition is constructed by integrating upward adiabatically (following the method presented in Sec. 4.3.4).

In principle, the adiabat constructed in this way may already be used as a starting approximation, since the bottom entropy is the decisive quantity that determines the final atmospheric stratification. However, it is crucial to also determine the size of the computation domain and the approximate geometrical height of the optical surface. One way to estimate the extent of the simulation is to expand from the closest known grid point, using the scaling of pressure scale height with stellar parameters (Magic et al. 2013a). Another way is to simply continue integrating the adiabat until the structure reaches the expected values from the extrapolation at the top, which provides the corresponding geometrical extension

of the atmosphere in hydrostatic equilibrium automatically.

Once a specific optical depth is surpassed, the true atmospheric structure is increasingly non-adiabatic (see Eq. 2.21). Although this does not impose a relevant problem for relaxation in M3DIS, it potentially has an impact because the opacity binning is based on this initial structure. To minimize the associated inconsistencies, a MARCS model – shifted in temperature and density to match the extrapolated quantities at the top of the atmosphere – can be used to replace the adiabat in photospheric layers.

The final result is shown as the solid red curve in Fig. 6.2, panel E. It should be noted that, generally, this procedure is designed to yield an approximate initial condition that results in a robust full 3D model atmosphere with similar effective temperature. Archiving a specific value with high precision may still involve fine-tuning of the bottom entropy. However, when constructing a grid of random models, this additional step is not necessary, making this procedure very useful to efficiently produce models outside the domain of available model grids, which then in turn may be used to interpolate between to obtain more precise initial conditions when required.

Beyond the potential of this extrapolation technique for expanding 3D model grids in the near future, it presently is applied in practice in the context of recent work by Ji et al. (in prep.), who identify and derive the detailed chemical composition of one of the most metal-poor red giant stars ever observed using M3DIS stellar atmosphere models. One of the model atmospheres computed in the course of this project (with parameters $T_{\rm eff} = 4700\,\mathrm{K}$, $\log g = 1.1$, and $[\mathrm{Fe/H}] = -4.5$) is shown in the top left of Fig. 6.2, panel F. Specifically, I show this red giant model in the Kiel diagram compared to other, solar metallicity M3DIS MS and sub-giant models (see Sec. 6.4 below for more details) on top of solar-metallicity Dartmouth (Dotter et al. 2008) isochrones.

The stellar parameters of this target place it outside the Stagger grid (outer edge indicated by the gray dotted line), which means extrapolation methods such as those described above are required. Due to the design of M3DIS as efficient end-to-end pipeline, input stellar parameters – including a potential chemically peculiar composition – can be converted to a stable red giant model in $\lesssim 50\,000\,\mathrm{CPU\text{-}h}$ from scratch, without significant fine-tuning involved. Note that the timescales for red giant models are significantly larger compared to the models presented in Sec. 4, as the intrinsic timescales associated with the convective turnover within red giant atmospheres increases (due to the larger pressure scale height, see also the size difference of models in Fig. 6.2, panel F as indicated in the axis labels) and thus are of physical nature rather than numerical. It will be very interesting to analyze potential implications on stellar abundance diagnostics for a larger sample of stars using M3DIS red giants models in the future.

The extrapolation method is naturally applicable to various regions of the parameter space.

In exoplanet research, for example, there is particular interest in simulating M dwarf atmospheres because of their smaller mass, radius, and luminosity, which results in habitable zones closer to the star, making planet detections through transit or radial-velocity measurements more likely (Olander et al. 2021). The atmospheres of M dwarfs are expected to exhibit significant dynamics over short periods (Wedemeyer et al. 2013), making 3D studies interesting. However, due to their low temperatures, attention must be paid to the molecular opacities of complex molecules such as TiO and VO, which play a crucial role in the modeling of these stars, despite being minor in FGK-type stars (Perdomo García et al. 2023).

When expanding towards the hotter end of the distribution (A-, B-, or O-type stars), the strength of the radiation field increases significantly, which means the LTE assumption starts to break down (Sander 2017). While a full 3D NLTE atmosphere simulation is currently not feasible, it may be interesting to explore to what extent 1D NLTE methods may be used to include departures at least approximately. One example for such a simplified NLTE treatment could be realized by computing opacity and source function departures based on a time-local <3D> snapshot as the full 3D simulation progresses, which may then be used to correct the wavelength-dependent LTE opacity table on the fly. This is especially useful for the H^- continuum (or H in hotter stars), but it may also be applied to line opacities from other species. It remains to be tested to what extent this approximation constitutes an improvement over LTE. For more extreme O-type stars, there additionally is a non-negligible radiative acceleration term that needs to be included in the momentum equation – as well as considerable line-driven winds – which makes the application of `M3DIS` to this parameter space more challenging (see e.g. Sander et al. 2017).

Exploring the Time Domain

Due to their dynamic nature, 3D atmosphere models furthermore provide direct access to the time dependence of stellar observables. As the model progresses in time, the atmospheric structure is continuously adjusted. The strength of this effect depends on the specific observable. As an example, I present an overview of the time variability of different aspects obtained from spectra of a solar `M3DIS` simulation in Fig. 6.3 and Fig. 6.4.

From the left image of Fig. 6.3 it becomes clear that even relaxed stellar atmospheres are not static. To highlight this, in panel A, I show how the spatially averaged 3D temperature stratification changes between snapshots of the same simulation as time passes, as a function of optical depth. Each (blue) line here corresponds to the difference between the temperature profile T_t of a snapshot at time t and the time average $< T >_t$, i.e. $\Delta T = T_t - < T >_t$.

Because the atmosphere is not static, the temperature fluctuates, especially towards the upper boundary. Although at optical depth $\log \tau_{ross} \sim -6$ most of the snapshots deviate

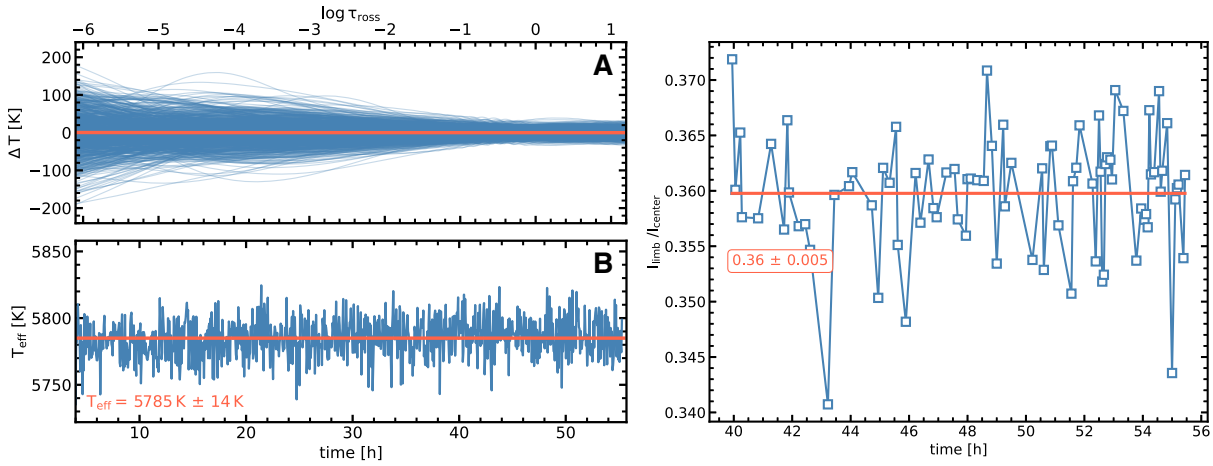

Figure 6.3: Time variability of different properties obtained from time sequence of a solar 3D M3DIS model atmosphere. Left (A): Time evolution of the average temperature stratification as a function of optical depth, relative to the time average. Left (B): Effective temperature evolution as determined from the bolometric flux at the surface of each snapshot. Right: Limb-darkening as a function of time. $I_{\rm limb}$ corresponds to $\mu = \cos(\theta) = 0.2$, $I_{\rm center}$ is the disk center at $\mu = \cos(\theta) = 1$.

between $\lesssim \pm 100\,$K around the time average, two randomly selected individual snapshots may be $\sim 400\,$K apart from each other. The average difference, as well as the deviation around the mean, decreases with increasing optical depth and becomes negligible below the photosphere, where $\Delta T \lesssim 20\,$K. Deeper in the atmosphere, the absolute temperature also rises, which means that the relative deviation among snapshots becomes even smaller.

This optical depth gradient manifests itself in the time dependence of observables that are sensitive to different atmospheric layers. An example of this is shown in panel B of Fig. 6.3, where $T_{\rm eff}$ is shown as a function of time for a relatively long time series of the 3D M3DIS solar model between 5 and 55 stellar hours. In contrast to 1D HE models, it is not constant because the bolometric flux itself is not constant. It may be seen that $T_{\rm eff}$ fluctuates on average 14 K around the mean, on a time scale comparable to the time spacing between individual snapshots, i.e. individual points in this figure. Because the effective temperature is mostly influenced by the layers close to the continuum ($T(\tau = 2/3) = T_{\rm eff}$ in the Eddington approximation of a gray atmosphere), the scatter observed in panel B is very similar to the temperature fluctuations in panel A around the optical surface (at $\log(\tau = 2/3) \approx -0.2$).

Another example can be found in the right panel of Fig. 6.3. Here, I show the corresponding time evolution of the limb-darkening ($I_{\rm limb}/I_{\rm center}$) as obtained from the angle-dependent intensity I at $\mu = 1$ (center) and $\mu = 0.2$ (limb), integrated over the spectral window between 3600 Å and 4000 Å. Because every angle μ probes a different atmospheric layer, angle-dependent intensities are subject to a different time evolution, which means that the limb-darkening changes as a function of time.

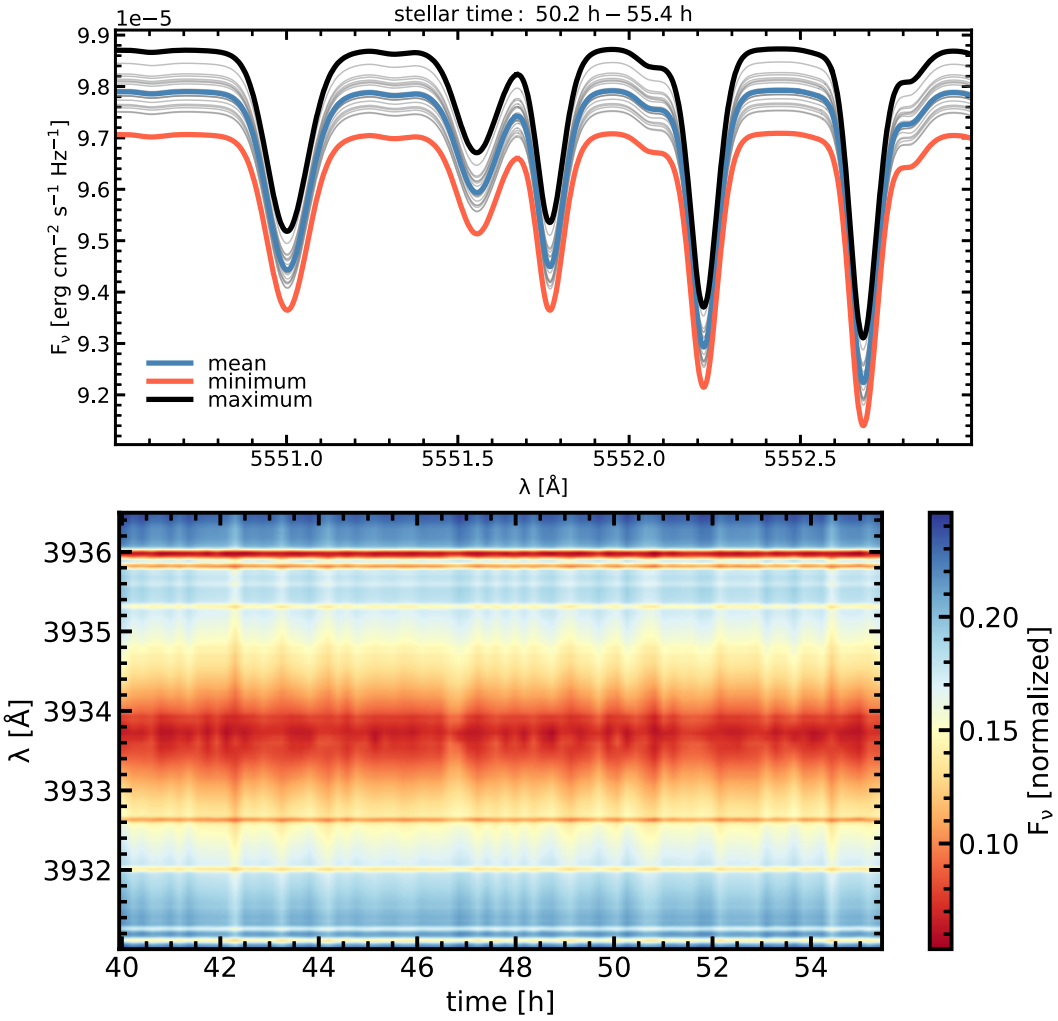

Figure 6.4: Time variability of observables from a solar 3D `M3DIS` model atmosphere. Top: Time variability of weak spectral lines and the continuum. Different snapshots are shown in gray. Mean (blue), maximum (black) and minimum (red) flux are overplotted. Bottom: Variability of the normalized flux in the core of the Ca II K line. The vertical axis corresponds to wavelength λ, horizontal axis shows the stellar time. Color corresponds to the normalized flux. Note that the Ca II K is very wide, which is why only the core region is shown here and the color scale does not reach the continuum.

In the specific case shown here, the spectrum at $\mu = 0.2$ darkens to about 36 % (on average) of the disk-center intensity, with a standard deviation of 0.5 % due to atmospheric dynamics. In extreme cases the limb-darkening varies by up to 2.5 % in a time span of $\sim$ 1 h. Note that the time sequence investigated in this image is significantly shorter (between 40 and 55 stellar hours) than in panel A and B because the CLVs are computed with high spectral resolution in post-processing, which is computationally expensive.

The impact of stellar variability is also visible in individual spectral lines. The top panel of Fig. 6.4 shows the absolute solar 3D model flux in the arbitrary optical wavelength window between 5550.5 Å and 5553.0 Å, where the influence on weak spectral lines is visualized by showing different snapshots, covering the same time span as in the right panel of Fig. 6.3.

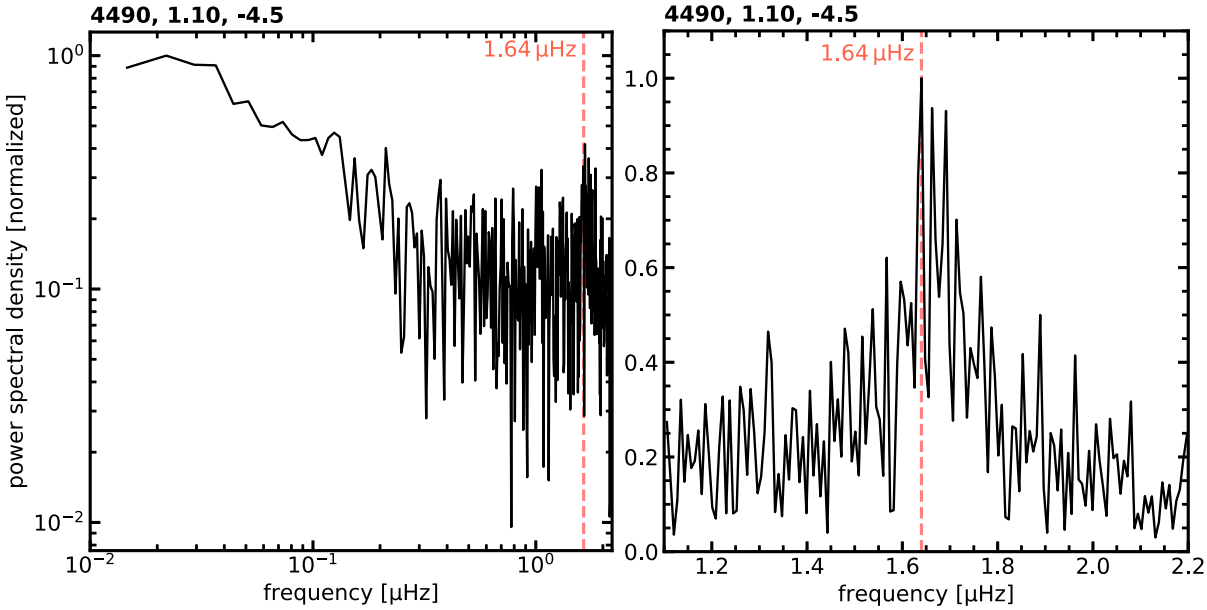

Figure 6.5: Fourier transformation of the bolometric flux from a red giant M3DIS stellar atmosphere model with stellar parameters $T_{\rm eff} \approx 4500\,\mathrm{K}$, $\log g = 1.1$, and $[\mathrm{Fe/H}] = -4.5$. Left: normalized power spectral density as a function of oscillation frequency obtained from surface flux in a log-log plot. Right: Zoom-in to the frequency interval where $\nu_{\rm max}$ is expected from theoretical scaling relations (e.g. Themeßl et al. 2018; Yu et al. 2018, estimate shown as red vertical line in both panels). To reduce granulation noise, the power spectrum deeper in the atmosphere is shown here.

Due to their low opacity, these lines form close to the continuum, which means the vertical shift that one may observe here is mainly reflecting the time evolution of the effective temperature. When continuum-normalizing the spectrum, the time dependence thus becomes negligible, with small effects towards the line core. For stronger lines, the situation is different. To motivate this, I show the time evolution of the normalized Ca II K line core region between 3931 Å and 3936.5 Å in the lower panel of Fig. 6.4. In this image the normalized flux is shown in color, the vertical axis corresponds to wavelength, and the horizontal axis to time. Due to the strength of the Ca II feature – spreading from the red line core region in the center of the image towards the blue line wings further out – the formation height is shifted towards higher atmospheric layers, which is why brightness variations at different wavelengths are sensitive to the stronger atmospheric temperature fluctuations at lower optical depth and thus visible also in the normalized spectrum.

Solar-like Oscillations

Because these fluctuations stem from the intrinsic convective flow pattern in the atmosphere, it is furthermore very interesting to investigate the periodicity of the simulated time sequence by translating it into Fourier space and to analyze the power spectral density as a

function of oscillation frequency. A study of this kind is useful because so-called *solar-like* oscillations – which are a powerful tool in global asteroseismology to infer stellar masses and radii from the frequency of maximum power $\nu_{\max}$ and mean large frequency spacing $\Delta\nu$ (e.g. Yu et al. 2018) – are stochastically excited by turbulent gas motions in the upper layers of stars (Hekker et al. 2011; Chaplin & Basu 2008) and thus, in principle, are contained in the time sequence of 3D stellar atmosphere simulations (Zhou et al. 2019).

To motivate the applicability of `M3DIS` models in this context, I show the power density spectrum obtained from the time sequence of an example red giant model with parameters $T_{\rm eff} \approx 4500\,\mathrm{K}$, $\log g = 1.1$, and $[\mathrm{Fe/H}] = -4.5$ in Fig. 6.5. In the left panel of this figure, the Fourier transformation of the logarithmic outgoing, angle-integrated, horizontally averaged, bolometric flux is shown as a function of logarithmic frequency. As expected, lower frequency regions are dominated by stochastic background noise from e.g. granulation (see Hekker et al. 2011, their Fig. 6). Toward higher frequencies, individual peaks of high power are visible. It is interesting to note that the maximum power is found around $\nu_{\max} \sim 1.64\,\mu\mathrm{Hz}$, which – depending on the assumed solar value – coincides with the expected location from scaling relations (e.g. Themeßl et al. 2018; Yu et al. 2018, the $\nu_{\max}$ prediction from scaling relations is indicated as red, dashed line here). This can especially be seen in the zoom-in around this location shown in the right panel of Fig. 6.5, where I show the flux deeper inside the atmosphere to reduce the noise associated with granulation.

Although a detailed asteroseismic investigation of the oscillation pattern requires more work (see e.g. the comprehensive analysis by Zhou et al. 2019) that is beyond the scope of this thesis, the fact that `M3DIS` models are able to develop solar-like oscillations naturally is reassuring and may be utilized to either predict the distribution of granular noise, or generally even $\nu_{\max}$ and $\Delta\nu$, from first principles. However, it should be noted that there is significant additional computational complexity involved. To obtain the data shown in Fig. 6.5, the giant model has evolved for a long time sequence of $44\,000\,\mathrm{h} \approx 5\,\mathrm{yr}$ stellar time. During this period ~ 800 snapshots have been stored with a spacing of $\sim 55\,\mathrm{h}$, which means that the frequency domain associated with time intervals smaller than that value has not been sampled.

Longer time series are furthermore required to better constrain the low-frequency end. Note that especially increasing the length of the time series involves significantly more computation resources, while a smaller time-separation to first order only requires more disk space. In addition, it has to be ensured that the acoustic cavity associated with the depth of the convective zone included in the simulation domain is covered for the modes of maximum power, which may require the inclusion of deeper layers that are usually omitted to ensure computational resources are spent on the photospheric layers.

Connection to Exoplanets

Regardless of the complexity involved, a systematic study of model oscillation modes is desirable, especially in exoplanetary science. Here, knowledge of planetary host parameters, such as stellar masses and radii – which are determined from solar-like oscillations, is crucial for extracting information about the planet from observations of the star-planet system (Batalha et al. 2011; Huber et al. 2013).

In the same context, it is additionally interesting to investigate to what extent the described limb-darkening modulations (Fig. 6.3) matter when modeling planetary transits (Klevas et al. in prep.). It is important to point out that the physical extent of 3D box-in-a-star models covers only a small part of the stellar surface, as they span only $\sim$ 10 granules. In the case of an Earth-Sun-like planet-star system, this means that upon transit the planet (radius $\sim$ 6 000 km) covers a surface area comparable to the horizontal extend of the simulation domain. If the size of the star increases, the size of granules increases ($\sim H_\mathrm{p} \sim T/g$), which means that for sub-giants and/or hotter stars the planet may cover only a single granule or less.

Assuming that the entirety of the stellar surface constitutes many of these model atmosphere boxes – distributed randomly at different points in their time evolution – the time variability of the model can be translated to a space variability. Thus, when the star is observed as a point source, the entire time sequence is observed in one instance and manifests itself as scatter around the mean brightness.

The impact of time variability on the resulting transit light-curve depends on the parameters of the star, the duration of the transit, and the convective pattern speed; Considering a static planet at a random location in-transit, the convective pattern that is blocked behind it evolves as shown in Fig. 6.3. The result is that at a certain time the planet covers darker inter-granular lanes and at a later time brighter granules, which causes the overall darkening of the observed system to fluctuate. If the underlying convective pattern changes on timescales much shorter than the transit of the planet, this may introduce significant scatter at a given position in the light-curve. The degree of fluctuation depends on the μ-angle and the wavelength at which the transit is observed, as different atmospheric regions are sampled (Fig. 6.3). If the system is observed for longer, the convective pattern changes during exposure, which means a longer time sequence is sampled and the resulting mean brightness is less sensitive to outliers.

In the opposite extreme, where the convective timescale is longer than the transit duration, the planet samples the time evolution by moving across a nearly static background star, which reduces the scatter associated with individual points in the light-curve but effectively stretches the fluctuations across the entire transit. For observed exoplanetary systems the truth lies in between these extreme cases; nevertheless, it has been shown that – in the

specific case of a solar-like star, where transit duration ($\sim$hours) and convective pattern speed ($\sim$ 10 min) are comparable – there is a notable influence on the parameters derived from transit light-curves, such as the planetary radius (Chiavassa et al. 2017). Thus, a deeper understanding of observations is only possible by using 3D models.

In addition to the time domain, 3D models are essential when modeling the average CLV and deriving model limb-darkening coefficients, which are important when fitting observed light-curves to estimate planetary radii (e.g. Csizmadia et al. 2013). By modeling the CLV in the sun and comparing it with resolved observations of the solar disk, it was shown that, depending on the spectral line, 1D models exhibit an EW-μ dependence that is not in agreement with observations, yielding an effective abundance gradient when fitting angle-dependent spectra, while 3D NLTE synthetic spectra reproduce CLV observations to a satisfactory degree (see e.g. Lind et al. 2017; Bergemann et al. 2021; Pietrow et al. 2023; Storm et al. 2024, for investigations of Fe, O, Eu, and Y lines).

Canocchi et al. (2024) make the connection to planetary observations by analyzing the resonance Na I D_1 and K I 7699 Å lines in the Sun in 3D NLTE. They find that the CLV discrepancy between 3D and 1D models is comparable to the depth of the absorption feature in transmission spectroscopy of a Jupiter-Sun system, which also underlines the necessity for 3D models of stellar atmospheres in planetary science. To enable this kind of analysis for a large number of exoplanet host stars, which will be observed by PLATO, an extensive grid of 3D model atmospheres is needed to accurately determine limb-darkening coefficients.

6.3 The Origin of CEMP-no stars

It is interesting to revisit the 3D corrected Galactic distribution of CEMP stars presented in Sec. 5 in the context of the Yoon-Beers diagram morphology. Specifically, I recall the shift of CEMP groups between 3D and 1D; I find a substantial net downward shift in 3D A(C) abundances in stars of Group III, which may be accounted for by a tilt of the ellipse in Fig. 5.8. In other words: The A(C) of CEMP-no stars in Group III is metallicity dependent in 3D. Although this provides a good agreement with the observed distribution, the question arises as to what extent this agrees with the proposed CEMP-no formation scenarios of Yoon et al. (2019).

An connection between CEMP formation channels and their chemical composition was originally made by Spite et al. (2013), who compile the C abundances of CEMP MS and turn-off stars from the literature and complement their sample with an analysis of UVES spectra (Dekker et al. 2000) obtained from selected targets. When investigating the morphology of their stars in the Yoon-Beers diagram, Spite et al. (2013) notice that CEMP stars appear to exhibit a bimodal, band-like structure, where CEMP stars with [Fe/H] $\gtrsim -3.5$ form a

high-C plateau with constant A(C) ~ 8.25 close to the solar value. Stars in this region of the parameter space furthermore show neutron-capture enhancement, which classifies them as CEMP-s or CEMP-r/s stars. Within this high-C region, furthermore, no obvious metallicity dependence of A(C) is visible. In contrast, Spite et al. (2013) find that at lower metallicities, [Fe/H] $\lesssim -3.5$, CEMP stars rather reside in a low-C plateau with A(C) ~ 6.8 and are predominantly CEMP-no stars. They conclude that stars in the high-C band obtained their C via mass transfer from an AGB companion (i.e. an *extrinsic* enrichment) and CEMP-no stars in the low-C band formed from the ejecta of massive star explosions (i.e. the enrichment is *intrinsic*).

This band structure was later confirmed by (Bonifacio et al. 2015), who measure C abundances from the G-band seen in X-Shooter and UVES spectra and qualitatively find the same morphology (their Fig. 6), leading them to an interpretation of CEMP formation similar to what was proposed by Spite et al. (2013). A similar result was also obtained by Hansen et al. (2015) in their analysis of high-resolution UVES spectra of 39 stars with $-4 \lesssim$ [Fe/H] $\lesssim -2$, although they notice the presence of a transition region between both bands – as well as a contamination of the high-C band with CEMP-no stars – which challenges the distinct formation picture.

In the study by Yoon et al. (2016), who compile a sample of 305 CEMP stars with [Fe/H] < -1 and abundance information from high-resolution spectra, a qualitatively similar behavior is seen in the Yoon-Beers diagram, however they find a more complicated sub-structure, which leads them to the three-group classification scheme discussed in Sec. 5.

Later, Yoon et al. (2019) investigate CEMP-no populations in the halo, as well as satellite galaxies, and find that Group III CEMP-no stars most likely formed from a mono-enriched gas cloud, which was polluted with [C/Fe] enhanced material ejected from a single faint SN event of a massive Pop III star. They further theorize that CEMP-no stars from Group II have been multi-enriched by several normal CC-SNe of Pop II stars. Yoon et al. (2019) conclude that the strong correlation they find between A(C) (as well as A(Mg) and A(Na), see Yoon et al. 2016, their Fig. 4) and [Fe/H] in their sample of Group II stars is evidence for their accretion from chemically evolved, massive dSph-like systems, while the higher A(C) values and no A(C)-metallicity dependence of Group III hint towards low-mass, chemically more simple, UFD-like systems as their birthplace (Yoon et al. 2019, their Sec. 7).

Given our revised 3D CEMP distribution, it is necessary to examine whether the core assumptions for their conclusions are still valid. For this purpose I show in Fig. 6.6 the Yoon-Beers diagram with the same abundance data as Fig. 5.8, however, this time I do not impose the Yoon et al. CEMP grouping but rather interpret the distribution as two C-bands, as originally done by Spite et al. (2013). In 1D (left) as well as in 3D (right) I use a generic Gaussian

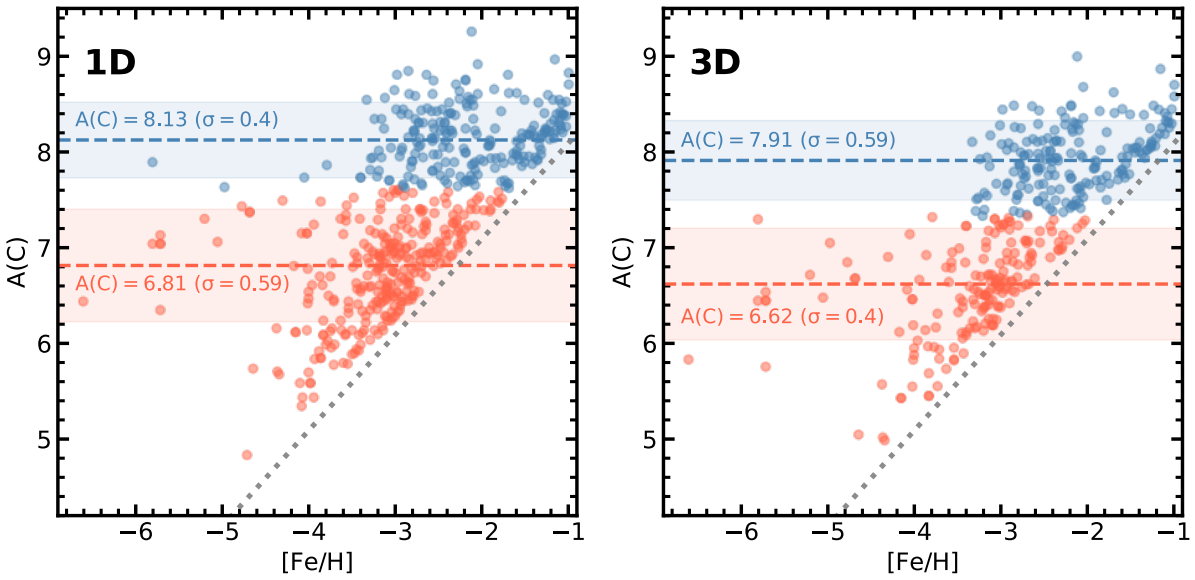

Figure 6.6: Yoon-Beers diagram of the metal-poor MS and sub-giant SAGA sample from Sec. 5, but interpreted in the band-like picture from Spite et al. (2013). Left: 1D LTE, right: 3D LTE. In 1D LTE, there is a non-negligible set of stars in the overlapping region between high-C (blue) and low-C (red) bands, suggesting a third group of stars in agreement with Yoon et al. (2016, 2019). In 3D, the metallicity dependence of 3D−1D abundance correction causes the distribution to shift in a way that substantially weakens the evidence for a third CEMP group. See text.

Mixture Model[1] (GMM) to group stars into a high-C (blue) and low-C (red) band based on their A(C) alone. The corresponding mean A(C) is shown as a dashed line in the respective color, while the shading indicates the 1–σ interval.

For the 1D data (left panel), the automatic GMM algorithm places the high-C band at A(C) = 8.13 ± 0.40 and the low-C band A(C) = 6.81 ± 0.59, which is similar to the values found by Spite et al. (2013). However, in agreement with Yoon et al. (2016) I find significant overlap between both bands, as there appears to be a number of stars at low metallicity that reside in between both bands and do not seem to coincide with either of the two populations. It may especially be noticed that the bulk of stars in the low-C band lie somewhat below the average, which would make these intermediate stars outliers of both populations. This indicates that there is indeed evidence for a third group of stars with intermediate A(C) and low [Fe/H], which is in-line with Yoon et al. (2016).

When investigating the 3D-corrected sample (right panel), the situation changes. The differential A(C) 3D corrections lead to a re-distribution of low-metallicity stars in the high-C band towards the low-C band. Not only that, the low-C band preferentially loses stars at the low-A(C) end – because they exhibit lower metallicities and hence larger 3D corrections – which effectively moves the mean of both bands slightly closer together. The combination

[1] publicly available at https://github.com/davidavdav/GaussianMixtures.jl

of both effects significantly reduces the overlapping region between both bands and, hence, causes the overall distribution to be in better agreement with the simple bimodal structure from Spite et al. (2013) than in 1D; the former CEMP-no Group II and III stars lie within the statistics of the low-C band, while Group I CEMP-r/s stars remain associated with the high-C band. Even the metallicity limit agrees with what was found by Spite et al. (2013), as in this classification there appears to be no star in the high-C band beyond metallicity $[\mathrm{Fe/H}] \lesssim -3.5$.

A more extensive analysis is needed to judge whether this is in agreement with the premise on which the conclusions of Yoon et al. (2019) are based. Generally, the variation of A(C) in the low-C band in our 3D data can equally well be explained as scatter around the mean value of $\mathrm{A(C)} = 6.62 \pm 0.4$, which means that there is no systematic metallicity dependence within this sub-group. Based on A(C) alone, there is therefore no need to assume a different enrichment channel for the Group II and III stars, as they revolve around the same average of the low-C band. Following this line of reasoning, the scenario originally proposed by Spite et al. (2013) and (Bonifacio et al. 2015) – in which enrichment by faint SNe causes the low-C plateau, whereas the high-C plateau is created by AGB stars – seems equally plausible. The average A(C) values of Group II and III now coincide, which means that there is no evidence for a different degree of A(C)-dilution by primordial gas in satellites of different mass, as proposed by (Yoon et al. 2019).

Even if the CEMP grouping is not adjusted, i.e. Group II and III are kept separate, 3D corrections cause an increasing A(C) gradient within Group III. This alone goes against the proposed scenario by (Yoon et al. 2019), where the absence of this gradient is interpreted as evidence that Group III stars form in chemically simple, UFD-like systems.

A detailed investigation of Mg and Al abundances has to be conducted in order to find out if there is a significant difference noticeable between the former Group II and III stars. It may be noted, however, that there is a 3D-bias in their distribution as well; especially when looking at Fig. 3 from Yoon et al. (2016), the expectation from C-corrections alone would be that the lower metallicity Group III stars shift towards Group II in the bottom panels, which causes them to blend together also in this parameter space.

Note that this shift would *not* remove potential differences in A(Mg) as seen in the right panels of their Fig. 4. However, it is not obvious to what extent these differences are indeed related to a different formation environment and a potential accretion history, or may instead reflect multi-enrichment pollution by normal CC-SNe as metallicity increases (Hartwig et al. 2018). A larger sample of high-resolution spectra of low-metallicity stars and the subsequent 3D NLTE analysis of CH – as well as Mg and Na – are needed to resolve these issues. The upcoming 4MOST survey is expected to provide this data in the near future, which will, in combination with the 3D NLTE tools developed in the course of this

thesis, make such an analysis possible.

It is important to note that I do not discriminate between CEMP-r/s and CEMP-no here because of the sparse availability of Ba and Eu measurements. It is thus not possible to evaluate to what extent there is a contamination of CEMP-no stars in the high-C band and CEMP-r/s or CEMP-s stars in the low-C band. However, I emphasize that also Yoon et al. (2016) find that each CEMP group contains CEMP sub-classes that do not coincide with the majority sub-class in this group. A extended 3D NLTE analysis of neutron-capture elements in metal-poor stars is needed in order to decide if the mixing is indeed there and statistically significant.

It has to be stressed that the results presented here are derived in LTE, for 3D and 1D models. Currently, there is no comprehensive 3D NLTE analysis of the CH molecule in metal-poor stars (although see Hoppe et al. subm. for the first 3D NLTE analysis of the Sun, using the solar `M3DIS` model presented in this thesis). The first 1D NLTE study was carried out by Popa et al. (2023), who use their newly developed model of the CH molecular structure to analyze the statistical equilibrium in the atmospheres of cool red giants for a range of different metallicities. They find that – due to its low dissociation energy – over-dissociation is the driver of NLTE departures, which leads to a higher destruction probability of CH molecules, a weaker G-band, and hence positive NLTE abundance corrections of ~ 0.2 dex at $[\mathrm{Fe/H}] = -4$, and ~ 0.05 dex at solar metallicity. Popa et al. (2023) furthermore investigate the dependence of abundance corrections on the assumed C abundance in the synthesis of the spectrum itself, and show that the effect is small and negative, decreasing the correction by ~ 0.05 dex at $[\mathrm{C/Fe}] = 3$. A dedicated 3D NLTE study of a sufficiently large sample of metal-poor stars is needed to make any quantitative statement.

6.4 On-The-Fly 3D NLTE Spectra for 4MOST & PLATO

Large spectroscopic surveys are set to uncover the Galactic history in unprecedented detail. The quality of observational instruments and data is constantly improving, enabling high-resolution, high signal-to-noise spectroscopic observations of millions of stars. Although 3D NLTE methods are advancing, they are still confined to small-scale analyses. A full 3D NLTE analysis of the entire Galaxy holds great promise; however, such an investigation is not yet possible.

The techniques developed by Ting et al. (2019), Kovalev et al. (2019), and Gerber et al. (2023) constitute an important advance in the right direction, as they implement interpolation techniques that remove the time constraints imposed by the solution of the statistical equilibrium, transitioning from 1D LTE to on-the-fly 1D NLTE abundance determination for selected elements that are applied to millions of stars efficiently. This methodology po-

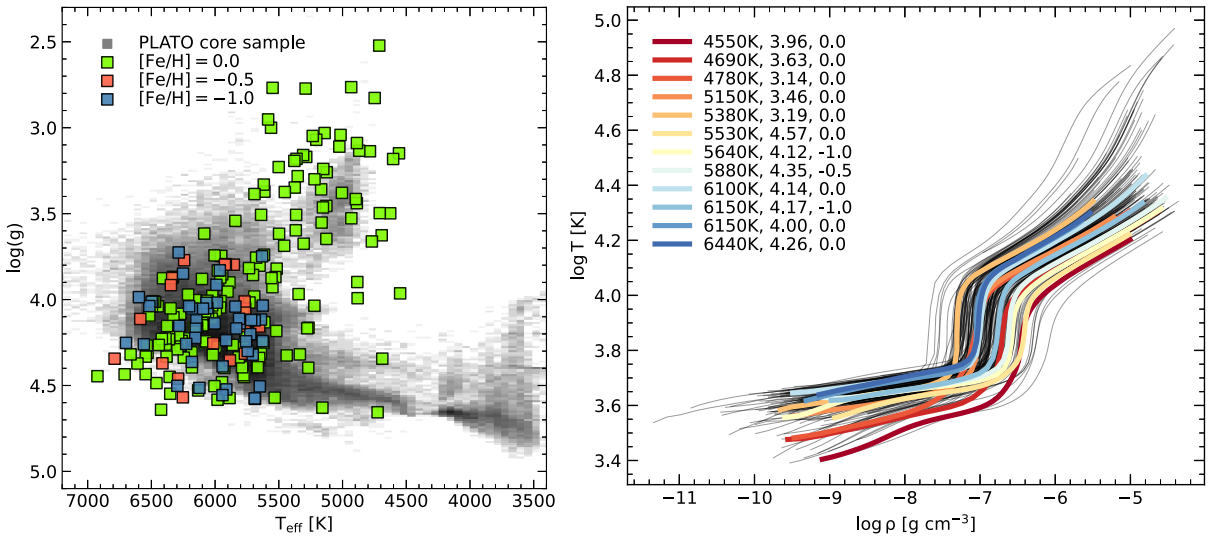

Figure 6.7: Left: Location of stellar atmosphere models (in color) of the first M3DIS sub-grid, randomly sampling the PLATO core targets (gray) in the Kiel diagram. Right: Average temperature-density structure of models in the M3DIS PLATO sub-grid (black). Randomly selected models are highlighted in color. Stellar parameters $T_{\rm eff}$, $\log g$, [Fe/H] are shown in the legend.

tentially extends to 3D LTE and eventually 3D NLTE spectrum synthesis. Similarly to 1D, the initial requirement in 3D is to develop dense grids of model atmospheres. Magic et al. (2013a) and Rodríguez Díaz et al. (2024) contributed to this by creating the first grid of 3D STAGGER atmospheres. Although this is an essential start, Fig. 2.8 shows the rather sparse grid resolution that limits its practical application in large surveys.

An important survey where 3D NLTE spectra are crucial is the PLATO space mission, which is planned to be launched towards Lagrange point L2 in 2026 (Rauer et al. 2014). The PLATO science mission revolves around the investigation of exoplanets in the habitable zone around solar-like stars, and will for this purpose also aim to study the corresponding host stars.

Due to its target selection strategy, PLATO is expected to observe primarily MS and sub-giant stars with stellar parameters and chemical composition similar to those of the Sun. For accurate modeling of stellar spectra, which in the case of PLATO will be provided via the synergy with the 4MOST survey, a grid specifically sampling the distribution of stars in the PLATO core sample is needed. Although there were additions to the STAGGER grid that aim to fill existing gaps in this region of the parameter space, the number of models remains comparably low.

This is precisely where DISPATCH comes in; Due to its unprecedented speed and streamlined pipeline – targeted at computing a large number of models and spectra in a short period of time – it is the ideal tool to provide 3D models that may be used to derive stellar parameters for PLATO targets. To showcase the capability of M3DIS, Fig. 6.7 summarizes the first grid of M3DIS 3D model atmospheres that were already computed at the time of writing, mainly

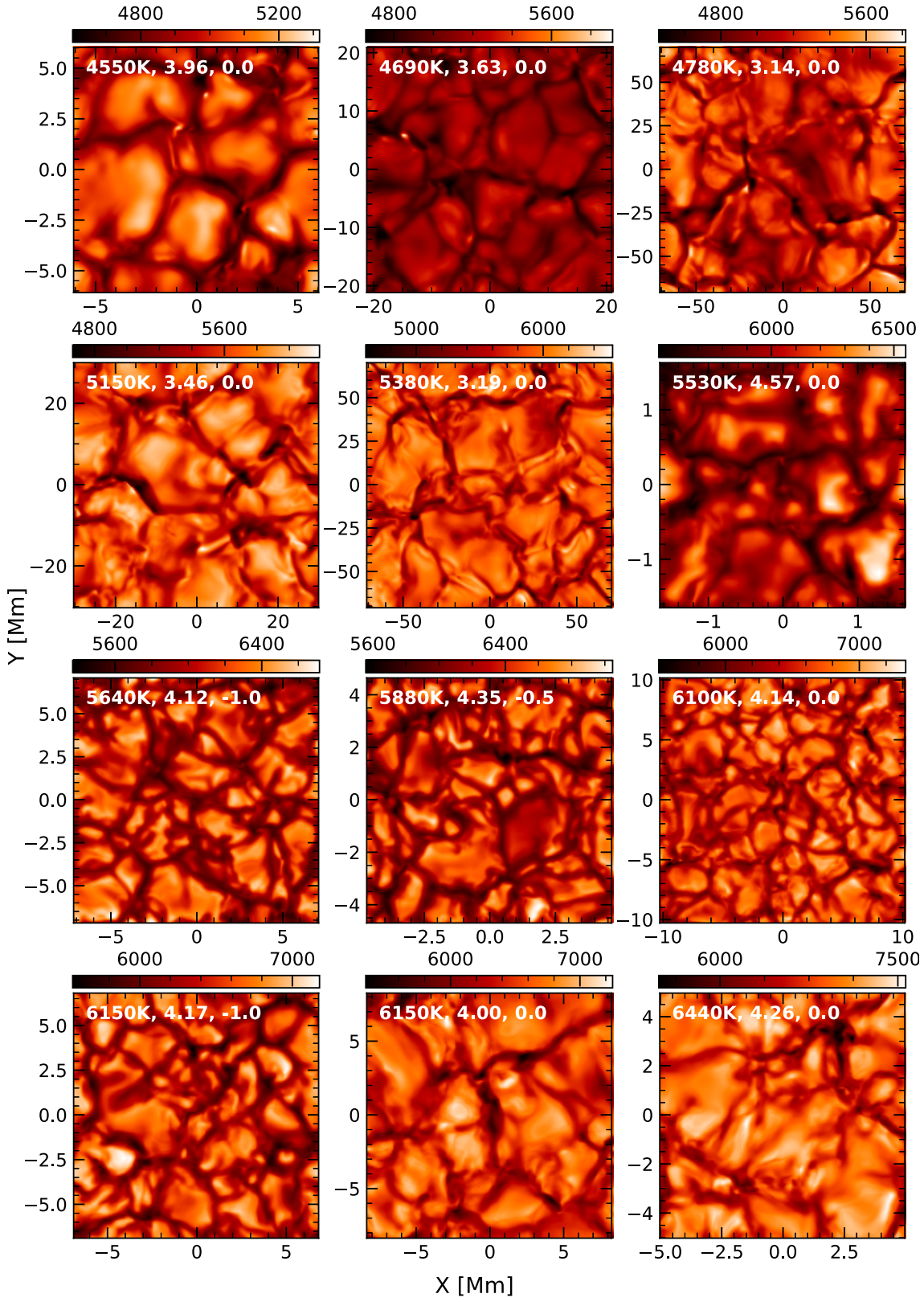

Figure 6.8: Horizontal temperature slice at the optical surface of randomly selected M3DIS stellar atmosphere models created as part of the first M3DIS sub-grid (Fig. 6.7). The colour-bars in each panel indicate the temperature in K. Stellar parameters $T_{\rm eff}$, $\log g$, [Fe/H] are shown at the top left of each panel.

at solar metallicity, but also including models up to [Fe/H] = −1. The locations of these models in the Kiel diagram, i.e. $T_{\rm eff}$ and $\log g$, are sampled randomly within the region of stars in the PLATO sample (black shading in the background). The average temperature-density structure for each of these models is shown in the right panel (black lines), where a few models with different parameters are highlighted in color. The temperature structures at the optical surface of these models are shown in Fig. 6.8.

It may be noted that this random parameter sampling has two advantages. When initiating a 3D atmosphere simulation, the effective temperature is not an input, but rather an output parameter. Targeting a specific $T_{\rm eff}$ hence involves a mapping from the actual inputs, i.e. bottom entropy, $\log g$, and chemical composition, to $T_{\rm eff}$, which a-priori is not known. In practice, this results in either a trial-and-error phase – which involves human interactions – or a more sophisticated feedback loop between the time-dependent radiation flux at the top and the entropy at the bottom of the atmosphere, which itself slows down the relaxation as the atmosphere needs time to adapt to structural changes. In any case, the effective computation time per model increases considerably. A random sampling makes this step meaningless, as the output effective temperature may be accepted at face value.

A second advantage arises when considering the end product of the pipeline, the spectra, and how the interpolation is done. In the case of 4MOST and PLATO the spectroscopic module that derives stellar parameters consists of an ANN (Ting et al. 2019; Kovalev et al. 2019) that emulates stellar spectra in real time and uses the predictions by the network to find the ideal match with observations (Gent et al. 2022). The training of this ANN will have to be done on the basis of the model atmosphere grid, which means that randomized parameters are generally preferred to avoid imprinting artificial structures onto the network output.

This first `M3DIS` sub-grid (at the time of writing) contains 167 models with [Fe/H] = 0.0, 18 models with [Fe/H] = −0.5, and 45 models at [Fe/H] = −1.0, and will steadily be extended in the near future. As the group of Maria Bergemann is heavily involved in PLATO work-package *WP122: Non-seismic parameters and model atmospheres*, the plan is to complement the default 1D NLTE derivation of stellar parameters with `M3DIS` 3D models as a first milestone. Due to the simultaneous involvement in the 4MOST *S4 Milky Way Bulge and Disk High Resolution survey* the extension to a broader parameter space – especially lower metallicities – is also desired and achievable within reasonable time.

With `M3DIS`, the expansion of 3D NLTE analyses to samples that are orders of magnitude larger than the sample by Storm et al. (2025) – and hence a much more complete representation of the Galactic abundance distribution – becomes realistic; The first PLATO sub-grid models (Fig. 6.7 and Fig. 6.8) evolve towards realistic $T-\rho$ structures and velocity fields in significantly less than 5 000 CPU-h, which is equivalent to only 24 h on two nodes of the

intermediate-sized Raven[2] high-performance computing cluster at the Max Planck Computing and Data Facility (MPCDF). Because of this, the first PLATO sub-grid models were computed in less than a month in total. The up-scaling to $\sim$ 5 000 models is therefore achievable on the time scales of a year. It remains to be investigated how many models indeed are needed for sufficiently accurate spectra emulation.

In a related study Różański et al. (2025), the capability of various ANN architectures to predict stellar spectra from input labels was examined. Their evaluation on high-resolution spectra showed that the traditional `Payne` achieves a mean absolute error of about 10^{-2} when trained on 10^4 1D spectra (see Fig. 4, top right panel of their study). For the PLATO core sample, the construction of such a grid is feasible with the methods developed in this thesis. It is yet to be determined whether these performance results are applicable to increasingly asymmetric 3D spectra, which are less characterized by effective temperature because of the exclusion of the radiative equilibrium assumption. If prediction time is not a limitation, Różański et al. also highlight that their advanced `TransformerPayne` can achieve similar accuracy using ten times fewer spectra, potentially reducing the number of required models. This alternative deserves future exploration.

[2] https://www.mpcdf.mpg.de/services/supercomputing/raven

7 Summary & Conclusion

In this thesis I investigate systematic biases in deriving stellar abundances arising from the assumption that stellar atmospheres are one-dimensional, as well as in hydrostatic- and local thermodynamic equilibrium. I furthermore examine how these biases influence the interpretation of abundance trends in the Galactic chemical evolution and present new methods to prevent these issues when analyzing large data sets from high-resolution spectroscopic stellar surveys in the future.

I elaborate in Sec. 3 how the [Ni/Fe] ratio in Galactic stars changes when moving away from the assumption of LTE. My co-authors and I analyze 264 Galactic stars using high-resolution, high signal-to-noise Gaia-ESO survey spectra, incorporating Gaia eDR3 photometry and photo-geometric distances from Bailer-Jones et al. (2021), along with NLTE corrected Fe and Ni abundances from Bensby et al. (2014). Our findings may be summarized as follows:

- Ni abundances determined assuming LTE are consistently lower. The NLTE—LTE offset varies with stellar evolutionary stage, reaching up to +0.3 dex in hot, low-metallicity MS stars or sub-giants, whereas stars of solar metallicity are less affected ($\sim$ 0.05 dex).
- Comparing NLTE and LTE [Ni/Fe] abundances as a function of [Fe/H] to predictions from a GCE models, which we modified to include M_{Ch} and sub-M_{Ch}SNe Ia with the respective DTDs, we find that in NLTE the best agreement is obtained by assuming a sub-M_{Ch} fraction of $\sim$ 80%, while in LTE the fraction is significantly lower ($\sim$ 20%), in agreement with our earlier work on Mn (75%, Eitner et al. 2020).
- Nomoto et al. (2013) yields from CC-SNe predict too low abundances of Ni. Limongi & Chieffi (2018) yields show a better agreement with our 1D NLTE Ni results, however they also generally under-predict 3D NLTE [(Mn , Co , Ni)/Fe] (Storm et al. 2025). Because of this, higher yields from SNe Ia are required to reach solar abundances, which is why other studies (such as e.g. Kobayashi et al. 2020a,b; Trueman et al. 2025; Alexander & Vincenzo 2025) arrive at the misconception of a high M_{Ch} SNe Ia contribution. Resolving the low-metallicity despondency between models and observations is thus key to this issue. According to Nomoto et al. (2013), higher CC-yields of Fe-

peak elements can be archived by reducing the electron-excess in Si-burning regions, which appears to be in-line with Galactic [Cr/Fe] abundances. Further, more quantitative investigations are necessary.

This result highlights the impact of improper stellar spectra modeling; Under the simplifying assumption of LTE, the data leads to the conclusion that M_{Ch}-SNe Ia are dominating the Galactic history. In NLTE the opposite is the case. Due to their varying explosion masses, the peak brightnesses of these events are not expected to be uniform (Shen et al. 2018, 2021a). It is still an open question that needs to be answered to what extend these high occurance rates of non-classical SNe Ia allows them to be trusted as standard candles. If some large fractions of these events are found to be non-standardizable and thus not follow the Phillips relation – and there furthermore is an environmental effect – this has implications for distances derived from them and consequently the determination of H_0.

Having established the importance of NLTE for abundance diagnostics of Fe-peak elements and the implications for the Galactic history, the next steps on the path towards a physically realistic, self-consistent analysis of large samples of stellar spectra is to relax the assumption that stellar atmospheres can be described by 1D models in hydrostatic-equilibrium. To archive this goal, we present our newly developed and highly efficient 3D radiation-hydrodynamics code `M3DIS` in Sec. 4. `M3DIS` is build upon the `DISPATCH` high-performance numerical framework for astrophysical applications. It solves the equations of hydrodynamics to advance an initial guess for the atmospheric structure in time, while simultaneously solving the radiative transfer equation to take radiative heating and cooling due to interactions between atmospheric gas and the radiation field into account. In the process of validating this new code, we arrive at the following results:

- The efficient numerical infrastructure of `M3DIS`, in combination with local time-stepping, enables the relaxation of 3D RHD models in $\lesssim 5\,000$ CPU-h (or ≤ 24 h on a medium-sized computer cluster), from scratch, without additional user interaction.
- Our new version of the `MULTI3D` code in the same framework is consistent in terms of microphysics and allows the efficient computation of 3D NLTE spectra for our models
- We validate that this speed-up compared to other 3D RHD codes does not come at the cost of physical realism by showing that the `M3DIS` solar model reproduces the observed solar center-to-limb variation to a satisfactory degree. We find that the average temperature structure agrees within $\sim 2\,\%$ and densities within 0.02 dex with `STAGGER` and `CO5BOLD` models
- To highlight the applicability of `M3DIS` to stars other than the sun, we compute several MS models with different temperatures and show that their average structure agrees well with what is expected from 1D HE `MARCS` models at solar metallicity.

- Although comparing different model quantities directly with other models is interesting, the true test lies in the synthetic observables they generate. Thus, we synthesize diagnostic Fe I lines, along with H_α and H_β, and compare the synthetic line profiles with the KPNO FTS atlas. Our results show that spectra from the M3DIS model are closely aligned with observations, particularly the Fe lines and the H_α wings. Moreover, differences in model resolution result in only minor changes in Fe abundance, about $\sim$ 0.02, without any systematic offset. Our M3DIS solar model effectively matches observed Fe lines without extra adjustment of hyperparameters or broadening mechanisms required for 1D HE models.

- We furthermore motivate the applicability of our new code in parameter spaces not explored in detail in this thesis. We present a simple extrapolation mechanism that can be used to generate models outside the limits of existing 3D grids. We further show that M3DIS is capable of generating red giant stars, which naturally reproduce the maximum mode frequency associated with solar-like oscillations. We furthermore show the variability of the bolometric flux – as well as for individual spectral bands – in long time-sequences of the solar simulation and motivate how they may be used in planetary science.

- Lastly, we present the first part of our newly created PLATO M3DIS sub-grid, which currently contains 240 MS and sub-giant models and was created within a month of wall-clock time.

With this, we have shown that our new M3DIS 3D RHD code – in combination with MULTI3D @DISPATCH – is capable of producing stellar model atmospheres with much smaller time investment, which at the same time compare well with predictions from other 3D RHD codes and furthermore produce synthetic observables that are in excellent agreement with observations. In addition to the efficiency of M3DIS, its flexibility and consistency in terms of microphysics via the synergy with MULTI3D @DISPATCH is a very important feature that needs to be highlighted. These new codes allow us to apply the superior 3D modeling techniques to one of the most compelling parameter spaces in Galactic archaeology: The most [Fe/H]-poor stars in the Galaxy. In addition to their immediate connection to Pop III stars, these stars are interesting because a substantial proportion of them are chemically peculiar, as they are characterized by large, super-solar [C/Fe] abundances. Yet, their analysis mostly relies on 1D HE model atmospheres even though it was already noted by Asplund et al. (1999) that there might be non-negligible 3D effects.

To address the question to what extent the high C-abundances found are physically realistic – or only an artifact of the modeling assumptions – and what the potential implications for the Galactic chemical evolution are, we analyze a sample of metal-poor stars from the SAGA database using our M3DIS stellar atmosphere models in Sec. 5. For this purpose, we create

main-sequence (MS) and sub-giant models for a range of metallicities between $[\mathrm{Fe/H}] = -6$ and $[\mathrm{Fe/H}] = -2$. In addition to scaled-solar composition, we compute 3D models with carbon enhancement included in their atmosphere, which we archive by developing the capability to generate extensive opacity tables using `MULTI3D@DISPATCH`. Our findings are:

- In agreement with previous studies, we find that metal-poor 3D atmospheres are significantly cooler ($\sim 1\,500\,\mathrm{K}$) in the upper layers of the atmosphere due to the neglect of adiabatic cooling in 1D HE. We furthermore note that the increased C content leads to a re-heating of low optical depth layers, which causes the temperature structure to be closer to the 1D radiative equilibrium solution.

- These structural differences cause the CH G-band to be significantly stronger in 3D compared to 1D with the same A(C). The result is that a strong, observed G-band feature may – at least partly – be explained by the 3D nature of the atmosphere rather than a large A(C).

- At low metallicity, we find that in 1D A(C) is overestimated by $\sim 0.7\,\mathrm{dex}$ and $\sim 0.6\,\mathrm{dex}$ for sub-giant and MS stars, respectively. There furthermore is a systematic offset of $\sim 0.2\,\mathrm{dex}$ ($\sim 0.1\,\mathrm{dex}$ for MS) between 3D CEMP and 3D scaled-solar models related to the additional C-enhancement in CEMP stars. As this effect works in the opposite direction, the overestimation would therefore be ~ 0.9 ($\sim 0.7\,\mathrm{dex}$ for MS) when using scaled-solar 3D models.

- We apply 3D CEMP − 1D corrections to a sample of metal-poor stars from SAGA and find that, especially at intermediate metallicities between $-4.5 < [\mathrm{Fe/H}] < -3.5$, the fraction of CEMP stars decreases by $\sim 30\,\%$, between $-3.5 < [\mathrm{Fe/H}] < -2.5$ by $\sim 15\,\%$. CEMP populations of Group II stars are most affected by 3D, as they reside close to the C-normal limit at lower metallicities. Group I stars exhibit smaller 3D corrections. The most metal-poor stars in Group III experience the strongest shifts. However, because of their extremely high [C/Fe] values, the population statistics remains nearly unchanged.

- Applying approximate CEMP sub-group splitting methods based on A(C), we find that the fraction of CEMP-no fraction is increased with respect to the CEMP-r/s stars, as the latter are either removed from the CEMP classification at higher metallicities or shifted in the A(C) regime of CEMP-no stars.

- Owing to the strong metallicity gradient of the 3D A(C) corrections, the initially flat Group III in the Yoon-Beers diagram appears tilted, indicating a metallicity dependence of their stars A(C) in 3D. This raises doubt on the interpretation that these stars were accreted from chemically simple UFD systems (Yoon et al. 2019). We notice that in 3D large parts of the former Group II and III overlap, which causes the distribution

to also be in good agreement with the band structure originally proposed by Spite et al. (2013), suggesting that low-C CEMP-no stars form from the [C/Fe]-rich ejecta of faint SNe, wile high-C CEMP-r/s stars have AGB contribution. A detailed 3D NLTE analysis of neutron-capture elements is needed to see how much mixing of CEMP sub-gropus there is in this simpler classification scheme.

- By comparing the CEMP fraction with semi-analytical models from Hartwig et al. (2018), we note that the 3D data suggests a 20 % lower occurrence rate of faint SNe. We conclude that improper 1D modeling of metal-poor stellar atmospheres and spectra leads to the misinterpretation of strong, observed CH G-band features as evidence for large [C/Fe] abundances and, in turn, the overestimation of the significance of faint SNe in the early Galaxy. We note that faint SNe generally produce small amounts of Fe-peak elements due to extensive fallback (Nomoto et al. 2013), which means that lower fractions of these events are qualitatively in agreement with our prediction of higher Fe-peak NLTE abundances. A comprehensive 3D NLTE investigations of metal-poor stars in 4MOST will be key to put further constraints on this topic.

With the work presented in this thesis, I highlight the importance of proper modeling of stellar atmospheres and spectra in the context of Galactic archaeology. I show that the neglect of 3D and/or NLTE effects potentially has a large impact on stellar diagnostics and Galactic abundance distributions, which leads to a skewed picture of the Galactic history that is – in parts – driven by modeling assumptions rather than physics.

By developing and validating the `M3DIS` code, which enables the mass production of 3D stellar atmosphere models and the corresponding grids of 3D NLTE stellar spectra on their basis, I take a significant step towards on-the-fly full 3D NLTE spectrum synthesis, when combined with sophisticated machine learning and/or interpolation methods.

With the advent of large, high-resolution spectroscopic surveys, one can only imagine what hidden physics will be revealed when the 1D LTE approximation has been removed from astrophysical data sets. The objective is to implement 3D NLTE modeling as the default technique for FGK-type spectral analysis. This advancement will ultimately eliminate the need for 3D and/or NLTE abundance corrections and inter-dependent hyperparameters, such as micro-turbulence and mixing-length, thereby enhancing the knowledge we can draw from the data that future high-quality spectral observation facilities will provide us.

List of Figures

List of Tables

Personal Bibliography

Papers published during the course of this thesis

Below a list of papers to which I contributed and that have been published (or have been submitted and currently are still under review) during the course of my thesis. Papers used directly for this thesis are marked with asterisk.

- Storm, N.; Bergemann, M.; **Eitner, P.**; Hoppe, R.; Kemp, A. J.; Ruiter, A. J.; Janka, H.-T.; Sieverding, A.; de Mink, S. E.; Seitenzahl, I. R.; Owusu, E. K. (2025):
  Observational constraints on the origin of the elements. IX. 3D NLTE abundances of metals in the context of Galactic Chemical Evolution models and 4MOST.
  Monthly Notices of the Royal Astronomical Society, https://ui.adsabs.harvard.edu/abs/2025MNRAS.538.3284S

- Hoppe, R.; Bergemann, M.; **Eitner, P.**; Ellwarth, M.; Nordlund, Å.; Leenaarts, J.; Plez, B.; Serenelli A. (2025):
  Solar carbon abundance from 3D non-LTE modelling of the diagnostic lines of the CH molecule
  submitted to Monthly Notices of the Royal Astronomical Society

- **Eitner, P.***; Bergemann M.; Hoppe, R.; Storm, N.; Lipatova, V.; Glover, S. C. O.; Klessen, R. S.; Nordlund, Å.; Popovas, A. (2025):
  M3DIS – A grid of 3D radiation-hydrodynamics stellar atmosphere models for stellar surveys. II. Carbon-enhanced metal-poor stars
  submitted to Astronomy & Astrophysics

- **Eitner, P.***; Bergemann, M.; Hoppe, R.; Nordlund, Å.; Plez, B.; Klevas, J. (2024):
  M3DIS – A grid of 3D radiation-hydrodynamics stellar atmosphere models for stellar surveys. I. Procedure, validation, and the Sun
  Astronomy & Astrophysics, https://ui.adsabs.harvard.edu/abs/2024A&A...688A..52E

- Gvozdenko, A.; Larsen, S. S.; Beasley, M. A.; Cabrera-Ziri, I.; **Eitner, P.**; Battaglia, G.; Leaman, R. (2024):

Detailed chemical composition of the globular cluster Sextans A GC-1 on the outskirts of the Local Group
Astronomy & Astrophysics, https://ui.adsabs.harvard.edu/abs/2024A&A...685A.154G

- Gent, M. R.; **Eitner, P.**; Serenelli, A.; Friske, J. K. S.; Koposov, S. E.; Laporte, C. F. P.; Buck, T.; Bergemann, M. (2024):
The Prince and the Pauper: Evidence for the early high-redshift formation of the Galactic α-poor disc population
Astronomy & Astrophysics, https://ui.adsabs.harvard.edu/abs/2024A&A...683A..74G

- Nielsen, J.; Gent, M. R.; Bergemann, M.; **Eitner, P.**; Johansen, A. (2023):
Planet formation throughout the Milky Way. Planet populations in the context of Galactic chemical evolution
Astronomy & Astrophysics, https://ui.adsabs.harvard.edu/abs/2023A&A...678A..74N

- **Eitner, P.***; Bergemann, M.; Ruiter, A. J.; Avril, O.; Seitenzahl, I. R.; Gent, M. R.; Côté, B. (2023):
Observational constraints on the origin of the elements. V. NLTE abundance ratios of [Ni/Fe] in Galactic stars and enrichment by sub-Chandrasekhar mass supernovae
Astronomy & Astrophysics, https://ui.adsabs.harvard.edu/abs/2023A&A...677A.151E

- Larsen, S. S.; **Eitner, P.**; Magg, E.; Bergemann, M.; Moltzer, C. A. S.; Brodie, J. P.; Romanowsky, A. J.; Strader, J. (2022):
The chemical composition of globular clusters in the Local Group
Astronomy & Astrophysics, https://ui.adsabs.harvard.edu/abs/2022A&A...660A..88L

Papers published before this thesis

- **Eitner, P.**; Bergemann, M.; Hansen, C. J.; Cescutti, G.; Seitenzahl, I. R.; Larsen, S.; Plez, B. (2020):
Observational constraints on the origin of the elements. III. Evidence for the dominant role of sub-Chandrasekhar SN Ia in the chemical evolution of Mn and Fe in the Galaxy
Astronomy & Astrophysics, https://ui.adsabs.harvard.edu/abs/2020A&A...635A..38E

- Bergemann, M.; Gallagher, A. J.; **Eitner, P.**; Bautista, M.; Collet, R.; Yakovleva, S. A.; Mayriedl, A.; Plez, B.; Carlsson, M.; Leenaarts, J.; Belyaev, A. K.; Hansen, C. (2019):

Observational constraints on the origin of the elements. I. 3D NLTE formation of Mn lines in late-type stars
Astronomy & Astrophysics, https://ui.adsabs.harvard.edu/abs/2019A&A...631A..80B

- **Eitner, P.**; Bergemann, M.; Larsen, S. (2019):
NLTE modelling of integrated light spectra. Abundances of barium, magnesium, and manganese in a metal-poor globular cluster
Astronomy & Astrophysics, https://ui.adsabs.harvard.edu/abs/2019A&A...627A..40E

Bibliography

Abdalla E., et al., 2022, Journal of High Energy Astrophysics, 34, 49

Adibekyan V. Z., Sousa S. G., Santos N. C., Delgado Mena E., González Hernández J. I., Israelian G., Mayor M., Khachatryan G., 2012, A&A, 545, A32

Alexander D. R., Ferguson J. W., 1994, ApJ, 437, 879

Alexander R. K., Vincenzo F., 2025, MNRAS, 538, 1127

Ali A. W., Griem H. R., 1965, Physical Review, 140, 1044

Allende Prieto C., Asplund M., García López R. J., Lambert D. L., 2002, ApJ, 567, 544

Amarsi A. M., Lind K., Asplund M., Barklem P. S., Collet R., 2016, MNRAS, 463, 1518

Antognini J. M. O., Thompson T. A., 2016, MNRAS, 456, 4219

Aoki W., Bisterzo S., Gallino R., Beers T. C., Norris J. E., Ryan S. G., Tsangarides S., 2006, ApJ, 650, L127

Aoki W., Beers T. C., Christlieb N., Norris J. E., Ryan S. G., Tsangarides S., 2007, ApJ, 655, 492

Arendt W., Urban K., 2023, Partial Differential Equations: An Introduction to Analytical and Numerical Methods, 1 edn. Graduate Texts in Mathematics, Springer Cham, doi:10.1007/978-3-031-13379-4

Asplund M., García Pérez A. E., 2001, A&A, 372, 601

Asplund M., Nordlund Å., Trampedach R., Stein R. F., 1999, A&A, 346, L17

Asplund M., Nordlund Å., Trampedach R., Allende Prieto C., Stein R. F., 2000, A&A, 359, 729

Asplund M., Grevesse N., Sauval A. J., Scott P., 2009, ARA&A, 47, 481

Athay R. G., Lites B. W., 1972, ApJ, 176, 809

Auvergne M., et al., 2009, A&A, 506, 411

Aver E., Olive K. A., Porter R. L., Skillman E. D., 2013, Journal of Cosmology and Astroparticle Physics, 2013, 017

Bailer-Jones C. A. L., Rybizki J., Fouesneau M., Mantelet G., Andrae R., 2018, AJ, 156, 58

Bailer-Jones C. A. L., Rybizki J., Fouesneau M., Demleitner M., Andrae R., 2021, AJ, 161, 147

Balthasar H., 1984, Sol. Phys., 93, 219

Barklem P. S., Piskunov N., 2003, in Piskunov N., Weiss W. W., Gray D. F., eds, Vol. 210, Modelling of Stellar Atmospheres. p. 28

Barklem P. S., Piskunov N., O'Mara B. J., 2000, A&A, 363, 1091

Barklem P. S., Stempels H. C., Allende Prieto C., Kochukhov O. P., Piskunov N., O'Mara B. J., 2002, A&A, 385, 951

Batalha N. M., et al., 2011, ApJ, 729, 27

Bauswein A., Goriely S., Janka H. T., 2013, ApJ, 773, 78

Beeck B., et al., 2012, A&A, 539, A121

Beers T. C., Christlieb N., 2005, ARA&A, 43, 531

Beers T. C., Preston G. W., Shectman S. A., 1985, AJ, 90, 2089

Beers T. C., Preston G. W., Shectman S. A., 1992, AJ, 103, 1987

Belczynski K., Kalogera V., Rasio F. A., Taam R. E., Zezas A., Bulik T., Maccarone T. J., Ivanova N., 2008, ApJS, 174, 223

Bell K. L., Berrington K. A., 1987, Journal of Physics B Atomic Molecular Physics, 20, 801

Benetti S., et al., 2004, MNRAS, 348, 261

Benetti S., et al., 2005, ApJ, 623, 1011

Bensby T., Feltzing S., Oey M. S., 2014, Exploring the Milky Way stellar disk. A detailed elemental abundance study of 714 F and G dwarf stars in the solar neighbourhood (arXiv:1309.2631), doi:10.1051/0004-6361/201322631

Bensby T., et al., 2019, The Messenger, 175, 35

Bergemann M., 2008, Physica Scripta Volume T, 133, 014013

Bergemann M., 2011, MNRAS, 413, 2184

Bergemann M., Cescutti G., 2010, A&A, 522, A9

Bergemann M., Gehren T., 2008, Astronomy and Astrophysics, Volume 492, Issue 3, 2008, pp.823-831, 492, 823

Bergemann M., Nordlander T., 2014, NLTE Radiative Transfer in Cool Stars. Springer International Publishing, Cham, pp 169–185, doi:10.1007/978-3-319-06956-2_16, https://doi.org/10.1007/978-3-319-06956-2_16

Bergemann M., Lind K., Collet R., Magic Z., Asplund M., 2012a, MNRAS, 427, 27

Bergemann M., Hansen C. J., Bautista M., Ruchti G., 2012b, A&A, 546, A90

Bergemann M., et al., 2014, A&A, 565, A89

Bergemann M., et al., 2019, A&A, 631, A80

Bergemann M., et al., 2021, MNRAS, 508, 2236

Bessell M. S., Christlieb N., Gustafsson B., 2004, ApJ, 612, L61

Bhatia T. S., Cameron R. H., Solanki S. K., Peter H., Przybylski D., Witzke V., Shapiro A., 2022, A&A, 663, A166

Bigot L., Kervella P., Thévenin F., Ségransan D., 2006, A&A, 446, 635

Bland-Hawthorn J., et al., 2019, MNRAS, 486, 1167

Blaom A. D., Kiraly F., Lienart T., Simillides Y., Arenas D., Vollmer S. J., 2020, Journal of Open Source Software, 5, 2704

Blondin S., Dessart L., Hillier D. J., Khokhlov A. M., 2017, MNRAS, 470, 157

Blondin S., Bravo E., Timmes F. X., Dessart L., Hillier D. J., 2022, A&A, 660, A96

Böhm-Vitense E., 1958, ZAp, 46, 108

Bonifacio P., et al., 2009, A&A, 501, 519

Bonifacio P., Caffau E., Ludwig H. G., Spite M., Plez B., Steffen M., Spite F., 2013, Memorie della Societa Astronomica Italiana Supplementi, 24, 138

Bonifacio P., et al., 2015, A&A, 579, A28

Bonifacio P., et al., 2018, A&A, 611, A68

Boos S. J., Townsley D. M., Shen K. J., Caldwell S., Miles B. J., 2021, ApJ, 919, 126

Branch D., 1998, ARA&A, 36, 17

Bravo E., Martínez-Pinedo G., 2012, Phys. Rev. C, 85, 055805

Bridgman T., Ng J., Schuler L., Jones I., 2021, A Big Sunspot from Solar Cycle 24. NASA's Scientific Visualization Studio, https://svs.gsfc.nasa.gov/4907/, retrieval date: 25.06.2025

Bromm V., Coppi P. S., Larson R. B., 2002, ApJ, 564, 23

Buder S., et al., 2021, MNRAS, 506, 150

Buder S., et al., 2024, arXiv e-prints, p. arXiv:2409.19858

Burke P. G., 2011, R-Matrix Theory of Atomic Collisions: Application to Atomic, Molecular and Optical Processes, 1 edn. Springer Series on Atomic, Optical, and Plasma Physics, Springer Berlin, Heidelberg, doi:10.1007/978-3-642-15931-2

Burns C. R., et al., 2014, ApJ, 789, 32

Caffau E., Ludwig H. G., Steffen M., Freytag B., Bonifacio P., 2011a, Sol. Phys., 268, 255

Caffau E., et al., 2011b, Nature, 477, 67

Canocchi G., Morello G., Lind K., Carleo I., Stangret M., Pallé E., 2024, A&A, 692, A43

Canuto V. M., Mazzitelli I., 1991, ApJ, 370, 295

Carbon D. F., Gingerich O., 1969, in Gingerich O., ed., Theory and Observation of Normal Stellar Atmospheres. p. 377

Carlsson M., 1992, in Giampapa M. S., Bookbinder J. A., eds, Astronomical Society of the Pacific Conference Series Vol. 26, Cool Stars, Stellar Systems, and the Sun. p. 499

Carlsson M., De Pontieu B., Hansteen V. H., 2019, ARA&A, 57, 189

Carson T. R., 1992, Rev. Mexicana Astron. Astrofis., 23, 151

Casagrande L., Portinari L., Flynn C., 2006, MNRAS, 373, 13

Casagrande L., Ramírez I., Meléndez J., Bessell M., Asplund M., 2010, A&A, 512, A54

Casagrande L., et al., 2020, arXiv e-prints, p. arXiv:2011.02517

Castelli F., Kurucz R. L., 2003, in Piskunov N., Weiss W. W., Gray D. F., eds, IAU Symposium Vol. 210, Modelling of Stellar Atmospheres. p. A20 (arXiv:astro-ph/0405087), doi:10.48550/arXiv.astro-ph/0405087

Cescutti G., Matteucci F., Lanfranchi G. A., McWilliam A., 2008, A&A, 491, 401

Chandrasekhar S., 1939, An introduction to the study of stellar structure

Chaplin W. J., Basu S., 2008, Sol. Phys., 251, 53

Chen Y. Q., Nissen P. E., Zhao G., Zhang H. W., Benoni T., 2000, A&AS, 141, 491

Chiaki G., Tominaga N., Nozawa T., 2017, MNRAS, 472, L115

Chiappini C., 2001, American Scientist, 89, 506

Chiappini C., Matteucci F., Gratton R., 1997, ApJ, 477, 765

Chiavassa A., Plez B., Josselin E., Freytag B., 2009, A&A, 506, 1351

Chiavassa A., et al., 2017, A&A, 597, A94

Childress M. J., Wolf C., Zahid H. J., 2014, MNRAS, 445, 1898

Choplin A., 2017, in Reylé C., Di Matteo P., Herpin F., Lagadec E., Lançon A., Meliani Z., Royer F., eds, SF2A-2017: Proceedings of the Annual meeting of the French Society of Astronomy and Astrophysics. p. Di

Christlieb N., Green P. J., Wisotzki L., Reimers D., 2001, A&A, 375, 366

Christlieb N., et al., 2002, Nature, 419, 904

Christlieb N., Schörck T., Frebel A., Beers T. C., Wisotzki L., Reimers D., 2008, A&A, 484, 721

Cikota A., et al., 2019, MNRAS, 490, 578

Claret A., 2004, A&A, 428, 1001

Cohen J. G., Christlieb N., Qian Y.-Z., Wasserburg G. J., 2003, The Astrophysical Journal, 588, 1082

Collet R., Asplund M., Trampedach R., 2007, A&A, 469, 687

Collet R., Magic Z., Asplund M., 2011, in Journal of Physics Conference Series. p. 012003 (arXiv:1110.5475), doi:10.1088/1742-6596/328/1/012003

Collet R., Nordlund Å., Asplund M., Hayek W., Trampedach R., 2018, MNRAS, 475, 3369

Cooke R. J., Pettini M., Steidel C. C., 2018, ApJ, 855, 102

Côté B., 2018, American Astronomical Society, AAS Meeting #232, id. 305.01, 232, 305.01

Côté B., Ritter C., 2018, ascl, p. ascl:1806.018

Côté B., Ritter C., O'Shea B. W., Herwig F., Pignatari M., Jones S., Fryer C. L., 2016, ApJ, 824, 82

Côté B., Belczynski K., Fryer C. L., Ritter C., Paul A., Wehmeyer B., O'Shea B. W., 2017, ApJ, 836, 230

Côté B., Silvia D. W., O'Shea B. W., Smith B., Wise J. H., 2018, The Astrophysical Journal, 859, 67

Côté B., Lugaro M., Reifarth R., Pignatari M., Világos B., Yagüe A., Gibson B. K., 2019, The Astrophysical Journal, 878, 156

Courant R., Friedrichs K., Lewy H., 1967, IBM Journal of Research and Development, 11, 215

Cristallo S., Straniero O., Piersanti L., 2015, in Kerschbaum F., Wing R. F., Hron J., eds, Astronomical Society of the Pacific Conference Series Vol. 497, Why Galaxies Care about AGB Stars III: A Closer Look in Space and Time. p. 301

Csizmadia S., Pasternacki T., Dreyer C., Cabrera J., Erikson A., Rauer H., 2013, A&A, 549, A9

Cyburt R. H., Fields B. D., Olive K. A., Yeh T.-H., 2016, Reviews of Modern Physics, 88, 015004

Dappen W., Anderson L., Mihalas D., 1987, ApJ, 319, 195

Das P., et al., 2025, Nature Astronomy

Dekker H., D'Odorico S., Kaufer A., Delabre B., Kotzlowski H., 2000, in Iye M., Moorwood A. F., eds, Society of Photo-Optical Instrumentation Engineers (SPIE) Conference Series Vol. 4008, Optical and IR Telescope Instrumentation and Detectors. pp 534–545, doi:10.1117/12.395512

Deng L.-C., et al., 2012, Research in Astronomy and Astrophysics, 12, 735

Dotter A., Chaboyer B., Jevremović D., Kostov V., Baron E., Ferguson J. W., 2008, ApJS, 178, 89

Doyle R., 1968, J. Quant. Spectr. Rad. Transf., 8, 1555

Dravins D., Lindegren L., Nordlund A., 1981, A&A, 96, 345

Drawin H.-W., 1968, Zeitschrift fur Physik, 211, 404

Dullemond 2011, Numerische Strömungsmechanik, Lecture Notes on Numerical Fluid Dynamics. https://www.ita.uni-heidelberg.de/~dullemond/lectures/num_fluid_2011/, retrieval date: 18.05.2025

Eitner P., Bergemann M., Larsen S., 2019, A&A, 627, A40

Eitner P., Bergemann M., Hansen C. J., Cescutti G., Seitenzahl I. R., Larsen S., Plez B., 2020, A&A, 635, A38

Eitner P., Bergemann M., Ruiter A. J., Avril O., Seitenzahl I. R., Gent M. R., Côté B., 2023, A&A, 677, A151

Eitner P., Bergemann M., Hoppe R., Nordlund Å., Plez B., Klevas J., 2024, A&A, 688, A52

Fabbian D., Khomenko E., Moreno-Insertis F., Nordlund Å., 2010, ApJ, 724, 1536

Feltzing S., Gustafsson B., 1998, A&AS, 129, 237

Feltzing S., Bensby T., Lundström I., 2003, A&A, 397, L1

Fink M., Röpke F. K., Hillebrandt W., Seitenzahl I. R., Sim S. A., Kromer M., 2010, A&A, 514, A53

Fink M., et al., 2014, MNRAS, 438, 1762

Flörs A., et al., 2020, MNRAS, 491, 2902

Foley R. J., et al., 2013, ApJ, 767, 57

Foreman-Mackey D., Hogg D. W., Lang D., Goodman J., 2013, pasp, 125, 306

François P., Matteucci F., Cayrel R., Spite M., Spite F., Chiappini C., 2004, A&A, 421, 613

François P., et al., 2018, A&A, 620, A187

Frebel A., Norris J. E., 2015, ARA&A, 53, 631

Frebel A., et al., 2005, in Hill V., Francois P., Primas F., eds, IAU Symposium Vol. 228, From Lithium to Uranium: Elemental Tracers of Early Cosmic Evolution. pp 207–212 (arXiv:astro-ph/0509658), doi:10.1017/S1743921305005569

Frebel A., et al., 2006, ApJ, 652, 1585

Frebel A., Johnson J. L., Bromm V., 2007, MNRAS, 380, L40

Freytag B., Höfner S., 2008, A&A, 483, 571

Freytag B., Ludwig H. G., Steffen M., 1996, A&A, 313, 497

Freytag B., Steffen M., Ludwig H. G., Wedemeyer-Böhm S., Schaffenberger W., Steiner O., 2012, Journal of Computational Physics, 231, 919

Fromang S., Hennebelle P., Teyssier R., 2006, A&A, 457, 371

Fuhrmann K., Axer M., Gehren T., 1993, A&A, 271, 451

Gaia Collaboration et al., 2016, A&A, 595, A1

Gaia Collaboration et al., 2018, A&A, 616, A1

Gaia Collaboration Brown A. G. A., Vallenari A., Prusti T., de Bruijne J. H. J., Babusiaux C., Biermann M., 2020, arXiv e-prints, p. arXiv:2012.01533

Gaia Collaboration et al., 2021, A&A, 649, A1

Gallagher A. J., Caffau E., Bonifacio P., Ludwig H. G., Steffen M., Spite M., 2016, A&A, 593, A48

Gallagher A. J., Caffau E., Bonifacio P., Ludwig H. G., Steffen M., Homeier D., Plez B., 2017, A&A, 598, L10

Gallagher A. J., Bergemann M., Collet R., Plez B., Leenaarts J., Carlsson M., Yakovleva S. A., Belyaev A. K., 2020, A&A, 634, A55

Gent M. R., et al., 2022, A&A, 658, A147

Gerber J. M., Magg E., Plez B., Bergemann M., Heiter U., Olander T., Hoppe R., 2023, A&A, 669, A43

Gibson B. K., Fenner Y., Renda A., Kawata D., Lee H.-c., 2003, PASA, 20, 401

Gieren W., et al., 2018, A&A, 620, A99

Gilfanov M., Bogdán Á., 2010, Nature, 463, 924

Gilliland R. L., et al., 2010, Publications of the Astronomical Society of the Pacific, 122, 131

Gilmore G., et al., 2012, The Messenger, 147, 25

Gilmore G., et al., 2022, A&A, 666, A120

Goldstein D. A., Kasen D., 2018, ApJ, 852, L33

Grand R. J. J., Kawata D., Cropper M., 2015, Monthly Notices of the Royal Astronomical Society, 447, 4018

Grand R. J. J., et al., 2017, MNRAS, 467, 179

Grand R. J. J., Fragkoudi F., Gómez F. A., Jenkins A., Marinacci F., Pakmor R., Springel V., 2024, MNRAS, 532, 1814

Gray D. F., 1973, ApJ, 184, 461

Gray D. F., 1992, The observation and analysis of stellar photospheres.. Vol. 20

Gray D. F., 2005, The Observation and Analysis of Stellar Photospheres, doi:10.1017/CBO9781316036570.

Grevesse N., Sauval A. J., 1998, Space Sci. Rev., 85, 161

Gronow S., Collins C., Ohlmann S. T., Pakmor R., Kromer M., Seitenzahl I. R., Sim S. A., Röpke F. K., 2020, A&A, 635, A169

Gronow S., Côté B., Lach F., Seitenzahl I. R., Collins C. E., Sim S. A., Röpke F. K., 2021, A&A, 656, A94

Grupp F., 2004, A&A, 420, 289

Gudiksen B. V., Carlsson M., Hansteen V. H., Hayek W., Leenaarts J., Martínez-Sykora J., 2011, A&A, 531, A154

Guiglion G., et al., 2024, A&A, 682, A9

Gull M., et al., 2018, ApJ, 862, 174

Gustafsson B., Bell R. A., Eriksson K., Nordlund A., 1975, A&A, 42, 407

Gustafsson B., Edvardsson B., Eriksson K., Jørgensen U. G., Nordlund Å., Plez B., 2008, A&A, 486, 951

Haberreiter M., Schmutz W., Hubeny I., 2008, A&A, 492, 833

Hampel M., Stancliffe R. J., Lugaro M., Meyer B. S., 2016, ApJ, 831, 171

Hansen T., et al., 2015, ApJ, 807, 173

Hansen T. T., Andersen J., Nordström B., Beers T. C., Placco V. M., Yoon J., Buchhave L. A., 2016a, A&A, 586, A160

Hansen C. J., et al., 2016b, A&A, 588, A37

Hansen T. T., et al., 2018, ApJ, 858, 92

Hartigan J. A., Wong M. A., 1979, Journal of the Royal Statistical Society. Series C (Applied Statistics), 28, 100

Hartwig T., et al., 2018, MNRAS, 478, 1795

Hartwig T., et al., 2022, ApJ, 936, 45

Hartwig T., Lipatova V., Glover S. C. O., Klessen R. S., 2024, MNRAS, 535, 516

Hawkins K., Masseron T., Jofré P., Gilmore G., Elsworth Y., Hekker S., 2016, A&A, 594, A43

Hayek W., Sing D., Pont F., Asplund M., 2012, A&A, 539, A102

Heger A., Woosley S. E., 2002, ApJ, 567, 532

Heger A., Woosley S. E., 2010, ApJ, 724, 341

Heiter U., Eriksson K., 2006, A&A, 452, 1039

Heiter U., et al., 2021, A&A, 645, A106

Hekker S., et al., 2011, A&A, 525, A131

Henyey L., Vardya M. S., Bodenheimer P., 1965, ApJ, 142, 841

Herwig F., 2005, ARA&A, 43, 435

Hillebrandt W., Kromer M., Röpke F. K., Ruiter A. J., 2013, Frontiers of Physics, 8, 116

Hirschi R., Fröhlich C., Liebendörfer M., Thielemann F.-K., 2006, Reviews in Modern Astronomy, 19, 101

Holzreuter R., Solanki S. K., 2013, A&A, 558, A20

Houdek G., Trampedach R., Aarslev M. J., Christensen-Dalsgaard J., 2017, MNRAS, 464, L124

Hubeny I., 2013, Stellar Atmospheres. Springer Netherlands, Dordrecht, pp 51–85, doi:10.1007/978-94-007-5615-1_2, https://doi.org/10.1007/978-94-007-5615-1_2

Hubeny I., Mihalas D., 2014, Theory of Stellar Atmospheres, by I. Hubeny and D. Mihalas. Princeton, NJ: Princeton University Press, 2014

Huber D., et al., 2013, The Astrophysical Journal, 767

Iben Icko J., Nomoto K., Tornambe A., Tutukov A. V., 1987, ApJ, 317, 717

Irwin A. W., 1981, ApJS, 45, 621

Ishigaki M. N., Tominaga N., Kobayashi C., Nomoto K., 2014, ApJ, 792, L32

Iwamoto N., Umeda H., Tominaga N., Nomoto K., Maeda K., 2005, Science, 309, 451

Izotov Y. I., Thuan T. X., Guseva N. G., 2014, MNRAS, 445, 778

Jacobson H. R., et al., 2015, ApJ, 807, 171

Janka H. T., Müller B., Kitaura F. S., Buras R., 2008, A&A, 485, 199

Jerkstrand A., et al., 2015, ApJ, 807, 110

Jha S. W., 2017, in Alsabti A. W., Murdin P., eds, , Handbook of Supernovae. p. 375, doi:10.1007/978-3-319-21846-5_42

Ji A. P., Frebel A., Bromm V., 2014, ApJ, 782, 95

Ji A. P., Frebel A., Chiti A., Simon J. D., 2016, Nature, 531, 610

Jiang J.-A., et al., 2017, Nature, 550, 80

Jin S., et al., 2024, MNRAS, 530, 2688

John T. L., 1975a, MNRAS, 170, 5

John T. L., 1975b, MNRAS, 172, 305

John T. L., 1994, MNRAS, 269, 871

Jonsell K., Barklem P. S., Gustafsson B., Christlieb N., Hill V., Beers T. C., Holmberg J., 2006, A&A, 451, 651

Jönsson H., et al., 2020, AJ, 160, 120

Jordan George C. I., Perets H. B., Fisher R. T., van Rossum D. R., 2012, ApJ, 761, L23

Joyce M., Tayar J., 2023, Galaxies, 11, 75

Karakas A. I., 2010, MNRAS, 403, 1413

Karakas A. I., Lattanzio J. C., 2014, Publications of the Astronomical Society of Australia, 31, e030

Karzas W. J., Latter R., 1961, ApJS, 6, 167

Kaulakys B., 1991, Journal of Physics B Atomic Molecular Physics, 24, L127

Keller S. C., et al., 2007, PASA, 24, 1

Kennicutt Robert C. J., 1998, ApJ, 498, 541

Khokhlov A. M., 1991, A&A, 245, 114

Kippenhahn R., Weigert A., 1990, Stellar Structure and Evolution

Kippenhahn R., Weigert A., Weiss A., 2012, Stellar Structure and Evolution, 2 edn. Astronomy and Astrophysics Library, Springer Berlin, Heidelberg, doi:10.1007/978-3-642-30304-3

Kirby E. N., et al., 2019, ApJ, 881, 45

Kirchhoff G., 1860, Annalen der Physik, 185, 148

Klessen R. S., Glover S. C. O., 2023, ARA&A, 61, 65

Klevas J., Wedemeyer S., Kučinskas A., Ludwig H. G., 2017, Mem. Soc. Astron. Italiana, 88, 100

Kobayashi C., Tsujimoto T., Nomoto K., 2000, ApJ, 539, 26

Kobayashi C., Umeda H., Nomoto K., Tominaga N., Ohkubo T., 2006, ApJ, 653, 1145

Kobayashi C., Karakas A. I., Umeda H., 2011, MNRAS, 414, 3231

Kobayashi C., Leung S.-C., Nomoto K., 2020a, ApJ, 895, 138

Kobayashi C., Karakas A. I., Lugaro M., 2020b, ApJ, 900, 179

Kollmeier J. A., et al., 2017, arXiv e-prints, p. arXiv:1711.03234

Kollmeier J., et al., 2019, in Bulletin of the American Astronomical Society. p. 274

Korol V., Rossi E. M., Groot P. J., Nelemans G., Toonen S., Brown A. G. A., 2017, MNRAS, 470, 1894

Kovalev M., Bergemann M., Ting Y.-S., Rix H.-W., 2019, A&A, 628, A54

Kromer M., et al., 2013a, MNRAS, 429, 2287

Kromer M., et al., 2013b, ApJ, 778, L18

Kromer M., et al., 2015, MNRAS, 450, 3045

Kromer M., Ohlmann S., Röpke F. K., 2017, Mem. Soc. Astron. Italiana, 88, 312

Kroupa P., 2001, MNRAS, 322, 231

Kurucz R. L., 1979, ApJS, 40, 1

Kurucz R. L., 2013, ATLAS12: Opacity sampling model atmosphere program, Astrophysics Source Code Library, record ascl:1303.024

Kurucz R. L., Furenlid I., Brault J., Testerman L., 1984, Solar flux atlas from 296 to 1300 nm. National Solar Observatory Atlas, Sunspot, New Mexico: National Solar Observatory, 1984

Kurucz R. L., van Dishoeck E. F., Tarafdar S. P., 1987, ApJ, 322, 992

Kuuttila J., Gilfanov M., Seitenzahl I. R., Woods T. E., Vogt F. P. A., 2019, MNRAS, 484, 1317

Kučinskas A., Klevas J., Ludwig H. G., Bonifacio P., Steffen M., Caffau E., 2018, A&A, 613, A24

Labbé I., et al., 2023, Nature, 616, 266

Lach F., Röpke F. K., Seitenzahl I. R., Coté B., Gronow S., Ruiter A. J., 2020, A&A, 644, A118

Lagae C., Amarsi A. M., Rodríguez Díaz L. F., Lind K., Nordlander T., Hansen T. T., Heger A., 2023, A&A, 672, A90

Lai D. K., Johnson J. A., Bolte M., Lucatello S., 2007, ApJ, 667, 1185

Lang D., Hogg D. W., Schlegel D. J., 2016, AJ, 151, 36

Larsen S. S., Eitner P., Magg E., Bergemann M., Moltzer C. A. S., Brodie J. P., Romanowsky A. J., Strader J., 2022, A&A, 660, A88

LeVeque R. J., 1997, Journal of Computational Physics, 131, 327

Leavitt H. S., Pickering E. C., 1912, Harvard College Observatory Circular, 173, 1

Lee Y. S., et al., 2013, AJ, 146, 132

Leenaarts J., Carlsson M., 2009, in Lites B., Cheung M., Magara T., Mariska J., Reeves K., eds, Astronomical Society of the Pacific Conference Series Vol. 415, The Second Hinode Science Meeting: Beyond Discovery-Toward Understanding. p. 87

Li G., Harrison J. J., Ram R. S., Western C. M., Bernath P. F., 2012, Journal of Quantitative Spectroscopy and Radiative Transfer, 113, 67

Limongi M., Chieffi A., 2018, ApJS, 237, 13

Limongi M., Chieffi A., Bonifacio P., 2003, ApJ, 594, L123

Lind K., Amarsi A. M., 2024, arXiv e-prints, p. arXiv:2401.00697

Lind K., Asplund M., Barklem P. S., 2009, A&A, 503, 541

Lind K., Bergemann M., Asplund M., 2012, MNRAS, 427, 50

Lind K., Melendez J., Asplund M., Collet R., Magic Z., 2013, A&A, 554, A96

Lind K., et al., 2017, MNRAS, 468, 4311

Liu C., et al., 2020, arXiv e-prints, p. arXiv:2005.07210

Livne E., 1990, ApJ, 354, L53

Löhner-Böttcher J., Schmidt W., Schlichenmaier R., Steinmetz T., Holzwarth R., 2019, A&A, 624, A57

López-Corredoira M., Melia F., Wei J. J., Gao C. Y., 2024, ApJ, 970, 63

Lucatello S., Tsangarides S., Beers T. C., Carretta E., Gratton R. G., Ryan S. G., 2005, ApJ, 625, 825

Ludwig H.-G., 1992, PhD Thesis, Kiel University

Ludwig H. G., Steffen M., 2016, Astronomische Nachrichten, 337, 844

Ludwig H. G., Steffen M., Rauch T., 1990, in Astronomische Gesellschaft Abstract Series. p. 38

Ludwig H. G., Caffau E., Steffen M., Freytag B., Bonifacio P., Kučinskas A., 2009a, Mem. Soc. Astron. Italiana, 80, 711

Ludwig H. G., Behara N. T., Steffen M., Bonifacio P., 2009b, A&A, 502, L1

Ludwig H. G., Steffen M., Freytag B., 2023, A&A, 679, A65

Magg E., 2023, Constraining stellar physics with the NLTE radiative transfer , Heidelberg University, doi:10.11588/heidok.00032934

Magg M., Hartwig T., Chen L.-H., Tarumi Y., 2022a, A-SLOTH: Semi-analytical model to connect first stars and galaxies to observables, Astrophysics Source Code Library, record ascl:2209.001

Magg E., et al., 2022b, A&A, 661, A140

Magic Z., Collet R., Asplund M., Trampedach R., Hayek W., Chiavassa A., Stein R. F., Nordlund Å., 2013a, A&A, 557, A26

Magic Z., Collet R., Hayek W., Asplund M., 2013b, A&A, 560, A8

Magic Z., Chiavassa A., Collet R., Asplund M., 2015, A&A, 573, A90

Majewski S. R., et al., 2007, in American Astronomical Society Meeting Abstracts. p. 132.08

Majewski S. R., et al., 2017, AJ, 154, 94

Marigo P., 2001, A&A, 370, 194

Mashonkina L., Gehren T., 2000, A&A, 364, 249

Mashonkina L. I., Romanovskaya A. M., 2022, Astronomy Letters, 48, 455

Mashonkina L., et al., 2008, A&A, 478, 529

Mashonkina L., et al., 2023, MNRAS, 523, 2111

Masseron T., et al., 2006, A&A, 455, 1059

Masseron T., Johnson J. A., Plez B., van Eck S., Primas F., Goriely S., Jorissen A., 2010, A&A, 509, A93

Masseron T., Johnson J. A., Lucatello S., Karakas A., Plez B., Beers T. C., Christlieb N., 2012, ApJ, 751, 14

Masseron T., et al., 2014, A&A, 571, A47

Matteucci F., 2001, The Chemical Evolution of the Galaxy, 1 edn. Astrophysics and Space Science Library, Springer Dordrecht, doi:10.1007/978-94-010-0967-6

Matteucci F., 2003, Models of Chemical Evolution (arXiv:astro-ph/0306034), https://arxiv.org/abs/astro-ph/0306034

Matteucci F., 2004, in McWilliam A., Rauch M., eds, Origin and Evolution of the Elements. p. 85 (arXiv:astro-ph/0306034)

Matteucci F., 2014, Saas-Fee Advanced Course, 37, 145

Matteucci F., 2016, in Journal of Physics Conference Series. IOP, p. 012004 (arXiv:1602.01004), doi:10.1088/1742-6596/703/1/012004

Matteucci F., Greggio L., 1986, A&A, 154, 279

Matteucci F., Panagia N., Pipino A., Mannucci F., Recchi S., Della Valle M., 2006, Monthly Notices of the Royal Astronomical Society, 372, 265

McClure R. D., Woodsworth A. W., 1990, ApJ, 352, 709

McLaughlin B. M., Stancil P. C., Sadeghpour H. R., Forrey R. C., 2017, Journal of Physics B Atomic Molecular Physics, 50, 114001

McWilliam A., Piro A. L., Badenes C., Bravo E., 2018, ApJ, 857, 97

Mészáros S., et al., 2012, AJ, 144, 120

Meynet G., Ekström S., Maeder A., 2006, A&A, 447, 623

Mihalas D., 1965, ApJS, 9, 321

Mihalas D., Dappen W., Hummer D. G., 1988, ApJ, 331, 815

Mihos J. C., Hernquist L., 1996, ApJ, 464, 641

Mishenina T., Gorbaneva T., Pignatari M., Thielemann F. K., Korotin S. A., 2015, MNRAS, 454, 1585

Mosumgaard J. R., Jørgensen A. C. S., Weiss A., Silva Aguirre V., Christensen-Dalsgaard J., 2020, MNRAS, 491, 1160

Neckel H., Labs D., 1994, Sol. Phys., 153, 91

Nelemans G., Yungelson L. R., Portegies Zwart S. F., 2001, A&A, 375, 890

Ness M., Hogg D. W., Rix H. W., Ho A. Y. Q., Zasowski G., 2015, ApJ, 808, 16

Nishimura N., Takiwaki T., Thielemann F.-K., 2015, ApJ, 810, 109

Nissen P. E., Schuster W. J., 1997, A&A, 326, 751

Nissen P. E., Amarsi A. M., Skúladóttir Á., Schuster W. J., 2024, A&A, 682, A116

Nomoto K., Tominaga N., Umeda H., Kobayashi C., Maeda K., 2006, Nuclear Physics A, 777, 424

Nomoto K., Kobayashi C., Tominaga N., 2013, ARA&A, 51, 457

Nordlander T., Amarsi A. M., Lind K., Asplund M., Barklem P. S., Casey A. R., Collet R., Leenaarts J., 2017, A&A, 597, A6

Nordlund A., 1982, A&A, 107, 1

Nordlund Å., Galsgaard K., 1995, Technical report, A 3D MHD code for Parallel Computers, `http://www.astro.ku.dk/~kg/Papers/MHD_code.ps.gz`. Niels Bohr Institute, University of Copenhagen, `http://www.astro.ku.dk/~kg/Papers/MHD_code.ps.gz`

Nordlund Å., Stein R. F., Asplund M., 2009, Living Reviews in Solar Physics, 6, 2

Nordlund Å., Ramsey J. P., Popovas A., Küffmeier M., 2018, MNRAS, 477, 624

Norris J. E., Yong D., 2019, ApJ, 879, 37

Norris J. E., Christlieb N., Korn A. J., Eriksson K., Bessell M. S., Beers T. C., Wisotzki L., Reimers D., 2007, ApJ, 670, 774

Ohkubo T., Umeda H., Maeda K., Nomoto K., Suzuki T., Tsuruta S., Rees M. J., 2006, ApJ, 645, 1352

Olander T., Heiter U., Kochukhov O., 2021, A&A, 649, A103

Olver P. J., 2014, Introduction to Partial Differential Equations, 1 edn. Undergraduate Texts in Mathematics, Springer Cham, doi:10.1007/978-3-319-02099-0

Pakmor R., Kromer M., Taubenberger S., Sim S. A., Röpke F. K., Hillebrandt W., 2012, ApJ, 747, L10

Pakmor R., Zenati Y., Perets H. B., Toonen S., 2021, MNRAS, 503, 4734

Pakmor R., et al., 2022, MNRAS, 517, 5260

Palla M., 2021, MNRAS, 503, 3216

Payne-Gaposchkin C. H., 1925, Stellar atmospheres: A contribution to the observational study of high temperature in the reversing layers of stars, Radcliffe College, United States

Peach G., 1970, MmRAS, 73, 1

Perdomo García A., Vitas N., Khomenko E., Collados M., Allende Prieto C., Hubeny I., Osorio Y., 2023, A&A, 675, A160

Perdomo García A., Vitas N., Khomenko E., Collados M., 2025, arXiv e-prints, p. arXiv:2507.00636

Perego A., Hempel M., Fröhlich C., Ebinger K., Eichler M., Casanova J., Liebendörfer M., Thielemann F. K., 2015, ApJ, 806, 275

Pereira T. M. D., Asplund M., Collet R., Thaler I., Trampedach R., Leenaarts J., 2013, A&A, 554, A118

Perets H. B., Zenati Y., Toonen S., Bobrick A., 2019, arXiv e-prints, p. arXiv:1910.07532

Perivolaropoulos L., Skara F., 2022, New Astronomy Reviews, 95, 101659

Perlmutter S., et al., 1997, in American Astronomical Society Meeting Abstracts. p. 85.04 (`arXiv:astro-ph/9812473`), doi:10.48550/arXiv.astro-ph/9812473

Phillips M. M., 1993, ApJ, 413, L105

Pietrow A. G. M., Hoppe R., Bergemann M., Calvo F., 2023, A&A, 672, L6

Pinna F., Walo-Martín D., Grand R. J. J., Martig M., Fragkoudi F., Gómez F. A., Marinacci F., Pakmor R., 2024, A&A, 683, A236

Placco V., Beers T. C., 2016, in American Astronomical Society Meeting Abstracts #227. p. 121.02

Placco V. M., et al., 2010, AJ, 139, 1051

Placco V. M., Frebel A., Beers T. C., Stancliffe R. J., 2014, ApJ, 797, 21

Placco V. M., et al., 2016, ApJ, 833, 21

Planck Collaboration et al., 2016, A&A, 594, A13

Plez B., 2008, Physica Scripta Volume T, 133, 014003

Plez B., 2012, Turbospectrum: Code for spectral synthesis, Astrophysics Source Code Library, record ascl:1205.004 (ascl:1205.004)

Plez B., Brett J. M., Nordlund A., 1992, A&A, 256, 551

Popa S. A., Hoppe R., Bergemann M., Hansen C. J., Plez B., Beers T. C., 2023, A&A, 670, A25

Portinari L., Chiosi C., Bressan A., 1998, A&A, 334, 505

Prandtl L., 1925, Zeitschrift Angewandte Mathematik und Mechanik, 5, 136

Prantzos N., 2008, in Charbonnel C., Zahn J. P., eds, EAS Publications Series Vol. 32, EAS Publications Series. pp 311–356 (arXiv:0709.0833), doi:10.1051/eas:0832009

Prantzos N., et al., 2011, Reviews of Modern Physics, 83, 1001

Prantzos N., Abia C., Limongi M., Chieffi A., Cristallo S., 2018, MNRAS, 476, 3432

Pruzhinskaya M. V., Novinskaya A. K., Pauna N., Rosnet P., 2020, MNRAS, 499, 5121

Przybylski D., Cameron R., Solanki S. K., Rempel M., Leenaarts J., Anusha L. S., Witzke V., Shapiro A. I., 2022, A&A, 664, A91

Randich S., et al., 2022, A&A, 666, A121

Rauer H., et al., 2014, Experimental Astronomy, 38, 249

Reimers D., 1990, The Messenger, 60, 13

Rempel M., 2014, ApJ, 789, 132

Rempel M., 2017, ApJ, 834, 10

Riess A. G., Press W. H., Kirshner R. P., 1995, ApJ, 438, L17

Riess A. G., et al., 1998, AJ, 116, 1009

Riess A. G., et al., 2018, ApJ, 861, 126

Riess A. G., et al., 2021a, arXiv e-prints, p. arXiv:2112.04510

Riess A. G., Casertano S., Yuan W., Bowers J. B., Macri L., Zinn J. C., Scolnic D., 2021b, ApJ, 908, L6

Riva F., Steiner O., Freytag B., 2024, A&A, 684, A7

Rodríguez Díaz L. F., et al., 2024, A&A, 688, A212

Roe P. L., 1986, Annual Review of Fluid Mechanics, 18, 337

Roederer I. U., Preston G. W., Thompson I. B., Shectman S. A., Sneden C., Burley G. S., Kelson D. D., 2014, AJ, 147, 136

Romano D., Karakas A. I., Tosi M., Matteucci F., 2010, A&A, 522, A32

Röpke F. K., et al., 2012, ApJ, 750, L19

Rosenthal C. S., Christensen-Dalsgaard J., Nordlund Å., Stein R. F., Trampedach R., 1999, A&A, 351, 689

Rosswog S., Korobkin O., Arcones A., Thielemann F. K., Piran T., 2014, MNRAS, 439, 744

Różański T., Ting Y.-S., Jabłońska M., 2025, ApJ, 980, 66

Ruchti G. R., et al., 2011, ApJ, 737, 9

Ruchti G. R., Bergemann M., Serenelli A., Casagrande L., Lind K., 2013, MNRAS, 429, 126

Ruiter A. J., 2020, arXiv e-prints, p. arXiv:2001.02947

Ruiter A. J., Seitenzahl I. R., 2025, A&A Rev., 33, 1

Ruiter A. J., Belczynski K., Fryer C., 2009, ApJ, 699, 2026

Ruiter A. J., Belczynski K., Benacquista M., Larson S. L., Williams G., 2010, ApJ, 717, 1006

Ruiter A. J., Belczynski K., Sim S. A., Hillebrandt W., Fryer C. L., Fink M., Kromer M., 2011, MNRAS, 417, 408

Ruiter A. J., et al., 2013, MNRAS, 429, 1425

Ruiter A. J., Belczynski K., Sim S. A., Seitenzahl I. R., Kwiatkowski D., 2014, MNRAS, 440, L101

Ruland F., Holweger H., Griffin R., Griffin R. F., Biehl D., 1980, A&A, 92, 70

Rutten R. J., 2003, Radiative Transfer in Stellar Atmospheres

Rybicki G. B., Hummer D. G., 1992, A&A, 262, 209

Rybizki J., Just A., Rix H.-W., 2017, A&A, 605, A59

Samadi R., Nordlund Å., Stein R. F., Goupil M. J., Roxburgh I., 2003, A&A, 404, 1129

Sander A. A. C., 2017, in Eldridge J. J., Bray J. C., McClelland L. A. S., Xiao L., eds, IAU Symposium Vol. 329, The Lives and Death-Throes of Massive Stars. pp 215–222 (arXiv:1702.04798), doi:10.1017/S1743921317003362

Sander A. A. C., Hamann W. R., Todt H., Hainich R., Shenar T., 2017, A&A, 603, A86

Sanders J. L., Belokurov V., Man K. T. F., 2021, MNRAS, 506, 4321

Sbordone L., et al., 2010, A&A, 522, A26

Schmidt M., 1959, ApJ, 129, 243

Schönrich R., Bergemann M., 2014, MNRAS, 443, 698

Schwarzschild M., 1958, Structure and evolution of the stars.

Schönrich R., Binney J., 2009, Monthly Notices of the Royal Astronomical Society, 396, 203

Scott P., Asplund M., Grevesse N., Bergemann M., Sauval A. J., 2015, A&A, 573, A26

Seaton M. J., Yan Y., Mihalas D., Pradhan A. K., 1994, MNRAS, 266, 805

Seitenzahl I. R., et al., 2013a, MNRAS, 429, 1156

Seitenzahl I. R., Cescutti G., Röpke F. K., Ruiter A. J., Pakmor R., 2013b, A&A, 559, L5

Seitenzahl I. R., Ghavamian P., Laming J. M., Vogt F. P. A., 2019, Phys. Rev. Lett., 123, 041101

Sellwood J. A., Binney J. J., 2002, MNRAS, 336, 785

Semenova E., et al., 2020, A&A, 643, A164

Shank D., et al., 2022, ApJ, 926, 26

Shappee B. J., Kochanek C. S., Stanek K. Z., 2013, ApJ, 765, 150

Shen K. J., Kasen D., Miles B. J., Townsley D. M., 2018, ApJ, 854, 52

Shen K. J., Blondin S., Kasen D., Dessart L., Townsley D. M., Boos S., Hillier D. J., 2021a, ApJ, 909, L18

Shen K. J., Boos S. J., Townsley D. M., Kasen D., 2021b, ApJ, 922, 68

Short C. I., Hauschildt P. H., 2005, ApJ, 618, 926

Sim S. A., 2007, MNRAS, 375, 154

Sim S. A., Röpke F. K., Hillebrandt W., Kromer M., Pakmor R., Fink M., Ruiter A. J., Seitenzahl I. R., 2010, ApJ, 714, L52

Sir Arthur S. Eddington 1926, The Internal Constitution of the Stars

Skrutskie M. F., et al., 2006, AJ, 131, 1163

Smith M. C., Sijacki D., Shen S., 2018, MNRAS, 478, 302

Sneden C., et al., 2003, ApJ, 591, 936

Sneden C., Cowan J. J., Kobayashi C., Pignatari M., Lawler J. E., Den Hartog E. A., Wood M. P., 2016, ApJ, 817, 53

Southworth J., 2008, MNRAS, 386, 1644

Spite F., Spite M., 1982a, A&A, 115, 357

Spite M., Spite F., 1982b, Nature, 297, 483

Spite M., Caffau E., Bonifacio P., Spite F., Ludwig H. G., Plez B., Christlieb N., 2013, A&A, 552, A107

Springel V., Di Matteo T., Hernquist L., 2005, MNRAS, 361, 776

Starkenburg E., et al., 2013, A&A, 549, A88

Starkenburg E., Shetrone M. D., McConnachie A. W., Venn K. A., 2014, MNRAS, 441, 1217

Starkenburg E., et al., 2017, MNRAS, 471, 2587

Stein R. F., Nordlund Å., 1998, ApJ, 499, 914

Stein R. F., Nordlund Å., 2001, ApJ, 546, 585

Steinmetz M., et al., 2020, AJ, 160, 83

Storm N., Bergemann M., 2023, MNRAS, 525, 3718

Storm N., et al., 2024, A&A, 683, A200

Storm N., et al., 2025, MNRAS, 538, 3284

Straumit I., et al., 2022, AJ, 163, 236

Strickland D. K., Heckman T. M., 2009, ApJ, 697, 2030

Struve O., Elvey C. T., 1934, ApJ, 79, 409

Suda T., Aikawa M., Machida M. N., Fujimoto M. Y., Iben Jr. I., 2004, ApJ, 611, 476

Suda T., et al., 2008, PASJ, 60, 1159

Suda T., Yamada S., Katsuta Y., Komiya Y., Ishizuka C., Aoki W., Fujimoto M. Y., 2011, MNRAS, 412, 843

Suda T., et al., 2017, PASJ, 69, 76

Taubenberger S., 2017, The Extremes of Thermonuclear Supernovae. p. 317, doi:10.1007/978-3-319-21846-5_37

Tennyson J., et al., 2016, Journal of Molecular Spectroscopy, 327, 73

Themeßl N., et al., 2018, MNRAS, 478, 4669

Thévenin F., Idiart T. P., 1999, ApJ, 521, 753

Timmes F. X., Woosley S. E., Weaver T. A., 1995, ApJS, 98, 617

Ting Y.-S., Conroy C., Rix H.-W., Cargile P., 2019, ApJ, 879, 69

Tinsley B. M., 1980, Fund. Cosmic Phys., 5, 287

Tominaga N., Umeda H., Nomoto K., 2007, ApJ, 660, 516

Toonen S., Perets H. B., Hamers A. S., 2018, A&A, 610, A22

Tornatore L., Borgani S., Dolag K., Matteucci F., 2007, MNRAS, 382, 1050

Toro E. F., 1997a, The HLL and HLLC Riemann Solvers. Springer Berlin Heidelberg, Berlin, Heidelberg, pp 293–311, doi:10.1007/978-3-662-03490-3_10, https://doi.org/10.1007/978-3-662-03490-3_10

Toro E. F., 1997b, Riemann Solvers and Numerical Methods for Fluid Dynamics: A Practical Introduction, 1 edn. Springer Berlin, Heidelberg, doi:10.1007/978-3-662-03490-3

Trueman T. C. L., Pignatari M., Cseh B., Keegans J. D., Côté B., Gibson B. K., 2025, A&A, 696, A164

Tully R. B., Fisher J. R., 1977, A&A, 54, 661

Uitenbroek H., Criscuoli S., 2011, ApJ, 736, 69

Umeda H., Nomoto K., 2002, ApJ, 565, 385

Umeda H., Tominaga N., Ohkubo T., Nomoto K., 2005, in Terasawa M., Kubano S., Kishida T., Kajino T., Motobayashi T., Nomato K., eds, Origin of Matter and Evolution of Galaxies. pp 163–174, doi:10.1142/9789812702739_0016

Vögler A., Schüssler M., 2007, A&A, 465, L43

Vögler A., Bruls J. H. M. J., Schüssler M., 2004, A&A, 421, 741

Vögler A., Shelyag S., Schüssler M., Cattaneo F., Emonet T., Linde T., 2005, A&A, 429, 335

Voronov Y. V., Yakovleva S. A., Belyaev A. K., 2022, ApJ, 926, 173

Wagoner R. V., Fowler W. A., Hoyle F., 1967, ApJ, 148, 3

Wanajo S., Müller B., Janka H.-T., Heger A., 2018, ApJ, 852, 40

Wang T., Burrows A., 2024, ApJ, 962, 71

Wedemeyer S., Ludwig H. G., Steiner O., 2013, Astronomische Nachrichten, 334, 137

Wedemeyer S., Kučinskas A., Klevas J., Ludwig H.-G., 2017, A&A, 606, A26

Weinberg D. H., Andrews B. H., Freudenburg J., 2017, ApJ, 837, 183

Weiss A., Schlattl H., 2008, apss, 316, 99

Werner K., Dreizler S., Rauch T., 2012, TMAP: Tübingen NLTE Model-Atmosphere Package, Astrophysics Source Code Library, record ascl:1212.015

Williamson J. H., 1980, Journal of Computational Physics, 35, 48

Wilson J. C., et al., 2019, PASP, 131, 055001

Wisotzki L., Christlieb N., Bade N., Beckmann V., Köhler T., Vanelle C., Reimers D., 2000, A&A, 358, 77

Witzke V., Duehnen H. B., Shapiro A. I., Przybylski D., Bhatia T. S., Cameron R., Solanki S. K., 2023, A&A, 669, A157

Wolf B. E., 1983, A&A, 127, 93

Woosley S. E., Weaver T. A., 1995, ApJS, 101, 181

Woosley S. E., Heger A., Weaver T. A., 2002, Reviews of Modern Physics, 74, 1015

Woosley S. E., Kasen D., Blinnikov S., Sorokina E., 2007, ApJ, 662, 487

Wyse R. F. G., 2016, in Skillen I., Balcells M., Trager S., eds, Astronomical Society of the Pacific Conference Series Vol. 507, Multi-Object Spectroscopy in the Next Decade: Big Questions, Large Surveys, and Wide Fields. p. 13 (arXiv:1604.04745), doi:10.48550/arXiv.1604.04745

Xiang M., et al., 2019, ApJS, 245, 34

Yang J., Turner M. S., Steigman G., Schramm D. N., Olive K. A., 1984, ApJ, 281, 493

Yanny B., et al., 2009, AJ, 137, 4377

Yates R. M., Henriques B., Thomas P. A., Kauffmann G., Johansson J., White S. D. M., 2013, MNRAS, 435, 3500

Yoon J., et al., 2016, ApJ, 833, 20

Yoon J., et al., 2018, The Astrophysical Journal, 861, 146

Yoon J., Beers T. C., Tian D., Whitten D. D., 2019, ApJ, 878, 97

Young M. E., Short C. I., 2014, ApJ, 787, 43

Yu J., Huber D., Bedding T. R., Stello D., Hon M., Murphy S. J., Khanna S., 2018, The Astrophysical Journal Supplement Series, 236, 42

Zatsarinny O., Bartschat K., 2013, Journal of Physics B Atomic Molecular Physics, 46, 112001

Zhou Y., Asplund M., Collet R., 2019, ApJ, 880, 13

de Jong R. S., et al., 2019, The Messenger, 175, 3

de los Reyes M. A. C., Kirby E. N., Seitenzahl I. R., Shen K. J., 2020, ApJ, 891, 85

van Leer B., 1977, Journal of Computational Physics, 23, 276

van Regemorter H., 1962, ApJ, 136, 906